

Connecting Theory to Observations in 21cm  
Cosmology: Development of Theoretical Tools and  
Mitigation of Systematics

Michael Pagano, Department of Physics

McGill University, Montreal

October, 2022

A thesis submitted to McGill University in partial fulfillment of the requirements

of the degree of

PhD of Physics

©MICHAEL PAGANO, October 2022



# Abstract

The Epoch of Reionization (EoR) is the period of our Universe’s history where the neutral hydrogen in the Inter Galactic Medium (IGM) is ionized. Despite its importance to our understanding of the Universe, it remains observationally unconstrained and poorly understood. One method to directly observe the EoR is to measure the 21cm photons emitted by the hyperfine transition of neutral hydrogen when the electron flips its spin relative to the atomic nucleus. Mapping the 21cm line in the IGM as a function of redshift can directly probe the EoR. In this thesis we consider two methods to measure the 21cm line. One method is to measure the spatial fluctuations of the 21cm brightness in the IGM using interferometric instruments while another method is to spatially average over the 21cm fluctuations using a global signal experiment. Both of these methods are hindered by systematics such as galactic synchrotron emission “foregrounds”. In this thesis we examine a variety of topics concerning both types of experiments, ranging from the systematic mitigation to theoretical interpretation. First, we study how the amplitude and structure of the errors in our radio foreground models affect forward modeled global signal experiments. We find that if unaccounted for, these errors can make unbiased recovery of the 21cm signal impossible. To remedy this, we introduce a Bayesian framework that can account for errors in the foreground models of global 21cm signal experiments. In this thesis we also consider the systematics that radio frequency interference (RFI) can introduce into 21cm interferometric measurements. We introduce a convolutional neural network that is capable of restoring or “inpainting” RFI corrupted data into the visibilities of 21cm interferometric data. Along with existing RFI inpainting techniques, we characterize the errors that inpainting introduces into the data analysis pipeline and then establish a relationship between each inpainting technique and their corresponding errors in the 21cm power

spectrum. These types of systematics (including but not limited to) have made the 21cm line difficult to measure and has therefore spurred an interest in probing the EoR using indirect means. Thus we also explore using Lyman Alpha Emitters (LAEs), as well as class of bright radio transients Fast Radio Bursts (FRBs) as an method to probe the astrophysics and morphological properties of the EoR. To quantify the morphological properties of the EoR we introduce a parameter  $\beta$  which can track the density-ionization correlation - a crucial descriptor of the EoR morphology. We then forecast the types of constraints that we can place on parametrizations commonly used to describe first-generation galaxies, as well as  $\beta$  by independently using FRBs and LAEs as probes. We find that with measurement of 100 high-redshift FRBs we can rule out scenarios where the Universe is entirely neutral at  $z = 10$  with 68% credibility. We also find that measurements of LAE statistics alone cannot distinguish between different density-ionization models at 68% credibility. However when the combining statistical measurements of LAEs with measurements of the 21cm power spectrum at the midpoint of ionization we can rule out classes of density-ionization correlation at 99% credibility.

# Abrégé

L'Époque de Réionisation (EoR) est la période de l'histoire de notre Univers où l'hydrogène neutre dans le Milieu Inter Galactique (IGM) est ionisé. Malgré son importance pour notre compréhension de l'Univers, il reste sans contrainte d'observation et mal compris. Une méthode pour observer directement l'EoR consiste à mesurer les photons de 21 cm émis par la transition hyperfine de l'hydrogène neutre lorsque l'électron inverse son spin par rapport au noyau atomique. La cartographie de la ligne de 21 cm dans l'IGM en fonction du décalage vers le rouge peut sonder directement l'EoR. Dans cette thèse, nous considérons deux méthodes pour mesurer la ligne de 21 cm. Une méthode consiste à mesurer les fluctuations spatiales de la luminosité de 21 cm dans l'IGM à l'aide d'instruments interférométriques, tandis qu'une autre méthode consiste à faire une moyenne spatiale sur les fluctuations de 21 cm à l'aide d'une expérience de signal global. Ces deux méthodes sont entravées par des systématiques telles que les "foregrounds" d'émission synchrotron galactique.

Dans cette thèse, nous examinons une variété de sujets concernant les deux types d'expériences, allant de l'atténuation systématique à l'interprétation théorique. Tout d'abord, nous étudions comment l'amplitude et la structure des erreurs dans nos modèles de premier plan radio affectent les expériences de signal global modélisées en avant. Nous constatons que si elles ne sont pas prises en compte, ces erreurs peuvent rendre impossible une récupération impartiale du signal de 21 cm. Pour remédier à cela, nous introduisons un cadre bayésien qui peut tenir compte des erreurs dans les modèles de premier plan des expériences globales de signal de 21 cm. Dans cette thèse, nous considérons également la systématique que les interférences radiofréquence (RFI) peuvent introduire dans les mesures interférométriques à 21 cm. Nous introduisons un réseau de neurones

convolutifs capable de restaurer ou de “ peindre ” des données RFI corrompues dans les visibilités de données interférométriques de 21 cm. Parallèlement aux techniques d’inpainting RFI existantes, nous caractérisons les erreurs que l’inpainting introduit dans le pipeline d’analyse de données, puis établissons une relation entre chaque technique d’inpainting et leurs erreurs correspondantes dans le spectre de puissance de 21 cm. Ces types de systématique (y compris, mais sans s’y limiter) ont rendu la ligne de 21 cm difficile à mesurer et ont donc suscité un intérêt pour sonder l’EoR en utilisant des moyens indirects. Ainsi, nous explorons également l’utilisation des émetteurs Lyman Alpha (LAE), ainsi que la classe des transitoires radio brillants Fast Radio Bursts (FRB) comme méthode pour sonder les propriétés astrophysiques et morphologiques de l’EoR.

Pour quantifier les propriétés morphologiques de l’EoR, nous introduisons un paramètre  $\beta$  qui peut suivre la corrélation densité-ionisation - un descripteur crucial de la morphologie de l’EoR. Nous prévoyons ensuite les types de contraintes que nous pouvons imposer aux paramétrisations couramment utilisées pour décrire les galaxies de première génération, ainsi qu’aux  $\beta$  en utilisant indépendamment les FRB et les LAE comme sondes. Nous constatons qu’avec la mesure de 100 FRB à décalage vers le rouge élevé, nous pouvons exclure les scénarios où l’Univers est entièrement neutre à  $z = 10$  avec une crédibilité de 68%. Nous constatons également que les mesures des statistiques LAE seules ne peuvent pas faire la distinction entre différents modèles de densité-ionisation à une crédibilité de 68%. Cependant, en combinant les mesures statistiques des LAE avec les mesures du spectre de puissance de 21 cm au point médian de l’ionisation, nous pouvons exclure des classes de corrélation densité-ionisation avec une crédibilité de 99

# Acknowledgements

An unbelievable journey. I would like to start by thanking my super-supervisor, Adrian Liu. Thank you to him for supporting me, guiding me and believing in me throughout these four years. His passion for cosmology has definitely transferred over to me. There is too much to say, so I'll just say that if given the ability I could not design a better supervisor<sup>1</sup>. Adrian's first year as a professor was my first year as a doctoral student and I have been so lucky to learn under him; I could not be prouder to be his first doctorate student.

Thank you to my academic siblings Hannah Fronenberg & Lisa McBride whom have made the term "academic family" less academic and more family. Just like family, they will be in my life forever. Thank you to Jordan Mirocha, who was almost like a second supervisor to me and carried me throughout my first year. A big shout out to Peter Sims for being a great mentor, Adélie Gorce for always looking out for me, and Bobby Pascua and Kai-Feng Chen (whom I wished had entered our group earlier!) for the warm support. To Andrei Mesinger, whom has made this last year fun and exciting, thank you for making me look towards the future.

**This thesis is devoted to all that made it possible:**

My grandfather, Amadio D'Antonio, who is responsible for my being a cosmologist and lived to me see start my doctorate degree. My family, who supported me, encouraged me, and most of all made it possible for me to focus on cosmology. It is not an exaggeration to say that this thesis would never exist without the support given to me by my parents, Silvia & Ralph Pagano, and my brother and sister, Chris & Sandra. Of course, my life partner in crime, Kelly Foran, who has loved

---

<sup>1</sup>Somehow along the way, I've been transformed from a theory minded person to a statistics minded person - wow!

me, supported me and made it possible for me to devote myself to this work (thanks as well to the Foran family for putting up with my work schedule!)

Above all else, this thesis is devoted to my daughter, Nova, whom came into my life somewhere between Chapter 3 and Chapter 4. Her love of exploration and pure faith in me have been my primary motivators throughout the last two years. I look forward to the day when I can explain this all to her and I hope it makes her proud<sup>2</sup>.

---

<sup>2</sup>And who knows, by the time you read this, maybe we will have detected reionization!

# Table of Contents

Abstract . . . . .	i
Abrégé . . . . .	iii
Acknowledgements . . . . .	v
List of Figures . . . . .	xxvi
List of Tables . . . . .	xxvii
<b>1 Introduction</b>	<b>1</b>
1.1 Overview . . . . .	1
1.1.1 21cm Cosmology . . . . .	2
1.1.2 Direct Probes . . . . .	4
1.1.3 Global Signal . . . . .	6
1.1.4 Systematics . . . . .	9
1.1.5 Indirect Probes . . . . .	12
1.1.6 Sources of Ly $\alpha$ Emission . . . . .	13
1.1.7 Ly $\alpha$ Emission As a Probe of The EoR . . . . .	15
1.1.8 Roadmap . . . . .	17
Bibliography . . . . .	20
<b>2 Quantifying Density-Ionization Correlations with the 21cm Power Spectrum</b>	<b>36</b>
2.1 Introduction . . . . .	37
2.2 Simulations . . . . .	40
2.2.1 Inside-out Reionization Simulations Using 21cmFAST . . . . .	41

2.2.2	Outside-in Reionization Simulations using 21cmFAST . . . . .	43
2.2.3	Simulating Arbitrary Correlations using 21cmFAST . . . . .	46
2.3	Temperature Field Statistics . . . . .	48
2.3.1	Variation of $\Delta_{21}^2$ as a Function of $\beta$ . . . . .	50
2.3.2	Redshift Evolution of the Signal . . . . .	52
2.4	HERA Forecasts . . . . .	53
2.4.1	Fiducial Instrument and Sensitivity . . . . .	54
2.4.2	Markov Chain Monte Carlo Setup . . . . .	56
2.5	Results . . . . .	57
2.5.1	Scenario (i): Measurement of $\Delta_{21}^2$ Over Redshifts $z = 6$ to $z = 10$ . . . . .	58
2.5.2	Scenarios (ii) to (iv): Measurements at Specific Redshifts and Scales . . . . .	59
2.5.3	Scenario (v): Fiducial Outside-in Reionization . . . . .	62
2.5.4	Early Limits . . . . .	63
2.6	Conclusion . . . . .	64
	Bibliography . . . . .	66
<b>3</b>	<b>Constraining the Epoch of Reionization With Highly Dispersed Fast Radio Bursts</b>	<b>77</b>
3.1	Introduction . . . . .	78
3.2	Simulation . . . . .	83
3.2.1	EoR Parameters . . . . .	83
3.2.2	Morphological Parametrization of the EoR . . . . .	84
3.2.3	Dispersion Measure . . . . .	85
3.3	Models . . . . .	88
3.3.1	DM Distributions . . . . .	89
3.3.2	Astrophysical Signature on $\overline{DM}$ . . . . .	90
3.3.3	Morphological Signature on $\overline{DM}$ . . . . .	93
3.4	Forecasts . . . . .	94
3.4.1	Intrinsic FRB Statistics . . . . .	95
3.4.2	Mock Catalogue of FRBs . . . . .	96

3.4.3	MCMC setup . . . . .	97
3.5	Results . . . . .	99
3.5.1	Larger Sample Sizes . . . . .	100
3.5.2	Smaller Sample Sizes . . . . .	102
3.6	Conclusion . . . . .	102
	Bibliography . . . . .	105

## 4 Lyman Alpha Emitters and the 21cm Power Spectrum as Probes of Density-Ionization

	<b>Correlation in the Epoch of Reionization</b>	<b>116</b>
4.1	Introduction . . . . .	117
4.2	EoR Simulation . . . . .	121
4.2.1	Extending 21cmFAST to outside-in . . . . .	122
4.2.2	$\beta$ Parametrization . . . . .	122
4.2.3	Variation of $\Delta_{21}^2(z)$ as a Function of $\beta$ . . . . .	125
4.3	LAE Models . . . . .	125
4.3.1	$\text{Ly}\alpha$ Optical Depth . . . . .	126
4.3.2	LAE Intrinsic Luminosity . . . . .	128
4.4	Dependence of LAE Statistics on $\beta$ . . . . .	132
4.4.1	Dependence of the Observed LAE Luminosity Function on $\beta$ . . . . .	133
4.4.2	Dependence of the Mean Number Density of LAEs on $\beta$ . . . . .	135
4.4.3	Dependence of the ACF on $\beta$ . . . . .	136
4.5	Forecasts and Constraints . . . . .	142
4.5.1	Subaru Survey . . . . .	142
4.5.2	HERA instrument and Sensitivities . . . . .	143
4.5.3	Markov Chain Monte Carlo Setup for Subaru Constraints . . . . .	145
4.5.4	Markov Chain Monte Carlo Setup for Joint Subaru & 21cm Forecasts . . . . .	146
4.6	Results . . . . .	148
4.6.1	Subaru Constraints . . . . .	148
4.6.2	Joint Subaru & HERA Forecasts . . . . .	151

4.7 Conclusion . . . . .	152
Bibliography . . . . .	154

**5 Characterization Of Inpaint Residuals In Interferometric Measurements of the Epoch Of Reionization 167**

5.1 Introduction . . . . .	169
5.2 HERA Observations . . . . .	171
5.2.1 RFI Flagging . . . . .	171
5.2.2 Power Spectrum . . . . .	172
5.2.3 Datasets . . . . .	176
5.3 Inpainting Techniques . . . . .	178
5.3.1 CLEAN . . . . .	179
5.3.2 Least Squares Spectral Analysis (LSSA) . . . . .	181
5.3.3 Covariance-Based Inpainting (GPR) . . . . .	183
5.3.4 DPSS Least Squares (DPSS-LS) . . . . .	185
5.3.5 U-Paint Architecture . . . . .	186
5.4 Inpaint Models . . . . .	190
5.5 Statistical Analysis Methodology . . . . .	191
5.6 Inpaint Error Quantification in the Visibilities of Simulated Data . . . . .	193
5.6.1 Error Characterisation . . . . .	195
5.6.2 Thermal Noise . . . . .	198
5.7 Power Spectrum Error Characterization . . . . .	199
5.7.1 P1V Spectral Window . . . . .	200
5.7.2 Relationship Between Visibility and Power Spectrum Errors . . . . .	205
5.8 Application to Phase 1 HERA Data . . . . .	207
5.8.1 Flagged Regions & Analysis Configuration . . . . .	209
5.8.2 Results . . . . .	210
5.8.3 Power Spectrum . . . . .	213
5.9 Conclusion . . . . .	215

Bibliography . . . . .	216
<b>6 A General Bayesian Framework to Account for Foreground Map Errors in Global 21-cm Experiments</b>	<b>228</b>
6.1 Introduction . . . . .	229
6.2 Fiducial Instrument and Analysis Pipeline . . . . .	233
6.2.1 Bayesian Evidence . . . . .	234
6.2.2 Data Simulations . . . . .	235
6.2.3 Spectral Model . . . . .	237
6.3 Foreground Errors . . . . .	239
6.3.1 Methodology For Assessing Foreground Errors in the Analysis . . . . .	239
6.3.2 Error Scenarios . . . . .	240
6.3.3 Fiducial Error Models . . . . .	243
6.4 Modeling Amplitude Perturbations in Our Foreground Model . . . . .	247
6.4.1 Amplitude Scale Factors . . . . .	248
6.4.2 Prior Maps & Limitations . . . . .	249
6.4.3 Map Reconstruction . . . . .	251
6.5 Isolated Amplitude Errors . . . . .	252
6.5.1 Spectrally Uniform . . . . .	253
6.5.2 Effect of the Amplitude of Fluctuations $\Delta$ and Correlation Length $\theta_{\text{FWHM}}$ of the Errors on the Analysis . . . . .	256
6.5.3 Limiting Cases . . . . .	257
6.6 Spatially Varying Spectral Index . . . . .	259
6.6.1 Error Selection . . . . .	261
6.6.2 Correlations Between $N_a$ and $N_\beta$ . . . . .	262
6.7 Conclusion . . . . .	265
Bibliography . . . . .	267
<b>7 Conclusion</b>	<b>278</b>

# List of Figures

1.1	Timeline of the Universe’s history from the time of recombination at $z = 1100$ (left) to today $z = 0$ (right). After recombination, the cosmic dark ages mark a time before the first stars. The black/grey contrast demarcates the neutral/ionized regions in the IGM. Notice how the IGM transitions from mostly neutral to mostly ionized by redshifts 6. Finally on the right we see the formation of collapsed structures. Image credit: Alexander Kaurov . . . . .	2
1.2	The top panel shows the global signal for different values of X-ray emissivity. In the bottom panel the global signal is shown for different values of Ly $\alpha$ emissivity. The black arrows indicate how the absorption trough changes as these parameters are increased. Image credit: Jonathan Pritchard. . . . .	7
1.3	The temperature of the radio sky at 408MHz. . . . .	9
1.4	The expected foreground bias in the estimated power spectrum due to the foregrounds as a function of $k_{\perp}$ and $k_{\parallel}$ . Bright red regions indicate the modes most affected by the foregrounds. Note that the foregrounds occupy a triangular wedge shape region of Fourier space. Image credit: [44]. . . . .	10
1.5	The UV luminosity function at redshifts $z = 4, 6, 8, 10$ . Note that the UV luminosity decreases rapidly after $z > 6$ . The red dots correspond to measurements of galaxies at $z \sim 10$ while the red solid lines correspond to best fitting Schechter function. Image credit: [52] . . . . .	14
1.6	Ly $\alpha$ forest for 19 high redshifts quasars from [22]. Note that quasars above $z > 6$ show no transmission in the Gunn-Peterson trough. Image credit: [22] . . . . .	16

- 2.1 Example ionization  $x_{\text{HII}}$ , density  $\delta$ , and brightness temperature  $\delta T_b$  fields at  $z = 9$  with fiducial parameters of  $\zeta_0 = 25$ ,  $M_{\text{turn},0} = 5 \times 10^8 M_\odot$ , and  $R_{\text{mfp},0} = 30$  Mpc. The ionized regions from the ionization field are superimposed as contours on the density field to emphasize the correlation between the two fields. Inside-out scenarios (with  $\beta > 0$ ) have positively correlated density and ionization fields. Conversely, outside-in scenarios (with  $\beta < 0$ ) have negatively correlated fields. The case  $\beta = 0$  refers to the scenario where the ionization field and density field are entirely uncorrelated. The 21 cm brightness temperature field is sensitive to the type of correlation between matter and ionization fields. For example, the outside-in model shown here has the highest brightness temperature, since regions of high density are also regions of highest neutral fraction. . . . . 44
- 2.2 Power Spectra for varying  $\beta$  at different redshifts, with the other EoR parameters fixed to fiducial values of  $\zeta_0 = 25$ ,  $M_{\text{turn},0} = 5 \times 10^8 M_\odot$ , and  $R_{\text{mfp},0} = 30$  Mpc. The mean ionized fractions  $\bar{x}_{\text{HII}}$  at redshifts,  $z = 10.5$ ,  $z = 8.5$  are 0.09, 0.2 and 0.4 respectively. The amplitude of  $\Delta_{21}^2$  increases as  $\beta$  is decreased from its maximal value  $\beta = 1$ , corresponding to inside-out models of reionization. The amplitude of the power is maximum at  $\beta = -1$ , corresponding to outside-in models. The contrast between these models is largest at the scale corresponding to the size of the ionized regions. The dotted line represents a model without any correlation between density and ionization fields. . . . . 49
- 2.3 Power spectra as a function of  $z$  and  $\beta$  at two chosen  $k$  values. The contrast between outside-in and inside-out models is largest at the midpoint of reionization. For the fiducial parameters of  $\zeta_0 = 25$ ,  $M_{\text{turn},0} = 5 \times 10^8 M_\odot$ , and  $R_{\text{mfp},0} = 30$  Mpc, this occurs at  $z \approx 8$ . The dotted curve represents a model without any correlations between  $\delta$  and  $x_{\text{HII}}$ . . . . . 50

2.4	Density boxes (left) alongside their resulting temperature fields (right), with contours showing the locations of ionized bubbles overlaid. Fourier modes with $k < 2 \text{ Mpc}^{-1}$ have been filtered out from $\delta T_b$ to elucidate the high $k$ behavior seen in Figure 2.2. In this high- $k$ regime, large amplitude brightness fluctuations are seen throughout the neutral regions . . . . .	52
2.5	Posterior distributions for Scenario (i) of Section 4.6, covering the redshift range of our forecasts, $6 \leq z \leq 10$ . The 68% credibility contours are entirely contained within the inside-out region of parameter space, suggesting that with such a measurement we can firmly rule out outside-in or uncorrelated models. . . . .	59
2.6	Same as Figure 2.5, but for a restricted redshift range of $7.5 \leq z \leq 8.5$ . Measurement over these redshifts can strongly rule out correlations that are inconsistent with inside-out models. The 68% credibility contours clearly distinguish inside-out and outside in regions of parameter space. . . . .	60
2.7	Same as Figure 2.5, but for a restricted redshift range of $9.5 \leq z \leq 11.5$ . Although many parameters are poorly constrained, an uncorrelated scenario of $\beta = 0$ can still be easily ruled out. . . . .	61
2.8	Same as Figure 2.5, but using only three $k$ bins centred on $k = 0.2 \text{ Mpc}^{-1}$ , $k = 0.25 \text{ Mpc}^{-1}$ , and $k = 0.3 \text{ Mpc}^{-1}$ at $z = 8.0$ . Because these bins contain the most information on $\beta$ , using them alone is sufficient for excellent constraints. . . . .	61
2.9	Same as Figure 2.6, but using an outside-in model with $\beta = -0.936$ as our fiducial reionization morphology. Displayed are the 68% CR contours. The 68% CR are entirely contained within $\beta < 0$ suggesting that if reionization proceeds as outside-in, measurement of $\Delta_{21}^2$ in this scenario can rule out uncorrelated and inside-out reionization with 68% credibility. . . . .	63

2.10	Marginalized posterior distributions on $\beta$ obtained through the measurement of $\Delta_{21}^2$ in Scenario (ii) of Section 4.6, but assuming 10 times larger error bars than the design HERA sensitivities to mimic potential upper limits. As the upper limits come down to 10 times the fiducial errors on $\Delta_{21}^2$ from Section 2.8, we will be able to rule out $\beta < 0$ with 99% credibility in our fiducial model. The dotted vertical lines demarcate $\beta = 0$ to guide the eye. . . . .	64
3.1	From the center of the Figure , outward: Lightcones of the density field $\delta$ , ionization fraction $x_{\text{HII}}$ and free electron field $n_e$ for the case of inside-out reionization (left three boxes) and outside-in reionization (right three boxes). Inside-out reionization (left) leads to a higher free electron number density $n_e$ in the ionized bubbles since the density field (center) couples to the ionized regions in $x_{\text{HII}}$ compared to outside-in models (right) where the underdense regions in $\delta$ couple to the ionized regions in $x_{\text{HII}}$ . . . . .	86
3.2	Redshift evolution of the DM probability distributions for our fiducial reionization scenario $\beta = 1$ , $\zeta = 25$ , $M_{\text{turn}} = 5 \times 10^8 M_{\odot}$ and $R_{\text{mfp}} = 30\text{Mpc}$ . At higher redshift the relative probability of high DM sightlines increases. . . . .	89
3.3	Evolution of the individual sightline DM probability distributions for a variety of reionization scenarios encapsulated by the density-ionization parameter $\beta$ , ionizing efficiency $\zeta$ and mass scale of the ionizing sources $M_{\text{turn}}$ . Notice how the different reionization scenarios begin to distinguish themselves at higher redshifts. In each panel, the gold distribution corresponds to the fiducial reionization scenario of $\beta = 1$ , $\zeta = 25$ , $M_{\text{turn}} = 5 \times 10^8 M_{\odot}$ and $R_{\text{mfp}} = 30\text{Mpc}$ . . . . .	91

3.4	$\overline{\text{DM}}$ for a variety of density-ionization correlations $\beta$ (upper left), mass scale of the ionizing sources $M_{\text{turn}}$ (upper right), ionizing efficiency $\zeta$ (lower left), and mean free path $R_{\text{mfp}}$ of the ionizing photons. Notice how high ionizing efficiency of the sources and smaller masses of the ionizing sources lead to an early onset reionization, and so an increase in $\overline{\text{DM}}$ at that redshift. Inside-out reionization models $\beta > 0$ , lead to an increase in $\overline{\text{DM}}$ , since the free electron number density in ionized regions is greater than the corresponding ionized region in outside-in models $\beta < 0$ . In each panel the dotted curve corresponds to same reionization scenario $\beta = 1$ , $\zeta = 25$ , $M_{\text{turn}} = 5 \times 10^8 M_{\odot}$ and $R_{\text{mfp}} = 30 \text{Mpc}$ . We use this fiducial reionization scenario in our forecasts in Section 4.5. . . . .	92
3.5	Posterior distributions for measurement of $\overline{\text{DM}}$ for $10^4$ FRBs distributed between redshifts $8 \leq z \leq 10$ according to the source count distribution in Section 3.4.1. The 68% credibility regions are shown. Such a measurement can rule out uncorrelated $\beta = 0$ and outside-in reionization $\beta < 0$ at 68%CR. . . . .	100
3.6	Posterior distributions for measurement of $\overline{\text{DM}}$ for $10^5$ FRBs distributed between redshifts $8 \leq z \leq 10$ according to the source count distribution in Section 3.4.1. Using such a measurement, we can rule out uncorrelated and outside-in reionization scenarios at 68%CR. . . . .	101
3.7	Posterior distributions for measurement of $\overline{\text{DM}}$ for 100 FRBs distributed between $8 \leq z \leq 10$ according to the source count distribution in Section 3.4.1. The 68% credibility regions of our measurements are shown. This measurement can rule out extreme EoR models, for example, scenarios where the Universe is ionized by $z = 8$ .	103

- 4.1 Example fields demonstrating the effect that different  $\beta$  correlations have on the observed LAEs. The intrinsic LAEs (left) roughly traces the underlying density field. When computing the Ly $\alpha$  optical depth using the ionization field  $x_{\text{HII}}$  (middle), we arrive at the observed LAEs (right). Neutral regions suppress Ly $\alpha$  radiation from the observer. The ionized regions from the ionization field are superimposed as contours on the observed LAEs to emphasize the correlation between the two fields. Inside-out scenarios (with  $\beta > 0$ ) have positively correlated density and ionization fields. Conversely, outside-in scenarios (with  $\beta < 0$ ) have negatively correlated fields. The case  $\beta = 0$  refers to the scenario where the ionization field and density field are entirely uncorrelated. These boxes are at redshift  $z = 7.6$  with fiducial astrophysical parameters  $\zeta_0 = 25$ ,  $M_{\text{turn},0} = 5 \times 10^8 M_{\odot}$ ,  $R_{\text{mfp},0} = 30 \text{Mpc}$ . . . . . 124
- 4.2 The Ly $\alpha$  luminosity function of LAEs as a function of  $\beta$ , at three different stages of reionization. In each panel, the dotted curve corresponds to the luminosity function of the intrinsic field (i.e. with  $\bar{x}_{\text{HII}} = 0$ ). Notice that extreme outside-in reionization scenarios ( $\beta \sim -1$ ), lead to concealing the intrinsically brightest LAEs. At high redshift, where there are fewer intrinsically bright LAEs, this leads to a sharp drop-off of the Ly $\alpha$  luminosity function. In each of these curves, the detection threshold  $\text{Ly}_{\alpha}^{\text{min}}$  corresponds to mass  $M_{\alpha}^{\text{min}} \sim 10^{10} M_{\odot}$  with  $f_{\text{duty}} = 1$ . . . . . 129
- 4.3 Evolution in the number of observed LAEs for positively correlated models ( $\beta > 1$ ), uncorrelated models ( $\beta = 0$ ), and negatively correlated models ( $\beta = -1$ ) at different mean ionized fractions. The mean number density of LAEs  $\bar{n}$ , for the extreme  $\beta = 1$  and  $\beta = -1$  models are noted. Notice the rapid change in the number of LAEs for  $\beta = -1$  models. As the ionized regions grow large enough to encompass the high density regions, the number of LAEs increases rapidly. The uncorrelated model has ionized regions which are random with respect to the underlying density field. Positively correlated models have the ionized regions that always correspond to the high density regions, where the intrinsic number density of LAEs is greatest. . . . . 130

4.4 Evolution of the number density of LAEs for different reionization morphologies. Inside-out driven models ( $\beta > 0$ ) initially have more observable LAEs since the intrinsically densest regions of the IGM are ionized first. As the ionized regions grow to encapsulate the underdense regions in  $\delta$ , the mean number density grows slowly as compared to outside-in driven models ( $\beta < 0$ ), where the underdense regions are first to be ionized. In this scenario, the number density of LAEs increases rapidly as the intrinsically densest regions are ionized. We use the same fiducial model as in Figure 4.1 . . . . . 134

4.5 ACF of various  $\beta$  scenarios at different stages of reionization. Outside-in driven reionization scenarios ( $\beta < 0$ ) produce the largest clustering of LAEs. The contrast between the different  $\beta$  models is greatest at high redshifts where the ionization of the IGM has the largest imprint on LAE observability. As reionization proceeds it becomes more difficult to distinguish between these scenarios. We use fiducial parameters  $\zeta_0 = 25$ ,  $M_{\text{turn},0} = 5 \times 10^8 M_\odot$ ,  $R_{\text{mfp},0} = 30 \text{ Mpc}$ , and  $\beta_0 = 0.936$ ,  $f_{\text{duty}} = 1$  and  $M_\alpha^{\text{min}} = 10^{10} M_\odot$ . . . . . 137

4.6 The number density of observed LAEs for different  $\beta$  models and at different redshifts. For inside-out models at high redshifts (top two rows), LAEs are spread across the entire ionized regions, while outside-in models produce fewer LAEs which are spread across a limited volume. This serves to increase the clustering of LAEs for  $\beta = -1$  models. The scale is binary to accentuate the difference in the spatial distributions of LAEs between the two models. Later in reionization (bottom two rows), the LAEs of both inside-out and outside-in models are spread over similar ionized volumes. However the number density of LAEs within these ionized volumes is larger for inside-out models which serves to increase the clustering of LAEs for  $\beta = -1$  models compared to  $\beta = +1$ . See Section 4.5.3 for the simulation parameters. . . . . 138

4.7 Angular correlation function as a function of  $z$  for various  $\beta$  models at separations of 10Mpc. Note the non-monotonic behaviour of  $\beta$ . Early in reionization, the LAEs of inside-out models are spread over larger volumes within the ionized regions as compared to outside-in models, where the LAEs tend to be more localized. This produces a stronger clustering signal for outside-in driven models. This behaviour is inverted later in reionization where there are enough intrinsic LAEs to fill the entire volume of ionized regions for outside-in models. . . . . 141

4.8 Posterior distribution for the EoR and LAE parameters using the Subaru data described in Section 4.5.3. Displayed are the 68% CR contours. Since the 68% CR contours include both the  $\beta > 0$ , and  $\beta < 0$  regions of parameter space, measurement of  $\bar{n}$  and  $\xi$  at  $z = 6.6$  cannot constrain the sign of  $\beta$  to within 68% credibility. . . . . 149

4.9 Posterior distribution for the EoR and LAE parameters using the Subaru data at  $z = 6.6$  and the 21cm power spectrum from  $7.5 \leq z \leq 8.5$ . The 68% CR are entirely contained within  $\beta > 0$  suggesting that if reionization proceeds as inside-out, measurement of  $\bar{n}$  and  $\xi$  of LAE as well as  $\Delta_{21}^2$  can rule out uncorrelated and outside-in reionization with 68% credibility. . . . . 151

5.1 Sample HERA flags split from 100MHz-200MHz. Frequency channels below 110MHz are reserved for FM radio. The ORBCOMM satellite is responsible for RFI at  $\nu = 136$ MHz. Frequency channels above  $\nu = 174$ MHz are flagged due to broadcast television. . . . . 176

5.2	The results of our parameter optimization procedure for CLEAN and LSSA inpainting methods. In the left image fractional increase in $\chi^2$ is plotted as a function of tolerance parameter values (see Section 5.3.1). The coloured curves represent different noise levels. As the thermal noise level in the dataset increases the optimal tolerance decreases. The inset provides a closer examination of $\chi^2/\chi_{\min}^2$ for fiducial noise level $\alpha = 1$ . Similarly on the right image, the fractional increase in $\chi^2$ is plotted as a function of $n_{\max}$ , the number of Fourier components to include in LSSA models. As we increase the thermal noise of the dataset, the optimal number of Fourier components to include in the model decreases. . . . .	179
5.3	Block diagram showing the U-Paint architecture. . . . .	183
5.4	First row: The amplitude and phase components of the RFI flagged visibilities are shown in the first and third column. In the second and fourth column are the amplitude and phase component of the true visibilities. The visibilities are simulated (see Section 5.2.3). Second through fifth rows: in each row we show the amplitude and phase components of the RFI flagged visibilities but with the inpaint models filled into the RFI gaps. Each subsequent row correspond to U-Paint, CLEAN, LSSA, GPR, and DPSS inpainting methods. In the second and fourth column of each row we show the fractional error of the model amplitude and the residuals of the model phase (see Section 5.5). . . . .	187

5.5 Top: LST averaged inpaint model visibilities. The true visibilities are shown with the dotted black curve. The vertical shaded regions correspond to the RFI flagged channels. The amount of shade is proportional to the frequency in which those channels are flagged. Thus the Wideband ORBCOMM feature is darkest since it is always flagged. Note that the inpaint models are only filled into RFI gaps, and so the inpaint models only deviate from the true visibilities in shaded regions. The orange curve corresponds to U-Paint, the yellow curve to LSSA, purple curve to CLEAN and blue curve to GPR. DPSS models are not shown since we feature the wideband feature in this image (see Section 5.3). Bottom: The residuals between inpaint models and the true visibilities. . . . . 194

5.6 Top row: probability distribution of the fractional errors  $p(\epsilon_{\text{frac}}^V)$  in the amplitude of the inpainted model visibilities. Second row: residuals in the inpainted model amplitudes  $p(\epsilon_r^V)$ . Third row: residuals of the phase component of the inpaint models  $p(\epsilon_{\text{phi}})$ . The blue curves corresponds to when only wideband RFI is used to construct the samples while the teal curve corresponds to samples constructed using only narrowband RFI. All inpaint methods are applied to the simulated visibilities discussed in Section 5.2.3. . . . . 195

5.7 The standard deviation of the fractional error in the visibilities  $\epsilon_{\text{frac}}^V$  as a function of the thermal noise level in the visibilities. The parameter  $\alpha$  is used as a proxy for the thermal noise level (see Equation 5.9). . . . . 198

5.8 The fractional errors in the wedge modes (left) and non-wedge modes (right) of inpaint model power spectra  $\epsilon_{\text{frac}}^P$  as a function of the number of flagged channels within the spectral window. The P1V spectral window is used to estimate the power spectra. . . . . 200

5.9 Each inpainting technique is applied to the simulated data discussed in Section 5.2.3. The P1V spectral window is used to estimate the inpaint model power spectra. Left column: blue curves correspond to inpaint model power spectra. The black curves correspond to the true power spectra and the red dotted curves correspond to the residuals. Each row corresponds to a different inpaint technique used to inpaint RFI flagged simulated visibilities. Second column (see Section 5.8.3): Same as first column but with real P1V data. Purple curves correspond to inpaint model power spectra and black curves the true power spectra. Red curves are the residuals. The third column corresponds to the fractional errors  $\epsilon_{\text{frac}}^{\text{P}}$  in inpaint model power spectra from simulated data (blue) and the P1V data (purple). The dotted teal line corresponds to the power spectrum of the thermal noise floor of P1V data [14]. . . . . 201

5.10 Blue curves correspond to simulated data and purple curves correspond to P1V data. Distribution of residuals (first row) and fractional errors (second through fourth rows) in the inpaint model power spectra. Residuals are shown for wedge modes while the fractional errors are separated according to  $\tau$  modes lying inside the wedge (second row) and outside the wedge (third and fourth rows). Third row corresponds to simulated data while the fourth row corresponds to P1V data. . . . 202

5.11 Relationship between the mean fractional errors in the inpaint model visibilities  $\bar{\epsilon}_{\text{frac}}^{\text{V}}$  and the mean fractional errors in their corresponding power spectra  $\bar{\epsilon}_{\text{frac}}^{\text{P}}$ . We compute the mean fractional error of the inpaint models in RFI flagged frequency channels within the P1V spectral window. This process is repeated at each LST. Their corresponding power spectra are estimated using the same P1V spectral window. The mean of the fractional errors in the model power spectra are computed using  $\tau$  modes inside the wedge. Each LST is plotted as a scatter point. The LSTs are colour coded according to the number of flagged frequency channels at that LST. In the top row this procedure is applied to simulated data while in the bottom row this procedure is applied to P1V data. . . . . 203

5.12 Same as Figure 5.4 but with the P1V visibilities from Section 5.2.3. The true visibilities in the first row (second and fourth column) have been initially inpainted with the CLEAN algorithm to generate placeholder data for the RFI flagged regions. The inpaint techniques are then applied to a set of flags which are shifted 40 channels to the left. This is done in order to avoid inpainting over the already CLEANed data. See Section 5.8 for more details regarding our procedure. Note that as compared to Figure 5.4 the fractional errors in the model visibilities increase. . . . . 208

5.13 First row: distribution of fractional errors in the amplitude of P1V visibilities. Second row: distribution of residuals in P1V visibilities. Third row: distributions of phase errors  $\epsilon_\phi$  in the phase of P1V visibilities. In each case the blue curves correspond to distributions constructed using wideband RFI samples only. Teal curves correspond to distributions constructed using narrowband RFI samples only 211

6.1 The spatial variation of the spectral index  $\beta$  as a function of position  $(\theta, \phi)$  on the sky. Bright yellow regions correspond to larger spectral indices while darker regions correspond to small spectral indices. The morphology of  $\beta(\theta, \phi)$  roughly follows the galactic morphology. . . . . 235

6.2 In each panel we show the division of the regions on the sky. The left column corresponds to splitting the spectral map shown in Figure 6.1 into 4 regions (top) and 8 regions (bottom). On the right column we split the Haslam map from [50] into 4 regions (top) and 8 regions (bottom). . . . . 236

6.3 Summary of the null test results described in Section 6.3.1 for the error scenarios described in Section 6.3.2. The horizontal axis corresponds to the FWHM of the error correlation length while the vertical axis corresponds to the amplitude of the fluctuations. A red panel indicates that the error scenario does leads to a systematic in the analysis large enough such that the null test fails. A blue panel indicates that the error scenario does not lead to a systematic large enough such that the null test fails. The left panel are error scenarios where the standard deviation of the errors are uniform across the sky while the right panel are error scenario that have standard deviation which is spatially dependent. . . . . 241

6.4 Signal recovery plot for the heteroscedastic error realisation with  $\Delta = 5\%$  and  $\theta_{\text{FWHM}} = 1^\circ$ . The systematic produced by the errors in the basemap prevent the model from passing the null test described in Section 6.3.1 . . . . . 242

6.5 Absolute errors in the temperature of the sky at 408MHz. Note that the errors roughly trace the galactic morphology. Also apparent are that many low frequency survey data are missing the southern pole which influences the eGSM model in this region. . . . . 244

6.6 In this figure we show our fiducial error scenarios at 408MHz. In the top left we show the a heteroskedatic error realization generated by drawing values from a Gaussian distribution of zero mean and standard deviation proportional to the absolute errors at 408MHz. Moving clockwise from the top left panel, the resulting error realisation is smoothed by a Gaussian beam of FWHM equal to  $1^\circ$  (top right),  $5^\circ$  (bottom left), and  $10^\circ$  (bottom right). . . . . 244

- 6.7 The Bayesian evidence,  $\ln(Z)$ , as a function of the number of amplitude scale factor regions  $N_a$ . The black curve indicates a scenario where no 21-cm signal is included into the sky model while the red curves indicates sky models when a 21-cm signal is included. Left panel: 21-cm signal is included into the dataset. We see that a 21-cm signal model component is preferred since the maximum value of  $\ln(Z)$  originated from the red curve. Right panel: no 21-cm signal is included in the dataset, in which case a sky model without a 21-cm signal component is preferred since the maximum value of  $\ln(Z)$  occurs in the black curve. The blue curves corresponds to a model where the fractional error map (see Equation 5.17) is used to define the regions. Note that the observation times in this simulation correspond to a one hour duration occurring at a time where the statistical anisotropies in Figure 6.6 in are mostly below the horizon. . . . . 253
- 6.8 Each plot shows the results of fitting our foreground model to the simulated data discussed in Section 6.5.1. The upper left panel corresponds to  $N_a = 1$ . Moving clockwise, we have models  $N_a = 3, 16, 32$ . The blue curves corresponds to the fitted 21-cm signal while the red curves correspond to the residuals of the dataset after the fitted foregrounds are removed. . . . . 254
- 6.9 The Bayesian evidence,  $\ln(Z)$ , as a function of the number of amplitude scale factor regions  $N_a$  for each error scenario described in Section 6.3.3. The black curve indicates a scenario where a 21-cm signal is included into the sky model while the red curves indicates sky models where no 21-cm signal is included. Note that 21-cm signal is included into the dataset leading to black curves having larger  $\ln(Z)$  than the blue curves. Also clear are the the number of amplitude scale factor regions required to maximize  $\ln(Z)$  increases with error fluctuation amplitude  $\Delta$  and correlation length  $\theta_{\text{FWHM}}$ . . . . . 255

- 6.10 The Bayesian evidence as a function of the number of spectral parameters  $N_\beta$ . The black curve indicates a scenario where a 21-cm signal is included into the sky model while the red curves indicates sky models where no 21-cm signal is included. Left panel: no 21-cm signal is included into the dataset. We see that a 21-cm signal model component is preferred since the maximum value of  $\ln(Z)$  originated from the red curve. Right panel: a 21-cm signal is included in the dataset, in which case a sky model without a 21-cm signal component is preferred since the maximum value of  $\ln(Z)$  occurs in the black curve. . . . . 259
- 6.11 The logarithm of the Bayes' Factor as a function of the number of spectral parameters  $N_\beta$  and amplitude scale factors  $N_a$ . The color in each square indicates the value of Bayes' factor, i.e.  $\ln(Z)_{\max} - \ln(Z)$  where the  $\ln(Z)_{\max} = 265$  is the model  $N_a = 8$  and  $N_\beta = 7$  which maximises the Bayesian evidence. All models with Bayes' factor  $< 240$  or negative Bayesian evidence are saturated at 240. Notice that models with  $N_a = 0$  are disfavoured even with large values of  $N_{\text{beta}}$ . . . . . 260
- 6.12 Signal recovery plot for the Bayesian evidence maximizing model ( $N_a = 7, N_\beta = 8$ ) of Figure 6.11. The blue curve indicates the temperature of the fitted 21-cm model while the red curve represents the dataset with the fitted foreground removed. The green curve indicates the simulated 21-cm signal that was inside the dataset. . . . 264

# List of Tables

2.1	Lexicon for physical models and their respective correlations . . . . .	48
3.1	Summary of Reionization Parameters and FRB Observables . . . . .	83
3.2	Lexicon for physical models and their respective correlations . . . . .	85
4.1	Lexicon for physical models and their respective correlations . . . . .	123
5.1	Summary of key error metrics for the amplitude component of simulated visibilities.	193
5.2	Summary of key error metrics for the amplitude component of P1V visibilities. . .	210

# Chapter 1

## Introduction

### 1.1 Overview

Measurements of the angular anisotropies in the temperature of Cosmic Microwave Background (CMB) photons have provided us with a window into the conditions of the Universe at redshifts  $z \sim 1100$ . Conversely, galaxy surveys provide a window into the Universe at much later times. Specifically, galaxy surveys have given us measurements of spatial inhomogeneities in the matter distribution at  $z < 2$ . Combining measurements from CMB angular anisotropes and matter power spectrum measurements from galaxy surveys have allowed us form a standard picture of our cosmological reality, the Lambda cold dark matter ( $\Lambda$ CDM) framework [33, 59, 62, 66, 76].

In Figure 1.1 we show a cartoon of the Universe's history from the time of recombination (left) to today (right). Notice that the Universe at low redshifts is vastly different picture than the Universe at the time of recombination. At lower redshifts the hydrogen in the intergalactic medium (IGM) is ionized and most neutral hydrogen is locked inside galaxies and stars. However a substantial portion of our Universe's history lay in between these times and thus the bulk of our universe's history is unconstrained. This still unconstrained period is mark by several milestones. First is cosmic dawn (CD) the time in which the first stars are formed. After CD, the first generation galaxies produce enough UV photons to begin ionizing the neutral hydrogen in the IGM. This gives rise to the Epoch of Reionization (EoR), the period in which the neutral hydrogen (which was formed at

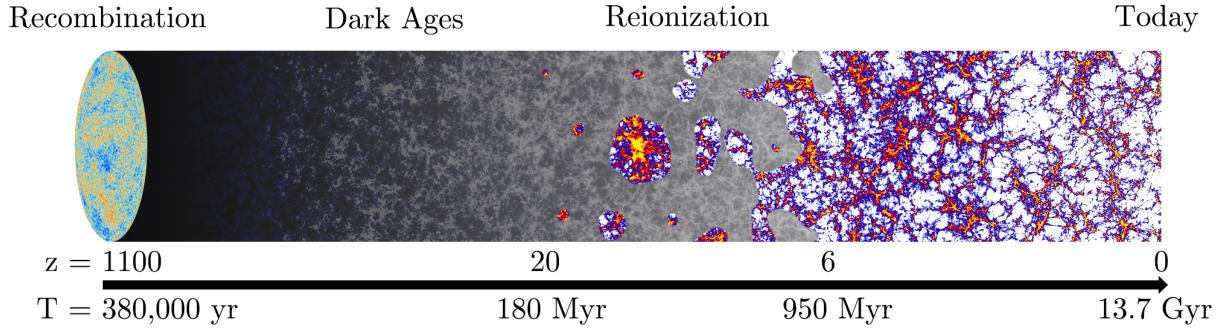


**Figure 1.1:** Timeline of the Universe’s history from the time of recombination at  $z = 1100$  (left) to today  $z = 0$  (right). After recombination, the cosmic dark ages mark a time before the first stars. The black/grey contrast demarcates the neutral/ionized regions in the IGM. Notice how the IGM transitions from mostly neutral to mostly ionized by redshifts 6. Finally on the right we see the formation of collapsed structures. Image credit: Alexander Kaurov

the time of the CMB) is ionized. These events give rise to the local Universe uncovered by galaxy surveys [25, 26]. Measurements of high redshifts quasars, the optical depth  $\tau$  from CMB studies, and high- $z$  galaxies have given us a lot of information about these epochs (see Sections 1.1.5, 1.1.6, and 1.1.7 for more details) however we do not have a complete picture of CD, or the timing and details of reionization [3, 62, 65].

### 1.1.1 21cm Cosmology

Hydrogen cosmology promises to bridge the gap between these measurements, unveiling the details of cosmic dawn and reionization. To do this one uses the hyperfine transition of hydrogen, the 21cm line. As an electron flips its spin relative to the proton in the nucleus, a 21cm photon is emitted. Since the emitted photon redshifts as the universe expands, one can track the distribution of redshifted photons to make three dimensional maps of the neutral hydrogen as a function of redshift. The 21cm photons are typically measured in contrast to the CMB temperature  $T_\gamma$ . Thus one measures an emission signature if there is an overabundance of 21cm photons relative to CMB predictions. Similarly, a net absorption of the CMB leads to a deficit of 21cm photons as compared to CMB blackbody predictions. To quantify this, we can define the brightness of 21cm photons

relative to the CMB, (see [25, 26]):

$$\begin{aligned} \delta T_b(\mathbf{r}, z) \approx & (27 \text{ mK}) \left( \frac{T_s(\mathbf{r}, z) - T_\gamma(z)}{T_s(\mathbf{r}, z)} \right) [1 - x_{\text{HII}}(\mathbf{r}, z)] [1 + \delta(\mathbf{r}, z)] \\ & \times \left[ \frac{H(z)/(1+z)}{dv_r/dr} \right] \left( \frac{1+z}{10} \frac{0.15}{\Omega_m h^2} \right)^{1/2} \left( \frac{\Omega_b h^2}{0.023} \right), \end{aligned} \quad (1.1)$$

where  $z$  is the redshift,  $\mathbf{r}$  is the position vector,  $\Omega_m$  is the normalized matter density,  $\Omega_b$  is the normalized baryon density,  $dv_r/dr$  is the line of sight velocity gradient,  $H(z)$  is the Hubble parameter and  $h$  is its dimensionless equivalent. The terms  $x_{\text{HII}}$  and  $\delta$  are the ionized fraction of hydrogen, and the overdensity. The term  $T_s$  is the spin temperature of the neutral hydrogen gas, which quantifies the number density  $n_1$  of neutral hydrogen atoms in the excited hyperfine states relative to the ground state  $n_0$ . The spin temperature can be written  $T_s$  as

$$\frac{n_1}{n_0} = \frac{g_1}{g_0} e^{E_*/k_B T_s} \quad (1.2)$$

where  $k_B$  is the Boltzmann constant,  $E_* = 5.9 \times 10^{-6} \text{ eV}$  is the hyperfine splitting energy and the factors  $g_1$  and  $g_0$  are statistical weights that indicate the number of ways the hydrogen atoms can end up in the excited state  $g_1$  and ground state  $g_0$ , i.e 3 and 1. One cannot detect the spin temperature directly, one instead measures the differential brightness temperature in Equation 1.1. Measurement of Equation 1.1 also allows us to trace primordial hydrogen as a function of redshift and position and can in principle probe CD and the EoR. In this thesis we consider two methods to measure the 21cm photons emitted by the neutral hydrogen. The first method is to measure the spatial fluctuations of the brightness temperature in Equation 1.1. The second method is measurement of the global signal. This is the spatially averaged 21cm signal described in Equation 1.1, i.e. the mean 21cm brightness temperature  $T_b \equiv \overline{\delta T_b}$ . In the following sections we discuss both of these methods.

### 1.1.2 Direct Probes

Notice that in Equation 1.1 we see that the distribution of baryons in the density field  $\delta$  is spatially dependent. Similarly the spin temperature  $T_s$  and the distribution of ionized hydrogen atoms in the ionization field  $x_{\text{HII}}$  are spatially dependent. Even if it were possible to measure the precise location of every hydrogen atom in the density field  $\delta$  (or ionized hydrogen in  $x_{\text{HII}}$ ), one would still need to connect such an observation to theory through comparison of statistical quantities derived from these fields. Thus to learn about the evolution of the Universe from CD through to the EoR, we are interested in the spatial fluctuations  $\delta T_b$  sourced by  $\delta$ ,  $x_{\text{HII}}$  and  $T_s$ . One method to connect the spatial fluctuations of  $\delta T_b$  to theory is by computing the power spectrum  $P(k)$  defined by

$$\langle \widetilde{\delta T_b}(\mathbf{k})^* \widetilde{\delta T_b}(\mathbf{k}') \rangle = (2\pi)^3 \delta^D(\mathbf{k} - \mathbf{k}') P(k) \quad (1.3)$$

where  $\mathbf{k}$  is the three dimensional Fourier wavenumber,  $k = |\mathbf{k}|$  is the spherically averaged wavenumber,  $\widetilde{\delta T_b}(\mathbf{k})$  is the Fourier transformed differential brightness temperature from Equation 1.1 and  $\delta^D(\mathbf{k} - \mathbf{k}')$  is the Dirac delta function. Through Equation 1.3 we can define the dimensionless power spectrum

$$\Delta_{21}^2(k) = \frac{k^3}{2\pi^2} P(k). \quad (1.4)$$

During CD, reionization has yet to have an impact on the neutral hydrogen in the IGM, i.e. in Equation 1.1, the term  $x_{\text{HII}}$  is trivially equal to zero. Thus during CD, the shape of  $\Delta_{21}^2$  is driven by fluctuations in  $\delta$  and  $T_s$ . Once the EoR is underway, the ionized bubbles grow around UV sources, eventually coalescing when reionization is complete. The shape of the power spectrum is driven by the morphology of the ionized regions. Most models of the IGM predict that  $\Delta_{21}^2$  has characteristic ‘‘knee’’ in  $\Delta_{21}^2$  corresponding to the size and arrangement of the ionized regions [50]. On small scales, fluctuations in the density field  $\delta$  still drive the shape of the power spectrum. It is clear that  $\Delta_{21}^2$  is rich with information regarding the physics of the IGM during CD and the EoR.

There are several ground based interferometric instruments that are capable at measuring  $\Delta_{21}^2$  (i.e. fluctuations of the 21cm line). These instruments include the Hydrogen Epoch of Reionization array (HERA) [14], Low Frequency Array (LOFAR) [77], Murchison Widefield Array (MWA) [48],

Precision Array for Probing the Epoch of Re-ionization (PAPER) [58], and the Square Kilometer Array (SKA) [15]. Although in principle most of the 21cm physics discussed in this thesis is applicable to any of the above experiments, I will focus on the efforts using the HERA array. HERA, and the aforementioned experiments, do not organically measure  $\Delta_{21}^2$  using spherically averaged wavenumbers  $|\mathbf{k}|$ . Instead, antennas separated by a baseline vector  $\mathbf{b}$  measure Fourier modes on the sky with a wavevector  $\mathbf{k}_\perp$  oriented perpendicular to the line of sight and wavevector  $k_\parallel$  oriented parallel to the line of sight. The wavenumber  $\mathbf{k}_\perp$  is given by  $\mathbf{k}_\perp \approx 2\pi\mathbf{b}/\lambda X$ , where  $\lambda$  is the observation wavelength and  $X$  is a conversion factor from angular separation  $\theta$  to transverse comoving distance  $r_\perp$ , and is given by

$$X \equiv \frac{r_\perp}{\theta} = \frac{c}{H_0} \int_0^z \frac{dz'}{E(z')} \quad (1.5)$$

where  $H_0$  the Hubble parameter,  $E(z) \equiv \sqrt{\Omega_m(1+z)^3 + \Omega_\Lambda}$  and  $\Omega_\Lambda$  the normalized dark energy densities. The wavenumber along the line of sight  $k_\parallel$ , is given by  $k_\parallel = \frac{2\pi\eta}{Y}$  where  $\eta$  is the Fourier dual to the frequency axis  $\nu$  with dimensions of  $1/\nu$ ,  $Y$  is a conversion factor converting between frequency interval  $\Delta\nu$  and increments in radial comoving distances  $\Delta r_\parallel$ :

$$Y \equiv \frac{\Delta r_\parallel}{\Delta\nu} = \frac{c}{H_0\nu_{21}} \frac{(1+z)^2}{E(z)}, \quad (1.6)$$

where  $\nu_{21} \approx 1420$  MHz is the rest frequency of the 21 cm line. Different observation frequencies correspond to different distances along the line of sight, which when Fourier transformed correspond to  $k_\parallel$ . Thus modes along the line of sight,  $k_\parallel$  are probed using the observation frequencies of the instrument. The wavenumbers  $k_\parallel$  and  $\mathbf{k}_\perp$  are cylindrical equivalents of the spherical averaged Fourier components in Equation 1.4. To compute Equation 1.4 given a cylindrically measured power spectrum, we need to rebin the power spectrum along rings of constant  $|\mathbf{k}| = \sqrt{k_\parallel^2 + \mathbf{k}_\perp^2}$ . Currently there have not been any experiments to claim a detection of the 21cm power spectrum, however many of these experiments have placed upper limits on Equation 1.4. Since most of these instruments place limits at different scales and redshift, there is no universal upper limit.

Rather, the upper limits on  $\Delta_{21}^2$  are dependent on  $k$  and  $z$ . For example, recently HERA found that  $\Delta_{21}^2 < (30.76)^2 \text{mK}^2$  at  $z = 7.9$  and  $k = 0.15 \text{Mpc}^{-1}$  at 95% confidence [30].

### 1.1.3 Global Signal

Measurement of the global 21cm signal is complementary to interferometric measurements. First, they are mathematically complementary since the the global signal is an example of a one point statistic, i.e. the mean, whereas the power spectrum is a two point statistic. Secondly, these probes are most sensitive to different features of reionization. For example, the 21cm power spectrum is more sensitive to morphological properties of the EoR, such as the bubble size distribution and the density-ionization correlation (the correlation between the  $\delta$  and  $x_{\text{HII}}$  in Equation 1.1). In contrast, since a global signal is averaged over the entire sky, it allows for a more direct measurement on the start and duration of the EoR, as well as the global properties of the first luminous sources. One of the technical advantages of performing a global signal experiment is that it is achievable instrumentally using a single antenna (which suffices to measure the mean signal). Conversely an adequate measurement of the power spectrum requires an interferometer, comprised on many dishes which besides being more expensive than a global signal analysis also potentially introduces more complications in the data analysis pipelines.

In Figure 1.2 we show representative sample global signal curves from one particular theoretical model. The shapes shown in Figure 1.2 are not specific to one set of EoR parameters, however the general evolution of  $\bar{T}_b$  follows a general qualitative trend. We first focus on the red curve in the top panel. After the time of recombination,  $T_s$  and  $T_k$  are coupled due to collisional excitations. The remaining free electrons from recombination scatter off CMB photons keeping  $T_\gamma$  coupled with  $T_s$  leading to no 21cm signal [64]. At  $z \sim 150$ , when the scatterings between electrons and photons become rare,  $T_s$  and  $T_k$  decouple from  $T_\gamma$ . As the Universe is expands the temperature of the neutral hydrogen gas  $T_k$  cools adiabatically. Thus due to collisional coupling and cooling gas temperature, the spin temperature  $T_s$  drops along with the gas temperature  $T_k$ . As the Universe expands, collisions become more infrequent and eventually  $T_k$  decouples with  $T_s$  which once again falls into thermal equilibrium with  $T_\gamma$  leading to  $\bar{T}_b = 0$ . However at the onset of CD, stars begin

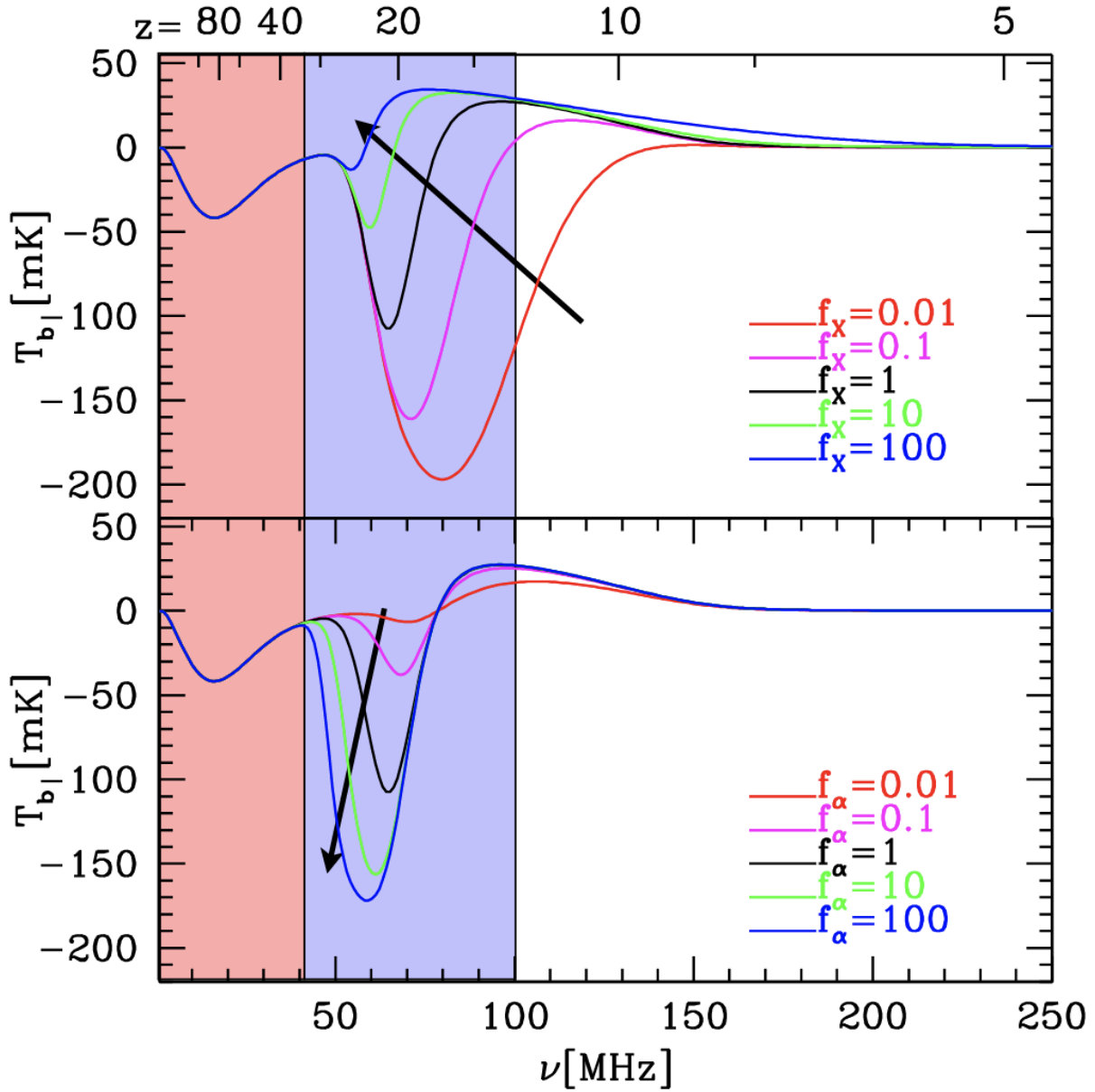


**Figure 1.2:** The top panel shows the global signal for different values of X-ray emissivity. In the bottom panel the global signal is shown for different values of Ly $\alpha$  emissivity. The black arrows indicate how the absorption trough changes as these parameters are increased. Image credit: Jonathan Pritchard.

emitting Ly $\alpha$  photons which again couple  $T_s$  to  $T_k$  through the Wouthuysen-Field effect [24, 81]. The spin temperature is again in equilibrium with the gas temperature  $T_k$  creating a large absorption signature relative to  $T_\gamma$ . With sustained star formation X-ray production heats the gas temperature, raising  $T_s$  significantly, resulting in an emission spectrum relative to  $T_\gamma$ . The astrophysical details of CD directly determine the central redshift, duration, and amplitude of the absorption trough (as well as the potential emission signal at the end of reionization). For example, in the top panel of Figure 1.2 we show example global signal curves where the emissivity of the X-rays,  $f_x$  is increased from  $f_x = 0.01$  to  $f_x = 100$ . Notice increasing the X-ray emissivity from  $f_x = 0.01$  to  $f_x = 100$  results in decreasing the depth of the absorption trough and quickly transitioning into an emission signal. Similarly in the bottom panel we increase the Ly $\alpha$  emissivity  $f_\alpha$  from 0.01 to 100. This results in the production of more Ly $\alpha$  photons by the first galaxies. Notice that as  $f_\alpha$  is increased from  $f_\alpha = 0.01$  to  $f_\alpha = 100$  the depth of the absorption trough increases. From this example we can see that the global 21cm signal is also rich with information about the astrophysics of the IGM. There are multiple experiments aiming to detect the global 21cm signal. These experiments include the Broadband Instrument for Global HydrOgen ReioNisation Signal (BIGHORNS) [74], Experiment to Detect the Global EoR Signature (EDGES) [7], Large aperture Experiment to detect the Dark Ages (LEDA) [63], Probing Radio Intensity at high-Z from Marion (PRIZM), [61], and the Radio Experiment for the Analysis of Cosmic Hydrogen (REACH), [12], and Shaped Antennas to measure the background RADio Spectrum (SARAS), [72]. Currently, only EDGES has claimed to detected the global signal [8], specifically the absorption trough due to Ly $\alpha$  coupling. However, the unexpectedly large amplitude and flattened profile was considerably larger than was predicted by cosmological models [67]. This has spurred theoretical interest in explaining the profile with excess radio background models, millicharged dark matter models and non- $\Lambda$ CDM cosmology [1, 21, 23, 31]. Other works have shown that the profile may be the result of an unaccounted for systematic [5, 9, 32, 69–71].

## Radio Sky at 408MHz

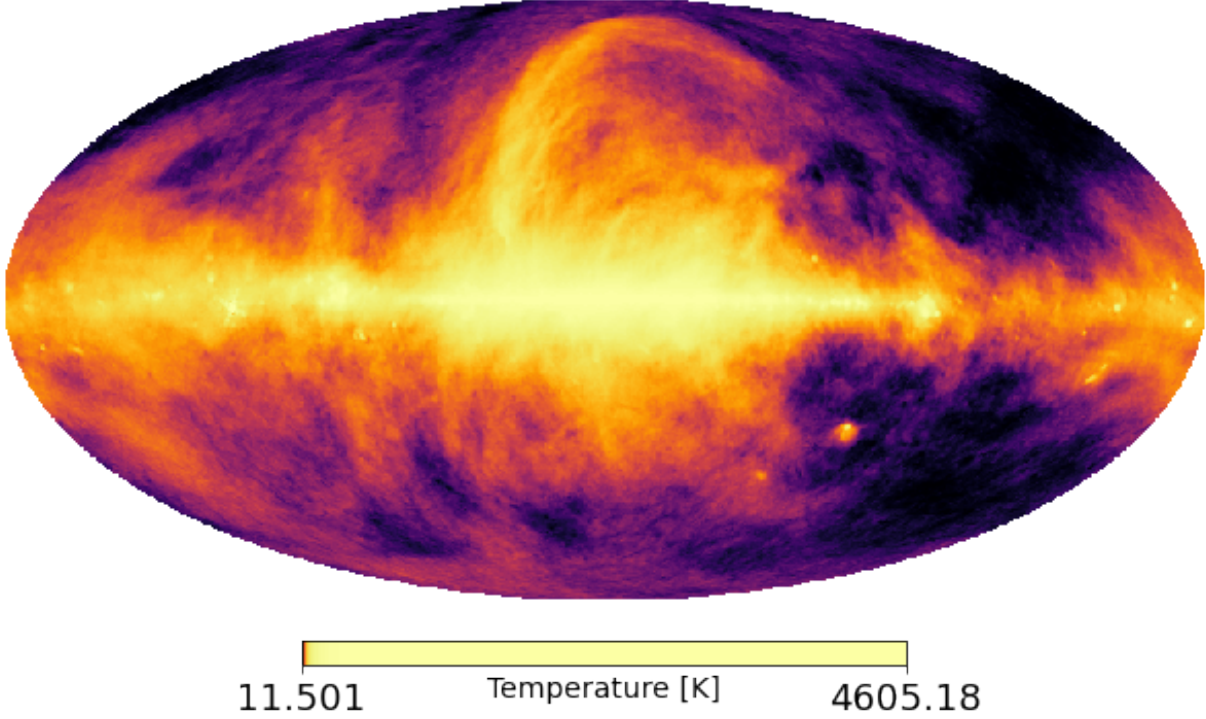


**Figure 1.3:** The temperature of the radio sky at 408MHz.

### 1.1.4 Systematics

In order for us to turn measurements of the radio sky into a 21cm detection we need to precisely understand all non-21cm sources of radio emission as well as the details of the instruments used to take them. The reason this precision is required is because at the observational frequencies of interest, the radio sky is dominated by galactic and extra galactic synchrotron radiation which we show in Figure 1.3 at 408MHz. We can see in Figure 1.3 that in some parts of the sky the temperature of the foregrounds is more than  $10^4\text{K}$  [13, 43, 68]. We can see in Figure 1.2 that the mean amplitude of the expected 21cm signal is on the order of  $10^{-1}\text{K}$ , making the foregrounds up to five orders of magnitude larger than  $\delta T_b$ . The foregrounds are mostly due to synchrotron, and therefore they are spectrally smooth. They can be well modeled as a power in frequency:

$$T_{\text{FG}}(\theta, \phi, \nu) = T_0(\theta, \phi, \nu_0) (\nu/\nu_0)^{-\beta} \quad (1.7)$$

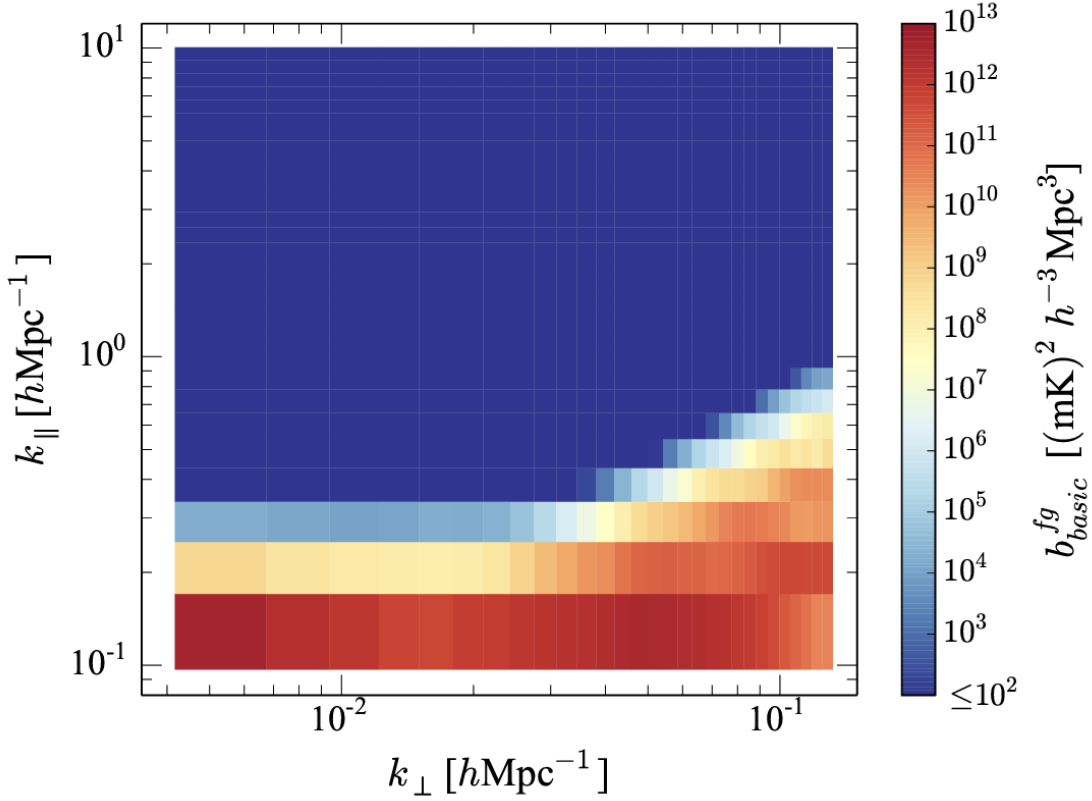


**Figure 1.4:** The expected foreground bias in the estimated power spectrum due to the foregrounds as a function of  $k_{\perp}$  and  $k_{\parallel}$ . Bright red regions indicate the modes most affected by the foregrounds. Note that the foregrounds occupy a triangular wedge shape region of Fourier space. Image credit: [44].

where  $\nu$  is the frequency of observation,  $T_0(\theta, \phi, \nu)$  is the temperature of the sky at location  $\theta$ ,  $\phi$  at reference frequency  $\nu_0$  and  $\beta$  is the spectral index that has typical range  $2 \leq \beta \leq 3.5$ . As a consequence of Equation 1.7, the foregrounds get even brighter at low frequencies, i.e. higher redshifts making these redshifts more difficult to access. The foregrounds affect both global 21cm signal experiments and interferometric measurements. Because interferometers probe angular and spectral fluctuations in different ways, their power spectrum measurements are most appropriately interpreted on the  $k_{\perp}$ - $k_{\parallel}$  plane. Since the foregrounds are spectrally smooth, they occupy the smallest values of  $k_{\parallel}$  in two-dimensional Fourier space. However the coupling between the foregrounds and instruments gives rise to a triangular region in Fourier space known as the wedge

that is given by

$$k_{\parallel} \leq \left( \frac{X}{\nu Y} \right) |\mathbf{k}_{\perp}|, \quad (1.8)$$

where  $\nu$  is the observation frequency [46] and  $X, Y$  are given by Equations 1.5 and 1.6 [44, 45]. In Figure 1.4 we show the expected bias in the estimated power spectrum due to the foregrounds. Notice that the brightest regions correspond to the lowest  $k_{\parallel}$  modes. Also notice how the foregrounds at larger  $\mathbf{k}_{\perp}$  proliferate into higher  $k_{\parallel}$ .

For global signal experiments, one needs to account for the mean of Equation 1.7. In this case the foregrounds are often fitted for with a combination of power laws of the form

$$\log(\bar{T}_{\text{FG}}(\nu)) = \sum_{i=0}^4 a_i \log \left( \frac{\nu}{\nu_i} \right)^i. \quad (1.9)$$

where  $a_i$  is the related to the logarithm of the mean sky temperature in Equation 1.7 and the additional spectral components relative to Equation 1.7 account for possible spatial variations in the spectral index  $\beta$  as well as instrumentation issues that can cause additional spectral structure. This was the approach for the EDGES detection [8]. Other experiments such as the REACH experiment base their approach on empirically tuned sky models rather than generic parametrizations of the foregrounds beyond generic statements about spectral smoothness. This approach can potentially provide stronger constraints on the 21cm signal.

Besides the radio foregrounds, there are other sources of radio emission which affect the data-analysis portion of 21cm experiments. These sources of contamination are called Radio Frequency Interference (RFI) and can be several orders of magnitude brighter than emission from astrophysical sources. RFI originates from artificial (i.e. human) processes. Leaving these artificial sources of radio emission in the data cause obvious problems in the analysis pipeline [39, 40, 42, 83]. Conversely, excising the RFI introduces gaps into the data. In the context of a global signal experiment, excising the RFI leads to reducing the signal to noise of the measurement. RFI excision is even more problematic for interferometric instruments which intend to measure the power spectrum. If these gaps are not accounted for, they can produce artifacts into the data analysis pipeline ultimately contaminating the power spectrum which can potentially make detection of  $\Delta_{21}^2$

difficult. Note that there are many other systematic challenges for REACH and HERA. Since my work is focused on RFI contamination (HERA) and foregrounds (REACH), this thesis is concentrated on these two types of systematics. Therefore this list is only a partial representation of the current work being done in resolving systematic issues in 21cm instruments.

Since other probes of the EoR are not limited by the same systematics that limit 21cm cosmology, there has been interest in exploring other indirect means to study reionization. In the following sections we discuss a few of these indirect probes: CMB optical depth  $\tau$ , FRBs, and UV luminosity functions as well as Ly $\alpha$  emission from high  $z$  galaxies.

### 1.1.5 Indirect Probes

The EoR transforms the ionization state of the IGM and thus imprints a unique signature on astrophysical (and cosmological) probes which are sensitive to the number of free electrons  $n_e$  in the IGM. As an example, consider the optical depth  $\tau$  from CMB anisotropy studies. In this case, CMB photons are Thomson scattered by the free electrons produced by the EoR. This reduces the amplitude of the observed primordial CMB anisotropies. Thus by measuring  $\tau$  one can place constraints on the EoR history. In this way the Planck experiment was able to constrain the midpoint (when the IGM is 50% ionized) of reionization to  $z = 7.68 \pm 0.79$  [62]. Similarly large-scale polarization of the CMB radiation is induced when CMB photons scatter off the free electrons in the IGM.

Another indirect probe of the EoR are FRBs. FRBs are a class of bright, millisecond duration, radio transients that have been detected at frequencies ranging from 110 MHz to 1.5 GHz [60, 78]. Although one FRB source has been localized within the Milky Way [11], most of the catalogued FRBs remain extragalactic sources and can thus probe out to cosmological distances [18, 37]. The key observable of an FRB is the Dispersion Measure (DM) which relates to the broadening of the radio pulse as the photons move from source of the FRB to the observer. The DM of an FRB is proportional to the integrated column density of ionized electron gas  $n_e$  along the line of sight. Since  $n_e$  implicitly depends on the underlying density field  $\delta$ , low  $z$  FRBs have already been used as a cosmological probe [80]. If high redshift FRBs ( $z > 6$ ) are shown to exist, the EoR will also

impact their observed DM. Thus by measuring the DM of high  $z$  FRBs one can infer the mean number density of free electrons of along the line of sight to probe the timeline of reionization. At this stage there has been little work done in this regard, and thus the type of constraints that FRBs can place on the EoR are relatively unexplored.

Since UV photons are thought to be responsible for reionization, one can also directly search for these ionizing sources to form the UV luminosity function  $\phi$ . This is the number density of galaxies as a function of their luminosity in the UV regime. A number of high redshift galaxies, i.e. by [4, 6, 10, 47, 53, 54] have placed constraints on  $\phi$ . Since the UV luminosity function tracks the most massive stars which have the shortest life span,  $\phi$  is a good indicator of the star formation rate (SFR). In the context of EoR models, the SFR influences how many ionizing photons are produced. Thus one can translate empirical constraints on  $\phi$  to a constraint on the number of ionizing photons produced, leading to a constraint on reionization. In Figure 1.5 we show the UV luminosity function for a variety of redshifts. Qualitatively we can see that  $\phi$  drops for  $z > 6$  indicating the presence of neutral hydrogen absorbing UV photons [52, 53]<sup>1</sup>. Recently, the James Webb Space Telescope (JWST) has observed ultra high- $z$  galaxies as well as candidates up to  $z \sim 17$  [19, 51]. These observations have shown unexpected abundance of early massive galaxies  $M \sim 10^9 M_\odot$  at high redshifts ( $z > 10$ ). Should these candidates be confirmed, this can have possible ramifications for the EoR since these are the typical galaxies that are thought to drive reionization.

### 1.1.6 Sources of Ly $\alpha$ Emission

One of the most widely studied indirect probes of the EoR is detection of Ly $\alpha$  emission from high redshift galaxies. Ly $\alpha$  emission is powered by two mechanisms which frequently occur during the EoR making Ly $\alpha$  radiation abundant during this epoch. The first such mechanism is through the recombination of ionized hydrogen. This is known as “recombination radiation”. Recombination radiation is driven by the ionizing radiation emitted by hot young stars which have ionized the surrounding interstellar gas. Since the gas in the vicinity of these stars is very dense, the recombination timescale of the ionized hydrogen is very short. It was shown in [34] that the

---

<sup>1</sup>Note that it is still unclear whether this is due to reionization or the evolution in galaxy properties

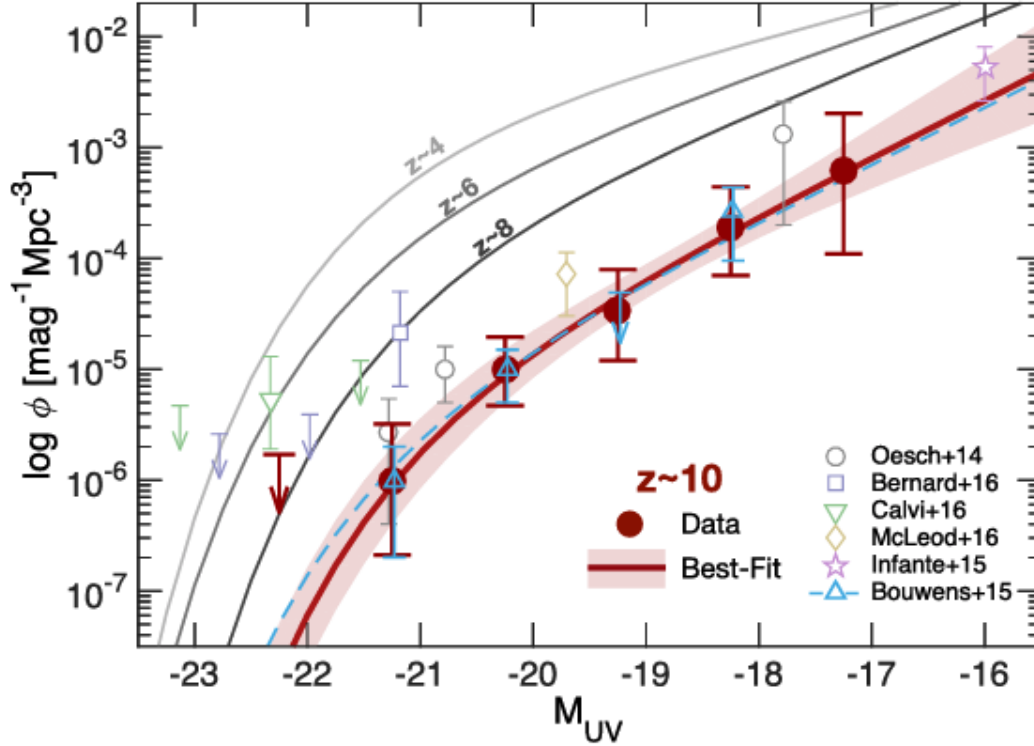


**Figure 1.5:** The UV luminosity function at redshifts  $z = 4, 6, 8, 10$ . Note that the UV luminosity decreases rapidly after  $z > 6$ . The red dots correspond to measurements of galaxies at  $z \sim 10$  while the red solid lines correspond to best fitting Schechter function. Image credit: [52]

recombination time is

$$t_{\text{rec}} = \frac{1}{\alpha(T)n_e} \quad (1.10)$$

where  $n_e$  is the number density of free electrons and  $\alpha(T)$  encodes the temperature dependent recombination coefficient of hydrogen. Equation 1.10 shows that recombinations are more frequent in regions with higher number densities of free electrons. Consequently, recombinations in the inter stellar medium (ISM), i.e. where  $n_e$  is much larger, are significantly more frequent than in the IGM. To see this, we can compute the recombination rate of ionized hydrogen in ionized bubbles by replacing  $n_e$  with the mean number density of free electrons ( $\delta = 0$ ) in the IGM. This has been shown to be  $n_e = 2 \times 10^{-7}(1+z)^3 \text{cm}^{-3}$  by [16, 17]<sup>2</sup>. In this case Equation 1.10 becomes  $t_{\text{rec}} = 9.3 \times 10^9 \left(\frac{1+z}{4}\right)^{-3} (T/10^4 \text{K})^{0.7} \text{yr}$  for ionized regions in the IGM. This is significantly larger

<sup>2</sup>Assuming cosmological parameters consistent with Planck [62]

than a Hubble time, i.e.  $t_{\text{Hubble}} \approx 24(1+z)^{3/2}\text{Gyr}$ . Thus we can neglect recombinations originating in the IGM and focus strictly in the ISM. When this hydrogen recombines, it often does so into an excited state, and then quickly cascades down to the ground state. This process gives rise to Ly $\alpha$  radiation. The Ly $\alpha$  energy emitted per unit time and volume due to recombination radiation is given by

$$j_{\text{rec}} = p(\text{Ly}\alpha)n_en_p \frac{\alpha(T)\phi(\nu)E_\alpha}{\sqrt{\pi}\Delta\nu_D} \quad (1.11)$$

where  $n_p$  is the number densities of the free protons,  $E_\alpha$  is the difference between the  $n = 2$  and  $n = 1$  states of hydrogen 10.2eV,  $\phi(\nu)$  is the Ly $\alpha$  absorption profile called the Voigt profile,  $\Delta\nu_D = 1.1 \times 10^{11}(T/10^4)^{1/2}\text{Hz}$  is the thermal broadening of the line and  $p(\text{Ly}\alpha)$  is the refers to the fraction of recombinations that ultimately lead to Ly $\alpha$  radiation, 0.68 [16, 17, 29, 75].

The second source of Ly $\alpha$  radiation is through collisionally excited hydrogen. In collisionally excited hydrogen, a free electron interacts with a neutral hydrogen atom via collision. The collision leads to a scenario where the electron of the neutral hydrogen atom is excited. Since the lifetime of the electron in the excited state is short ( $10^{-9}\text{s}$ ), a Ly $\alpha$  photon is emitted shortly after. It has been shown in [16, 17] that this leads to a Ly $\alpha$  energy emitted per unit time and volume identical to Equation 1.11 but with the probability of obtaining a Ly $\alpha$  photon  $p(\text{Ly}\alpha) = n_{\text{HI}}8.63 \times 10^{-6}T^{-1/2}\langle\Omega_{\text{tr}}\rangle\exp(-E_\alpha/k_{\text{B}}T)$  where  $\langle\Omega_{\text{tr}}\rangle$  is the velocity averaged collision strength and  $n_{\text{HI}}$  is the number density of neutral hydrogen. The EoR creates perfect conditions for the production of Ly $\alpha$  photons via recombination radiation and collisionally excitement since at high redshift the gas surrounding stars is dense and battered with ionizing radiation.

### 1.1.7 Ly $\alpha$ Emission As a Probe of The EoR

A galaxy that emits Ly $\alpha$  radiation is known as a Ly $\alpha$  emitter (LAE). One can use the clustering, number density and UV luminosity of LAEs to set constraints on reionization (see Chapter 4 for a more details regarding how these can be used to set constraints on reionization). In order to constrain the timeline of reionization using Ly $\alpha$  flux from LAEs, one must know the intrinsic Ly $\alpha$  flux leaving the ISM of the emitting galaxy. Thus making connections between observed Ly $\alpha$  flux

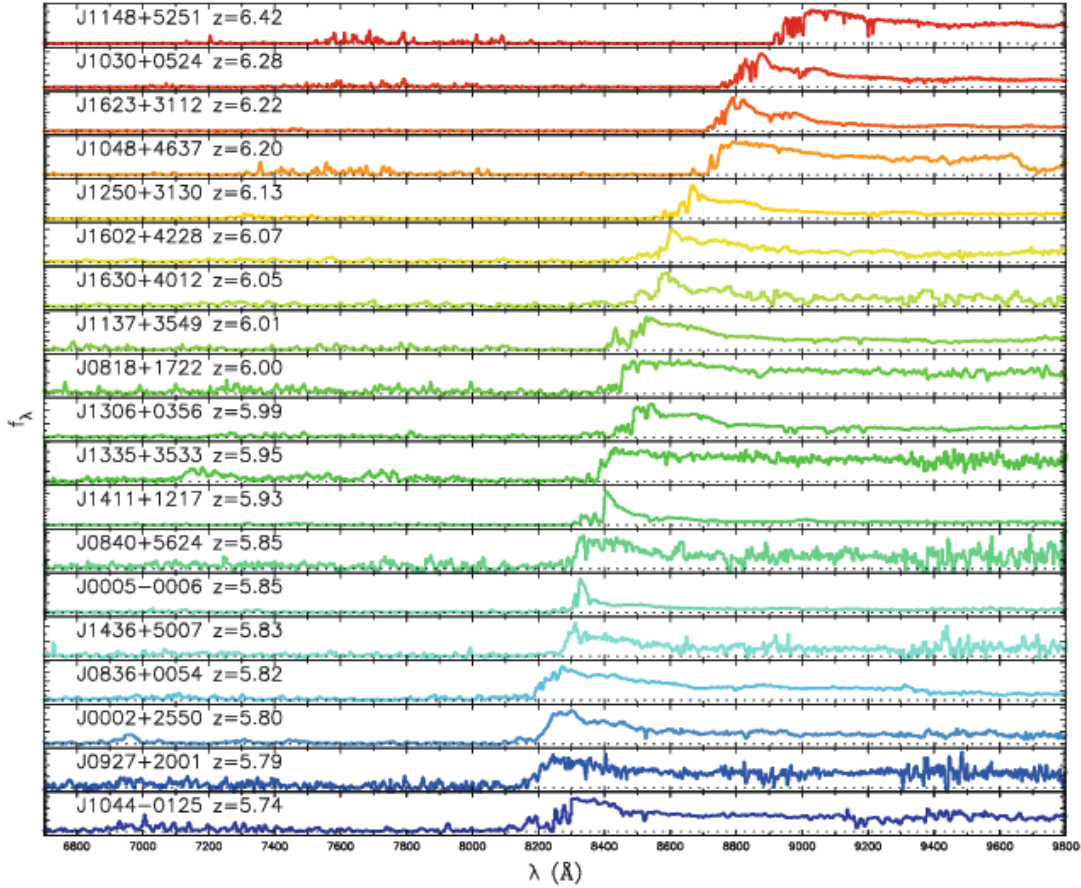


**Figure 1.6:** Ly $\alpha$  forest for 19 high redshifts quasars from [22]. Note that quasars above  $z > 6$  show no transmission in the Gunn-Peterson trough. Image credit: [22]

and the neutral properties of the IGM are prone to the complex radiative transfer physics which determine how much Ly $\alpha$  flux is transmitted through the ISM [17,27,28]. For example, the spectral line profile of Ly $\alpha$  emission, the distribution of dust, as well as the escape fraction of Ly $\alpha$  photons all determine how much Ly $\alpha$  emission leaves the ISM [28, 35, 79, 82]. This intrinsic Ly $\alpha$  flux is therefore degenerate with a reduction in transmission in the IGM due to neutral hydrogen. Thus this is a systematic issue preventing LAEs from setting tighter constraints on reionization. In the future JWST may provide detailed characterization of ISM physics which can potentially break some of these degeneracies. This has led other works to instead focus on the statistics of LAEs which are less dependent on the intrinsic flux emitted from the ISM. For example, [49, 73] have used the clustering of LAEs to set constraints on the EoR model parameters.

Some of the strongest EoR constraints using the Ly $\alpha$  line come from the spectra of high redshift quasars. Photons emitted from the quasar are progressively redshifted as they move through the IGM. Eventually their redshifted energy will match the energy of the Ly $\alpha$  line. Since Ly $\alpha$  is resonant with neutral hydrogen, any Ly $\alpha$  photon is readily absorbed by the neutral hydrogen in the IGM. Thus the redshifted photon can be absorbed if it is in the presence of neutral hydrogen. By identifying Ly $\alpha$  absorption lines in the spectra of high redshift quasars, we can infer the ionization properties of the IGM. This is known as the Ly $\alpha$  forest. In Figure 1.6 we show example spectra of various high  $z$  quasars from [22]. Notice that below  $z = 6$ , Ly $\alpha$  transmission is frequently observed. Conversely that at  $z \geq 6$  many spectra show complete absorption of the Ly $\alpha$  forest. This is known as the Gunn-Peterson trough [3]. It has been shown in [3] that if the IGM is ionized to better than 1 part in  $10^4$  then Ly $\alpha$  emission will be saturated by the residual neutral hydrogen in the IGM. Thus the saturation of Ly $\alpha$  flux above redshifts  $z = 6$  have been used as evidence of the end of reionization. Recently, however, it has been shown that the Ly $\alpha$  forest of some quasars between redshifts 5.9 – 6.0 still have appreciable suppression of Ly $\alpha$  flux below  $z < 6$  [2, 20, 36, 79]. This has been used as evidence of neutral islands of hydrogen still remaining at redshifts below  $z < 6$ . Recent work has shown that late-ending reionization models, e.g. [38, 41] are in good agreement with the observations.

### 1.1.8 Roadmap

There are two main objectives of this thesis. First, to forecast the types of constraints that we can place on CD and the EoR using both direct and indirect probes. This is the subject of the first three chapters:

- **Chapter 2**, titled ‘*Quantifying Density-Ionization Correlations with the 21cm Power Spectrum*’. Here we develop a method to parametrize the density-ionization correlations during the EoR. This parametrization is used as a tool to rule out classes of EoR models. This work is based on a published paper [56]. The paper was written by me, with feedback given by my supervisor Adrian Liu. I performed all the calculations with the guidance and advice from Adrian Liu. I am the primary author of this paper.

- **Chapter 3**, titled '*Constraining the Epoch of Reionization With Highly Dispersed Fast Radio Bursts*'. This work explores whether the DM of high redshift FRBs are sensitive to the details of reionization. We also examine the types of constraints that measurement of high redshift DMs can place on the timeline of reionization. This work is based on published work [55] done in collaboration with my colleague Hannah Fronenberg. We collaborated on the big picture of the project. I produced the mock dataset, computations, model fitting and result interpretations. Hannah produced the intrinsic number count of FRBs (Section 4.2). I wrote Sections 2,3,4,5,6 (with the exception of Section 4.2 which was entirely written by Hannah). We collaborated on Sections 1 and 6. I am primary author of the paper.
- **Chapter 4**, titled '*Lyman Alpha Emitters and the 21cm Power Spectrum as Probes of Density-Ionization Correlation in the Epoch of Reionization*'. This work examines the effect that density-ionization correlation has on the statistics of LAEs. We forecast the types of constraints that can be placed on the EoR using measurement of the 21cm power spectrum and observations of LAEs. This is the result of published work [57]. I performed all the calculations with the guidance and advice from Adrian Liu. I wrote the paper with feedback give by Adrian Liu. I am primary author of this paper.

The second objective of this thesis is devoted to overcoming systematics that are present in the data analysis pipeline of 21cm interferometric measures and global signal measurements. Specifically I focus on RFI contamination in 21cm interferometric measurements using HERA as the fiducial instrument for this analysis. I also examine foreground systematics in global signal experiments, using REACH as a testbed for the study. This work is the subject of the following chapters:

- **Chapter 5**, titled '*Error Characterization Of Inpaint Methods In Interferometric Measurements of the Epoch Of Reionization*'. This work characterizes the types of errors that inpainting RFI corrupted data has on the data analysis pipeline of interferometric measurements of the 21cm signal. We also introduce a convolutional neural network (CNN) capable of inpainting RFI corrupted data. This work is based on a yet to be published paper written in collaboration with Jing Liu, an undergraduate student at McGill University, my super-

visor Adrian Liu, Siamak Ravanbakhsh from the Computer Science department at McGill University as well as members of the HERA collaboration: Nick Kern, Aaron-Ewall Wice, Phil Bull, Bobby Pascua. The paper is completed and is waiting for the HERA collaboration mandate of 2 weeks before it can be officially submitted. I built the CNN which is based on the barebones structure created by Jing Liu and Siamak Ravanbakhsh. My modifications were of the hyperparameters, loss function, input shapes. I added additional layers to the network. I performed all the error characterization of the project. The HERA collaborators provided technical support for implementation of the inpainting techniques. The entire work was supervised by Adrian Liu. I wrote all paper with comments and feedback provided by Adrian Liu. Members of the HERA collaboration (Nick Kern, Phil Bull, Bryna Hazelton, Steven Murray, James Aguirre, Josh Dillon) provided additional comments. I am primary author of the paper.

- **Chapter 6**, titled '*A General Bayesian Framework to Account for Foreground Map Errors in Global 21-cm Experiments*'. This work explores the effect that errors in the foreground models have on the REACH data analysis pipeline as well as develop a framework that can account for them. This is the result of yet to be published work. The paper is completed and is waiting for the REACH collaboration mandate of 2 weeks before it can be officially submitted. This work was done in collaboration with Peter Sims, a postdoctoral scholar from McGill University as well as Adrian Liu. I performed all the computations, analysis and writing. Peter Sims and Adrian Liu provided comments to the writing. Peter Sims provided guidance throughout the project as well as aided with the interpretation of the results. Adrian Liu supervised the project and provided critical feedback and advice. I am primary author of the paper.

In the context of systematics, I work on RFI contamination (HERA) and foregrounds systematics (REACH). I therefore focus on these two types of systematics in this thesis. However it should be noted that this is only a partial list of all systematics that are pervasive in 21cm instruments and so there are many other systematic challenges faced by HERA and REACH.

## Bibliography

- [1] Rennan Barkana. Possible interaction between baryons and dark-matter particles revealed by the first stars. , 555(7694):71–74, March 2018.
- [2] George D. Becker, Max Pettini, Marc Rafelski, Valentina D’Odorico, Elisa Boera, Lise Christensen, Guido Cupani, Sara L. Ellison, Emanuele Paolo Farina, Michele Fumagalli, Sebastian López, Marcel Neeleman, Emma V. Ryan-Weber, and Gábor Worseck. The Evolution of O I over  $3.2 < z < 6.5$ : Reionization of the Circumgalactic Medium. , 883(2):163, October 2019.
- [3] Robert H. Becker, Xiaohui Fan, Richard L. White, Michael A. Strauss, Vijay K. Narayanan, Robert H. Lupton, James E. Gunn, James Annis, Neta A. Bahcall, J. Brinkmann, A. J. Connolly, István Csabai, Paul C. Czarapata, Mamoru Doi, Timothy M. Heckman, G. S. Hennessy, Željko Ivezić, G. R. Knapp, Don Q. Lamb, Timothy A. McKay, Jeffrey A. Munn, Thomas Nash, Robert Nichol, Jeffrey R. Pier, Gordon T. Richards, Donald P. Schneider, Chris Stoughton, Alexander S. Szalay, Aniruddha R. Thakar, and D. G. York. Evidence for Reionization at  $z \sim 6$ : Detection of a Gunn-Peterson Trough in a  $z=6.28$  Quasar. , 122(6):2850–2857, December 2001.
- [4] S. R. Bernard, D. Carrasco, M. Trenti, P. A. Oesch, J. F. Wu, L. D. Bradley, K. B. Schmidt, R. J. Bouwens, V. Calvi, C. A. Mason, M. Stiavelli, and T. Treu. GALAXY CANDIDATES AT  $z \sim 10$  IN ARCHIVAL DATA FROM THE BRIGHTEST OF REIONIZING GALAXIES (BORG[ $z8$ ]) SURVEY. *The Astrophysical Journal*, 827(1):76, aug 2016.
- [5] H. T. J. Bevens, W. J. Handley, A. Fialkov, E. de Lera Acedo, L. J. Greenhill, and D. C. Price. MAXSMOOTH: rapid maximally smooth function fitting with applications in Global 21-cm cosmology. , 502(3):4405–4425, April 2021.
- [6] R. J. Bouwens, G. D. Illingworth, P. A. Oesch, M. Trenti, I. Labbé, L. Bradley, M. Carollo, P. G. van Dokkum, V. Gonzalez, B. Holwerda, M. Franx, L. Spitler, R. Smit, and D. Magee. UV Luminosity Functions at Redshifts  $z \sim 4$  to  $z \sim 10$ : 10,000 Galaxies from HST Legacy Fields. , 803(1):34, April 2015.

- [7] Judd D. Bowman, Alan E. E. Rogers, and Jacqueline N. Hewitt. Toward Empirical Constraints on the Global Redshifted 21 cm Brightness Temperature During the Epoch of Reionization. , 676(1):1–9, March 2008.
- [8] Judd D. Bowman, Alan E. E. Rogers, Raul A. Monsalve, Thomas J. Mozdzen, and Nivedita Mahesh. An absorption profile centred at 78 megahertz in the sky-averaged spectrum. , 555(7694):67–70, March 2018.
- [9] Richard F. Bradley, Keith Tauscher, David Rapetti, and Jack O. Burns. A Ground Plane Artifact that Induces an Absorption Profile in Averaged Spectra from Global 21 cm Measurements, with Possible Application to EDGES. , 874(2):153, April 2019.
- [10] V. Calvi, M. Trenti, M. Stiavelli, P. Oesch, L. D. Bradley, K. B. Schmidt, D. Coe, G. Brammer, S. Bernard, R. J. Bouwens, D. Carrasco, C. M. Carollo, B. W. Holwerda, J. W. MacKenty, C. A. Mason, J. M. Shull, and T. Treu. Bright Galaxies at Hubble’s Redshift Detection Frontier: Preliminary Results and Design from the Redshift  $z \sim 9$ -10 BoRG Pure-Parallel HST Survey. , 817(2):120, February 2016.
- [11] CHIME/FRB Collaboration, B. C. Andersen, K. M. Bandura, M. Bhardwaj, A. Bij, M. M. Boyce, P. J. Boyle, C. Brar, T. Cassanelli, P. Chawla, T. Chen, J. F. Cliche, A. Cook, D. Cubranic, A. P. Curtin, N. T. Denman, M. Dobbs, F. Q. Dong, M. Fandino, E. Fonseca, B. M. Gaensler, U. Giri, D. C. Good, M. Halpern, A. S. Hill, G. F. Hinshaw, C. Höfer, A. Josephy, J. W. Kania, V. M. Kaspi, T. L. Landecker, C. Leung, D. Z. Li, H. H. Lin, K. W. Masui, R. McKinven, J. Mena-Parra, M. Merryfield, B. W. Meyers, D. Michilli, N. Milutinovic, A. Mirhosseini, M. Münchmeyer, A. Naidu, L. B. Newburgh, C. Ng, C. Patel, U. L. Pen, T. Pinsonneault-Marotte, Z. Pleunis, B. M. Quine, M. Rafiei-Ravandi, M. Rahman, S. M. Ransom, A. Renard, P. Sanghavi, P. Scholz, J. R. Shaw, K. Shin, S. R. Siegel, S. Singh, R. J. Smegal, K. M. Smith, I. H. Stairs, C. M. Tan, S. P. Tendulkar, I. Tretyakov, K. Vanderlinde, H. Wang, D. Wulf, and A. V. Zwaniga. A bright millisecond-duration radio burst from a Galactic magnetar. , 587(7832):54–58, November 2020.

- [12] Eloy de Lera Acedo. Reach: Radio experiment for the analysis of cosmic hydrogen. *2019 International Conference on Electromagnetics in Advanced Applications (ICEAA)*, pages 0626–0629, 2019.
- [13] Angélica de Oliveira-Costa, Max Tegmark, B. M. Gaensler, Justin Jonas, T. L. Landecker, and Patricia Reich. A model of diffuse Galactic radio emission from 10 MHz to 100 GHz. , 388(1):247–260, July 2008.
- [14] David R. DeBoer, Aaron R. Parsons, James E. Aguirre, Paul Alexander, Zaki S. Ali, Adam P. Beardsley, Gianni Bernardi, Judd D. Bowman, Richard F. Bradley, Chris L. Carilli, Carina Cheng, Eloy de Lera Acedo, Joshua S. Dillon, Aaron Ewall-Wice, Gcobisa Fadana, Nicolas Fagnoni, Randall Fritz, Steve R. Furlanetto, Brian Glendenning, Bradley Greig, Jasper Grobbelaar, Bryna J. Hazelton, Jacqueline N. Hewitt, Jack Hickish, Daniel C. Jacobs, Austin Julius, MacCalvin Kariseb, Saul A. Kohn, Telalo Lekalake, Adrian Liu, Anita Loots, David MacMahon, Lourence Malan, Cresshim Malgas, Matthys Maree, Zachary Martinot, Nathan Mathison, Eunice Matsetela, Andrei Mesinger, Miguel F. Morales, Abraham R. Neben, Nipanjana Patra, Samantha Pieterse, Jonathan C. Pober, Nima Razavi-Ghods, Jon Ringuette, James Robnett, Kathryn Rosie, Raddwine Sell, Craig Smith, Angelo Syce, Max Tegmark, Nithyanandan Thyagarajan, Peter K. G. Williams, and Haoxuan Zheng. Hydrogen Epoch of Reionization Array (HERA). , 129(974):045001, April 2017.
- [15] P. E. Dewdney, P. J. Hall, R. T. Schilizzi, and T. J. L. W. Lazio. The Square Kilometre Array. *IEEE Proceedings*, 97(8):1482–1496, August 2009.
- [16] Mark Dijkstra. Ly $\alpha$  Emitting Galaxies as a Probe of Reionisation. , 31:e040, October 2014.
- [17] Mark Dijkstra, Andrei Mesinger, and J. Stuart B. Wyithe. The detectability of Ly $\alpha$  emission from galaxies during the epoch of reionization. , 414(3):2139–2147, July 2011.
- [18] K. Dolag, B. M. Gaensler, A. M. Beck, and M. C. Beck. Constraints on the distribution and energetics of fast radio bursts using cosmological hydrodynamic simulations. , 451(4):4277–4289, August 2015.

- [19] C. T. Donnan, D. J. McLeod, J. S. Dunlop, R. J. McLure, A. C. Carnall, R. Begley, F. Cullen, M. L. Hamadouche, R. A. A. Bowler, H. J. McCracken, B. Milvang-Jensen, A. Moneti, and T. Targett. The evolution of the galaxy UV luminosity function at redshifts  $z \sim 8-15$  from deep JWST and ground-based near-infrared imaging. *arXiv e-prints*, page arXiv:2207.12356, July 2022.
- [20] Anna-Christina Eilers, Joseph F. Hennawi, Frederick B. Davies, and Jose Oñorbe. Anomaly in the Opacity of the Post-reionization Intergalactic Medium in the Ly $\alpha$  and Ly $\beta$  Forest. , 881(1):23, August 2019.
- [21] A. Ewall-Wice, T. C. Chang, J. Lazio, O. Doré, M. Seiffert, and R. A. Monsalve. Modeling the Radio Background from the First Black Holes at Cosmic Dawn: Implications for the 21 cm Absorption Amplitude. , 868(1):63, November 2018.
- [22] Xiaohui Fan, Michael A. Strauss, Robert H. Becker, Richard L. White, James E. Gunn, Gillian R. Knapp, Gordon T. Richards, Donald P. Schneider, J. Brinkmann, and Masataka Fukugita. Constraining the Evolution of the Ionizing Background and the Epoch of Reionization with  $z \sim 6$  Quasars. II. A Sample of 19 Quasars. , 132(1):117–136, July 2006.
- [23] Anastasia Fialkov and Rennan Barkana. Signature of excess radio background in the 21-cm global signal and power spectrum. , 486(2):1763–1773, June 2019.
- [24] George B. Field. Excitation of the Hydrogen 21-CM Line. *Proceedings of the IRE*, 46:240–250, January 1958.
- [25] Steven R. Furlanetto, S. Peng Oh, and Frank H. Briggs. Cosmology at low frequencies: The 21 cm transition and the high-redshift Universe. , 433(4-6):181–301, October 2006.
- [26] Steven R. Furlanetto, Matias Zaldarriaga, and Lars Hernquist. Statistical Probes of Reionization with 21 Centimeter Tomography. , 613(1):16–22, September 2004.
- [27] Max Gronke, Mark Dijkstra, Michael McCourt, and S. Peng Oh. From Mirrors to Windows: Lyman-alpha Radiative Transfer in a Very Clumpy Medium. , 833(2):L26, December 2016.

- [28] Max Gronke, Mark Dijkstra, Michael McCourt, and S. Peng Oh. Resonant line transfer in a fog: using Lyman-alpha to probe tiny structures in atomic gas. , 607:A71, November 2017.
- [29] Zoltán Haiman. The Detectability of High-Redshift Ly $\alpha$  Emission Lines prior to the Reionization of the Universe. , 576(1):L1–L4, September 2002.
- [30] HERA Collaboration, Zara Abdurashidova, James E. Aguirre, Paul Alexander, Zaki S. Ali, Yanga Balfour, Adam P. Beardsley, Gianni Bernardi, Tashalee S. Billings, Judd D. Bowman, Richard F. Bradley, Philip Bull, Jacob Burba, Steve Carey, Chris L. Carilli, Carina Cheng, David R. DeBoer, Matt Dexter, Eloy de Lera Acedo, Taylor Dibblee-Barkman, Joshua S. Dillon, John Ely, Aaron Ewall-Wice, Nicolas Fagnoni, Randall Fritz, Steven R. Furlanetto, Kingsley Gale-Sides, Brian Glendenning, Deepthi Gorthi, Bradley Greig, Jasper Grobbelaar, Ziyaad Halday, Bryna J. Hazelton, Jacqueline N. Hewitt, Jack Hickish, Daniel C. Jacobs, Austin Julius, Nicholas S. Kern, Joshua Kerrigan, Piyanat Kittiwisit, Saul A. Kohn, Matthew Kolopanis, Adam Lanman, Paul La Plante, Telalo Lekalake, David Lewis, Adrian Liu, David MacMahon, Lourence Malan, Cresshim Malgas, Matthys Maree, Zachary E. Martinot, Eunice Matsetela, Andrei Mesinger, Mathakane Molewa, Miguel F. Morales, Tshegofalang Mosiane, Steven G. Murray, Abraham R. Neben, Bojan Nikolic, Chuneeta D. Nunhokee, Aaron R. Parsons, Nipanjana Patra, Robert Pascua, Samantha Pieterse, Jonathan C. Pober, Nima Razavi-Ghods, Jon Ringuette, James Robnett, Kathryn Rosie, Peter Sims, Saurabh Singh, Craig Smith, Angelo Syce, Nithyanandan Thyagarajan, Peter K. G. Williams, Haoxuan Zheng, and HERA Collaboration. First Results from HERA Phase I: Upper Limits on the Epoch of Reionization 21 cm Power Spectrum. , 925(2):221, February 2022.
- [31] J. Colin Hill and Eric J. Baxter. Can early dark energy explain EDGES? , 2018(8):037, August 2018.
- [32] Richard Hills, Girish Kulkarni, P. Daniel Meerburg, and Ewald Puchwein. Concerns about modelling of the EDGES data. , 564(7736):E32–E34, December 2018.

- [33] G. Hinshaw, D. Larson, E. Komatsu, D. N. Spergel, C. L. Bennett, J. Dunkley, M. R. Nolta, M. Halpern, R. S. Hill, N. Odegard, L. Page, K. M. Smith, J. L. Weiland, B. Gold, N. Jarosik, A. Kogut, M. Limon, S. S. Meyer, G. S. Tucker, E. Wollack, and E. L. Wright. Nine-year Wilkinson Microwave Anisotropy Probe (WMAP) Observations: Cosmological Parameter Results. , 208(2):19, October 2013.
- [34] Lam Hui and Nickolay Y. Gnedin. Equation of state of the photoionized intergalactic medium. , 292(1):27–42, November 1997.
- [35] Anne Hutter, Pratika Dayal, Adrian M. Partl, and Volker Müller. The visibility of Lyman  $\alpha$  emitters: constraining reionization, ionizing photon escape fractions and dust. , 441(4):2861–2877, July 2014.
- [36] Linhua Jiang, Ian D. McGreer, Xiaohui Fan, Fuyan Bian, Zheng Cai, Benjamin Clément, Ran Wang, and Zhou Fan. DISCOVERY OF EIGHT  $z \sim 6$  QUASARS IN THE SLOAN DIGITAL SKY SURVEY OVERLAP REGIONS. *The Astronomical Journal*, 149(6):188, may 2015.
- [37] J. I. Katz. Inferences from the Distributions of Fast Radio Burst Pulse Widths, Dispersion Measures, and Fluences. , 818(1):19, February 2016.
- [38] Laura C. Keating, Girish Kulkarni, Martin G. Haehnelt, Jonathan Chardin, and Dominique Aubert. Constraining the second half of reionization with the Ly  $\beta$  forest. , 497(1):906–915, September 2020.
- [39] Joshua Kerrigan, Paul La Plante, Saul Kohn, Jonathan C. Pober, James Aguirre, Zara Abdurashidova, Paul Alexander, Zaki S. Ali, Yanga Balfour, Adam P. Beardsley, Gianni Bernardi, Judd D. Bowman, Richard F. Bradley, Jacob Burba, Chris L. Carilli, Carina Cheng, David R. DeBoer, Matt Dexter, Eloy de Lera Acedo, Joshua S. Dillon, Julia Estrada, Aaron Ewall-Wice, Nicolas Fagnoni, Randall Fritz, Steve R. Furlanetto, Brian Glendenning, Bradley Greig, Jasper Grobbelaar, Deepthi Gorthi, Ziyaad Halday, Bryna J. Hazelton, Jack Hickish, Daniel C. Jacobs, Austin Julius, Nicholas S. Kern, Piyanat Kittiwisit, Matthew Kolopanis,

- Adam Lanman, Telalo Lekalake, Adrian Liu, David MacMahon, Lourence Malan, Cresshim Malgas, Matthys Maree, Zachary E. Martinot, Eunice Matsetela, Andrei Mesinger, Mathakane Molewa, Miguel F. Morales, Tshegofalang Mosiane, Abraham R. Neben, Aaron R. Parsons, Nipanjana Patra, Samantha Pieterse, Nima Razavi-Ghods, Jon Ringuette, James Robnett, Kathryn Rosie, Peter Sims, Craig Smith, Angelo Syce, Nithyanandan Thyagarajan, Peter K. G. Williams, and Haoxuan Zheng. Optimizing sparse RFI prediction using deep learning. , 488(2):2605–2615, September 2019.
- [40] S. A. Kohn, J. E. Aguirre, C. D. Nunhokee, G. Bernardi, J. C. Pober, Z. S. Ali, R. F. Bradley, C. L. Carilli, D. R. DeBoer, N. E. Gugliucci, D. C. Jacobs, P. Klima, D. H. E. MacMahon, J. R. Manley, D. F. Moore, A. R. Parsons, I. I. Stefan, and W. P. Walbrugh. CONSTRAINING POLARIZED FOREGROUNDS FOR EoR EXPERIMENTS. i. 2d POWER SPECTRA FROM THE PAPER-32 IMAGING ARRAY. *The Astrophysical Journal*, 823(2):88, may 2016.
- [41] Girish Kulkarni, Laura C. Keating, Martin G. Haehnelt, Sarah E. I. Bosman, Ewald Puchwein, Jonathan Chardin, and Dominique Aubert. Large Ly  $\alpha$  opacity fluctuations and low CMB  $\tau$  in models of late reionization with large islands of neutral hydrogen extending to  $z < 5.5$ . , 485(1):L24–L28, May 2019.
- [42] P. La Plante, P. K. G. Williams, M. Kolopanis, J. S. Dillon, A. P. Beardsley, N. S. Kern, M. Wilensky, Z. S. Ali, Z. Abdurashidova, J. E. Aguirre, P. Alexander, Y. Balfour, G. Bernardi, T. S. Billings, J. D. Bowman, R. F. Bradley, P. Bull, J. Burba, S. Carey, C. L. Carilli, C. Cheng, D. R. DeBoer, M. Dexter, E. de Lera Acedo, J. Ely, A. Ewall-Wice, N. Fagnoni, R. Fritz, S. R. Furlanetto, K. Gale-Sides, B. Glendenning, D. Gorthi, B. Greig, J. Grobbelaar, Z. Halday, B. J. Hazelton, J. N. Hewitt, J. Hickish, D. C. Jacobs, A. Julius, J. Kerrigan, P. Kittiwisit, S. A. Kohn, A. Lanman, T. Lekalake, D. Lewis, A. Liu, D. MacMahon, L. Malan, C. Malgas, M. Maree, Z. E. Martinot, E. Matsetela, A. Mesinger, M. Molewa, M. F. Morales, T. Mosiane, S. Murray, A. R. Neben, B. Nikolic, A. R. Parsons, R. Pascua, N. Patra, S. Pieterse, J. C. Pober, N. Razavi-Ghods, J. Ringuette, J. Robnett, K. Rosie, M. G. Santos, P. Sims, C. Smith,

- A. Syce, N. Thyagarajan, and H. Zheng. A Real Time Processing system for big data in astronomy: Applications to HERA. *Astronomy and Computing*, 36:100489, July 2021.
- [43] T. L. Landecker and R. Wielebinski. The Galactic Metre Wave Radiation: A two-frequency survey between declinations  $+25^\circ$  and  $-25^\circ$  and the preparation of a map of the whole sky. *Australian Journal of Physics Astrophysical Supplement*, 16:1, January 1970.
- [44] Adrian Liu, Aaron R. Parsons, and Cathryn M. Trott. Epoch of reionization window. I. Mathematical formalism. , 90(2):023018, July 2014.
- [45] Adrian Liu, Aaron R. Parsons, and Cathryn M. Trott. Epoch of reionization window. II. Statistical methods for foreground wedge reduction. , 90(2):023019, July 2014.
- [46] Adrian Liu and J. Richard Shaw. Data Analysis for Precision 21 cm Cosmology. , 132(1012):062001, June 2020.
- [47] R. C. Livermore, S. L. Finkelstein, and J. M. Lotz. Directly Observing the Galaxies Likely Responsible for Reionization. , 835(2):113, February 2017.
- [48] C. J. Lonsdale, R. J. Cappallo, M. F. Morales, F. H. Briggs, L. Benkevitch, J. D. Bowman, J. D. Bunton, S. Burns, B. E. Corey, L. Desouza, S. S. Doeleman, M. Derome, A. Deshpande, M. R. Gopala, L. J. Greenhill, D. E. Herne, J. N. Hewitt, P. A. Kamini, J. C. Kasper, B. B. Kincaid, J. Kocz, E. Kowald, E. Kratzenberg, D. Kumar, M. J. Lynch, S. Madhavi, M. Matejek, D. A. Mitchell, E. Morgan, D. Oberoi, S. Ord, J. Pathikulangara, T. Prabu, A. Rogers, A. Roshi, J. E. Salah, R. J. Sault, N. U. Shankar, K. S. Srivani, J. Stevens, S. Tingay, A. Vaccarella, M. Waterson, R. B. Wayth, R. L. Webster, A. R. Whitney, A. Williams, and C. Williams. The Murchison Widefield Array: Design Overview. *IEEE Proceedings*, 97(8):1497–1506, August 2009.
- [49] Matthew McQuinn, Lars Hernquist, Matias Zaldarriaga, and Suvendra Dutta. Studying reionization with  $\text{Ly}\alpha$  emitters. , 381(1):75–96, October 2007.

- [50] Andrei Mesinger, Bradley Greig, and Emanuele Sobacchi. The Evolution Of 21 cm Structure (EOS): public, large-scale simulations of Cosmic Dawn and reionization. , 459(3):2342–2353, July 2016.
- [51] Rohan P. Naidu, Pascal A. Oesch, Pieter van Dokkum, Erica J. Nelson, Katherine A. Suess, Katherine E. Whitaker, Natalie Allen, Rachel Bezanson, Rychard Bouwens, Gabriel Brammer, Charlie Conroy, Garth Illingworth, Ivo Labbe, Joel Leja, Ecaterina Leonova, Jorryt Matthee, Sedona H. Price, David J. Setton, Victoria Strait, Mauro Stefanon, Sandro Tacchella, Sune Toft, John R. Weaver, and Andrea Weibel. Two Remarkably Luminous Galaxy Candidates at  $z \approx 11 - 13$  Revealed by JWST. *arXiv e-prints*, page arXiv:2207.09434, July 2022.
- [52] P. A. Oesch, R. J. Bouwens, G. D. Illingworth, I. Labbé, and M. Stefanon. The Dearth of  $z \sim 10$  Galaxies in All HST Legacy Fields—The Rapid Evolution of the Galaxy Population in the First 500 Myr. , 855(2):105, March 2018.
- [53] P. A. Oesch, G. Brammer, P. G. van Dokkum, G. D. Illingworth, R. J. Bouwens, I. Labbé, M. Franx, I. Momcheva, M. L. N. Ashby, G. G. Fazio, V. Gonzalez, B. Holden, D. Magee, R. E. Skelton, R. Smit, L. R. Spitler, M. Trenti, and S. P. Willner. A Remarkably Luminous Galaxy at  $z=11.1$  Measured with Hubble Space Telescope Grism Spectroscopy. , 819(2):129, March 2016.
- [54] P. A. Oesch, P. G. van Dokkum, G. D. Illingworth, R. J. Bouwens, I. Momcheva, B. Holden, G. W. Roberts-Borsani, R. Smit, M. Franx, I. Labbé, V. González, and D. Magee. A Spectroscopic Redshift Measurement for a Luminous Lyman Break Galaxy at  $z = 7.730$  Using Keck/MOSFIRE. , 804(2):L30, May 2015.
- [55] Michael Pagano and Hannah Fronenberg. Constraining the epoch of reionization with highly dispersed fast radio bursts. , 505(2):2195–2206, August 2021.
- [56] Michael Pagano and Adrian Liu. Quantifying density-ionization correlations with the 21-cm power spectrum. , 498(1):373–384, August 2020.

- [57] Michael Pagano and Adrian Liu. Lyman-alpha emitters and the 21 cm power spectrum as probes of density-ionization correlation in the epoch of reionization. , 508(2):1915–1928, December 2021.
- [58] Aaron R. Parsons, Donald C. Backer, Griffin S. Foster, Melvyn C. H. Wright, Richard F. Bradley, Nicole E. Gugliucci, Chaitali R. Parashare, Erin E. Benoit, James E. Aguirre, Daniel C. Jacobs, Chris L. Carilli, David Herne, Mervyn J. Lynch, Jason R. Manley, and Daniel J. Werthimer. The Precision Array for Probing the Epoch of Re-ionization: Eight Station Results. , 139(4):1468–1480, April 2010.
- [59] P. J. E. Peebles. The natural science of cosmology. In *Journal of Physics Conference Series*, volume 484 of *Journal of Physics Conference Series*, page 012001, March 2014.
- [60] E. Petroff, E. D. Barr, A. Jameson, E. F. Keane, M. Bailes, M. Kramer, V. Morello, D. Tabbara, and W. van Straten. FRBCAT: The Fast Radio Burst Catalogue. , 33:e045, September 2016.
- [61] L. Philip, Z. Abdurashidova, H. C. Chiang, N. Ghazi, A. Gumba, H. M. Heilgendorff, J. M. Jáuregui-García, K. Malepe, C. D. Nunhokee, J. Peterson, J. L. Sievers, V. Simes, and R. Spann. Probing Radio Intensity at High-Z from Marion: 2017 Instrument. *Journal of Astronomical Instrumentation*, 8(2):1950004, January 2019.
- [62] Planck Collaboration, P. A. R. Ade, N. Aghanim, M. Arnaud, M. Ashdown, J. Aumont, C. Baccigalupi, A. J. Banday, R. B. Barreiro, J. G. Bartlett, N. Bartolo, E. Battaner, R. Battye, K. Benabed, A. Benoît, A. Benoit-Lévy, J. P. Bernard, M. Bersanelli, P. Bielewicz, J. J. Bock, A. Bonaldi, L. Bonavera, J. R. Bond, J. Borrill, F. R. Bouchet, F. Boulanger, M. Bucher, C. Burigana, R. C. Butler, E. Calabrese, J. F. Cardoso, A. Catalano, A. Challinor, A. Chamballu, R. R. Chary, H. C. Chiang, J. Chluba, P. R. Christensen, S. Church, D. L. Clements, S. Colombi, L. P. L. Colombo, C. Combet, A. Coulais, B. P. Crill, A. Curto, F. Cuttaia, L. Danese, R. D. Davies, R. J. Davis, P. de Bernardis, A. de Rosa, G. de Zotti, J. Delabrouille, F. X. Désert, E. Di Valentino, C. Dickinson, J. M. Diego, K. Dolag, H. Dole, S. Donzelli, O. Doré, M. Douspis, A. Ducout, J. Dunkley, X. Dupac, G. Efstathiou, F. Elsner,

T. A. Enßlin, H. K. Eriksen, M. Farhang, J. Fergusson, F. Finelli, O. Forni, M. Frailis, A. A. Fraisse, E. Franceschi, A. Frejsel, S. Galeotta, S. Galli, K. Ganga, C. Gauthier, M. Gerbino, T. Ghosh, M. Giard, Y. Giraud-Héraud, E. Giusarma, E. Gjerløw, J. González-Nuevo, K. M. Górski, S. Gratton, A. Gregorio, A. Gruppuso, J. E. Gudmundsson, J. Hamann, F. K. Hansen, D. Hanson, D. L. Harrison, G. Helou, S. Henrot-Versillé, C. Hernández-Monteagudo, D. Herranz, S. R. Hildebrandt, E. Hivon, M. Hobson, W. A. Holmes, A. Hornstrup, W. Hovest, Z. Huang, K. M. Huffenberger, G. Hurier, A. H. Jaffe, T. R. Jaffe, W. C. Jones, M. Juvela, E. Keihänen, R. Keskitalo, T. S. Kisner, R. Kneissl, J. Knoche, L. Knox, M. Kunz, H. Kurki-Suonio, G. Lagache, A. Lähteenmäki, J. M. Lamarre, A. Lasenby, M. Lattanzi, C. R. Lawrence, J. P. Leahy, R. Leonardi, J. Lesgourgues, F. Levrier, A. Lewis, M. Liguori, P. B. Lilje, M. Linden-Vørnle, M. López-Cañiego, P. M. Lubin, J. F. Macías-Pérez, G. Maggio, D. Maino, N. Mandolesi, A. Mangilli, A. Marchini, M. Maris, P. G. Martin, M. Martinelli, E. Martínez-González, S. Masi, S. Matarrese, P. McGehee, P. R. Meinhold, A. Melchiorri, J. B. Melin, L. Mendes, A. Mennella, M. Migliaccio, M. Millea, S. Mitra, M. A. Miville-Deschênes, A. Moneti, L. Montier, G. Morgante, D. Mortlock, A. Moss, D. Munshi, J. A. Murphy, P. Naselsky, F. Nati, P. Natoli, C. B. Netterfield, H. U. Nørgaard-Nielsen, F. Noviello, D. Novikov, I. Novikov, C. A. Oxborrow, F. Paci, L. Pagano, F. Pajot, R. Paladini, D. Paoletti, B. Partridge, F. Pasian, G. Patanchon, T. J. Pearson, O. Perdereau, L. Perotto, F. Perrotta, V. Pettorino, F. Piacentini, M. Piat, E. Pierpaoli, D. Pietrobon, S. Plaszczynski, E. Pointecouteau, G. Polenta, L. Popa, G. W. Pratt, G. Prézeau, S. Prunet, J. L. Puget, J. P. Rachen, W. T. Reach, R. Rebolo, M. Reinecke, M. Remazeilles, C. Renault, A. Renzi, I. Ristorcelli, G. Rocha, C. Rosset, M. Rossetti, G. Roudier, B. Rouillé d'Orfeuill, M. Rowan-Robinson, J. A. Rubiño-Martín, B. Rusholme, N. Said, V. Salvatelli, L. Salvati, M. Sandri, D. Santos, M. Savelainen, G. Savini, D. Scott, M. D. Seiffert, P. Serra, E. P. S. Shellard, L. D. Spencer, M. Spinelli, V. Stolyarov, R. Stompor, R. Sudiwala, R. Sunyaev, D. Sutton, A. S. Suur-Uski, J. F. Sygnet, J. A. Tauber, L. Terenzi, L. Toffolatti, M. Tomasi, M. Tristram, T. Trombetti, M. Tucci, J. Tuovinen, M. Türlér, G. Umana, L. Valenziano, J. Valiviita, F. Van Tent, P. Vielva, F. Villa, L. A. Wade, B. D. Wandelt, I. K. Wehus, M. White, S. D. M. White, A. Wilkinson,

- D. Yvon, A. Zacchei, and A. Zonca. Planck 2015 results. XIII. Cosmological parameters. , 594:A13, September 2016.
- [63] D. C. Price, L. J. Greenhill, A. Fialkov, G. Bernardi, H. Garsden, B. R. Barsdell, J. Kocz, M. M. Anderson, S. A. Bourke, J. Craig, M. R. Dexter, J. Dowell, M. W. Eastwood, T. Eftekhari, S. W. Ellingson, G. Hallinan, J. M. Hartman, R. Kimberk, T. Joseph W. Lazio, S. Leiker, D. MacMahon, R. Monroe, F. Schinzel, G. B. Taylor, E. Tong, D. Werthimer, and D. P. Woody. Design and characterization of the Large-aperture Experiment to Detect the Dark Age (LEDA) radiometer systems. , 478(3):4193–4213, August 2018.
- [64] Jonathan R. Pritchard and Abraham Loeb. 21 cm cosmology in the 21st century. *Reports on Progress in Physics*, 75(8):086901, August 2012.
- [65] Yuxiang Qin, Vivian Poulin, Andrei Mesinger, Bradley Greig, Steven Murray, and Jaehong Park. Reionization inference from the CMB optical depth and E-mode polarization power spectra. , 499(1):550–558, November 2020.
- [66] Beth A. Reid, Will J. Percival, Daniel J. Eisenstein, Licia Verde, David N. Spergel, Ramin A. Skibba, Neta A. Bahcall, Tamas Budavari, Joshua A. Frieman, Masataka Fukugita, J. Richard Gott, James E. Gunn, Željko Ivezić, Gillian R. Knapp, Richard G. Kron, Robert H. Lupton, Timothy A. McKay, Avery Meiksin, Robert C. Nichol, Adrian C. Pope, David J. Schlegel, Donald P. Schneider, Chris Stoughton, Michael A. Strauss, Alexander S. Szalay, Max Tegmark, Michael S. Vogeley, David H. Weinberg, Donald G. York, and Idit Zehavi. Cosmological constraints from the clustering of the Sloan Digital Sky Survey DR7 luminous red galaxies. , 404(1):60–85, May 2010.
- [67] Itamar Reis, Anastasia Fialkov, and Rennan Barkana. The subtlety of Ly  $\alpha$  photons: changing the expected range of the 21-cm signal. , 506(4):5479–5493, October 2021.
- [68] M. Remazeilles, C. Dickinson, A. J. Banday, M. A. Bigot-Sazy, and T. Ghosh. An improved source-subtracted and destriped 408-MHz all-sky map. , 451(4):4311–4327, August 2015.

- [69] Peter H. Sims and Jonathan C. Pober. Testing for calibration systematics in the EDGES low-band data using Bayesian model selection. , 492(1):22–38, February 2020.
- [70] Saurabh Singh, Nambissan T. Jishnu, Ravi Subrahmanyam, N. Udaya Shankar, B. S. Girish, A. Raghunathan, R. Somashekar, K. S. Srivani, and Mayuri Sathyanarayana Rao. On the detection of a cosmic dawn signal in the radio background. *Nature Astronomy*, 6:607–617, February 2022.
- [71] Saurabh Singh and Ravi Subrahmanyam. The Redshifted 21 cm Signal in the EDGES Low-band Spectrum. , 880(1):26, July 2019.
- [72] Saurabh Singh, Ravi Subrahmanyam, N. Udaya Shankar, Mayuri Sathyanarayana Rao, Anastasia Fialkov, Aviad Cohen, Rennan Barkana, B. S. Girish, A. Raghunathan, R. Somashekar, and K. S. Srivani. First Results on the Epoch of Reionization from First Light with SARAS 2. , 845(2):L12, August 2017.
- [73] Emanuele Sobacchi and Andrei Mesinger. The clustering of Lyman  $\alpha$  emitters at  $z \approx 7$ : implications for reionization and host halo masses. , 453(2):1843–1854, October 2015.
- [74] Marcin Sokolowski, Steven E. Tremblay, Randall B. Wayth, Steven J. Tingay, Nathan Clarke, Paul Roberts, Mark Waterson, Ronald D. Ekers, Peter Hall, Morgan Lewis, Mehran Mossammaparast, Shantanu Padhi, Franz Schlagenhauser, Adrian Sutinjo, and Jonathan Tinker. BIGHORNS - Broadband Instrument for Global Hydrogen Reionisation Signal. , 32:e004, February 2015.
- [75] Argyro Tasitsiomi. Ly $\alpha$  radiative transfer in cosmological simulations and application to  $z \approx 8$  Ly $\alpha$  emitter. *The Astrophysical Journal*, 645(2):792–813, jul 2006.
- [76] Max Tegmark, Michael R. Blanton, Michael A. Strauss, Fiona Hoyle, David Schlegel, Roman Scoccimarro, Michael S. Vogeley, David H. Weinberg, Idit Zehavi, Andreas Berlind, Tamás Budavari, Andrew Connolly, Daniel J. Eisenstein, Douglas Finkbeiner, Joshua A. Frieman, James E. Gunn, Andrew J. S. Hamilton, Lam Hui, Bhuvnesh Jain, David Johnston, Stephen

Kent, Huan Lin, Reiko Nakajima, Robert C. Nichol, Jeremiah P. Ostriker, Adrian Pope, Ryan Scranton, Uroš Seljak, Ravi K. Sheth, Albert Stebbins, Alexander S. Szalay, István Szapudi, Licia Verde, Yongzhong Xu, James Annis, Neta A. Bahcall, J. Brinkmann, Scott Burles, Francisco J. Castander, Istvan Csabai, Jon Loveday, Mamoru Doi, Masataka Fukugita, III Gott, J. Richard, Greg Hennessy, David W. Hogg, Željko Ivezić, Gillian R. Knapp, Don Q. Lamb, Brian C. Lee, Robert H. Lupton, Timothy A. McKay, Peter Kunszt, Jeffrey A. Munn, Liam O’Connell, John Peoples, Jeffrey R. Pier, Michael Richmond, Constance Rockosi, Donald P. Schneider, Christopher Stoughton, Douglas L. Tucker, Daniel E. Vanden Berk, Brian Yanny, Donald G. York, and SDSS Collaboration. The Three-Dimensional Power Spectrum of Galaxies from the Sloan Digital Sky Survey. , 606(2):702–740, May 2004.

- [77] M. P. van Haarlem, M. W. Wise, A. W. Gunst, G. Heald, J. P. McKean, J. W. T. Hessels, A. G. de Bruyn, R. Nijboer, J. Swinbank, R. Fallows, M. Brentjens, A. Nelles, R. Beck, H. Falcke, R. Fender, J. Hörandel, L. V. E. Koopmans, G. Mann, G. Miley, H. Röttgering, B. W. Stappers, R. A. M. J. Wijers, S. Zaroubi, M. van den Akker, A. Alexov, J. Anderson, K. Anderson, A. van Ardenne, M. Arts, A. Asgekar, I. M. Avruch, F. Batejat, L. Bähren, M. E. Bell, M. R. Bell, I. van Bemmell, P. Bennema, M. J. Bentum, G. Bernardi, P. Best, L. Bîrzan, A. Bonafede, A. J. Boonstra, R. Braun, J. Bregman, F. Breitling, R. H. van de Brink, J. Broderick, P. C. Broekema, W. N. Brouw, M. Brüggen, H. R. Butcher, W. van Cappellen, B. Ciardi, T. Coenen, J. Conway, A. Coolen, A. Corstanje, S. Damstra, O. Davies, A. T. Deller, R. J. Dettmar, G. van Diepen, K. Dijkstra, P. Donker, A. Doorduyn, J. Dromer, M. Drost, A. van Duin, J. Eislöffel, J. van Enst, C. Ferrari, W. Frieswijk, H. Gankema, M. A. Garrett, F. de Gasperin, M. Gerbers, E. de Geus, J. M. Grießmeier, T. Grit, P. Gruppen, J. P. Hamaker, T. Hassall, M. Hoeft, H. A. Holties, A. Horneffer, A. van der Horst, A. van Houwelingen, A. Huijgen, M. Iacobelli, H. Intema, N. Jackson, V. Jelic, A. de Jong, E. Juette, D. Kant, A. Karastergiou, A. Koers, H. Kollen, V. I. Kondratiev, E. Kooistra, Y. Koopman, A. Koster, M. Kuniyoshi, M. Kramer, G. Kuper, P. Lambropoulos, C. Law, J. van Leeuwen, J. Lemaitre, M. Loose, P. Maat, G. Macario, S. Markoff, J. Masters, R. A. McFadden, D. McKay-Bukowski, H. Meijering, H. Meulman, M. Mevius, E. Middelberg, R. Millenaar, J. C. A. Miller-Jones, R. N. Mohan,

J. D. Mol, J. Morawietz, R. Morganti, D. D. Mulcahy, E. Mulder, H. Munk, L. Nieuwenhuis, R. van Nieuwpoort, J. E. Noordam, M. Norden, A. Noutsos, A. R. Offringa, H. Olofsson, A. Omar, E. Orrú, R. Overeem, H. Paas, M. Pandey-Pommier, V. N. Pandey, R. Pizzo, A. Polatidis, D. Rafferty, S. Rawlings, W. Reich, J. P. de Reijer, J. Reitsma, G. A. Renting, P. Riemers, E. Rol, J. W. Romein, J. Roosjen, M. Rüter, A. Scaife, K. van der Schaaf, B. Scheers, P. Schellart, A. Schoenmakers, G. Schoonderbeek, M. Serylak, A. Shulevski, J. Sluman, O. Smirnov, C. Sobey, H. Spreuw, M. Steinmetz, C. G. M. Sterks, H. J. Stiepel, K. Stuurwold, M. Tagger, Y. Tang, C. Tasse, I. Thomas, S. Thoudam, M. C. Toribio, B. van der Tol, O. Usov, M. van Veelen, A. J. van der Veen, S. ter Veen, J. P. W. Verbiest, R. Vermeulen, N. Vermaas, C. Vocks, C. Vogt, M. de Vos, E. van der Wal, R. van Weeren, H. Weggemans, P. Weltevrede, S. White, S. J. Wijnholds, T. Wilhelmsson, O. Wucknitz, S. Yatawatta, P. Zarka, A. Zensus, and J. van Zwieten. LOFAR: The LOw-Frequency ARray. , 556:A2, August 2013.

- [78] M. P. van Haarlem, M. W. Wise, A. W. Gunst, G. Heald, J. P. McKean, J. W. T. Hessels, A. G. de Bruyn, R. Nijboer, J. Swinbank, R. Fallows, M. Brentjens, A. Nelles, R. Beck, H. Falcke, R. Fender, J. Hörandel, L. V. E. Koopmans, G. Mann, G. Miley, H. Röttgering, B. W. Stappers, R. A. M. J. Wijers, S. Zaroubi, M. van den Akker, A. Alexov, J. Anderson, K. Anderson, A. van Ardenne, M. Arts, A. Asgekar, I. M. Avruch, F. Batejat, L. Bähren, M. E. Bell, M. R. Bell, I. van Bemmelen, P. Bennema, M. J. Bentum, G. Bernardi, P. Best, L. Bîrzan, A. Bonafede, A. J. Boonstra, R. Braun, J. Bregman, F. Breitling, R. H. van de Brink, J. Broderick, P. C. Broekema, W. N. Brouw, M. Brüggen, H. R. Butcher, W. van Cappellen, B. Ciardi, T. Coenen, J. Conway, A. Coolen, A. Corstanje, S. Damstra, O. Davies, A. T. Deller, R. J. Dettmar, G. van Diepen, K. Dijkstra, P. Donker, A. Doorduyn, J. Dromer, M. Drost, A. van Duin, J. Eislöffel, J. van Enst, C. Ferrari, W. Frieswijk, H. Gankema, M. A. Garrett, F. de Gasperin, M. Gerbers, E. de Geus, J. M. Grießmeier, T. Grit, P. Gruppen, J. P. Hamaker, T. Hassall, M. Hoeft, H. A. Holties, A. Horneffer, A. van der Horst, A. van Houwelingen, A. Huijgen, M. Iacobelli, H. Intema, N. Jackson, V. Jelic, A. de Jong, E. Jütte, D. Kant, A. Karastergiou, A. Koers, H. Kollen, V. I. Kondratiev, E. Kooistra, Y. Koopman, A. Koster, M. Kuniyoshi, M. Kramer, G. Kuper, P. Lambropoulos, C. Law, J. van Leeuwen, J. Lemaître, M. Loose, P. Maat,

G. Macario, S. Markoff, J. Masters, R. A. McFadden, D. McKay-Bukowski, H. Meijering, H. Meulman, M. Mevius, E. Middelberg, R. Millenaar, J. C. A. Miller-Jones, R. N. Mohan, J. D. Mol, J. Morawietz, R. Morganti, D. D. Mulcahy, E. Mulder, H. Munk, L. Nieuwenhuis, R. van Nieuwpoort, J. E. Noordam, M. Norden, A. Noutsos, A. R. Offringa, H. Olofsson, A. Omar, E. Orrú, R. Overeem, H. Paas, M. Pandey-Pommier, V. N. Pandey, R. Pizzo, A. Polatidis, D. Rafferty, S. Rawlings, W. Reich, J. P. de Reijer, J. Reitsma, G. A. Renting, P. Riemers, E. Rol, J. W. Romein, J. Roosjen, M. Rüter, A. Scaife, K. van der Schaaf, B. Scheers, P. Schellart, A. Schoenmakers, G. Schoonderbeek, M. Serylak, A. Shulevski, J. Sluman, O. Smirnov, C. Sobey, H. Spreew, M. Steinmetz, C. G. M. Sterks, H. J. Stiepel, K. Stuurwold, M. Tagger, Y. Tang, C. Tasse, I. Thomas, S. Thoudam, M. C. Toribio, B. van der Tol, O. Usov, M. van Veelen, A. J. van der Veen, S. ter Veen, J. P. W. Verbiest, R. Vermeulen, N. Vermaas, C. Vocks, C. Vogt, M. de Vos, E. van der Wal, R. van Weeren, H. Weggemans, P. Weltevrede, S. White, S. J. Wijnholds, T. Wilhelmsson, O. Wucknitz, S. Yatawatta, P. Zarka, A. Zensus, and J. van Zwieten. LOFAR: The LOw-Frequency ARray. , 556:A2, August 2013.

- [79] Anne Verhamme, Ivana Orlitová, Daniel Schaerer, and Matthew Hayes. Using Lyman- $\alpha$  to detect galaxies that leak Lyman continuum. , 578:A7, June 2015.
- [80] Anthony Walters, Amanda Weltman, B. M. Gaensler, Yin-Zhe Ma, and Amadeus Witzemann. Future cosmological constraints from fast radio bursts. *The Astrophysical Journal*, 856(1):65, mar 2018.
- [81] S. A. Wouthuysen. On the excitation mechanism of the 21-cm (radio-frequency) interstellar hydrogen emission line. , 57:31–32, January 1952.
- [82] Zheng Zheng, Renyue Cen, Hy Trac, and Jordi Miralda-Escudé. Radiative Transfer Modeling of Ly $\alpha$  Emitters. II. New Effects on Galaxy Clustering. , 726(1):38, January 2011.
- [83] Paul La Plante. Zhile Chen. Using deep learning to identify rfi in hera data,. *HERA Memorandum*, (108), 12 2021.

## Chapter 2

# Quantifying Density-Ionization Correlations with the 21cm Power Spectrum

### Addendum for thesis

Density-ionization correlation describes the way that ionized regions correlate with the underlying density field  $\delta$  during reionization. Previous works have considered three classes of density-ionization correlations: inside-out reionization (where the ionized regions are sourced to overdense regions in  $\delta$ ), outside-in reionization (where the ionized regions are linked to underdense regions in  $\delta$ ) and uncorrelated reionization (where the ionized bubbles are random with respect to  $\delta$ ). Although inside-out reionization is preferred by most models, outside-in and uncorrelated reionization have not been ruled out.

In this work, Adrian Liu and I designed a procedure capable of producing a continuous range of density-ionization correlation scenarios. This means that inside-out, outside-in and uncorrelated are just special cases of this spectrum of correlations. We developed a parametrization  $\beta$  to track the density-ionization correlation, so placing constraints on  $\beta$  is tantamount to ruling out reionization models.

To find these constraints, we studied how the 21cm power spectrum depends on our parametrization of the density-ionization correlation. We also used a mock HERA observation to forecast the types

of constraints that a HERA measurement of the power spectrum can place on  $\beta$ . Since upper limits of the 21cm power spectrum are dropping, we will soon be at the stage where we can use this parametrization as a tool to rule out density-ionization correlation models.

## Abstract

The Epoch of Reionization (EoR)—when neutral hydrogen in the intergalactic medium was systematically ionized—is a period in our Universe’s history that is currently poorly understood. However, a key prediction of most models is a correlation between the density and ionization field during the EoR. This has consequences for the 21cm power spectrum. Here, we propose a parametrization for the density-ionization correlation and study the dependence of the 21cm power spectrum on this parameterization. We use this formalism to forecast the ability of current and future observations to constrain these correlations. We find that upper limits on the dimensionless power spectrum at redshifts  $7.5 < z < 8.5$  using  $k$  bins between  $0.1 \text{ Mpc}^{-1} < k < 0.75 \text{ Mpc}^{-1}$  with error bars at the level of  $\sim 20 \text{ mK}^2$  about our fiducial model would rule out uncorrelated reionization at 99% credibility. Beyond upper limits, we find that at its full sensitivity, the Hydrogen Epoch of Reionization Array (HERA) will be able to place strong constraints on the sign and magnitude of density-ionization correlations.

## 2.1 Introduction

A key event in our Universe’s history is the Epoch of Reionization (EoR) where the neutral hydrogen (HI) making up the intergalactic medium (IGM) is ionized by the first generation of stars and galaxies. The broad timeline of this landmark process is bound by two important measurements: the Cosmic Microwave Background (CMB) and measurements of high redshift quasars at  $z < 7$ . The CMB suggests that the Universe is neutral by redshift  $z \approx 1100$  [44] while measurement of the Gunn-Peterson trough at  $z \approx 6$  tells us that the universe must have undergone a transition from neutral to ionized by this time [4, 16, 25, 36], although recent studies have hinted at a more

complicated picture than previously thought [2,3,6,8,11,12,14,28,31,41]. Beyond just its timeline, the astrophysical details of the EoR remain relatively unconstrained observationally. Without direct observational evidence deep into EoR redshifts, the period remains a crucial missing piece in our understanding of galaxy formation.

One of the most promising ways to explore this epoch is to use the hyperfine transition of hydrogen, where 21cm-wavelength photons are absorbed or emitted as electrons in hydrogen atoms flip their spins relative to their protons. (For reviews, see [22,33,34,40,49]). The 21cm signal allows us to trace primordial hydrogen as a function of redshift and position and can in principle be an incisive probe of first-generation stars and galaxies. The photon lies in the radio part of the electromagnetic spectrum and its absorption or emission is measured relative to the CMB. One therefore measures a *differential* differential brightness temperature  $\delta T_b$ , which is given by

$$\delta T_b(\mathbf{r}, z) \approx (27 \text{ mK}) \left( \frac{T_s(\mathbf{r}, z) - T_\gamma(z)}{T_s(\mathbf{r}, z)} \right) [1 - x_{\text{HII}}(\mathbf{r}, z)] [1 + \delta(\mathbf{r}, z)] \times \left[ \frac{H(z)/(1+z)}{dv_r/dr} \right] \left( \frac{1+z}{10} \frac{0.15}{\Omega_m h^2} \right)^{1/2} \left( \frac{\Omega_b h^2}{0.023} \right), \quad (2.1)$$

where  $\mathbf{r}$  is a position vector,  $z$  is the redshift,  $x_{\text{HII}}$  is the ionized fraction of hydrogen,  $\delta$  is the overdensity,  $H(z)$  is the Hubble parameter (with  $h$  as its dimensionless counterpart),  $T_\gamma(z)$  is the CMB temperature,  $\Omega_m$  is the normalized matter density,  $\Omega_b$  is the normalized baryon density, and  $dv_r/dr$  is the line of sight velocity gradient. The differential brightness temperature depends on the spin temperature  $T_s(\mathbf{r}, z)$  of the neutral hydrogen gas, which measures the relative number of HI atoms that are in the excited versus ground hyperfine states. Throughout this paper we consider redshift ranges where the spin temperature is heated above that of the CMB, i.e.  $T_s \gg T_\gamma$  so that the  $T_s$  drops out of Equation (2.1), thus allowing us to neglect the spin temperature in our simulations. In this work we set the  $\Lambda$ CDM parameters to  $\sigma_8 = 0.81$ ,  $\Omega_m = 0.31$ ,  $\Omega_b = 0.048$ ,  $h = 0.68$ ,  $n_s = 0.9603$  consistent with Planck 2015 results [44].

Reionization does not occur instantaneously throughout our Universe. Instead, ionized bubbles begin to grow in certain parts of our Universe, eventually coalescing as the process completes [21]. Most models predict that these ionized bubbles are not random; they are tightly correlated with

their corresponding density field. There are two extremes in how the ionization field couples to the density field. The ionized bubbles can be positively correlated with the corresponding density field so that the highest density regions correspond to regions of high fractions of ionized hydrogen  $x_{\text{HII}}$  [10, 39]. This is the “inside-out” model of reionization, where reionization happens first in the most overdense regions before the ionizing photons escape the high density regions and ionize the lower density regions of the IGM. Conversely, the ionization field can be negatively correlated with the density field. Here regions of the highest density correspond to the lowest fractions of ionized hydrogen and low density regions map to high fractions of ionized hydrogen. This is the “outside-in” model of reionization. Outside-in models generally require hydrogen recombination rates to dominate the ionizing effects of UV sources so that the most overdense regions have the strongest recombination rates which keep them mostly neutral. In this scenario, reionization happens first in lower density regions where recombination effects are diminished. Outside-in models can also occur if x-rays - which more easily escape high dense regions - play a significant role in ionizing the IGM. In either of these scenarios the highest density regions are last to be ionized. It is also possible for reionization to unfold as a combination of both inside-out and outside-in models [20, 35]. This scenario entails statistical combinations of the individual inside-out and outside-in statistics between density and ionization fields.

In this paper we build on the work of [54] and [5], where the task of distinguishing between inside-out and outside-in scenarios was treated as a discrete model selection problem. Here we take the complementary approach of parametrizing the density-ionization correlation in a continuous manner. This enables us to quantify this correlation, converting the model selection exercise into one of parameter fitting. We can therefore quantitatively constrain outside-in or inside-out morphologies as well as rule out models that predict random uncorrelated bubbles. To this end, we parametrize the correlation between ionization and density field using a single parameter and explore how variation of this parameter affects the 21cm power spectrum. We examine the range of constraints that can be placed on the amount of correlation between these fields using upcoming Hydrogen Epoch of Reionization Experiment (HERA; [13]). In our forecasts, we also include other model parameters that have traditionally been used to capture EoR physics, exploring any new

degeneracies that arise from the inclusion of arbitrary density-ionization correlations. This paper therefore serves as a generalization of forecasts such as those of [45] and [26]. We do not include as many astrophysical and cosmological parameters as [32], [15], [27], [29], or [42] do, but this is simply to avoid obscuring the discussion of density-ionization correlation, and our formalism can be easily adapted to include any extra parameters that are considered relevant.

The rest of this paper is organized as follows. In Section 2.2, we introduce our new correlation parameter and describe how it is incorporated into our simulations. We show how this parameter affects the 21 cm power spectra in Section 2.3. In Section 2.4 we describe the HERA instrument and its sensitivity, as well as our forecasting methodology. In Section 4.6 we present the results of our forecasts, emphasizing what one might learn about the morphology of reionization from early observational limits. We summarize our conclusions in Section 6.7.

## 2.2 Simulations

In inside-out models, ionizing photons are produced in the highest density regions and these photons ionize the surrounding hydrogen before escaping into the lower density regions of the IGM. The correlation between  $\delta$  and  $x_{\text{HII}}$  in inside-out models has consequences for the 21cm brightness temperature because the product  $x_{\text{HII}}\delta$  appears in Equation 2.1. A correlation between density and ionization fields suggests that whenever the overdensity  $\delta$  is large, the ionized fraction  $x_{\text{HII}}$  is large. Therefore the product  $x_{\text{HII}}\delta$  is typically much larger than the equivalent cross term for outside-in models, leading to lower  $\delta T_b$  in general.

In contrast, if recombination rates dominate the reionization process, one ends up with an outside-in scenario. Here, ionizing photons created in high density regions escape and ionize the lower density regions, where recombination rates are lower. As a result, the low density regions remain neutral while the high density regions are kept overall neutral. As reionization proceeds, these high density regions ionize last, and  $\delta$  and  $x_{\text{HII}}$  are negatively correlated. This boosts the brightness temperature contrast, leading to higher  $\delta T_b$ .

In general, one expects that reionization involves both inside-out and outside-in processes, with the former being important on large scales during early reionization and the latter being important on small scales during late reionization [20]. However, this separation will not necessarily be perfect, and it is possible (for instance) to construct theoretical models where strong, biased sources can result in outside-in effects being important on large scales [19, 23]. Constraining the sign of the  $\delta$ - $x_{\text{HII}}$  correlation is therefore not just an interesting problem in its own right, but one that may be important in shedding light on the nature of ionizing sources during the EoR [17]. In the subsections that follow, we walk through how one can begin with a semi-numerical simulation of inside-out, map it onto a “mirror” outside-in simulation, and then finally to generalize to a continuum of simulations with arbitrary density-ionization correlations.

### 2.2.1 Inside-out Reionization Simulations Using 21cmFAST

In order to generate density and ionization fields indicative of a variety of reionization scenarios, we use the publicly available 21cmFAST package [37]. This semi-numerical code produces an initial density box at high redshift before smoothing the density field to a coarser box corresponding to the same comoving side length. The density field is then evolved through redshift using first order perturbation theory. The cosmological parameters used in our simulations are described in Section 2.1. Throughout our simulations, we use high resolutions boxes of  $450^3$  voxels corresponding to a comoving side length of 225 Mpc and coarser boxes of  $150^3$  voxels corresponding to the same comoving side length. The code then implements the excursion set formalism of [24] for reionization, and predominantly assumes inside-out reionization. This approach evolves the overdensity field  $\delta$  as a function of position and smoothing scale and then declares a region ionized if there are enough photons to ionize each baryon within that region of mass  $m_{\text{ion}}$ . These regions must have produced at least enough photons to ionize each of the baryons, satisfying

$$m_{\text{ion}} = \zeta m_{\text{gal}} \tag{2.2}$$

where  $m_{\text{gal}}$  is the mass in collapsed objects, and  $\zeta$  is the ionizing efficiency of the sources. This condition is continually checked as the density field is smoothed from large scales to small scales. A particular location is flagged as ionized at the first scale in which this condition is satisfied.

The 21cmFAST package contains a number of adjustable parameters whose goal is to capture variations in the detailed astrophysics of reionization. We choose three such parameters to vary in this paper:

1. The mean free path of ionizing photons,  $R_{\text{mfp}}$ . This is the mean distance an ionizing photon travels before being absorbed by a dense region of hydrogen. This sets the effective horizon for an ionizing photon. We consider values of  $R_{\text{mfp}}$  between 3 Mpc and 50 Mpc.
2. The ionizing efficiency,  $\zeta$ . The effectiveness of the ionizing sources is summarized by a single parameter

$$\zeta = \frac{f_{\text{esc}} f_* N_\gamma}{(1 + n_{\text{rec}})}, \quad (2.3)$$

which takes into account the amount of ionizing photons produced per stellar baryon  $N_\gamma$ , the rate of stellar production  $f_*$ , and the fraction of these ionizing photons that escape into the IGM,  $f_{\text{esc}}$ . The recombination rate,  $n_{\text{rec}}$ , acts to lower the ionizing efficiency. The ionizing efficiency,  $\zeta$ , is sometimes taken to vary according to halo mass; however, throughout this work, we treat  $\zeta$  to be constant during reionization. We consider values of  $\zeta$  between 25 and 50.

3. The turnover mass,  $M_{\text{turn}}$ . This describes the mass of a halo below which there is an exponential suppression in star formation efficiency. A turnover mass of  $10^8 M_\odot$  corresponds roughly to  $\sim 10^4$  K virial temperature, at which point gas in a halo can start to cool via Ly $\alpha$  emission. We consider values of  $M_{\text{turn}}$  between  $10^7 M_\odot$  and  $10^9 M_\odot$ .

Variation of these parameters modify the onset and duration of reionization, and for fixed redshift can also change the size of the ionized bubbles. Models with large values of  $\zeta$  imply that emitters are very effective at ionizing the IGM and increasing this parameter shifts the onset of reionization to higher redshifts. The size and scale of the bubbles are also dependent on the turnover mass.

Smaller values of  $M_{\text{turn}}$  allow for smaller sources to contribute to the EoR. As a result, ionized bubbles tend to be smaller and more numerous. Reionization is complete when these bubbles merge together to form a complete ionized IGM. Modification of  $R_{\text{mfp}}$  also sets the maximum size of the ionized bubbles which can have consequences for large scales as the ionized bubbles grow large enough to approach the maximum size  $R_{\text{mfp}}$ . Variation of these parameters have consequences for the structure of the temperature field  $\delta T_b$ . However, these variations are still within the context of a predominantly inside-out formalism, with the ionized fraction field  $x_{\text{HII}}$  generally correlated with the overdensity field  $\delta$ . We therefore now need to modify the prescription by which the ionized fraction field (or equivalently, the ionization field) is generated from an overdensity field.

### 2.2.2 Outside-in Reionization Simulations using 21cmFAST

In order to make outside-in temperature maps using 21cmFAST we require that the temperature maps be produced from density and ionized fraction fields that are negatively correlated. To do so starting from an inside-out simulation package, we adapt methods from the structure formation literature and use the idea of sign-flipped initial conditions [48, 53]. In particular, we can produce  $\delta$  and  $x_{\text{HII}}$  fields that are negatively correlated with one another by pairing a sign-flipped overdensity field with its original ionization field. A sign flip will invert  $\delta$  while preserving the rest of its structure. Importantly, this sign flip must be applied to the initial (i.e., high-redshift) density field while  $\delta$  is still in the linear regime. This ensures that the sign flipped density and velocity fields have undergone the correct non-linear evolution, resulting in physically plausible probability distribution functions for both quantities. The evolved sign flipped density field will contain the same statistics as the original density field except overdense regions become underdense regions and vice versa. When  $\delta^{\text{flip}}$  is paired with its original ionization field  $x_{\text{HII}}$ , the regions of lowest baryonic overdensities now correspond to regions of high ionized fractions of hydrogen in the ionization field. Similarly, regions of high baryonic overdensities in  $\delta^{\text{flip}}$  correspond to neutral regions of hydrogen in  $x_{\text{HII}}$ . The fields  $x_{\text{HII}}$  and  $\delta_b^{\text{flip}}$  are therefore anti-correlated. Temperature maps computed using Equation (2.1) with fields  $\delta_b^{\text{flip}}$  and  $x_{\text{HII}}$  will have statistics representative of outside-in reionization.

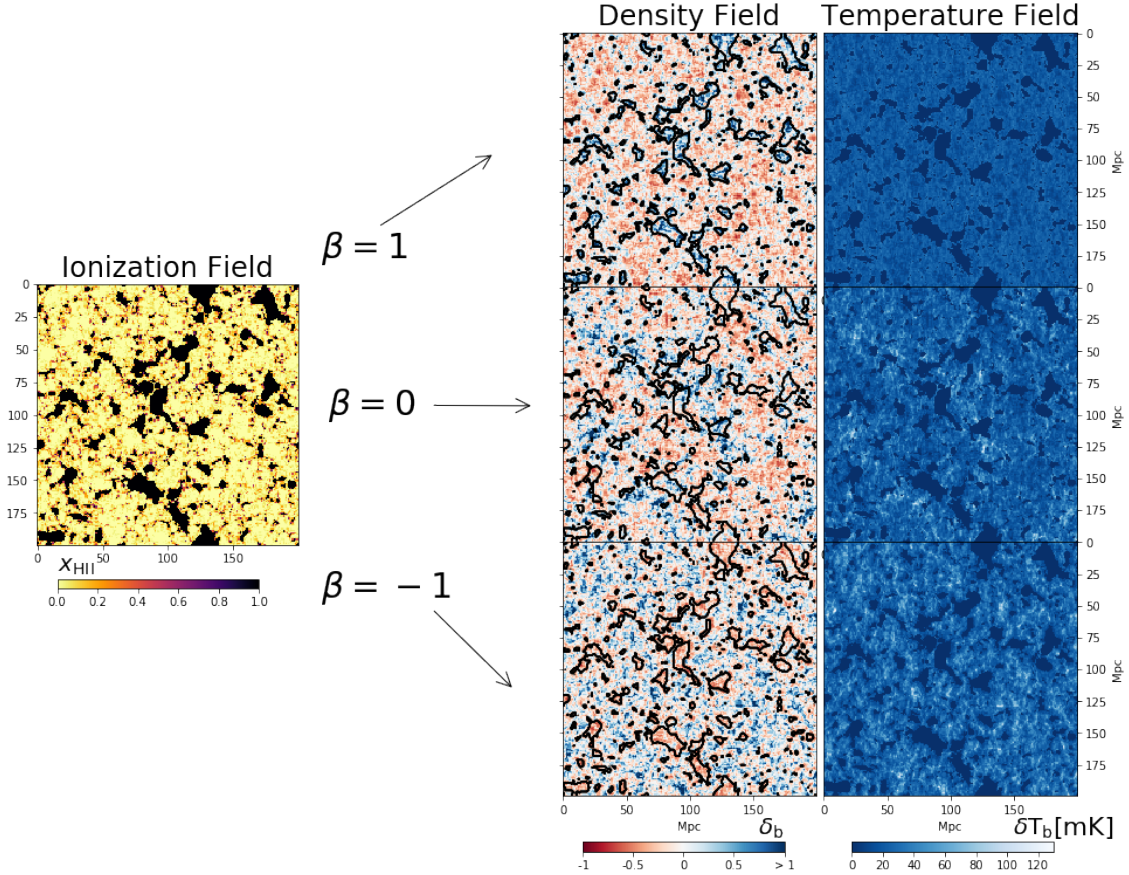


**Figure 2.1:** Example ionization  $x_{\text{HII}}$ , density  $\delta$ , and brightness temperature  $\delta T_b$  fields at  $z = 9$  with fiducial parameters of  $\zeta_0 = 25$ ,  $M_{\text{turn},0} = 5 \times 10^8 M_\odot$ , and  $R_{\text{mfp},0} = 30 \text{ Mpc}$ . The ionized regions from the ionization field are superimposed as contours on the density field to emphasize the correlation between the two fields. Inside-out scenarios (with  $\beta > 0$ ) have positively correlated density and ionization fields. Conversely, outside-in scenarios (with  $\beta < 0$ ) have negatively correlated fields. The case  $\beta = 0$  refers to the scenario where the ionization field and density field are entirely uncorrelated. The 21 cm brightness temperature field is sensitive to the type of correlation between matter and ionization fields. For example, the outside-in model shown here has the highest brightness temperature, since regions of high density are also regions of highest neutral fraction.

In Figure 2.1, we provide some visual intuition for our inside-out and outside-in models. The leftmost picture is of an ionization field that can be paired with density fields (middle column) that are either anticorrelated (bottom row), uncorrelated (middle row), or correlated (top row). Contours around ionized bubbles from the ionization field are superimposed on each density field. The positively correlated density field is the original density field from which 21cmFAST produced the ionization field; it therefore represents an inside-out scenario, and one sees that regions of high density correspond to regions of high ionization. The negatively correlated density field comes from the sign-flipped method, where high density regions correspond to regions of high neutral fraction; this represents an outside-in scenario. The  $x_{\text{HII}}\delta$  term of Equation 2.1 then predicts a lower brightness temperature for inside-out models than for outside-in models, as is visually confirmed in maps of  $\delta T_b$  (right column).

The morphologies for our outside-in maps differ from outside-in maps that model the sub-grid physics. For example, [10] produce outside-in maps by modeling the inhomogeneous recombinations that occur near overdense regions and then parametrize the degree to which recombinations affect reionization by tuning the recombination timescale. This approach produces outside-in maps which are driven by self-shielded overdense regions. In this scenario, reionization begins as inside-out but the morphology changes after the midpoint of reionization when the shielded high-density neutral regions ionize the IGM. These overdense neutral regions are found inside the ionized bubbles and increase the small scale structure while also limiting the size of coherently ionized regions. This decreases the variance on large scales (i.e., the power spectrum at low  $k$ ; see Section 2.3) as compared to our model. We find that the variance on all scales between these two approaches diverge as reionization progresses. Thus, unlike the very physically motivated model such as that of [10], our outside-in model should be viewed more as a phenomenological parametrization to bracket the possibilities. Our approach is similar to that of [54] which produces an outside-in model by implementing an inversion operation on a fiducial inside-out model. Should early data favour outside-in reionization, our framework is general enough that one could adopt a physically motivated outside-in model and to decorrelate the density field from there. We are mostly interested in the

correlation statistics indicative of these reionization morphologies in order to rule out uncorrelated reionization scenarios.

Note that our procedure for creating outside-in maps from inside-out maps changes the mass-weighted ionization history. This occurs because the sign flip acts on the density field and not the ionization field. By keeping the ionization field the same, the total volume of the ionized regions remains constant, but these regions are now paired with different density values thereby changing the mass weighted global ionized fraction. The largest difference between the mass-weighted ionization histories of these extreme models is about  $\pm 0.1$ , occurring near the midpoint of reionization. This does not constitute a significant difference in our results.

### 2.2.3 Simulating Arbitrary Correlations using 21cmFAST

It is also possible to generate temperature fields from  $x_{\text{HII}}$  and  $\delta$  where  $\delta$  and  $x_{\text{HII}}$  are correlated by some arbitrary amount. To do this, we draw a random phase  $\phi$  from a Gaussian of standard deviation  $\sigma$  and apply this phase constant to each point of the Fourier transformed density field  $\tilde{\delta}$  in  $k$  space, such that  $\tilde{\delta}(k) \rightarrow \tilde{\delta}(k)e^{i\phi}$ . This shifts the phase of each Fourier mode while leaving the overall variance of the field for each Fourier mode unchanged. Just as with the sign-flipped overdensity box, this ensures that the statistics of the density field (in particular, the power spectrum—see Section 2.3) remain unchanged. However, upon returning the overdensity box to configuration space, high- and low-density regions will have shifted from their original positions, somewhat decorrelating the field from its corresponding neutral fraction box. This procedure is carried out on the fine resolution boxes of  $450^3$  voxels. This allows for the smallest Fourier modes to be decorrelated before they are smoothed over to the coarser resolution box. Our results in Section 2.3 do not depend on the resolution of the fine resolution box—so long as they fall within the acceptable range of resolutions set by 21cmFAST.

The degree of correlation between the ionization field and the density field is governed by  $\sigma$ . If  $\sigma$  is small, then the randomly chosen values  $\phi$  are also typically small and so the Fourier modes are not significantly shifted. Once the field is transformed back to configuration space, the resulting density field only be slightly perturbed. As  $\sigma$  is increased,  $\phi$  are chosen from an

increasingly broad range, and so can produce large deviations from their original configurations. Upon transformation to configuration space, the density field becomes increasingly decorrelated from its original ionization field. As  $\sigma$  approaches  $\pi$ , the multiplicative factor  $e^{i\phi}$  essentially randomizes the phases, and the resulting density field is completely uncorrelated. The quantity  $\sigma$  therefore quantifies the amount that the density field has been decorrelated from the  $x_{\text{HII}}$  field: for the special case of  $\sigma = 0$  we recover the original density field while for  $\sigma \sim \pi$  the density field is entirely decoupled from  $x_{\text{HII}}$ . Identical applications of a given value of  $\sigma$  with different random seeds lead to slight different realizations of the density field. However the fluctuations in the resulting statistics (defined in Section 2.3) are insignificant (a fractional shift of  $10^{-4}$  in the variance of the field) and do not impact our results in Section 4.6.

If the above decorrelation method is combined with the sign flip from Section 2.2.2, we can also introduce arbitrary levels of anticorrelation between  $\delta$  and  $x_{\text{HII}}$  for outside-in models of reionization. The sign flip and decorrelation can then be folded into a single parameter  $\beta$ , which is defined as

$$\beta \equiv \begin{cases} \text{sgn}(\sigma) \left(1 - \frac{|\sigma|}{\pi}\right) & \sigma \neq 0 \\ \pm 1 & \sigma = 0 \end{cases} \quad (2.4)$$

where as shorthand, we use the sign  $\text{sgn}(\sigma)$  of  $\sigma$  to record whether we are decorrelating from an inside-out model ( $\text{sgn}(\sigma) = +1$ ) or an outside-in model ( $\text{sgn}(\sigma) = -1$ ). The special case  $\sigma = 0$  is multivalued in  $\beta$ , but since those correspond to the original inside-out and outside-in models, we simply assign those to  $\beta = +1$  and  $\beta = -1$  respectively. With our definition of  $\beta$ , we therefore have a parameter that can be continuously dialled from  $+1$  to  $-1$  to go from a fully inside-out scenario to a fully outside-in scenario: a positive value of  $\beta$  indicates a scenario where an initially correlated matter and ionization field are decorrelated by  $\sigma$  while a negative  $\beta$  indicates a scenario where a negatively correlated matter and ionization field are decorrelated by  $\sigma$ . Table 4.1 summarizes the terminology used to describe the type of correlation as well as the model it pertains to. In the sections that follow, we will consider  $\beta$  to be another one of our EoR parameters (joining  $\zeta$ ,  $R_{\text{mfp}}$  or  $M_{\text{turn}}$ ) that can be potentially constrained by 21 cm observations.

**Table 2.1:** Lexicon for physical models and their respective correlations

$\beta$	Moniker for Field correlations $x_{\text{HII}} \delta$	Physical Model
1	Correlated	Inside-out
$1 < \beta < 0$	Increasingly correlated	Mostly inside-out
0	Uncorrelated	Uncorrelated
$0 < \beta < -1$	Increasingly anti-correlated	Mostly outside-in
-1	Anti-correlated	Outside-in

## 2.3 Temperature Field Statistics

In Section 2 we gained intuition for how correlations between ionization and density fields can affect the 21cm temperature maps. In this section we compute the statistical properties of these maps that can be measured by upcoming 21cm instruments. In particular, we compute the “dimensionless” 21cm power spectrum  $\Delta_{21}^2$  which is defined through the brightness temperature field as

$$\Delta_{21}^2(k) \equiv \frac{k^3}{2\pi^2} \frac{\langle |\widetilde{\delta T_b(\mathbf{k})}|^2 \rangle}{V} \quad (2.5)$$

where  $V$  is the survey volume,  $\widetilde{\delta T_b}$  is the Fourier transform of the brightness temperature field (into a space defined by spatial wavevector  $\mathbf{k}$ ), and the angular brackets indicate an average over shells of constant  $k \equiv |\mathbf{k}|$ . Physically,  $\Delta_{21}^2$  measures the contribution to the brightness temperature variance per logarithmic interval in  $k$ . The brightness temperature is sensitive to the inside-out versus outside-in morphology via the  $x_{\text{HII}}\delta$  cross term in Equation (2.1). Importantly, notice that the power spectrum does not depend on the phases of the complex Fourier field. Defining the analogous quantity for the density field (i.e., defining the matter power spectrum) then immediately reveals that our decorrelation procedure from Section 2.2.3—which only involved altering the Fourier phases of our density field—preserves the statistics of the matter distribution. Each decorrelated field is therefore a perfectly legitimate realization of  $\delta$ .

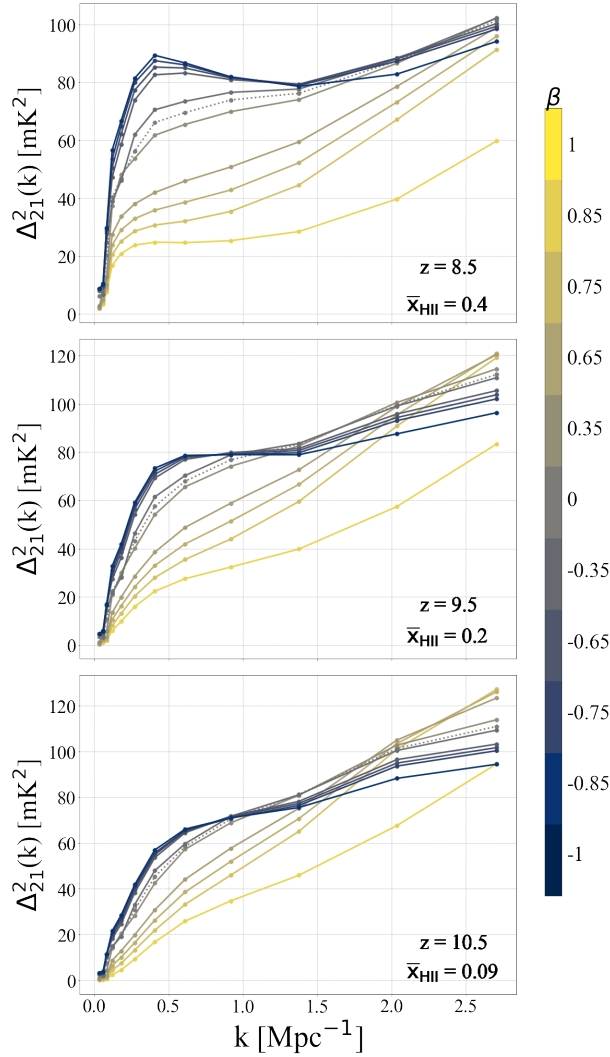


**Figure 2.2:** Power Spectra for varying  $\beta$  at different redshifts, with the other EoR parameters fixed to fiducial values of  $\zeta_0 = 25$ ,  $M_{\text{turn},0} = 5 \times 10^8 M_\odot$ , and  $R_{\text{mrp},0} = 30 \text{ Mpc}$ . The mean ionized fractions  $\bar{x}_{\text{HII}}$  at redshifts,  $z = 10.5$ ,  $z = 8.5$  are 0.09, 0.2 and 0.4 respectively. The amplitude of  $\Delta_{21}^2$  increases as  $\beta$  is decreased from its maximal value  $\beta = 1$ , corresponding to inside-out models of reionization. The amplitude of the power is maximum at  $\beta = -1$ , corresponding to outside-in models. The contrast between these models is largest at the scale corresponding to the size of the ionized regions. The dotted line represents a model without any correlation between density and ionization fields.

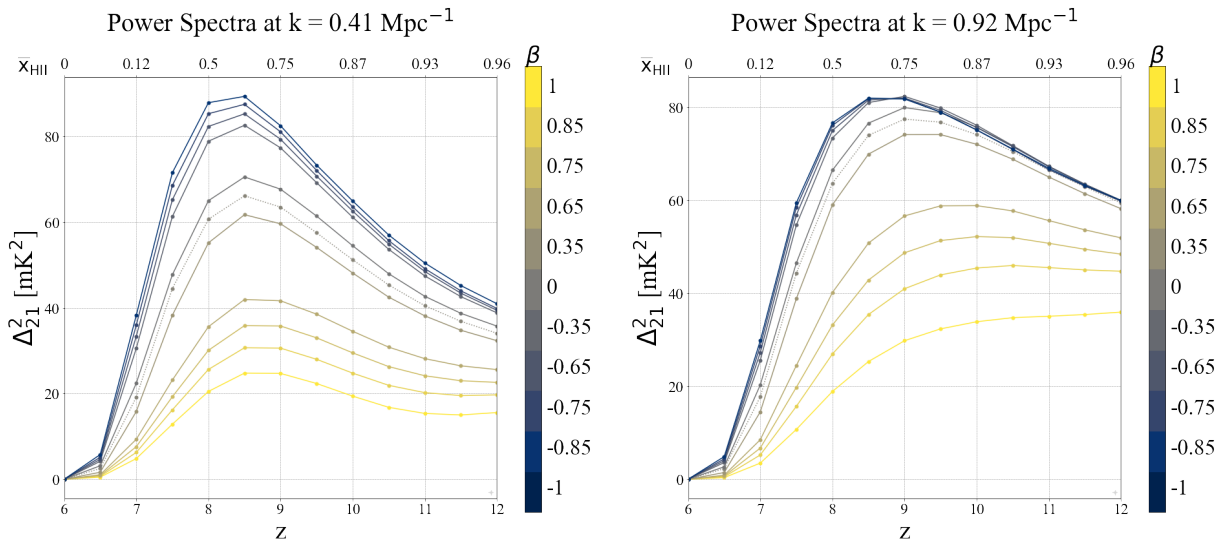


**Figure 2.3:** Power spectra as a function of  $z$  and  $\beta$  at two chosen  $k$  values. The contrast between outside-in and inside-out models is largest at the midpoint of reionization. For the fiducial parameters of  $\zeta_0 = 25$ ,  $M_{\text{turn},0} = 5 \times 10^8 M_\odot$ , and  $R_{\text{mfp},0} = 30$  Mpc, this occurs at  $z \approx 8$ . The dotted curve represents a model without any correlations between  $\delta$  and  $x_{\text{HII}}$ .

### 2.3.1 Variation of $\Delta_{21}^2$ as a Function of $\beta$

Figure 2.2 illustrates the effect of varying  $\beta$  on the power spectrum at three different redshifts. Beginning from an inside-out ( $\beta = 1$ ) model, decreasing  $\beta$  reduces the density field's original correlation with  $x_{\text{HII}}$ , and increases the chances that neutral regions overlap with overdense regions in  $\delta$ . As a result, we find increasing power on large scales as we decrease  $\beta$  from +1 to  $-1$ . The intermediate scenario with  $\beta = 0$  is one where the density field and the ionization field are uncorrelated, and as expected, we find that the predictions for  $\Delta_{21}^2$  in this case are the same whether we decorrelate from an initially inside-out model or an outside-in model (i.e., whether we approach  $\beta = 0$  from below or above). We also find that the qualitative behaviour of Figure 2.2 is insensitive to the exact form of our  $\beta$  parametrization, Equation (2.4). Modifying the parameterization changes the precise rate with which  $\Delta_{21}^2$  changes as a function of  $\beta$ , but the extreme scenarios remain the same and are given by the  $\beta = \pm 1$  curves of Figure 2.2.

One curious feature seen in Figure 2.2 is the fact that the behaviour in  $\Delta_{21}^2$  is non-monotonic with  $\beta$  at high  $k$ . That is, at high  $k$  we see that it is in fact the uncorrelated case with  $\beta = 0$  that has the

highest power, with the extreme cases of  $\beta = \pm 1$  having lower power at  $k > 1.5 \text{ Mpc}^{-1}$ . To get some intuition for why this is the case, consider Figure 2.4, where we show high-pass filtered versions of the brightness temperature field for  $\beta = +1, 0$ , and  $-1$  at  $z = 9$ . These filtered temperature fields contain only power at  $k > 1.5 \text{ Mpc}^{-1}$ , and for clarity (to bring out the fluctuations) we plot their absolute values. Also plotted are the density fields for comparison, and overlaid on both fields are contours demarcating the ionized bubbles. What one sees is that as expected, for the extreme inside-out ( $\beta = +1$ ) or outside-in ( $\beta = -1$ ) cases, the locations of high density regions are dictated by the ionized bubbles. As before, the inside-out case places its highest density peaks inside the ionized bubbles, “squandering” the opportunity to achieve high brightness temperatures. The outside-in case places its highest density peaks in neutral regions. But the fact that it preferentially places its peaks away from bubbles means that there is less volume available in this scenario to produce high brightness temperature spots. In contrast, the uncorrelated scenario indiscriminately places bright spots throughout the volume, thus utilizing more of it to give a large integrated signal.

Our interpretation of this high- $k$  behaviour is bolstered by the redshift dependence seen in Figure 2.2. The non-monotonic behaviour with  $\beta$  is strongest during the earliest phases of reionization, where most of the universe is neutral. In such a regime, not utilizing the full volume results in a greater reduction in the fluctuation power. As reionization proceeds, a random indiscriminate distribution of density peaks (as is the case with  $\beta = 0$ ) becomes more and more disadvantageous as these peaks become more and more likely to fall into an ionized bubble. The outside-in model thus begins to get brighter relative to the uncorrelated model. Indeed, we find that after the midpoint of reionization ( $z \sim 8$  for our fiducial simulations), when there is less neutral volume remaining, the trends in the power spectra are once again monotonic in  $\beta$ .

Although the behaviour at high  $k$  is interesting, it has essentially no impact on the forecasts that we will present in Section 4.6, given that instrument sensitivities tend to be low in those regimes. However, for future-generation instruments, the high- $k$  trend may be a signature that is worth pursuing, as it may break some of the parameter degeneracies that we will find in Section 4.6.

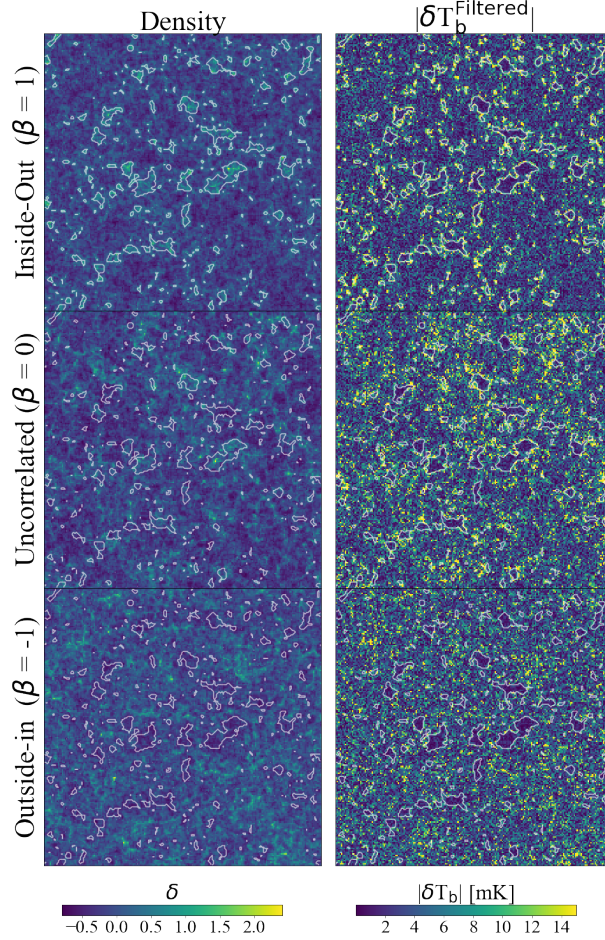


**Figure 2.4:** Density boxes (left) alongside their resulting temperature fields (right), with contours showing the locations of ionized bubbles overlaid. Fourier modes with  $k < 2 \text{ Mpc}^{-1}$  have been filtered out from  $\delta T_b$  to elucidate the high  $k$  behavior seen in Figure 2.2. In this high- $k$  regime, large amplitude brightness fluctuations are seen throughout the neutral regions

### 2.3.2 Redshift Evolution of the Signal

Focusing now on the low- $k$  regime that drives our forecasts, Figure 2.3 shows how  $\Delta_{21}^2$  evolves as a function of  $z$  and  $\beta$ . During the first half of reionization, the ionized bubbles are still small and so reionization has yet to make a significant imprint on the brightness temperature field. Altering the density-ionization correlation via  $\beta$  thus has little effect on the power spectrum and all the curves converge at high  $z$ . As one approaches a global ionization fraction of  $\sim 0.5$ , the ionized bubble morphology has its largest influence on the power spectrum, and thus it is there that one sees the

greatest sensitivity to  $\beta$ . As one approaches the end of reionization, the 21cm signal vanishes and  $\Delta_{21}^2$  once again loses its sensitivity to  $\beta$ .

The redshift space distortions contained in the temperature maps also affect  $\Delta_{21}^2$ . Redshift space distortions induce an angular structure to  $P(\mathbf{k})$ , but also boost the power evenly in the angularly averaged  $P(k)$  by a geometric factor of 1.87 [1]. We find that they primarily affect outside-in maps and not their inside-out counterparts. The effect of redshift space distortions on  $\delta T_b$  are greatest near high density regions, which are first to be ionized in an inside-out scenario. Therefore, the effect of redshift space distortions on  $\Delta_{21}^2$  is small for redshifts  $z < 12$  [37] in the inside-out scenario. Conversely, the high density regions are ionized last in outside-in maps allowing for a more impactful effect on  $\Delta_{21}^2$  throughout reionization. We find a maximum boost of  $15 \text{ mK}^2$  in  $\Delta_{21}^2$  due to redshift space distortions occurring in the extreme outside-in scenarios of  $\beta = -1$  near the midpoint of reionization. The effects on the corresponding inside-out case is negligible within the same regime. In producing  $\Delta_{21}^2$ , we take a more conservative approach and average over the angular dependence for all  $\beta$  realisations. The results presented in Figure 2.2 include these effects. We take this conservative approach in producing our forecasts in Section 4.6. This approach is more appropriate for early limits, where experiments are not expected to have a high enough signal-to-noise per Fourier mode for characterizing the angular patterns in  $\mathbf{k}$  needed to easily measure redshift space distortions. In the future, however, one could imagine using redshift space distortions as another avenue for constraining density-ionization correlations in a more extended analysis.

In addition to the sensitivity of  $\Delta_{21}^2$  on  $\beta$ , the other EoR parameters described in Section 1 will also affect the power spectrum. We want to explore the extent to which one can uniquely constrain  $\beta$  from measurements of  $\Delta_{21}^2$ . We perform these numerical forecasts in the following sections.

## 2.4 HERA Forecasts

We now bring together the parametrization and intuition of Section 2.2 and the power spectrum predictions of Section 2.3 to provide forecasts on potential observational constraints on our corre-

lation parameter  $\beta$ . In this section we lay out our forecasting methodology, reserving a discussion of our results for Section 4.6.

### 2.4.1 Fiducial Instrument and Sensitivity

We use HERA as the fiducial instrument for our forecasts, although similar results can be easily obtained for other current and upcoming instruments such as the Low Frequency Array [52], the Murchison Widefield Array [7,51], and the Square Kilometre Array [30]. When completed, HERA will consist of 350 parabolic dishes, each 14 m in diameter observing from 50 MHz to 250 MHz. Its forecasted sensitivity is such that  $> 20\sigma$  detections of the 21 cm power spectrum from the EoR should be possible [13,45].

To model HERA's expected error bars on a power spectrum measurement, we make use of the publicly available code 21cmSense [45,47]. At a given instant, a particular pair of antennas of the interferometer separated by a baseline vector  $\mathbf{b}$  approximately samples a Fourier mode of the sky with a wavevector  $\mathbf{k}_\perp$  oriented perpendicular to the line-of-sight. The sampled wavevector is given by  $\mathbf{k}_\perp \approx 2\pi\mathbf{b}/\lambda X$ , where  $\lambda$  is the observation wavelength and  $X$  is a conversion factor from angular separation  $\theta$  to transverse comoving distance  $r_\perp$ , and is given by

$$X \equiv \frac{r_\perp}{\theta} = \frac{c}{H_0} \int_0^z \frac{dz'}{E(z')} \quad (2.6)$$

with  $c$  the speed of light,  $H_0$  the Hubble parameter today,  $E(z) \equiv \sqrt{\Omega_m(1+z)^3 + \Omega_\Lambda}$  and  $\Omega_\Lambda$  the normalized dark energy density. Fourier modes along the line of sight are probed using the frequency spectrum, since different observed frequencies correspond to different redshifts, with a conversion factor  $Y$  converting between frequency interval  $\Delta\nu$  and increments in radial comoving distances  $\Delta r_\parallel$ :

$$Y \equiv \frac{\Delta r_\parallel}{\Delta\nu} = \frac{c}{H_0\nu_{21}} \frac{(1+z)^2}{E(z)}, \quad (2.7)$$

where  $\nu_{21} \approx 1420$  MHz is the rest frequency of the 21 cm line. The 21cmSense package computes the amount of time  $t_{\text{int}}$  that an interferometer spends observing a particular mode in  $k_\perp$ - $k_\parallel$  space

and assigns an error bar  $\varepsilon$  to a hypothetical power spectrum measurement, where

$$\varepsilon(k) = X^2 Y \frac{k^3 \Omega_{\text{eff}} T_{\text{sys}}^2}{2\pi^2 2t_{\text{int}}} \quad (2.8)$$

where  $T_{\text{sys}}$  is the system temperature of the telescope (generally dominated by the brightness temperature of the sky at these frequencies), and  $\Omega_{\text{eff}}$  is the effective solid angle of the primary beam of each dish [43].

Beyond signal-to-noise considerations, a realistic forecast must account for foreground contaminants. Astrophysical—but non-cosmological—sources of emission are bright in the low-frequency radio spectrum, and these foregrounds are expected to be brighter than the cosmological 21 cm signal by many orders of magnitude in brightness temperature. Fortunately, these foregrounds are expected to be spectrally smooth, and thus they predominantly contaminate a select triangular region in Fourier space known as “the wedge” that is given by

$$k_{\parallel} \leq \left( \frac{X}{\nu Y} \right) k_{\perp}, \quad (2.9)$$

where  $\nu$  is the observation frequency. (For a derivation and a discussion of various subtleties associated with this equation, see [33] and references therein). In our forecasts, we employ the “moderate” foreground setting in 21cmSense, which simply states that modes satisfying Equation (2.9), plus those that are up to  $0.1 h\text{Mpc}^{-1}$  higher in  $k_{\parallel}$ , are considered irretrievably contaminated by foregrounds and are discarded in one’s analysis. The extra buffer of  $0.1 h\text{Mpc}^{-1}$  accounts for the possibility that low levels of spectral unsmoothness in one’s foregrounds may cause a bleed to higher  $k_{\parallel}$  than one might theoretically expect [46]. In generating the full error bars for our forecasts, we add sample variance to the telescope sensitivities computed in Equation 2.8. The sample variance is generated using a fiducial EoR inside-out model. Using a fiducial outside-in or uncorrelated EoR model to generate the sample variance does not qualitatively change the results in Section 4.6.

## 2.4.2 Markov Chain Monte Carlo Setup

With a model for power spectrum sensitivities, performing a forecast is tantamount to evaluating the posterior probability distribution for the parameters of interest. In particular, suppose we measure a power spectrum  $\Delta_{21}^2(k, z)$  from HERA and group all the measurements from different  $k$  and  $z$  bins into a data vector  $\mathbf{d}$ . Grouping our model parameters  $\beta$ ,  $M_{\text{turn}}$ ,  $R_{\text{mfp}}$ , and  $\zeta$  into another vector  $\theta$ , our goal is to use Bayes' theorem to find the posterior  $p(\theta|\mathbf{d})$ , i.e.,

$$p(\theta|\mathbf{d}) \propto p(\mathbf{d}|\theta)p(\theta), \quad (2.10)$$

where  $p(\mathbf{d}|\theta)$  is the likelihood function and  $p(\theta)$  is our prior.

In our forecasts, we impose uniform priors on all parameters. For  $\zeta$  we pick  $10 < \zeta < 100$  which is broadly consistent with CMB and Ly $\alpha$  constraints on reionization [38]. For  $R_{\text{mfp}}$  we say that  $3 \text{ Mpc} < R_{\text{mfp}} < 80 \text{ Mpc}$  to span a reasonable range in uncertainty on the parameter [50]. For  $M_{\text{turn}}$  we use  $10^7 M_{\odot} < M_{\text{turn}} < 9 \times 10^9 M_{\odot}$ . This is motivated by the atomic cooling threshold and by current constraints on the faint end of UV luminosity functions [42]. Finally, for  $\beta$  we adopt a uniform prior with  $-1 \leq \beta \leq 1$ , which spans the full range of density-ionization correlations discussed in Section 2.2.

The likelihood  $p(\mathbf{d}|\theta)$  is non-analytic in the EoR parameters. To compute it, we generate model predictions for the density and ionization fields from 21cmFAST simulations, given a combination of  $\zeta$ ,  $R_{\text{mfp}}$ , and  $M_{\text{turn}}$ . We then regenerate the density field as appropriate for the desired level of decorrelation from the ionization field as specified by the  $\beta$  parameter. This updated density field is then used in conjunction with the original ionization field to form a brightness temperature field using Equation (2.1). The power spectrum of the resulting maps  $\Delta_{\text{model}}^2$  are then computed and compared to the “measured” power spectrum  $\Delta_{21}^2(k, z)$  via a Gaussian likelihood of the form through the chi squared  $\chi^2$  statistic given by

$$p(\mathbf{d}|\theta) \propto \exp \left[ -\frac{1}{2} \sum_{z,k} \frac{\left( \Delta_{\text{model}}^2 - \Delta_{21}^2 \right)^2}{\epsilon^2} \right], \quad (2.11)$$

where we have assumed that all the  $k$  and  $z$  bins are statistically independent. Our forecasts consider different combinations (see Section 4.6) of redshifts  $z = 6$  to  $z = 10$  in steps of  $\Delta z = 0.5$ , with an observational bandwidth  $\Delta\nu \equiv \nu_{21}\Delta z/(1+z)^2\Delta z$  for each redshift bin.

We exclude bins  $k > 0.75 \text{ Mpc}^{-1}$  for computational simplicity as the HERA error bars are large in that regime and including those  $k$  bins do not add alter our forecasts significantly.

To sample our posterior distribution, we use a Markov Chain Monte Carlo (MCMC) approach, as implemented by the affine invariant MCMC package `emcee` [18]. Of course, since we do not have a real HERA observation of the power spectrum, we must pick a fiducial set of parameter values for our mock observation. In this paper, we adopt fiducial values  $\zeta_0 = 25$ ,  $M_{\text{turn},0} = 5 \times 10^8 M_\odot$ ,  $R_{\text{mfp},0} = 30 \text{ Mpc}$ , and  $\beta_0 = 0.936$  unless otherwise indicated.

## 2.5 Results

In this section we present the results of our MCMCs and discuss their implications. We perform our computations for four different scenarios:

1. A HERA measurement of the 21cm power spectrum over an extended period of the EoR history, from  $z = 6$  to  $z = 10$ .
2. Radio frequency interference (RFI) makes measurements impossible in certain frequency bands. Based on preliminary observations using HERA, we assume that a measurement can be made in a relatively clean way from  $z = 7.5$  to  $z = 8.5$  (using the discrete bands described in Section 2.4.2).
3. A similar RFI-free window from  $z = 9.5$  to  $z = 11.5$ .
4. A measurement of a  $z = 8.0$  power spectrum at three separate bins centred on  $k = 0.2 \text{ Mpc}^{-1}$ ,  $k = 0.25 \text{ Mpc}^{-1}$ , and  $k = 0.3 \text{ Mpc}^{-1}$  of widths  $\Delta k = 0.05 \text{ Mpc}^{-1}$ . These were selected by numerical experimentation to determine a minimal set of measurements required to constrain  $\beta$ .

5. The same measurement as scenario (ii), but assuming outside-in reionization as our fiducial model. We use the same fiducial parameters for  $\zeta_0$ ,  $M_{\text{turn},0}$  and  $R_{\text{mfp},0}$  as described in Section 2.4.2, but pair it with new fiducial correlation parameter of the opposite sign, i.e.,  $\beta_0 = -0.936$ .

### 2.5.1 Scenario (i): Measurement of $\Delta_{21}^2$ Over Redshifts $z = 6$ to $z = 10$

In Figure 2.5 we show our forecasts for a full HERA measurement in the range  $6 < z < 10$ . Immediately clear are degeneracies between certain parameters in our model. For example, since both  $\zeta$  and  $M_{\text{turn}}$  control the timing of reionization as well as the size of the ionized bubbles at a fixed redshift, we find a considerable degeneracy between these parameters. This result is consistent with previous parameter studies such as [45], [26], and [32].

Our new correlation parameter  $\beta$  also exhibits slight degeneracies with  $M_{\text{turn}}$  and  $\zeta$ . The origin of this degeneracy can be deduced by studying how  $\beta$  and  $\zeta$  affect  $\Delta_{21}^2$  at  $k$  bins and redshifts where HERA is the most sensitive to changes in the model. Most of the information comes from  $z \sim 8$  and  $0.2 \text{ Mpc}^{-1} < k < 0.5 \text{ Mpc}^{-1}$ . This redshift is slightly lower than the redshift at which the power spectrum peaks because the error bars on the power spectrum are lower at lower redshifts. The  $k$  range is a balance between where the power spectrum is the most sensitive to changes in  $\beta$  (see Figure 2.2), foreground contamination at low  $k$ , and instrumental noise limitations at high  $k$ . In this context, consider the left panel of Figure 2.3. One sees that decreasing  $\beta$  increases the amplitude of  $\Delta_{21}^2$ . Since  $z = 8$  comes after the midpoint of reionization in our fiducial model, the power spectrum is declining as one moves to lower redshifts. A decrease in  $\beta$  can therefore be mimicked by a delay in reionization that shifts all the curves in Figure 2.3 to the left, bringing the power up to closer to its peak value. This can be accomplished by a decrease in  $\zeta$ , and indeed, one sees a positive degeneracy between  $\beta$  and  $\zeta$  in Figure 2.5.

Our timing argument does not translate directly to the degeneracy between  $\beta$  and  $M_{\text{turn}}$ . Indeed, if one only considered the fact that lowering  $M_{\text{turn}}$  results in earlier reionization, one would predict an opposite trend to what is seen in Figure 2.5. However, whereas  $\zeta$  mainly affects the timing of reionization,  $M_{\text{turn}}$  also somewhat affects the shape of the power spectrum [45]. Moreover,

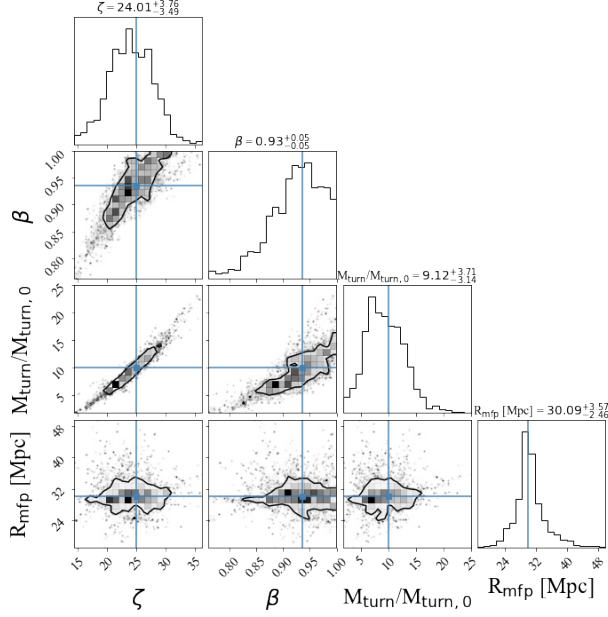


**Figure 2.5:** Posterior distributions for Scenario (i) of Section 4.6, covering the redshift range of our forecasts,  $6 \leq z \leq 10$ . The 68% credibility contours are entirely contained within the inside-out region of parameter space, suggesting that with such a measurement we can firmly rule out outside-in or uncorrelated models.

the aforementioned degeneracy between  $M_{\text{turn}}$  and  $\zeta$  works in the opposite direction as the timing argument. It is therefore not obvious *a priori* how  $\beta$  and  $M_{\text{turn}}$  should be correlated, and Figure 2.5 reveals that the net effect is a positive degeneracy.

In any case, one sees that despite the degeneracies between  $\beta$  and the other parameters, it is still possible to obtain strong constraints on the former. Examining the marginalized distributions, for instance, one sees that the 68% credibility regions (CR) strongly rule out both outside-in and uncorrelated scenarios. We find that the 95% CR is also entirely contained within the inside-out portion of the posterior. This allows us to rule out other reionization scenarios at 95% credibility.

## 2.5.2 Scenarios (ii) to (iv): Measurements at Specific Redshifts and Scales

Early HERA measurements will likely come at particular redshifts and  $k$  bins, and in Figures 2.6 and 2.7, we show our forecasts for the clean  $7.5 \leq z \leq 8.5$  and  $9.5 \leq z \leq 11.5$  spectral windows.

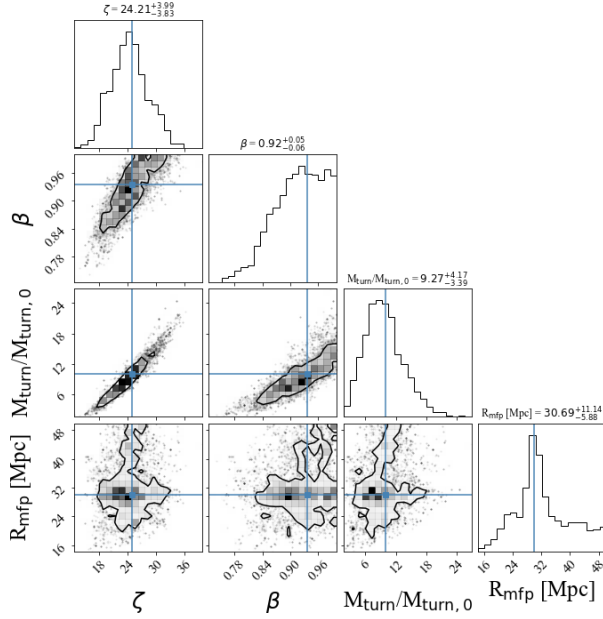


**Figure 2.6:** Same as Figure 2.5, but for a restricted redshift range of  $7.5 \leq z \leq 8.5$ . Measurement over these redshifts can strongly rule out correlations that are inconsistent with inside-out models. The 68% credibility contours clearly distinguish inside-out and outside in regions of parameter space.

What we find is that measurements of the power spectrum at specific key redshifts can be enough to constrain the sign of  $\beta$ .

Consider first the  $7.5 \leq z \leq 8.5$  window (Figure 2.6). The conclusions drawn for this redshift window are comparable with the results over the expanded history of the EoR (i.e., the previous scenario with measurements from  $z = 6$  to 10). This is unsurprising since the bulk of the information of  $\beta$  comes from precisely these redshifts: recall from Figure 2.3 that this range coincides to redshifts where the power spectrum peaks, as well as where the differences between different  $\beta$  are the greatest. Indeed, to take this to an extreme, Figure 2.8 shows the constraints from measuring just three  $k$  bins (centred on  $0.2 \text{ Mpc}^{-1}$ ,  $0.25 \text{ Mpc}^{-1}$ , and  $0.3 \text{ Mpc}^{-1}$ ) at redshift  $z = 8.0$ . These are the  $k$  and  $z$  bins that contain the most information about  $\beta$ . The results are again similar. Of course, the constraints are slightly worse than one obtains over the full redshift range. However, the differences are quantitative rather than qualitative, and one can easily distinguish between inside-out and outside-in models of reionization as the  $\beta$  contours are entirely contained

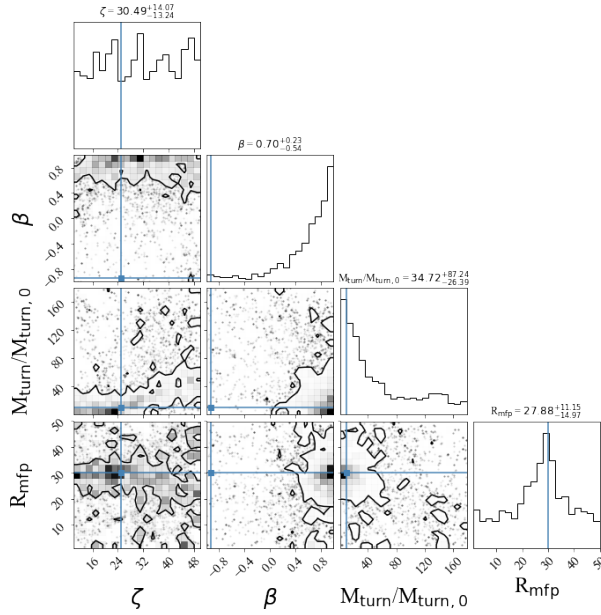


**Figure 2.7:** Same as Figure 2.5, but for a restricted redshift range of  $9.5 \leq z \leq 11.5$ . Although many parameters are poorly constrained, an uncorrelated scenario of  $\beta = 0$  can still be easily ruled out.

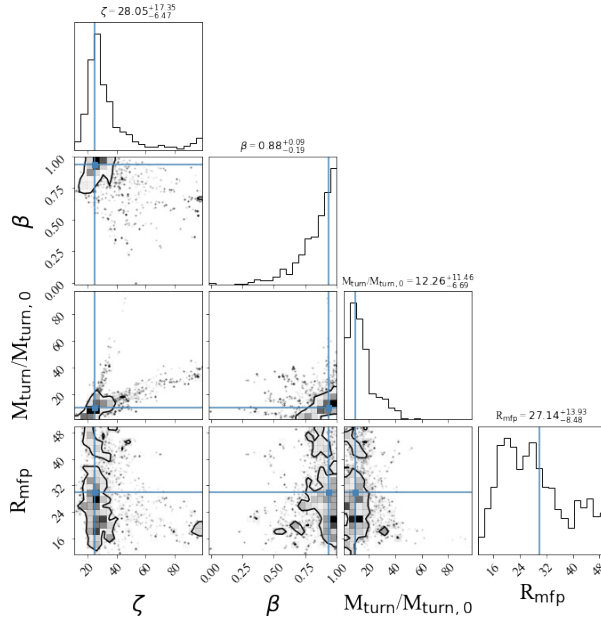


**Figure 2.8:** Same as Figure 2.5, but using only three  $k$  bins centred on  $k = 0.2 \text{ Mpc}^{-1}$ ,  $k = 0.25 \text{ Mpc}^{-1}$ , and  $k = 0.3 \text{ Mpc}^{-1}$  at  $z = 8.0$ . Because these bins contain the most information on  $\beta$ , using them alone is sufficient for excellent constraints.

within the inside-out region of parameter space. We find that our ability to distinguish between these models is also valid at 95% CR.

With the  $9.5 \leq z \leq 11.5$  window,<sup>1</sup> we are probing the early stages of reionization, where the process has yet to make a significant imprint on the temperature field. The power spectrum is therefore less sensitive to  $\beta$ . Correspondingly, these redshifts are not as effective at numerically constraining the value of  $\beta$ ; however, we can still confidently determine the sign of  $\beta$ . Outside-in morphologies, for example, are inconsistent with our mock observation of a fiducial inside-out model. Importantly, we note that this is true even though the limited redshift range is unable to provide strong constraints on other parameters, although it is important to acknowledge that for this scenario the constraint on  $\zeta$  is mostly driven by our prior.

In principle, the value of  $\beta$  need not be constant in time, and could vary throughout the EoR history. In this scenario  $\beta$  would obtain a redshift dependence. Given this reality, one can then confine measurements of  $\beta$  to epochs where the correlations between  $\delta$  and  $x_{\text{HII}}$  remain constant. For example, our forecast for  $\beta$  between  $7.5 < z < 8.5$  is entirely contained within the ‘‘Ionized Fibre’’ stage of reionization in [9]. Since forecast scenarios (ii) through (iv) are small enough redshift windows, they each fall within a particular ‘‘stage’’ of reionization morphology. Making the correspondence between each of these scenarios and a particular stage of reionization morphology becomes more difficult for scenario (i) which takes place over  $6 < z < 10$ .

### 2.5.3 Scenario (v): Fiducial Outside-in Reionization

In figure 2.9, we show the MCMC posterior for measurement of  $\Delta_{21}^2$  with parameters identical to scenario (ii), but using a fiducial outside-in morphology ( $\beta_0 = -0.936$ ). In an outside-in scenario,  $\Delta_{21}^2$  varies slowly as a function of  $\beta$  in the regime  $\beta \simeq -1$  (see Figure 2.2). As a result, it is difficult to numerically distinguish the particular value of  $\beta$  for extreme outside-in models. However this does not prevent us from being able to distinguish outside-in models from uncorrelated or inside-out reionization. The 1D posterior for  $\beta$  is non-Gaussian around  $\beta = -1$  and the posterior drops

---

<sup>1</sup>For this scenario only, we exclude  $k > 0.75 \text{ Mpc}^{-1}$  for computational simplicity. There is little sensitivity to the power spectrum here anyway, and thus there is a negligible change to our results.

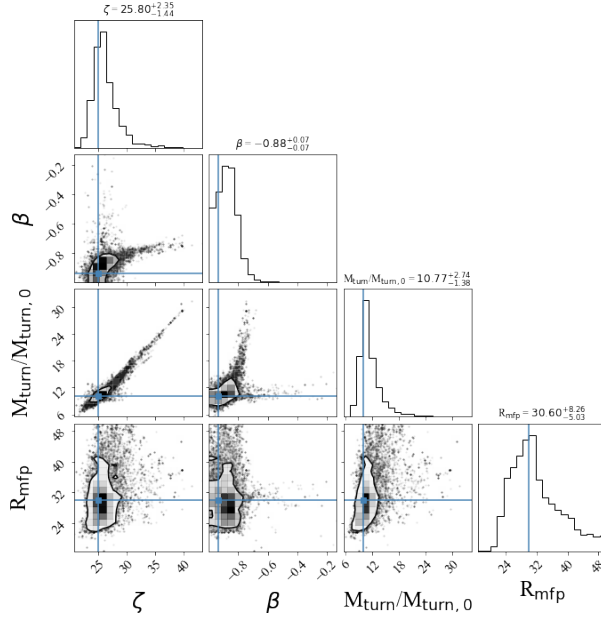


**Figure 2.9:** Same as Figure 2.6, but using an outside-in model with  $\beta = -0.936$  as our fiducial reionization morphology. Displayed are the 68% CR contours. The 68% CR are entirely contained within  $\beta < 0$  suggesting that if reionization proceeds as outside-in, measurement of  $\Delta_{21}^2$  in this scenario can rule out uncorrelated and inside-out reionization with 68% credibility.

dramatically around  $\beta \simeq -0.7$ , which is where  $\Delta_{21}^2$  becomes very sensitive to changes in correlation. This allows us to properly distinguish between the signs of  $\beta$ . The 68% CR contours of such a measurement are entirely contained within  $\beta < 0$ . Therefore for this fiducial reionization scenario, measurements of  $\Delta_{21}^2$  across the midpoint of reionization can fully distinguish between signs of  $\beta$ . This conclusion is also valid at a 95% CR level. That is, the 95% credibility region is entirely contained within the outside-in regime of the posterior.

## 2.5.4 Early Limits

In closing, we note an interesting trend that will likely manifest as upper limits from early data slowly come down. From Figure 2.3, note that the brightest power spectra come from outside-in scenarios. Thus, early upper limits will first rule out (or detect!) these morphologies. As we alluded to in Section 4.2.1, however, the curves for  $\beta < 0$  (outside-in) are typically closer together than those for  $\beta > 0$ . Therefore, although the outside-in scenarios are the easiest to rule out or

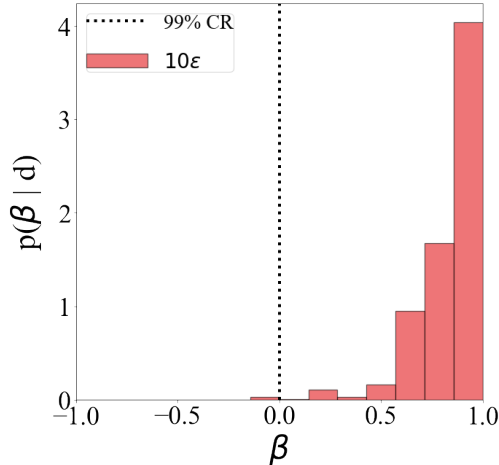


**Figure 2.10:** Marginalized posterior distributions on  $\beta$  obtained through the measurement of  $\Delta_{21}^2$  in Scenario (ii) of Section 4.6, but assuming 10 times larger error bars than the design HERA sensitivities to mimic potential upper limits. As the upper limits come down to 10 times the fiducial errors on  $\Delta_{21}^2$  from Section 2.8, we will be able to rule out  $\beta < 0$  with 99% credibility in our fiducial model. The dotted vertical lines demarcate  $\beta = 0$  to guide the eye.

detect, a generic quantification of the density-ionization correlation is easier (i.e., the error bars on  $\beta$  will be smaller) if our Universe ends up being one where reionization proceeded in an inside-out fashion.

We expect that as upper limits descend to roughly 10 times the design sensitivity of HERA (i.e., error bars approach  $\sim 10\epsilon$  on a measurement of  $\Delta_{21}^2$ ), we will be able to rule out uncorrelated reionization ( $\beta = 0$ ) at  $\sim 99\%$  credibility, assuming the same  $z$  and  $k$  bins as Scenario (ii) in Section 4.6. This is illustrated in Figure 2.10 which shows the posterior on  $\beta$  from upper limits where the power spectrum is constrained with errors on the order of  $\epsilon \sim 20 \text{ mK}^2$  (corresponding to 10 times the HERA design errors), for bands described in Section 2.4.2.

## 2.6 Conclusion

The first measurements of the 21 cm power spectrum are upcoming and a key prediction of many EoR models is the correlation between ionization and density fields. The way these two fields correlate is an indicator of the morphology of reionization. A number of discrete cases of correlations have

been studied in previous works pertaining to inside-out or outside-in models. We build upon these works by proposing a continuous parameter  $\beta$  that encompasses all possible correlation scenarios to provide an alternative method for model selection.

A key effect of changing  $\beta$  in 21cm temperature maps is to alter the contrast between ionized bubbles and neutral regions. The temperature contrast between these regions is larger for values of  $\beta < 0$ , corresponding to outside-in models of reionization. Inside-out models, with  $\beta > 0$ , have decreased contrast. Similarly, we find that outside-in models of reionization produce an increase in the amplitude in the 21cm power spectrum compared to their inside-out counterparts. The distinction between these models is greatest at the midpoint of reionization.

Upcoming limits on the 21cm power spectrum will allow us to place constraints on  $\beta$ , potentially ruling out or favouring various models. As a test case, we carry out a numerical forecast using the HERA experiment, which has the sensitivity to place  $> 20\sigma$  limits on  $\Delta_{21}^2$ . We perform an MCMC over the entire history of reionization and find that the fiducial inside-out model used produces a unique imprint on the 21cm power spectrum. Measurement of  $\Delta_{21}^2$  over this redshift range can fully distinguish between the two classes of correlations. Because measurements of  $\Delta_{21}^2$  over a wide range of  $z$  and  $k$  bins are unlikely in early observations, we select a smaller range of redshifts to measure  $\Delta_{21}^2$ . Motivated by the high sensitivity of  $\Delta_{21}^2$  on  $\beta$  at the midpoint of reionization, we identify redshift  $z \sim 8$  as the most effective regime to distinguish between types of correlations. Measurements in just a few select  $k$  bins at these redshifts are sufficient for learning about the broad morphology of reionization. Along the way, such measurements will test a key measure of reionization—the degree of correlation between the density and ionization fields—laying the groundwork for increasingly detailed 21 cm constraints that will considerably enhance our knowledge of the EoR.

## Acknowledgements

The authors are delighted to acknowledge helpful discussions with Phil Bull, Adélie Gorce, Jordan Mirocha, and Steven Murray, as well as Steve Furlanetto for posing the original question that inspired

this work. We acknowledge support from the New Frontiers in Research Fund Exploration grant program, a Natural Sciences and Engineering Research Council of Canada (NSERC) Discovery Grant and a Discovery Launch Supplement, the Sloan Research Fellowship, the William Dawson Scholarship at McGill, as well as the Canadian Institute for Advanced Research (CIFAR) Azrieli Global Scholars program. This research was enabled in part by support provided by Calcul Quebec ([www.calculquebec.ca](http://www.calculquebec.ca)), WestGrid ([www.westgrid.ca](http://www.westgrid.ca)) and Compute Canada ([www.computecanada.ca](http://www.computecanada.ca)). The authors would like to thank the anonymous referee for the insightful comments which have improved this paper.

## Data Availability

The software code underlying this article will be shared on reasonable request to the corresponding author.

## Bibliography

- [1] Rennan Barkana and Abraham Loeb. A Method for Separating the Physics from the Astrophysics of High-Redshift 21 Centimeter Fluctuations. *ApJ*, 624(2):L65–L68, May 2005.
- [2] George D. Becker, James S. Bolton, Piero Madau, Max Pettini, Emma V. Ryan-Weber, and Bram P. Venemans. Evidence of patchy hydrogen reionization from an extreme Ly $\alpha$  trough below redshift six. *MNRAS*, 447(4):3402–3419, March 2015.
- [3] George D. Becker, Frederick B. Davies, Steven R. Furlanetto, Matthew A. Malkan, Elisa Boera, and Craig Douglass. Evidence for Large-scale Fluctuations in the Metagalactic Ionizing Background Near Redshift Six. *ApJ*, 863(1):92, August 2018.
- [4] Robert H. Becker, Xiaohui Fan, Richard L. White, Michael A. Strauss, Vijay K. Narayanan, Robert H. Lupton, James E. Gunn, James Annis, Neta A. Bahcall, J. Brinkmann, A. J. Connolly, István Csabai, Paul C. Czarapata, Mamoru Doi, Timothy M. Heckman, G. S.

- Hennessy, Željko Ivezić, G. R. Knapp, Don Q. Lamb, Timothy A. McKay, Jeffrey A. Munn, Thomas Nash, Robert Nichol, Jeffrey R. Pier, Gordon T. Richards, Donald P. Schneider, Chris Stoughton, Alexander S. Szalay, Aniruddha R. Thakar, and D. G. York. Evidence for Reionization at  $z \sim 6$ : Detection of a Gunn-Peterson Trough in a  $z=6.28$  Quasar. *AJ*, 122(6):2850–2857, December 2001.
- [5] T. Binnie and J. R. Pritchard. Bayesian model selection with future 21cm observations of the epoch of reionization. *MNRAS*, 487(1):1160–1177, July 2019.
- [6] Sarah E. I. Bosman, Xiaohui Fan, Linhua Jiang, Sophie Reed, Yoshiki Matsuoka, George Becker, and Martin Haehnelt. New constraints on Lyman- $\alpha$  opacity with a sample of 62 quasars at  $z > 5.7$ . *MNRAS*, 479(1):1055–1076, September 2018.
- [7] Judd D. Bowman, Iver Cairns, David L. Kaplan, Tara Murphy, Divya Oberoi, Lister Staveley-Smith, Wayne Arcus, David G. Barnes, Gianni Bernardi, Frank H. Briggs, Shea Brown, John D. Bunton, Adam J. Burgasser, Roger J. Cappallo, Shami Chatterjee, Brian E. Corey, Anthea Coster, Avinash Deshpande, Ludi deSouza, David Emrich, Philip Erickson, Robert F. Goeke, B. M. Gaensler, Lincoln J. Greenhill, Lisa Harvey-Smith, Bryna J. Hazelton, David Herne, Jacqueline N. Hewitt, Melanie Johnston-Hollitt, Justin C. Kasper, Barton B. Kincaid, Ronald Koenig, Eric Kratzenberg, Colin J. Lonsdale, Mervyn J. Lynch, Lynn D. Matthews, S. Russell McWhirter, Daniel A. Mitchell, Miguel F. Morales, Edward H. Morgan, Stephen M. Ord, Joseph Pathikulangara, Thiagaraj Prabu, Ronald A. Remillard, Timothy Robishaw, Alan E. E. Rogers, Anish A. Roshi, Joseph E. Salah, Robert J. Sault, N. Udaya Shankar, K. S. Srivani, Jamie B. Stevens, Ravi Subrahmanyan, Steven J. Tingay, Randall B. Wayth, Mark Waterson, Rachel L. Webster, Alan R. Whitney, Andrew J. Williams, Christopher L. Williams, and J. Stuart B. Wyithe. Science with the Murchison Widefield Array. *Publ. Astron. Soc. Australia*, 30:e031, April 2013.
- [8] Jonathan Chardin, Ewald Puchwein, and Martin G. Haehnelt. Large-scale opacity fluctuations in the Ly $\alpha$  forest: evidence for QSOs dominating the ionizing UV background at  $z \sim 5.5-6$ ? *MNRAS*, 465(3):3429–3445, March 2017.

- [9] Zhaoting Chen, Yidong Xu, Yougang Wang, and Xuelei Chen. Stages of Reionization as Revealed by the Minkowski Functionals. *ApJ*, 885(1):23, November 2019.
- [10] Tirthankar Roy Choudhury, Martin G. Haehnelt, and John Regan. Inside-out or outside-in: the topology of reionization in the photon-starved regime suggested by  $\text{Ly}\alpha$  forest data. *MNRAS*, 394(2):960–977, April 2009.
- [11] Anson D’Aloisio, Matthew McQuinn, and Hy Trac. Large Opacity Variations in the High-redshift  $\text{Ly}\alpha$  Forest: The Signature of Relic Temperature Fluctuations from Patchy Reionization. *ApJ*, 813(2):L38, November 2015.
- [12] Frederick B. Davies and Steven R. Furlanetto. Large fluctuations in the hydrogen-ionizing background and mean free path following the epoch of reionization. *MNRAS*, 460(2):1328–1339, August 2016.
- [13] David R. DeBoer, Aaron R. Parsons, James E. Aguirre, Paul Alexander, Zaki S. Ali, Adam P. Beardsley, Gianni Bernardi, Judd D. Bowman, Richard F. Bradley, Chris L. Carilli, Carina Cheng, Eloy de Lera Acedo, Joshua S. Dillon, Aaron Ewall-Wice, Gcobisa Fadana, Nicolas Fagnoni, Randall Fritz, Steve R. Furlanetto, Brian Glendenning, Bradley Greig, Jasper Grobbelaar, Bryna J. Hazelton, Jacqueline N. Hewitt, Jack Hickish, Daniel C. Jacobs, Austin Julius, MacCalvin Kariseb, Saul A. Kohn, Telalo Lekalake, Adrian Liu, Anita Loots, David MacMahon, Lourence Malan, Cresshim Malgas, Matthys Maree, Zachary Martinot, Nathan Mathison, Eunice Matsetela, Andrei Mesinger, Miguel F. Morales, Abraham R. Neben, Nipanjana Patra, Samantha Pieterse, Jonathan C. Pober, Nima Razavi-Ghods, Jon Ringuette, James Robnett, Kathryn Rosie, Raddwine Sell, Craig Smith, Angelo Syce, Max Tegmark, Nithyanandan Thyagarajan, Peter K. G. Williams, and Haoxuan Zheng. Hydrogen Epoch of Reionization Array (HERA). *PASP*, 129(974):045001, April 2017.
- [14] Anna-Christina Eilers, Joseph F. Hennawi, Frederick B. Davies, and Jose Oñorbe. Anomaly in the Opacity of the Post-reionization Intergalactic Medium in the  $\text{Ly}\alpha$  and  $\text{Ly}\beta$  Forest. *ApJ*, 881(1):23, August 2019.

- [15] Aaron Ewall-Wice, Jacqueline Hewitt, Andrei Mesinger, Joshua S. Dillon, Adrian Liu, and Jonathan Pober. Constraining high-redshift X-ray sources with next generation 21-cm power spectrum measurements. *MNRAS*, 458(3):2710–2724, May 2016.
- [16] Xiaohui Fan, Michael A. Strauss, Robert H. Becker, Richard L. White, James E. Gunn, Gillian R. Knapp, Gordon T. Richards, Donald P. Schneider, J. Brinkmann, and Masataka Fukugita. Constraining the Evolution of the Ionizing Background and the Epoch of Reionization with  $z \sim 6$  Quasars. II. A Sample of 19 Quasars. *AJ*, 132(1):117–136, July 2006.
- [17] Chang Feng, Asantha Cooray, and Brian Keating. A Halo Model Approach to the 21 cm and  $\text{Ly}\alpha$  Cross-correlation. *ApJ*, 846(1):21, September 2017.
- [18] Daniel Foreman-Mackey, David W. Hogg, Dustin Lang, and Jonathan Goodman. emcee: The MCMC Hammer. *PASP*, 125(925):306, March 2013.
- [19] Steven R. Furlanetto, Zoltán Haiman, and S. Peng Oh. Fossil Ionized Bubbles around Dead Quasars during Reionization. *ApJ*, 686(1):25–40, October 2008.
- [20] Steven R. Furlanetto and S. Peng Oh. Taxing the rich: recombinations and bubble growth during reionization. *MNRAS*, 363(3):1031–1048, November 2005.
- [21] Steven R. Furlanetto and S. Peng Oh. Reionization through the lens of percolation theory. *MNRAS*, 457(2):1813–1827, April 2016.
- [22] Steven R. Furlanetto, S. Peng Oh, and Frank H. Briggs. Cosmology at low frequencies: The 21 cm transition and the high-redshift Universe. *Phys. Rep*, 433(4-6):181–301, October 2006.
- [23] Steven R. Furlanetto, Matias Zaldarriaga, and Lars Hernquist. Statistical Probes of Reionization with 21 Centimeter Tomography. *ApJ*, 613(1):16–22, September 2004.
- [24] Steven R. Furlanetto, Matias Zaldarriaga, and Lars Hernquist. The Growth of H II Regions During Reionization. *ApJ*, 613(1):1–15, September 2004.

- [25] S. Gallerani, A. Ferrara, X. Fan, and T. Roy Choudhury. Glimpsing through the high-redshift neutral hydrogen fog. *MNRAS*, 386(1):359–369, May 2008.
- [26] Bradley Greig and Andrei Mesinger. 21CMMC: an MCMC analysis tool enabling astrophysical parameter studies of the cosmic 21 cm signal. *MNRAS*, 449(4):4246–4263, June 2015.
- [27] Bradley Greig and Andrei Mesinger. Simultaneously constraining the astrophysics of reionization and the epoch of heating with 21CMMC. *MNRAS*, 472(3):2651–2669, December 2017.
- [28] Laura C. Keating, Lewis H. Weinberger, Girish Kulkarni, Martin G. Haehnelt, Jonathan Chardin, and Dominique Aubert. Long troughs in the Lyman- $\alpha$  forest below redshift 6 due to islands of neutral hydrogen. *MNRAS*, 491(2):1736–1745, January 2020.
- [29] Nicholas S. Kern, Adrian Liu, Aaron R. Parsons, Andrei Mesinger, and Bradley Greig. Emulating Simulations of Cosmic Dawn for 21 cm Power Spectrum Constraints on Cosmology, Reionization, and X-Ray Heating. *ApJ*, 848(1):23, October 2017.
- [30] L. Koopmans, J. Pritchard, G. Mellema, J. Aguirre, K. Ahn, R. Barkana, I. van Bemmell, G. Bernardi, A. Bonaldi, and F. Briggs. The Cosmic Dawn and Epoch of Reionisation with SKA. In *Advancing Astrophysics with the Square Kilometre Array (AASKA14)*, page 1, Apr 2015.
- [31] Girish Kulkarni, Laura C. Keating, Martin G. Haehnelt, Sarah E. I. Bosman, Ewald Puchwein, Jonathan Chardin, and Dominique Aubert. Large Ly  $\alpha$  opacity fluctuations and low CMB  $\tau$  in models of late reionization with large islands of neutral hydrogen extending to  $z \lesssim 5.5$ . *MNRAS*, 485(1):L24–L28, May 2019.
- [32] Adrian Liu and Aaron R. Parsons. Constraining cosmology and ionization history with combined 21 cm power spectrum and global signal measurements. *MNRAS*, 457(2):1864–1877, April 2016.

- [33] Adrian Liu and J. Richard Shaw. Data Analysis for Precision 21 cm Cosmology. *PASP*, 132(1012):062001, June 2020.
- [34] Abraham Loeb and Steven R. Furlanetto. *The First Galaxies in the Universe*. Princeton University Press, 2013.
- [35] Piero Madau and Francesco Haardt. Cosmic Reionization after Planck: Could Quasars Do It All? *ApJ*, 813(1):L8, November 2015.
- [36] Ian D. McGreer, Andrei Mesinger, and Valentina D’Odorico. Model-independent evidence in favour of an end to reionization by  $z \approx 6$ . *MNRAS*, 447(1):499–505, February 2015.
- [37] Andrei Mesinger, Steven Furlanetto, and Renyue Cen. 21CMFAST: a fast, seminumerical simulation of the high-redshift 21-cm signal. *MNRAS*, 411(2):955–972, February 2011.
- [38] Andrei Mesinger, Matthew McQuinn, and David N. Spergel. The kinetic Sunyaev-Zel’dovich signal from inhomogeneous reionization: a parameter space study. *MNRAS*, 422(2):1403–1417, May 2012.
- [39] Jordi Miralda-Escudé, Martin Haehnelt, and Martin J. Rees. Reionization of the Inhomogeneous Universe. *ApJ*, 530(1):1–16, February 2000.
- [40] Miguel F. Morales and J. Stuart B. Wyithe. Reionization and Cosmology with 21-cm Fluctuations. *ARA&A*, 48:127–171, September 2010.
- [41] Fahad Nasir and Anson D’Aloisio. Observing the tail of reionization: neutral islands in the  $z = 5.5$  Lyman- $\alpha$  Forest. *MNRAS*, April 2020.
- [42] Jaehong Park, Andrei Mesinger, Bradley Greig, and Nicolas Gillet. Inferring the astrophysics of reionization and cosmic dawn from galaxy luminosity functions and the 21-cm signal. *MNRAS*, 484(1):933–949, March 2019.
- [43] Aaron R. Parsons, Adrian Liu, James E. Aguirre, Zaki S. Ali, Richard F. Bradley, Chris L. Carilli, David R. DeBoer, Matthew R. Dexter, Nicole E. Gugliucci, Daniel C. Jacobs, Pat

Klima, David H. E. MacMahon, Jason R. Manley, David F. Moore, Jonathan C. Pober, Irina I. Stefan, and William P. Walbrugh. New Limits on 21 cm Epoch of Reionization from PAPER-32 Consistent with an X-Ray Heated Intergalactic Medium at  $z = 7.7$ . *ApJ*, 788(2):106, June 2014.

- [44] Planck Collaboration, P. A. R. Ade, N. Aghanim, M. Arnaud, M. Ashdown, J. Aumont, C. Baccigalupi, A. J. Banday, R. B. Barreiro, J. G. Bartlett, N. Bartolo, E. Battaner, R. Battye, K. Benabed, A. Benoît, A. Benoit-Lévy, J. P. Bernard, M. Bersanelli, P. Bielewicz, J. J. Bock, A. Bonaldi, L. Bonavera, J. R. Bond, J. Borrill, F. R. Bouchet, F. Boulanger, M. Bucher, C. Burigana, R. C. Butler, E. Calabrese, J. F. Cardoso, A. Catalano, A. Challinor, A. Chamballu, R. R. Chary, H. C. Chiang, J. Chluba, P. R. Christensen, S. Church, D. L. Clements, S. Colombi, L. P. L. Colombo, C. Combet, A. Coulais, B. P. Crill, A. Curto, F. Cuttaia, L. Danese, R. D. Davies, R. J. Davis, P. de Bernardis, A. de Rosa, G. de Zotti, J. Delabrouille, F. X. Désert, E. Di Valentino, C. Dickinson, J. M. Diego, K. Dolag, H. Dole, S. Donzelli, O. Doré, M. Douspis, A. Ducout, J. Dunkley, X. Dupac, G. Efstathiou, F. Elsner, T. A. Enßlin, H. K. Eriksen, M. Farhang, J. Fergusson, F. Finelli, O. Forni, M. Frailis, A. A. Fraisse, E. Franceschi, A. Frejsel, S. Galeotta, S. Galli, K. Ganga, C. Gauthier, M. Gerbino, T. Ghosh, M. Giard, Y. Giraud-Héraud, E. Giusarma, E. Gjerløw, J. González-Nuevo, K. M. Górski, S. Gratton, A. Gregorio, A. Gruppuso, J. E. Gudmundsson, J. Hamann, F. K. Hansen, D. Hanson, D. L. Harrison, G. Helou, S. Henrot-Versillé, C. Hernández-Monteagudo, D. Herranz, S. R. Hildebrandt, E. Hivon, M. Hobson, W. A. Holmes, A. Hornstrup, W. Hovest, Z. Huang, K. M. Huffenberger, G. Hurier, A. H. Jaffe, T. R. Jaffe, W. C. Jones, M. Juvela, E. Keihänen, R. Keskitalo, T. S. Kisner, R. Kneissl, J. Knoche, L. Knox, M. Kunz, H. Kurki-Suonio, G. Lagache, A. Lähteenmäki, J. M. Lamarre, A. Lasenby, M. Lattanzi, C. R. Lawrence, J. P. Leahy, R. Leonardi, J. Lesgourgues, F. Levrier, A. Lewis, M. Liguori, P. B. Lilje, M. Linden-Vørnle, M. López-Cañiego, P. M. Lubin, J. F. Macías-Pérez, G. Maggio, D. Maino, N. Mandolesi, A. Mangilli, A. Marchini, M. Maris, P. G. Martin, M. Martinelli, E. Martínez-González, S. Masi, S. Matarrese, P. McGehee, P. R. Meinhold, A. Melchiorri, J. B. Melin, L. Mendes, A. Mennella, M. Migliaccio, M. Millea, S. Mitra, M. A. Miville-

Deschênes, A. Moneti, L. Montier, G. Morgante, D. Mortlock, A. Moss, D. Munshi, J. A. Murphy, P. Naselsky, F. Nati, P. Natoli, C. B. Netterfield, H. U. Nørgaard-Nielsen, F. Noviello, D. Novikov, I. Novikov, C. A. Oxborrow, F. Paci, L. Pagano, F. Pajot, R. Paladini, D. Paoletti, B. Partridge, F. Pasian, G. Patanchon, T. J. Pearson, O. Perdereau, L. Perotto, F. Perrotta, V. Pettorino, F. Piacentini, M. Piat, E. Pierpaoli, D. Pietrobon, S. Plaszczynski, E. Pointecouteau, G. Polenta, L. Popa, G. W. Pratt, G. Prézeau, S. Prunet, J. L. Puget, J. P. Rachen, W. T. Reach, R. Rebolo, M. Reinecke, M. Remazeilles, C. Renault, A. Renzi, I. Ristorcelli, G. Rocha, C. Rosset, M. Rossetti, G. Roudier, B. Rouillé d'Orfeuill, M. Rowan-Robinson, J. A. Rubiño-Martín, B. Rusholme, N. Said, V. Salvatelli, L. Salvati, M. Sandri, D. Santos, M. Savelainen, G. Savini, D. Scott, M. D. Seiffert, P. Serra, E. P. S. Shellard, L. D. Spencer, M. Spinelli, V. Stolyarov, R. Stompor, R. Sudiwala, R. Sunyaev, D. Sutton, A. S. Suur-Uski, J. F. Sygnet, J. A. Tauber, L. Terenzi, L. Toffolatti, M. Tomasi, M. Tristram, T. Trombetti, M. Tucci, J. Tuovinen, M. Türler, G. Umana, L. Valenziano, J. Valiviita, F. Van Tent, P. Vielva, F. Villa, L. A. Wade, B. D. Wandelt, I. K. Wehus, M. White, S. D. M. White, A. Wilkinson, D. Yvon, A. Zacchei, and A. Zonca. Planck 2015 results. XIII. Cosmological parameters. *A&A*, 594:A13, September 2016.

[45] Jonathan C. Pober, Adrian Liu, Joshua S. Dillon, James E. Aguirre, Judd D. Bowman, Richard F. Bradley, Chris L. Carilli, David R. DeBoer, Jacqueline N. Hewitt, Daniel C. Jacobs, Matthew McQuinn, Miguel F. Morales, Aaron R. Parsons, Max Tegmark, and Dan J. Werthimer. What Next-generation 21 cm Power Spectrum Measurements can Teach us About the Epoch of Reionization. *ApJ*, 782(2):66, February 2014.

[46] Jonathan C. Pober, Aaron R. Parsons, James E. Aguirre, Zaki Ali, Richard F. Bradley, Chris L. Carilli, Dave DeBoer, Matthew Dexter, Nicole E. Gugliucci, Daniel C. Jacobs, Patricia J. Klima, Dave MacMahon, Jason Manley, David F. Moore, Irina I. Stefan, and William P. Walbrugh. Opening the 21 cm Epoch of Reionization Window: Measurements of Foreground Isolation with PAPER. *ApJ*, 768(2):L36, May 2013.

- [47] Jonathan C. Pober, Aaron R. Parsons, David R. DeBoer, Patrick McDonald, Matthew McQuinn, James E. Aguirre, Zaki Ali, Richard F. Bradley, Tzu-Ching Chang, and Miguel F. Morales. The Baryon Acoustic Oscillation Broadband and Broad-beam Array: Design Overview and Sensitivity Forecasts. *AJ*, 145(3):65, March 2013.
- [48] Andrew Pontzen, Anže Slosar, Nina Roth, and Hiranya V. Peiris. Inverted initial conditions: Exploring the growth of cosmic structure and voids. *Phys. Rev. D*, 93(10):103519, May 2016.
- [49] Jonathan R. Pritchard and Abraham Loeb. 21 cm cosmology in the 21st century. *Reports on Progress in Physics*, 75(8):086901, August 2012.
- [50] Antoinette Songaila and Lennox L. Cowie. The Evolution of Lyman Limit Absorption Systems to Redshift Six. *ApJ*, 721(2):1448–1466, October 2010.
- [51] S. J. Tingay, R. Goeke, J. D. Bowman, D. Emrich, S. M. Ord, D. A. Mitchell, M. F. Morales, T. Boller, B. Crosse, R. B. Wayth, C. J. Lonsdale, S. Tremblay, D. Pallot, T. Colegate, A. Wicenec, N. Kudryavtseva, W. Arcus, D. Barnes, G. Bernardi, F. Briggs, S. Burns, J. D. Bunton, R. J. Cappallo, B. E. Corey, A. Deshpande, L. Desouza, B. M. Gaensler, L. J. Greenhill, P. J. Hall, B. J. Hazelton, D. Herne, J. N. Hewitt, M. Johnston-Hollitt, D. L. Kaplan, J. C. Kasper, B. B. Kincaid, R. Koenig, E. Kratzenberg, M. J. Lynch, B. Mckinley, S. R. Mcwhirter, E. Morgan, D. Oberoi, J. Pathikulangara, T. Prabu, R. A. Remillard, A. E. E. Rogers, A. Rosh, J. E. Salah, R. J. Sault, N. Udaya-Shankar, F. Schlagenhauser, K. S. Srivani, J. Stevens, R. Subrahmanyam, M. Waterson, R. L. Webster, A. R. Whitney, A. Williams, C. L. Williams, and J. S. B. Wyithe. The Murchison Widefield Array: The Square Kilometre Array Precursor at Low Radio Frequencies. *Publ. Astron. Soc. Australia*, 30:e007, January 2013.
- [52] M. P. van Haarlem, M. W. Wise, A. W. Gunst, G. Heald, J. P. McKean, J. W. T. Hessels, A. G. de Bruyn, R. Nijboer, J. Swinbank, R. Fallows, M. Brentjens, A. Nelles, R. Beck, H. Falcke, R. Fender, J. Hörandel, L. V. E. Koopmans, G. Mann, G. Miley, H. Röttgering, B. W. Stappers, R. A. M. J. Wijers, S. Zaroubi, M. van den Akker, A. Alexov, J. Anderson, K. Anderson, A. van Ardenne, M. Arts, A. Asgekar, I. M. Avruch, F. Batejat, L. Bähren, M. E. Bell, M. R.

Bell, I. van Bemmelen, P. Bennema, M. J. Bentum, G. Bernardi, P. Best, L. Bîrzan, A. Bonafede, A. J. Boonstra, R. Braun, J. Bregman, F. Breitling, R. H. van de Brink, J. Broderick, P. C. Broekema, W. N. Brouw, M. Brüggen, H. R. Butcher, W. van Cappellen, B. Ciardi, T. Coenen, J. Conway, A. Coolen, A. Corstanje, S. Damstra, O. Davies, A. T. Deller, R. J. Dettmar, G. van Diepen, K. Dijkstra, P. Donker, A. Doorduyn, J. Dromer, M. Drost, A. van Duin, J. Eislöffel, J. van Enst, C. Ferrari, W. Frieswijk, H. Gankema, M. A. Garrett, F. de Gasperin, M. Gerbers, E. de Geus, J. M. Grießmeier, T. Grit, P. Gruppen, J. P. Hamaker, T. Hassall, M. Hoeft, H. A. Holties, A. Horneffer, A. van der Horst, A. van Houwelingen, A. Huijgen, M. Iacobelli, H. Intema, N. Jackson, V. Jelic, A. de Jong, E. Juette, D. Kant, A. Karastergiou, A. Koers, H. Kollen, V. I. Kondratiev, E. Kooistra, Y. Koopman, A. Koster, M. Kuniyoshi, M. Kramer, G. Kuper, P. Lambropoulos, C. Law, J. van Leeuwen, J. Lemaitre, M. Loose, P. Maat, G. Macario, S. Markoff, J. Masters, R. A. McFadden, D. McKay-Bukowski, H. Meijering, H. Meulman, M. Mevius, E. Middelberg, R. Millenaar, J. C. A. Miller-Jones, R. N. Mohan, J. D. Mol, J. Morawietz, R. Morganti, D. D. Mulcahy, E. Mulder, H. Munk, L. Nieuwenhuis, R. van Nieuwpoort, J. E. Noordam, M. Norden, A. Noutsos, A. R. Offringa, H. Olofsson, A. Omar, E. Orrú, R. Overeem, H. Paas, M. Pandey-Pommier, V. N. Pandey, R. Pizzo, A. Polatidis, D. Rafferty, S. Rawlings, W. Reich, J. P. de Reijer, J. Reitsma, G. A. Renting, P. Riemers, E. Rol, J. W. Romein, J. Roosjen, M. Rüter, A. Scaife, K. van der Schaaf, B. Scheers, P. Schellart, A. Schoenmakers, G. Schoonderbeek, M. Serylak, A. Shulevski, J. Sluman, O. Smirnov, C. Sobey, H. Spreuw, M. Steinmetz, C. G. M. Sterks, H. J. Stiepel, K. Stuurwold, M. Tagger, Y. Tang, C. Tasse, I. Thomas, S. Thoudam, M. C. Toribio, B. van der Tol, O. Usov, M. van Veelen, A. J. van der Veen, S. ter Veen, J. P. W. Verbiest, R. Vermeulen, N. Vermaas, C. Vocks, C. Vogt, M. de Vos, E. van der Wal, R. van Weeren, H. Weggemans, P. Weltevrede, S. White, S. J. Wijnholds, T. Wilhelmsson, O. Wucknitz, S. Yatawatta, P. Zarka, A. Zensus, and J. van Zwieten. LOFAR: The LOw-Frequency ARray. *A&A*, 556:A2, August 2013.

- [53] Francisco Villaescusa-Navarro, Sigurd Naess, Shy Genel, Andrew Pontzen, Benjamin Wandelt, Lauren Anderson, Andreu Font-Ribera, Nicholas Battaglia, and David N. Spergel. Statistical Properties of Paired Fixed Fields. *ApJ*, 867(2):137, November 2018.
- [54] C. A. Watkinson and J. R. Pritchard. Distinguishing models of reionization using future radio observations of 21-cm 1-point statistics. *MNRAS*, 443(4):3090–3106, October 2014.

# Chapter 3

## Constraining the Epoch of Reionization With Highly Dispersed Fast Radio Bursts

### Addendum for thesis

This chapter explores Fast Radio Bursts (FRBs) as an indirect probe to reionization. This work was inspired by a talk given by Dr. Wenbin Lu in October 2020 at McGill University on the possible progenitors of FRBs. My colleague, Hannah Fronenberg, and I were inspired to explore how we could use the dispersion measure (DM) of FRBs to place constraints on EoR model parameters.

At the time of this work, there was minimal investigation into the use of FRBs to probe the EoR. One of the assumptions we made, which has been a main point of feedback from the community after publication, is that all FRBs are localized in redshift.

This chapter examines how the DM of FRBs might be affected by reionization. Since the DM of an FRB is proportional to the integrated column of free electrons in the IGM, we established a relationship between the mean DM and the morphology of reionization. One fascinating aspect of this approach is that measurement of the DMs have relatively few systematics when compared to 21cm cosmology. This makes FRBs an interesting probe of the EoR.

Although we do not currently have the ability to localize high  $z$  FRBs, this work should be interpreted as proof of concept. We plan on addressing the lack of redshift localization in future work.

## Abstract

The period in which hydrogen in the intergalactic medium (IGM) is ionized, known as the Epoch of Reionization (EoR), is still poorly understood. The timing and duration of the EoR is expected to be governed by the underlying astrophysics. Furthermore, most models of reionization predict a correlation between the density and ionization field. Here we consider using the mean dispersion measure (DM) of high redshift Fast Radio Bursts (FRBs) as a probe of the underlying astrophysics and morphology of the EoR. To do this, we forecast observational scenarios by building mock data sets of non-repeating FRBs between redshifts  $8 \leq z \leq 10$ . In our forecasts we assume a fiducial inside-out reionization scenario with midpoint of reionization  $z = 7.8$ , and duration (i.e. the duration between mean ionized fraction of 0.25 to 0.75)  $\Delta z = 2.0$ . It is assumed that all FRBs have accompanying spectroscopic redshift measurements. We find that samples of 100 high redshift FRBs, in the above mentioned narrow redshift range, can rule out uncorrelated reionization at 68% credibility, while larger samples,  $\geq 10^4$  FRBs, can rule out uncorrelated reionization at 95% credibility. We also find 100 high redshift FRBs can rule out scenarios where the Universe is entirely neutral at  $z = 10$  with 68% credibility. Further, with  $\geq 10^5$  FRBs, we can constrain the duration  $\Delta z$  of reionization to  $\Delta z = 2.0^{+0.5}_{-0.4}$  and the midpoint of reionization to  $z = 7.8^{+0.4}_{-0.2}$  at 95% credibility.

## 3.1 Introduction

The Epoch of Reionization (EoR) is a transitional period in our Universe's history when the neutral Hydrogen (HI) making up the intergalactic medium (IGM) was ionized by the first generation of stars and galaxies. The Cosmic Microwave Background (CMB) has given us a peek into the early

universe and measurements of quasars at  $z < 7$  teach us about early galaxy evolution. Cosmic dawn and the EoR remain the missing piece of our understanding at  $z_{\text{CMB}} > z > 7$ . Understanding this period not only provides insight into the very early universe, but also teaches us about the first generation of stars and galaxies. A number of observational probes have begun making measurements of the EoR through the 21cm line [4, 5, 10, 22, 49]. The advantage of using this line as a direct probe IGM during the EoR is that neutral hydrogen is abundant in the early Universe and that, by measuring the redshifting of this photon, we can trace primordial hydrogen along the line of sight. For a comprehensive review of 21cm cosmology, the reader is encouraged to read [43], [17], [55], [31] and [29].

21cm cosmology, however, does not come without its challenges. Making a detection of the 21 cm line during the EoR is exceptionally difficult since the frequency of the line is redshifted into the 50-300 MHz range [29]. Systematics, radio frequency interference (RFI), galactic synchrotron emission, and radio bright sources have made the 21 cm signal difficult to measure, and thus limit our ability to constrain the astrophysics during this epoch [30]. As a result, many look to other probes of the EoR.

Fast Radio Bursts (FRBs) are a class of bright, millisecond duration, radio transients that have been detected at frequencies ranging from 110 MHz to 1.5 GHz and whose dispersion measures (DMs) lie between 110 and 2600 pc cm<sup>-3</sup> [50, 53]. Thanks to current and upcoming broad-band wide-field-of-view instruments, such as the Canadian hydrogen Intensity Mapping Experiment (CHIME; [1]), the hydrogen Intensity and Real-time Analysis eXperiment (HIRAX; [45]), Five-hundred metre Aperture Spherical Telescope (FAST; [44]), Australian Square Kilometer Array Pathfinder (ASKAP; [21]) and the Square Kilometer Array (SKA; [11]), we have seen a large increase in the number of FRBs detected. It is estimated that when SKA is online, its event detection rate may be as high as  $\sim 1000$  FRBs sky<sup>-1</sup> day<sup>-1</sup> [14].

Since their discovery by [32], the number of FRBs detected has increased tremendously. CHIME alone has detected over 1000 bursts since 2018. While one source has now been localized within the Milky Way [7], the vast majority of FRBs remain extragalactic sources and can thus probe out

to cosmological distances [12, 23]. Many questions remain about the astrophysical origin of these bursts as well as their intrinsic distribution out to high DM [26, 33, 52].

While the progenitor of FRBs remains unknown, the DMs of these bursts are, on the contrary, well understood and could thus prove yet another direct probe of the IGM during the EoR. The DM of an FRB is defined as the integrated column density of free electrons along the line of sight from source to observer. As the FRB travels through the IGM, it experiences a frequency dependent time delay,  $\Delta t = e^2/(2\pi m_e c)(v_0^2 v_1^2)DM$ , where  $v_1$  and  $v_2$  represent the high and low frequency boundaries of the pulse and DM is given by

$$DM(\mathbf{x}, z) = \int \frac{n_e(\mathbf{x}, z)}{1+z} dl, \quad (3.1)$$

where  $dl$  is the line element along the light of sight,  $n_e(\mathbf{x}, z)$  is the free electron density at comoving position  $\mathbf{x}$  and redshift  $z$ . Measuring the DM of an FRB at redshift  $z$  can therefore probe the integrated number density of free electrons along the line of sight in the IGM. To evaluate 3.1 for each reionization scenario, we express the line element  $dl$  in terms of the Hubble parameter

$$dl = c dt = \frac{-cdz}{H(z)(1+z)} \quad (3.2)$$

where  $H(z)$  is given in terms of the  $\Lambda$ CDM parameters through

$$H(z) = H_0 \sqrt{\Omega_m(1+z)^3 + \Omega_\Lambda} \equiv H_0 E(z). \quad (3.3)$$

The free electron number density in the IGM can be written as a function of the ionization and density field,

$$n_e = \frac{f_H f_{\text{IGM}} \Omega_m \rho_0(z)}{m_H} (1+z)^3 (1 + \delta(\mathbf{x}, z)) x_{\text{HII}}(\mathbf{x}, z), \quad (3.4)$$

where  $f_H$  is the fraction of baryonic matter that is hydrogen,  $f_{\text{IGM}}$  is the fraction of hydrogen that is found in the IGM,  $m_H$  is the mass of hydrogen and  $\rho_0$  is the mean density of the IGM at redshift  $z$ .

The dispersion measure of FRBs detected after the EoR can be approximated to be  $x_{\text{HII}}(\mathbf{x}) = 1$ , i.e. the IGM is entirely ionized. Note that helium reionization does increase the number density

of free electrons at low redshift ( $z \sim 2$ ), however this is independent of the reionization model. Therefore, we do not take this into account in our models for Equation 3.1. For interested readers, there is a growing body of literature on constraining helium reionization using the DMs of FRBs [3, 6, 27, 64]. Unlike at low redshift, the ionization field  $x_{\text{HII}}$  during the Epoch of Reionization is patchy, composed of regions of ionized bubbles and neutral regions, whose placements and evolution depend highly on the astrophysics governing reionization. In this case, the number density of electrons  $n_e$  will depend on the state of the ionization field. High redshift FRBs detected during the Epoch of Reionization will therefore be sensitive to the astrophysics that have imprinted itself onto  $x_{\text{HII}}$ .

Furthermore, referring to Equation 3.4, the number density of free electrons is dependent on the product of the density and ionization field  $x_{\text{HII}}\delta$ . The method in which the ionization field  $x_{\text{HII}}$  maps to the underlying density field  $\delta$  is known as the density-ionization correlation, which affects the morphology of the EoR. The cross term in Equation 3.4 contains information of the density-ionisation correlation, which affects the observed DM of an FRB. Most EoR models predict morphologies where the ionized regions are not random with respect to the underlying density field. Instead, there are two extreme ways in which the ionization field couples to the density field. The density field can be positively correlated to the ionization field. In this scenario, overdense regions correspond to high ionization fraction. In this model, ionizing sources ionize their immediate surroundings before ionizing the lower density regions of the IGM. We say that reionization happens ‘inside-out’. The second extreme model is the scenario where the underlying density field  $\delta$  is negatively correlated with the ionization field  $x_{\text{HII}}$ . In this scenario, the ionizing sources first ionize the low density regions before ionizing the high density regions. We say that reionization happens ‘outside-in’. In this model, the high density regions in  $\delta$  correspond to regions of low ionization fraction in  $x_{\text{HII}}$ . This model usually requires the recombination of hydrogen atoms in high density regions to dominate the effects of UV ionization [8, 42, 61]. Outside-in morphologies can also be achieved by having reionization driven by x-ray photons, which can more easily “leak” into the underdense regions of the IGM [38, 41]. It is also possible for reionization to unfold as a

combination of both inside-out and outside-in, in which case, the correlations between  $\delta$  and  $x_{\text{HII}}$  are statistical combination of the inside-out and outside-in models [16, 36].

The way in which the mean DM depends on the broad timeline of the reionization history has been previously studied [2, 19, 34, 63]. Most recently, [19] show that one year’s worth of observing with SKA phase 2 can reveal our cosmic reionization history, and [2] show that both DM and the differential FRB source count distribution prove useful probes of reionization even with limited redshift information. In this paper we build on the techniques outlined by these authors by performing a study of how the morphology, astrophysics and evolution of the EoR affect the mean DM of high redshift FRBs. We use a set of astrophysical and morphological parameters to bracket the physical range of EoR scenarios and study how DM– $z$  probability distributions and the mean DM of FRBs at each redshift depend on these parameters. We then forecast the types of constraints that we can place on the EoR using measurements of the DMs of high redshift FRBs. Since FRBs at high redshift have yet to be observed, we create a mock sample of highly dispersed FRBs under a fiducial reionization model and forecast the type of constraints one can place on the astrophysics and morphology of the EoR given such a measurement. We perform this forecast with  $10^2$ ,  $10^4$ , and  $10^5$  high DM samples.

This paper is structured as follows. In Section 4.2 we describe the astrophysical and morphological parameters used in our simulation to bracket the physical range of EoR scenarios. In Section 3.3 we discuss how the mean DM and the DM probability distributions of high redshift FRBs depend on these parameters. In Section 4.5, we describe our fiducial reionization model, the mock FRB measurements made for this reionization scenario. We forecast the constraints that can be placed on the EoR parameters using such a measurement and in Section 3.5 we present the results. We summarize our conclusions in Section 6.7. Throughout this work we set the  $\Lambda$ CDM parameters to  $\sigma_8 = 0.81$ ,  $\Omega_m = 0.31$ ,  $\Omega_b = 0.048$ ,  $h = 0.68$ ,  $n_s = 0.9603$  [51].

**Table 3.1:** Summary of Reionization Parameters and FRB Observables

Symbol	Parameter Name	Description/Definition
$z_{\text{EoR}}$	Reionization Redshift	The redshift indicating the onset of reionization.
$\beta$	Morphological Parameter	Determines the correlation between $\delta$ and $x_{\text{HII}}$
$M_{\text{turn}}$	The turnover mass	Halo mass scale in which star formation is efficient
$\zeta$	Ionizing Efficiency	Number of ionizing photons released per stellar baryon
$R_{\text{mfp}}$	Radius of The Mean Free Path	Maximize size of the ionized regions
$\text{DM}(\mathbf{x}, z)$	Dispersion Measure	DM of individual FRB at redshift $z$ along a single line of sight.
$\overline{\text{DM}}(z)$	Mean Dispersion Measure	Mean DM of a collection of FRBs observed at redshift $z$

## 3.2 Simulation

To generate density and ionization boxes representative of different EoR models we use 21cmFAST package [39]. Density fields are obtained through the Zeldovich approximation while ionization and halo boxes implement the excursion set formalism of [18]. For further details about how 21cmFAST generates reionization models see [39]. Throughout this paper we use high resolution boxes of  $800^3$  voxels corresponding to a comoving side length of 300 Mpc and coarser boxes of  $200^3$  voxels corresponding to the same comoving side length. A voxel thus represents the smallest volume unit of our pixelized simulation cube. Throughout our simulations we use the cosmological parameters described in Section 3.1.

### 3.2.1 EoR Parameters

We use 21cmFAST to generate different EoR scenarios by varying a number of adjustable parameters which encapsulate variations in the detailed astrophysics of reionization. We bracket the physical range of EoR scenarios by adjusting the parameters  $M_{\text{turn}}$ ,  $R_{\text{mfp}}$ , and  $\zeta$ . Physically, the turnover mass,  $M_{\text{turn}}$ , determines the mass of a halo in which star formation is efficient. Values of  $M_{\text{turn}} \simeq 5 \times 10^8 M_{\odot}$  correspond to a virial temperature of  $T_{\text{vir}} \simeq 10^4$ . Values below  $M_{\text{turn}}$  have exponential suppression in star formation. Roughly, this sets the mass scale for the ionizing sources. The unitless astrophysical parameter  $\zeta$ , determines the ionizing efficiency of the sources. This parameter is an amalgamation of other parameters which describe the small scale astrophysics of the UV sources. A large value

of  $\zeta$  will imply more ionizing photons per stellar baryon, while a smaller ionizing efficiency will entail less ionizing photons are emitted for each ionizing source. The cutoff-radius  $R_{\text{mfp}}$  sets the maximum size of the ionized bubbles [57]. Variation of these parameters effect the timing and duration of reionization, and have been studied in previous works [13,25,28,48,54]. For this work, we use these parameters to generate a wide variety of EoR models that bracket physical scenarios. These parameters operate under an inside-out reionization formalism in which the density field  $\delta$  is correlated with the ionization field  $x_{\text{HII}}$  and therefore do not capture the different  $\delta$   $x_{\text{HII}}$  correlations indicative of different EoR morphologies. In the next Section we introduce a parametrization that extends the physical scenarios bracketed by the astrophysical parameters to EoR morphologies of arbitrary ionization-density correlations.

### 3.2.2 Morphological Parametrization of the EoR

To simulate EoR scenarios where the density field and ionization field are correlated by some arbitrary amount, we use the  $\beta$  parametrization introduced in [47]. This parameter continuously tracks the correlation between  $x_{\text{HII}}\delta$ . We briefly describe this parametrization here. The  $\beta$  parameter has bounds  $-1 \leq \beta \leq 1$  and controls the amount of correlation between  $x_{\text{HII}}$  and  $\delta$ . The sign of  $\beta$  indicates the overall sign of the correlation between  $x_{\text{HII}}$  and  $\delta$ . Positive values of  $\beta$ , indicate a positive correlation between density and ionization fields, and so overdense regions in  $\delta$  couple to regions of high ionization fraction in  $x_{\text{HII}}$ . This sign of correlation is indicative of inside-out reionization scenarios, where the overdense regions of the IGM are first to be ionized. Conversely, negative signs of  $\beta$  indicate an overall negative correlation between ionization field and density field so that overdense regions in  $\delta$  correspond to regions of low ionized fraction of hydrogen. This is indicative of outside-in reionization, where overdense regions of the IGM are last to be ionized. The magnitude,  $|\beta|$ , indicates how strong that correlation sign is between ionization and density fields. A value of  $\beta = 0$  indicates a random placement of the ionized regions, in which case there is no correlation between ionization and density fields. As we increase  $\beta$  from 0 to 1, the relative likelihood of finding overdense regions of  $\delta$  corresponding to ionized regions in  $x_{\text{HII}}$  increases, until finally at  $\beta$  of 1, all overdense regions in  $\delta$  always correspond to regions of

**Table 3.2:** Lexicon for physical models and their respective correlations

$\beta$	Correlations between $x_{\text{HII}} \delta$	Physical Model
1	Correlated	Inside-out
$1 < \beta < 0$	Increasingly correlated	Mostly inside-out
0	Uncorrelated	Random
$0 > \beta > -1$	Increasingly anti-correlated	Mostly outside-in
-1	Anti-correlated	Outside-in

ionized hydrogen. Similarly, as we decrease  $\beta$  from 0 to  $-1$ , the relative likelihood of finding overdense regions of  $\delta$  corresponding to ionized regions in  $x_{\text{HII}}$  increases until at  $\beta = -1$ , all overdense regions in  $\delta$  correspond to regions of low  $x_{\text{HII}}$ . The intermediate, non-extreme values of  $\beta$ , i.e.  $-1 < \beta < 1$  indicate reionization scenarios that contain the statistics of both inside-out and outside-in. Figure 3.1 demonstrates the affect of inside-out, or outside-in reionization, on the free electron number density  $n_e$  in the IGM. For a more detailed discussion on this parametrization, the reader is encouraged to read [47]. Table 4.1 summarizes the terminology used to describe the type of correlation as well as the model to which it pertains. The  $\beta$  parameter encodes only the correlation statistics between density and ionization fields and is treated as independent from the other EoR parameters in our models. This makes  $\beta$  phenomenological compared to the other parameters. Although  $\beta$  is a not a physically derived quantity, it correctly predicts the statistics for different density-ionization correlations. In the following Section we shall see that our models only use the statistics of DMs, and so our results do not depend on the nature of  $\beta$ .

### 3.2.3 Dispersion Measure

The observed dispersion in Equation 3.1 is sensitive to all sources of free electrons encountered by the radio burst as the electromagnetic wave travels from source to observer. This includes the free electrons found within the host galaxy as the FRB leaves the source, as well as the free electrons encountered in the Milky Way (MW) as the FRB arrives to the observer. The FRB also has exposure

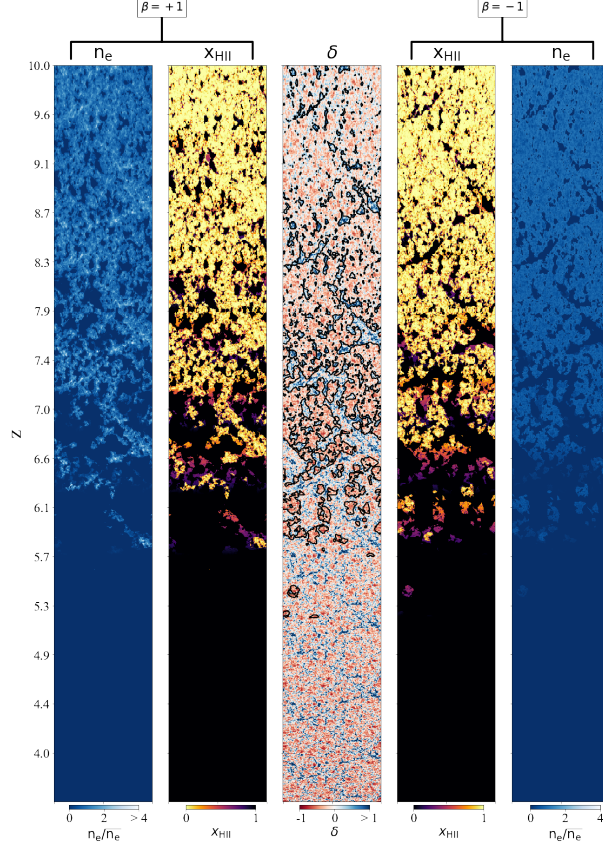


**Figure 3.1:** From the center of the Figure , outward: Lightcones of the density field  $\delta$ , ionization fraction  $x_{\text{HII}}$  and free electron field  $n_e$  for the case of inside-out reionization (left three boxes) and outside-in reionization (right three boxes). Inside-out reionization (left) leads to a higher free electron number density  $n_e$  in the ionized bubbles since the density field (center) couples to the ionized regions in  $x_{\text{HII}}$  compared to outside-in models (right) where the underdense regions in  $\delta$  couple to the ionized regions in  $x_{\text{HII}}$ .

to the free electrons found in the circumgalactic medium (CGM) and IGM. We split Equation 3.1 into its respective components

$$\text{DM}_{\text{obs}}(\mathbf{x}, z) = \text{DM}_{\text{host}} + \text{DM}_{\text{MW}} + \text{DM}_{\text{CGM}}(\mathbf{x}, z) + \text{DM}_{\text{IGM}}(\mathbf{x}, z). \quad (3.5)$$

The dispersion  $\text{DM}_{\text{IGM}}(\mathbf{x}, z)$  is due to the free electrons found in the IGM between the FRB source and the observer. This is the DM attributed to cosmic reionization and is the DM of interest in order study the evolution of  $x_{\text{HII}}$ . The DM attributed to the host galaxy, MW and CGM are subject to

uncertainties surrounding the gas dynamics within these regimes, and as a result make them difficult to model. We treat them as contaminants in our measurement of the contributions of  $\overline{DM}_{\text{IGM}}$  to  $\overline{DM}_{\text{obs}}$ . The DM contribution due to the interstellar medium (ISM) of intervening galaxies have also been shown to be negligible [56]. The inhomogeneity of  $x_{\text{HII}}$ ,  $\delta$  and the gas dynamics as a function of position  $\mathbf{x}$  make it unreasonable to draw conclusions on the state of the IGM through a single line of sight. We instead compute the mean value of  $\overline{DM}_{\text{obs}}$  due to all sightlines. This removes single line of sight fluctuations in  $\delta$  and  $x_{\text{HII}}$  as well as averages over the contributions due to the CGM,

$$\overline{DM}_{\text{obs}} = \overline{DM}_{\text{host}} + \overline{DM}_{\text{MW}} + \overline{DM}_{\text{CGM}} + \overline{DM}_{\text{IGM}}. \quad (3.6)$$

Studies such as [24] model the DM contribution of the Milky Way, which is something which may be possible to accurately account for in the future. Other studies have found that the photon incurs an average DM of  $\overline{DM}_{\text{MW}} \sim 200 \text{pc cm}^{-2}$  when leaving the MW and host galaxy [58, 59]. We treat the average contribution of the MW and host galaxy to  $\overline{DM}_{\text{obs}}$  as an offset  $\sim 200 \text{pc cm}^{-2}$ .

$$\overline{DM}_{\text{obs}} - (\overline{DM}_{\text{host}} + \overline{DM}_{\text{MW}}) = \overline{DM}_{\text{CGM}} + \overline{DM}_{\text{IGM}}. \quad (3.7)$$

We assume high redshift FRBs have  $\overline{DM}_{\text{obs}}$  dominated by the IGM, we neglect the contribution due to the CGM. The remaining fluctuations in DM are attributed to cosmic reionization. Henceforth we refer to  $\overline{DM}_{\text{IGM}}$  as  $\overline{DM}_{\text{obs}}$ . This model isn't meant to be overly realistic, we intend to capture first order effects due to  $\overline{DM}_{\text{IGM}}$ . In order for precise measurements to be made of the impact that the EoR has  $\overline{DM}_{\text{obs}}$ , a method to subtract out the effects due to the CGM needs to be studied. We leave such a study to future work. The mean DM of a high redshift FRB observed at redshift  $z$  due to free electrons in the IGM is then evaluated using Equation 3.1 as

$$\overline{DM}_{\text{obs}}(z) = - \int cdz \frac{f_{\text{H}} f_{\text{IGM}} \Omega_m \rho_0 (1+z)}{m_{\text{H}} H_0 E(z)} \left( \bar{x}_{\text{HII}}(z) + \overline{\delta x_{\text{HII}}}(z) \right). \quad (3.8)$$

The  $\overline{DM}_{\text{obs}}$  of high redshift FRBs will be proportional to the mean ionization fraction  $\bar{x}_{\text{HII}}$  of the IGM as well as to the mean product  $\overline{x_{\text{HII}} \delta}$ . This cross term captures the density-ionization

correlation of the EoR which describes how the underlying density field  $\delta$  couples to the ionization field  $x_{\text{HII}}$ . The  $\beta$  parameter quantifies the different possibilities of this correlation. The astrophysics of the EoR, affect both of these terms. Since the astrophysics set the size and morphological features of the ionization field  $x_{\text{HII}}$ , they too have consequences for  $\overline{\text{DM}}$ . In addition, the astrophysics of the EoR determine the onset and duration of the EoR, i.e. they determine the mean ionization fraction  $\bar{x}_{\text{HII}}$  at each redshift  $z$ . Previous studies have looked at how broad modeling the mean ionization fraction  $\overline{x_{\text{HII}}\delta}$  to redshift affects the observed DM of high redshift FRBs, i.e. the  $\overline{x_{\text{HII}}\delta}$  term in Equation 3.8 [63]. Here we build on that by including both terms and studying how the detailed astrophysics as well as density-ionization correlation affect both terms. For readers who are less familiar with the parameters that have been discussed, they are summarized in Table 3.1 for easy reference. In the following Sections, we study how the astrophysical parameters, and the  $\beta$  parameter, which parameterizes the density ionization correlation, affect  $\overline{\text{DM}}_{\text{obs}}$ .

In the following section, we evaluate Equation 3.8 by simulating  $10^5$  sightlines, computing the individual DM of each sightline, and by averaging the DMs. This is done for each reionization model.

### 3.3 Models

Equation 3.8, states that  $\overline{\text{DM}}_{\text{IGM}}$  of an FRB depends on the cumulative of both the mean ionization fraction,  $\bar{x}_{\text{HII}}$ , and the density-ionization correlation,  $\overline{x_{\text{HII}}\delta}$ , along the line of sight. If  $z_{\text{EoR}}$  is the redshift in which the IGM becomes increasingly neutral, then  $\bar{x}_{\text{HII}} = 1$  for all  $z < z_{\text{EoR}}$  and so the relationship between  $\overline{\text{DM}}_{\text{IGM}}$  and  $z$  is linear up until the onset of reionization [9]. The linear relationship breaks down at  $z_{\text{EoR}}$  since  $\bar{x}_{\text{HII}}$  decreases rapidly due to the increasingly neutral IGM. As a result, the EoR produces a flattening of  $\overline{\text{DM}}$  for high redshift FRBs. The shape and positioning of this flattening is highly dependent on the onset, duration and morphology of reionization. In this Section we use the astrophysical and correlation parameters to study how EoR models affect the DM of FRBs observed in the EoR. We consider the distribution of DM at each  $z$  of the individual DM sightlines as a function of the astrophysics and morphology of the EoR. In Section 3.5, we

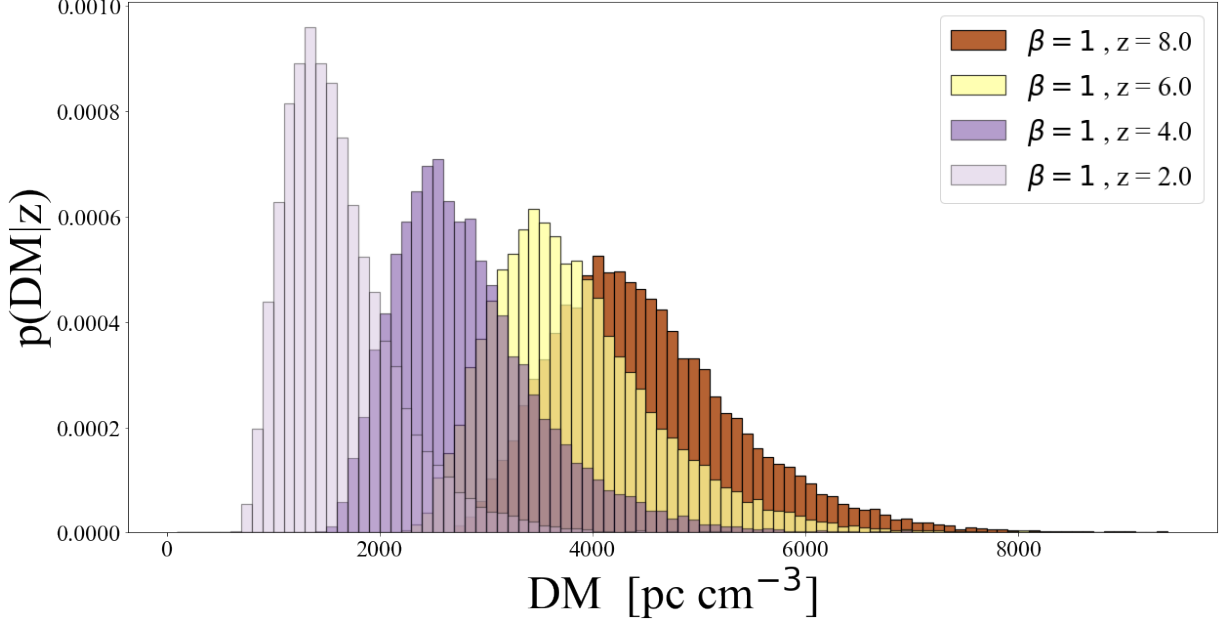


**Figure 3.2:** Redshift evolution of the DM probability distributions for our fiducial reionization scenario  $\beta = 1$ ,  $\zeta = 25$ ,  $M_{\text{turn}} = 5 \times 10^8 M_{\odot}$  and  $R_{\text{mfp}} = 30 \text{Mpc}$ . At higher redshift the relative probability of high DM sightlines increases.

forecast that the constraints that can be placed on these parameters through measurement of high redshift FRBs.

### 3.3.1 DM Distributions

We consider the distribution of the individual DM sightlines as a function of the astrophysics and morphology of the EoR. FRBs observed at low  $z$  are more likely to have low DM sightlines due to less chance of interactions with free electrons in the IGM. From Figure 3.2 we see that the resulting DM probability distribution is highly non-Gaussian and skewed to low DM. Note that the contaminants  $\overline{\text{DM}}_{\text{CGM}}$  and  $\overline{\text{DM}}_{\text{ISM}}$  can produce high DM fluctuations, even at low redshift. Removal of these contaminated sightlines are required in order to make precise deductions about the state of the IGM using FRB DM statistics. This might be especially difficult to do for high redshift FRBs since FRBs observed at high redshift are more likely to interact with free electrons from the IGM and so large DM sightlines become more likely (see Figure 3.2). At higher redshifts, **the skewness of the distribution functions are noticeably reduced.** Previous studies such as [62],

use the variance,  $\sigma^2 = \langle (\text{DM} - \overline{\text{DM}})^2 \rangle$ , of the DM distributions to estimate the maximum size of the ionized regions at each  $z$ . Since the maximum size of the ionized regions depends on the astrophysical parameters, our approach is complimentary. The astrophysics driving the EoR will determine the evolution of the  $\text{DM}(z)$  probability distributions. For example, scenarios with larger  $\zeta$  or smaller  $M_{\text{turn}}$  tend to have DM distributions skewed to higher DM since reionization begins early, which increases the relative likelihood of finding high DM sightlines by increasing the likelihood of interaction with free electrons. Meanwhile, scenarios where the EoR unfolds as inside-out, tend to have high density regions in  $\delta$  couple to regions of high fraction of ionized hydrogen, i.e. the product  $\overline{x_{\text{HII}}\delta} \sim n_e$  is larger than the corresponding outside-in scenario where the high density regions couple to low fraction of ionized hydrogen. In this scenario, the free electron regions tend to be denser in inside-out models than the corresponding outside-in models. As a result, scenarios where reionization unfolds with  $\beta > 0$  increases the likelihood of high DM sightlines. This is reflected in the  $\text{DM}(z)$  distributions in Figure 3.3 where there is a larger portion of distribution in the high DM portion of the distribution compared to outside-in maps where the distribution is skewed to lower DMs.

These parameters influence the shape of the DM distribution as well as their evolution in redshift. Since  $\overline{\text{DM}}$  is derived from these DM distributions, then the underlying astrophysics and morphology of the EoR can be detected directly from  $\overline{\text{DM}}$ . In the following Sections, we build our intuition on how the astrophysics and morphology of the EoR affect  $\overline{\text{DM}}$ .

### 3.3.2 Astrophysical Signature on $\overline{\text{DM}}$

Local fluctuations in  $n_e$  make it difficult to deduce the astrophysics from individual sightlines. Instead we average over all sightlines to remove these fluctuations. In doing so, we can predict the signature of the astrophysical parameters on  $\overline{\text{DM}}$  in Equation 3.8. Since the presence of neutral hydrogen in the IGM causes a flattening of the  $\overline{\text{DM}}$  curve at the onset of neutral hydrogen, then the astrophysical parameters, which determine the timing of this flattening, can be deduced from  $\overline{\text{DM}}$ . For example, the ionizing efficiency  $\zeta$  increases the output of UV photons from the ionizing sources, which for larger values of  $\zeta$ , results in shifting the onset of reionization to higher redshifts.

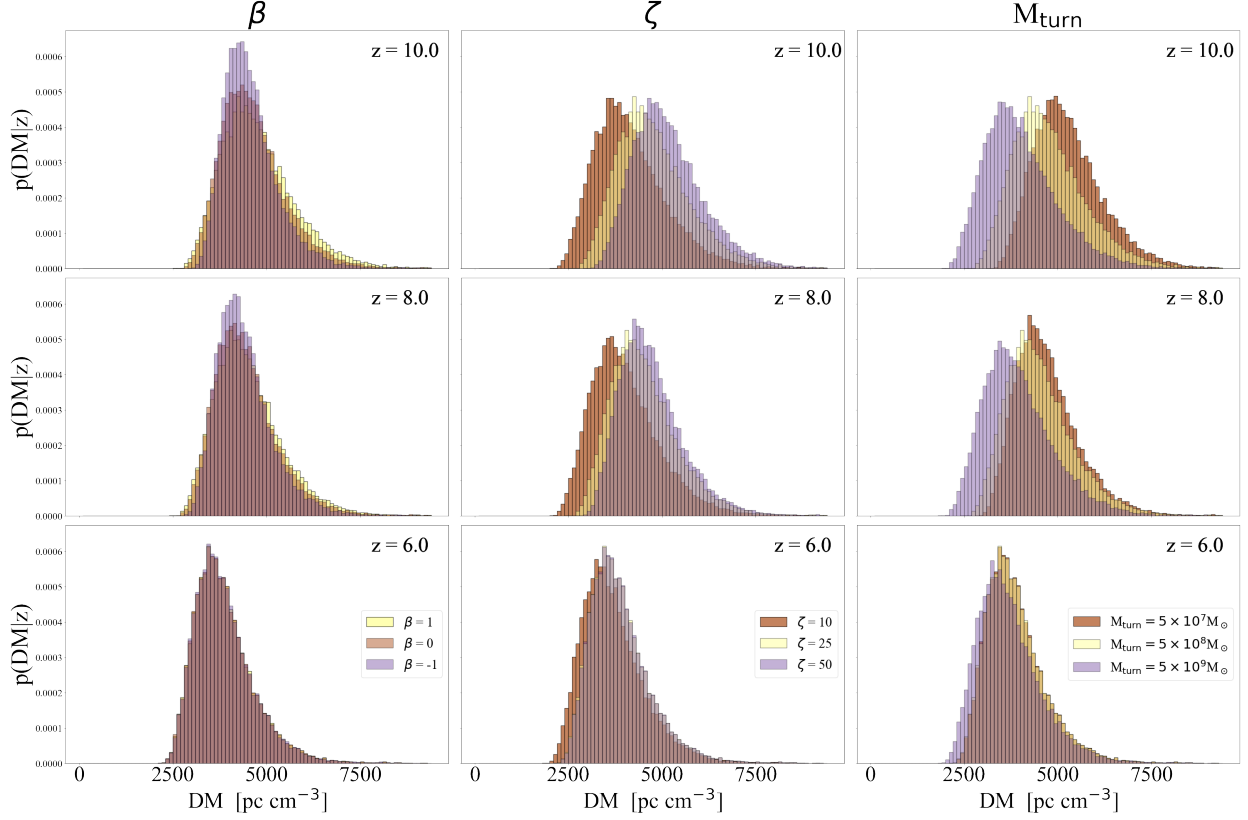


**Figure 3.3:** Evolution of the individual sightline DM probability distributions for a variety of reionization scenarios encapsulated by the density-ionization parameter  $\beta$ , ionizing efficiency  $\zeta$  and mass scale of the ionizing sources  $M_{\text{turn}}$ . Notice how the different reionization scenarios begin to distinguish themselves at higher redshifts. In each panel, the gold distribution corresponds to the fiducial reionization scenario of  $\beta = 1$ ,  $\zeta = 25$ ,  $M_{\text{turn}} = 5 \times 10^8 M_{\odot}$  and  $R_{\text{mfp}} = 30\text{Mpc}$ .

In this scenario, the IGM is ionized earlier and the flattening of the  $\overline{\text{DM}}$  curve occurs at larger  $z$ . Conversely, decreasing the ionizing efficiency of the sources shifts the flattening of the  $\overline{\text{DM}}$  curve to lower redshifts. Therefore, if we study the dependence of  $\overline{\text{DM}}$  on  $\zeta$  at fixed  $z$  (within the EoR), increasing the ionizing efficiency will increase the mean DM of the FRBs at that redshift. We find a similar dependence for  $\overline{\text{DM}}$  on  $M_{\text{turn}}$ . This is the mass scale for a source to begin efficiently producing UV photons which similarly alters the onset of reionization. Lower values of  $M_{\text{turn}}$  allow the EoR to start early, which shifts the flattening of  $\overline{\text{DM}}$  to higher redshifts, while larger values of  $M_{\odot}$ , delays reionization, pushing the flattening of  $\overline{\text{DM}}$  to lower redshifts. We find that  $\overline{\text{DM}}$  is less

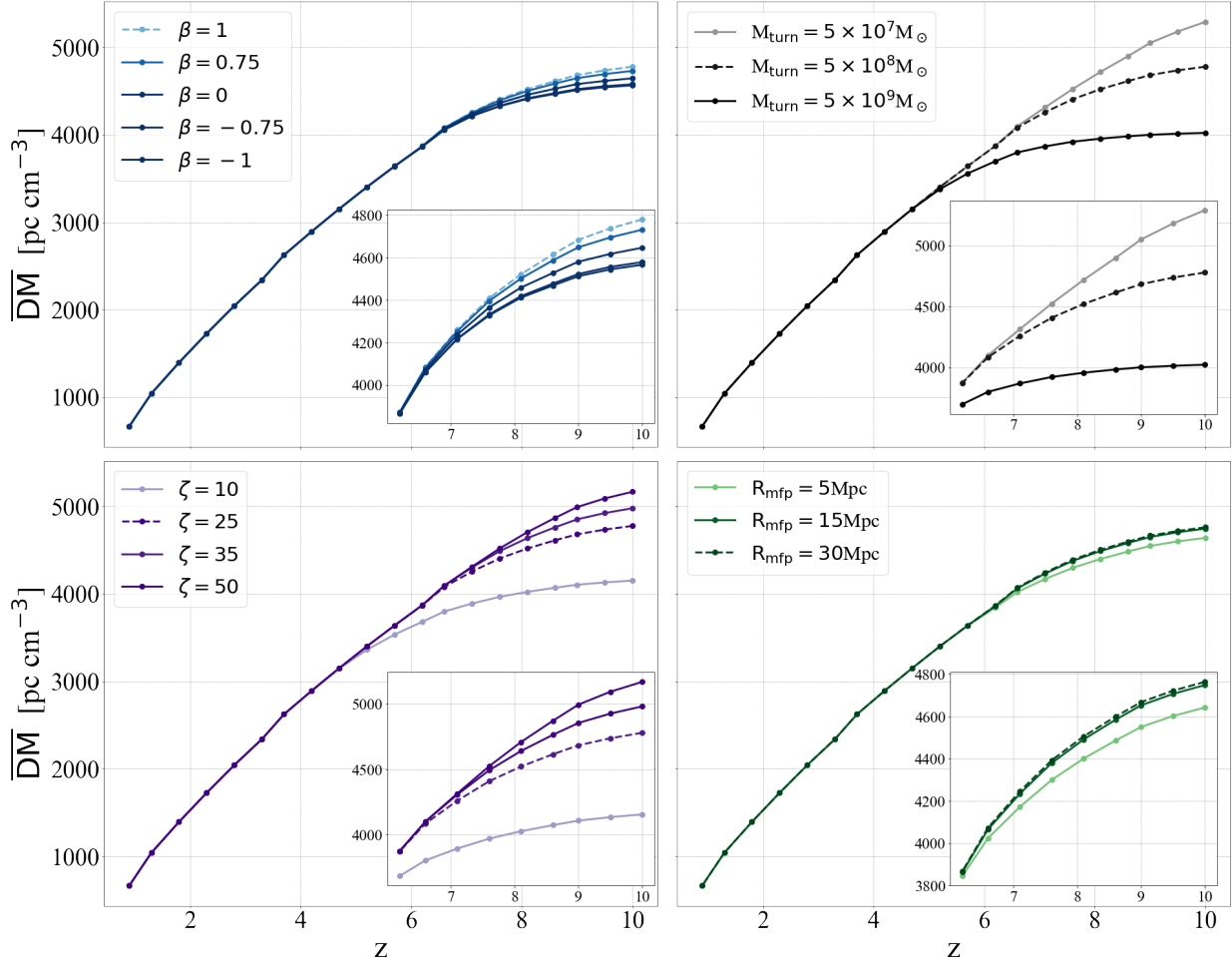


**Figure 3.4:**  $\overline{DM}$  for a variety of density-ionization correlations  $\beta$  (upper left), mass scale of the ionizing sources  $M_{\text{turn}}$  (upper right), ionizing efficiency  $\zeta$  (lower left), and mean free path  $R_{\text{mfp}}$  of the ionizing photons. Notice how high ionizing efficiency of the sources and smaller masses of the ionizing sources lead to an early onset reionization, and so an increase in  $\overline{DM}$  at that redshift. Inside-out reionization models  $\beta > 0$ , lead to an increase in  $\overline{DM}$ , since the free electron number density in ionized regions is greater than the corresponding ionized region in outside-in models  $\beta < 0$ . In each panel the dotted curve corresponds to same reionization scenario  $\beta = 1$ ,  $\zeta = 25$ ,  $M_{\text{turn}} = 5 \times 10^8 M_\odot$  and  $R_{\text{mfp}} = 30 \text{ Mpc}$ . We use this fiducial reionization scenario in our forecasts in Section 4.5.

sensitive to  $R_{\text{mfp}}$  as compared to the other EoR parameters. Once  $R_{\text{mfp}}$  is increased beyond the size that is physically possible at given  $z$ ,  $\overline{\text{DM}}$  loses all sensitivity to the parameter.

In general, these astrophysical parameters determine the mean ionization fraction  $\bar{x}_{\text{HII}}$  at each redshift  $z$ , which  $\overline{\text{DM}}$  depends on. One could approach the study of  $\overline{\text{DM}}$  on  $\bar{x}_{\text{HII}}$  by adopting a model for the evolution of  $\bar{x}_{\text{HII}}$  on  $z$  without invoking the dependence of astrophysical parameters. However, these parameters can also have a secondary effect on  $\overline{\text{DM}}$  through the cross term in Equation 3.8. For example, if the Universe reionizes with turnover masses  $M_{\text{turn}} \simeq 10^{10}M_{\odot}$ , then the size of the ionized regions are larger compared to a scenario with smaller turnover which increases the cross term in Equation 3.8. Physically this means that there are more free electrons for the FRBs to interact with. Increasing the maximum size of the ionized regions  $R_{\text{mfp}}$  will maximize the interaction between FRBs and free electrons for given EoR model with fixed  $\zeta$  and  $M_{\odot}$ . This maximises  $\overline{\text{DM}}$ .

The sensitivity of  $\overline{\text{DM}}$  to  $\zeta$ ,  $M_{\text{turn}}$  and  $R_{\text{mfp}}$  increases as we observe to FRBs at higher redshifts. This is due to the FRBs having interacted with the ionization history of the universe for longer and so Equation 3.8 carries more information about the EoR. Conversely,  $\overline{\text{DM}}$  loses all sensitivity to the astrophysics of the EoR as the entire Universe is reionized, referring to Figures 3.4, all models converge at  $z = 6$  which in our models correspond to an entirely ionized IGM.

### 3.3.3 Morphological Signature on $\overline{\text{DM}}$

From Equation 3.8, the mean DM of high redshift FRBs is sensitive to the density-ionization product  $\delta x_{\text{HII}}$ . The method in which  $x_{\text{HII}}$  couples to the underlying density field  $\delta$ , will have consequences for the  $\overline{\text{DM}}$ . Inside-out scenarios, i.e. scenarios where  $\beta > 0$  (positive correlation between  $\delta$  and  $x_{\text{HII}}$ ), high density regions couple to high ionized fractions in  $x_{\text{HII}}$ . This results in the ionized regions being denser in free electrons, leading to an increase in  $\overline{\text{DM}}$  compared to other morphologies. For example, the outside-in scenario, where  $\delta$  and  $x_{\text{HII}}$  are negatively correlated ( $\beta < 0$ ), the underdense regions in  $\delta$  correspond to high fractions of ionized hydrogen. As a result, the free electron density within the ionized regions are comparatively smaller. Referring to Figure 3.4, we see that inside-out morphologies lead to an increase in the mean DM of high

redshift FRBs as compared to outside-in models. Intermediate values of  $\beta$  can be interpreted as follows; as  $\beta$  is increased from the uncorrelated scenario,  $\beta = 0$ , (where the ionized regions are random with respect to  $\delta$ ) to  $\beta = 1$ , the high density regions in  $\delta$  becoming increasingly likely to couple to ionized regions in  $x_{\text{HII}}$ . The mean  $n_e$  within bubbles monotonically increases until  $\beta = 1$  where all high density regions correspond to ionized bubbles and  $\overline{\text{DM}}$  is maximized with respect to  $\beta$ . Conversely, as we decrease  $\beta$  from  $\beta = 0$  to  $\beta = -1$ , the high density regions increasingly couple to regions of low ionized fraction in  $x_{\text{HII}}$  which monotonically decreases the mean  $n_e$  of the ionized regions. As a result, the product  $n_e \sim \delta x_{\text{HII}}$  is decreased, which leads to a decrease in the mean DM of these models. As a result, inside-out scenarios receive a boost in average DM due to the increase of  $\bar{n}_e$  compared to outside-in driven models. The morphological signature on  $\overline{\text{DM}}$  is different than the astrophysical parameters since the morphology directly influences the mean density of free electrons,  $n_e$  within the ionized bubbles without changing the timing of reionization. The contrast in  $\overline{\text{DM}}$  between the extreme morphologies is greatest for FRBs observed at highest redshift. The longer the exposure of the FRB to the ionization history, the more sensitive  $\overline{\text{DM}}$  will be to the morphology. Conversely, as we observe FRBs at lower redshifts, there hasn't been enough exposure to the EoR morphology to distinguish between different  $\beta$  models. Therefore  $\overline{\text{DM}}$  loses all sensitivity to  $\beta$  as  $\bar{x}_{\text{HII}} \rightarrow 1$ . In Section 3.5, we determine the number of FRBs required to make a measurement of  $\overline{\text{DM}}$  precise enough to place constraints on  $\beta$  as well as the astrophysical parameters.

In the following Section, we use generate mock data by sampling the fiducial DM distributions at each redshift given our choice of fiducial EoR and morphological parameters. In Section 3.4.3, we forecast the type of constraints that can be placed on  $\beta$  as well as the remaining EoR parameters through measurement of  $\overline{\text{DM}}$ .

## 3.4 Forecasts

In this Section we use the formalism of Section 3.3 to forecast the constraints that can be placed on the EoR through measurement of high redshift FRB DMs. Since high redshift FRBs have not yet been

detected, we simulate a mock observation of high DM FRBs under a fiducial reionization scenario. It should be noted that it is assumed that all generated FRBs are observed with accompanied redshift localization where we take the uncertainty on the redshift,  $\sigma_z = 0$ . This may seem an ambitious assumption, but [60] notes that with a mid- to large-size optical survey, it should be feasible to obtain about 10 redshifts for host galaxies per night. In this Section, we outline our model for generating this mock observation as well as discuss our fiducial reionization scenario. In Section 3.5, we present the results of these forecasts.

### 3.4.1 Intrinsic FRB Statistics

Since FRBs observed after the EoR do not contain any information about the ionization history of the Universe, only high redshift FRBs observed during the EoR contribute to our forecasts. FRBs at these redshifts have not yet been observed and may be rare. To get a more realistic sense of how many intrinsic FRBs that can potentially be observed given a capable high DM experiment, we use an existing theoretical model of source count distributions of FRBs at each DM. From this theoretically motivated count of FRBs within  $z > z_{\text{EoR}}$ , we can populate our mock catalogue. We first define an intrinsic source count distribution of FRBs. It will be from this distribution that we populate the redshift bins of our fiducial sample for our forecasts. For this, we choose a source count distribution that traces the star formation rate (SFR) [9]. While other source count distributions have been proposed, [46] shows that the density of FRBs ( $\rho_{\text{FRB}}$ ) increases with redshift, closely resembling cosmic star formation history. We follow this prescription and use the following simple top-heavy distribution for the number of FRBs per DM,

$$\frac{dn}{dDM} = \frac{\rho_{\text{FRB}}(z)}{(1+z)} \frac{dV}{dz} \frac{dz}{dDM} \quad (3.9)$$

where,  $\frac{dV}{dz}$  is the comoving volume element.

Tracing the cosmic star formation history, we take the density to be proportional to the SFR density [35, 37],

$$\rho_{\text{FRB}}(z) \propto \rho_{\text{SFR}}(z) = 0.015 \frac{(1+z)^{2.7}}{1 + ((1+z)/2.9)^{5.6}} \text{ M}_{\odot} \text{ yr}^{-1} \text{ Mpc}^{-3} \quad (3.10)$$

What relies on the model in this source count distribution is the  $\frac{dz}{d\text{DM}}$  factor. As mentioned in Sections 3.3.2 and 3.3.3, the DM– $z$  relation is sensitive to reionization parameters. Currently, the widely used DM– $z$  relation is linear

$$\text{DM}(z) = C \times z \text{ pc cm}^3 \quad (3.11)$$

where  $C$  is often taken to be 1000 [46] or 1200 [20]. These linear relations approximate the redshift to an accuracy of about 2% for  $z < 2$  [50]. As shown in Figure 3.4, the model of reionization affects the shape of the DM– $z$  relation, especially at high redshift. In order to place constraints on reionization, high redshift samples are paramount. Therefore, in order to compute the source count distribution for the fiducial model, we calculate  $\frac{dz}{d\text{DM}}$  by taking numerical derivatives of the corresponding fiducial DM– $z$  curve. Measurements of the EoR parameters have not yet been made, so in order to produce a mock sample of observed high redshift FRBs, we must assume a fiducial reionization scenario. Our fiducial EoR model is produced by fixing the astrophysical and morphological parameter  $\beta$  from Section 3.3. We choose EoR parameters  $\zeta_0 = 25$ ,  $M_{\text{turn},0} = 5 \times 10^8 \text{ M}_{\odot}$ , and  $R_{\text{mfp},0} = 30 \text{ Mpc}$  as well as  $\beta = 1$ . The astrophysical parameters are consistent with previous studies such as [40], while the morphological parameter,  $\beta = 1$ , corresponds to an inside-out reionization scenario.

The fiducial DM– $z$  curve is the light blue dashed line ( $\beta = 1$ ) shown in the top left panel of Figure 3.4. Now that the CDF is defined, we can build our mock data set.

### 3.4.2 Mock Catalogue of FRBs

We build our sample of FRBs using inverse transform sampling whereby a given number of random samples is drawn from a probability distribution given its CDF. This populates each redshift bin, of bin width  $\delta_z = 1$ , with FRBs according to the CDF. The method is the following, where our random variable  $X$  is the FRB source count:

1. Define a random variable,  $X$ , whose distribution is described by the CDF,  $F_X$ .
2. Generate a random number  $u$  from a uniform distribution in the interval  $[0, 1]$ . This number will be interpreted as a probability.
3. Compute the inverse of of the CDF, that is  $F_X^{-1}(u)$ .
4. Compute  $X = F_X^{-1}(u)$ . Now the random variable  $X$  with distribution  $F_X$  has been generated.

Using this method, we in fact draw a distribution of DM counts per DM bin. Then, using our fiducial DM- $z$  relation, convert this to counts per redshift bin. We simply proceed to use the probability distribution in 3.2 to draw the given number of DMs per redshift bin. This method guarantees that our sample has line of sight fluctuations, ensuring that every FRB has a unique DM, even when in the same redshift bin.

It may be noted that we only account for fluctuations in the DM distribution of FRBs. The spatial distribution of FRBs is not accounted for here, that is, the sources are taken to have random positions. In actuality, the spacial distribution of FRBs will be positively correlated with the underlying matter distribution and so one may posit that FRBs emitted inside an ionized region would acquire considerable DM from the host bubble. We find that the contribution of the host bubble, or lack there of, to the total DM from the line of sight during reionization is negligible and we proceed without populating halos with sources. At this point, we are ready to move on to performing the MCMC on the sample.

### 3.4.3 MCMC setup

We place the mean of the individual sightline DMs of our mock FRB catalogue into a vector  $\overline{\text{DM}}_S$  corresponding to the mean of the sample FRBs for each redshift  $z$ . For such a measurement, the uncertainties on  $\overline{\text{DM}}_S$  are the sum of the instrumental systematic errors in measuring the individual sightline DMs and the uncertainties in  $\overline{\text{DM}}_S$  due to sample variance. The instrument errors on the individual DM are assumed to be small and so we do not model the instrumental errors and only include the errors due to sample variance. The uncertainties due to sample variances on  $\overline{\text{DM}}_S$  are

$$\sigma_s = \frac{s_{N-1}}{\sqrt{N}} \quad (3.12)$$

where  $N$  are the number of FRBs comprising the sample and  $s_{N-1}$  is the measured sample variance given by

$$s_{N-1}^2 = \frac{1}{N-1} \sum_{i=0}^N (\text{DM}_i - \overline{\text{DM}}_S)^2 \quad (3.13)$$

where  $\text{DM}_i$  are the individual sightline DMs sampled from the probability density functions generated by our fiducial model, and  $\overline{\text{DM}}$  is the mean of such a sample. Our forecasts consider different cases of  $\sigma_s$  by considering different total number  $N$  of FRBs observed. To place constraints on the on the EoR parameters  $\theta = \beta, \zeta, M_{\text{turn}}, R_{\text{mfp}}$ , we evaluate the probability of  $\theta$  given measurement of the mean DM from the samples from our fiducial EoR model defined in Section 3.4.2. This is the posterior  $p(\theta|\overline{\text{DM}}_S)$ . We can evaluate the posterior  $p(\theta|\overline{\text{DM}}_S)$  through Bayes theorem:

$$p(\theta|\overline{\text{DM}}_S) \propto p(\overline{\text{DM}}_S|\theta)p(\theta), \quad (3.14)$$

where  $p(\overline{\text{DM}}_S|\theta)$  is the likelihood function and  $p(\theta)$  is the prior on the EoR parameters  $\theta$ . Since the likelihood function is non-analytic in the EoR parameters  $\theta$ , we use 21cmFAST to generate a model density and ionization field representative of the IGM with parameters  $\beta, \zeta, M_{\text{turn}}, R_{\text{mfp}}$ . To generate the density and ionization field with the morphology indicative of the model  $\beta$ , we use the same procedure described in [47]. From this model reionization and density field, we generate a lightcone for each line of sight, and evaluate DM for each of these lines of sight. We then average all sightlines together to evaluate  $\overline{\text{DM}}$  for this reionization model. The mean DM of all sightlines for this model is compared to the fiducial mean DM of the mock FRBs through the  $\chi^2$  statistic. The likelihood  $p(\theta|\overline{\text{DM}}_S)$  is then computed as:

$$p(\overline{\text{DM}}_S|\theta) \propto \exp \left[ -\frac{1}{2} \sum_z \frac{(\overline{\text{DM}}_{\text{model}} - \overline{\text{DM}}_S)^2}{\sigma_s^2} \right], \quad (3.15)$$

where we have assumed the errors on  $\overline{\text{DM}}_{\mathbf{S}}$  to be Gaussian and independent. The Gaussianity of the likelihood is a valid assumption since for larger samples of DM, the mean  $\overline{\text{DM}}$ , of these samples tend to be Gaussian distributed according to the central limit theorem. However since there are indeed correlations between redshift bins, the independence of the likelihood in terms of  $z$  serves as an approximation. We consider the mean DM of FRBs measured from redshifts  $z = 8$  to  $z = 10$  in steps of  $\Delta z = 1$  corresponding to the redshifts that contain the largest sensitivity to the EoR parameters. Inclusion of more redshifts do not significantly alter our conclusions and so for computational simplicity we exclude them from our forecasts. We place uniform priors on each of the EoR parameters  $\theta$  within  $p(\theta)$ . Since  $\beta$  is only defined from  $-1 \leq \beta \leq 1$ , we place the prior  $-1 \leq \beta \leq 1$  which covers the entire possible physical range of EoR morphologies. For  $R_{\text{mfp}}$  we use  $5 \text{ Mpc} < R_{\text{mfp}} < 160 \text{ Mpc}$  which spans the all possible sizes consistent with the length of our simulation boxes. For  $\zeta$ , we place the range  $5 < \zeta < 100$  which encapsulates the entire physically allowed duration of reionization histories [40]. Finally for  $M_{\text{turn}}$ , we use values of  $10^7 M_{\odot} < M_{\text{turn}} < 10^{10} M_{\odot}$ , which are physically motivated by the atomic cooling threshold and by constraints on the faint end of UV luminosity functions [48]. Using the sampling discussed in Section 3.4.1, we generate mock data and fit to them via the likelihood

$$p(\overline{\text{DM}}_{\mathbf{S}_z} | \theta) \propto \exp \left[ -\frac{1}{2} \sum_z \frac{(\overline{\text{DM}}_{\text{model}} - \overline{\text{DM}}_{\mathbf{S}_z})^2}{\sigma_{S_z}^2} \right]. \quad (3.16)$$

where here we are summing over redshift bins,  $z = \{8, 9, 10\}$ . To sample our posterior distribution, we use a Markov Chain Monte Carlo (MCMC) approach, as implemented by the affine invariant MCMC package `emcee` [15].

### 3.5 Results

Here we present the MCMC results of our forecast discussed in Section 3.4.3 corresponding to measurement of  $N$  high redshift FRBs observed between  $z = 8$  to  $z = 10$ , and distributed in  $z$  according to the CDF described in Section 3.4.1. We repeat this mock observation for three

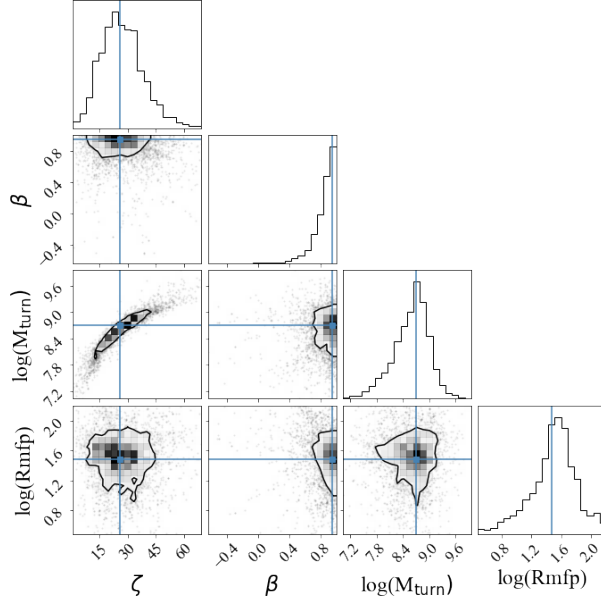


**Figure 3.5:** Posterior distributions for measurement of  $\overline{\text{DM}}$  for  $10^4$  FRBs distributed between redshifts  $8 \leq z \leq 10$  according to the source count distribution in Section 3.4.1. The 68% credibility regions are shown. Such a measurement can rule out uncorrelated  $\beta = 0$  and outside-in reionization  $\beta < 0$  at 68%CR.

different total number of measured FRBs. We use  $N = 10^2, 10^4, 10^5$ , where these observed FRB counts span a reasonable range of sample variances. In each case we assume that the  $\overline{\text{DM}}$  of these FRBs is dominated by the contribution of the IGM. As discussed in Section 3.2.3, we neglect the contributions due to the CGM and ISM and leave their inclusion for future work. The fiducial reionization scenario has parameters  $\beta = 1$ ,  $\zeta = 25$ ,  $M_{\text{turn}} = 5 \times 10^8 M_{\odot}$  and  $R_{\text{mfp}} = 30 \text{Mpc}$ .

### 3.5.1 Larger Sample Sizes

In this scenario we detect  $N$  FRBs, distributed across the redshift bins  $z = 8 - 10$  according to the theoretically motivated source count distribution discussed in Section 3.4.1. Figure 3.5 and 3.6 show the results of this forecast for cases corresponding to  $N = 10^4$  and  $N = 10^5$  respectively. From the posterior of both Figures, we see that there are clear degeneracies between  $\zeta$  and  $M_{\text{turn}}$ . This is due to both parameters establishing the redshift in which the flattening of  $\overline{\text{DM}}$  occurs. This degeneracy is pronounced in Figure 3.3 where changing the values of  $\zeta$  and  $M_{\text{turn}}$  result in

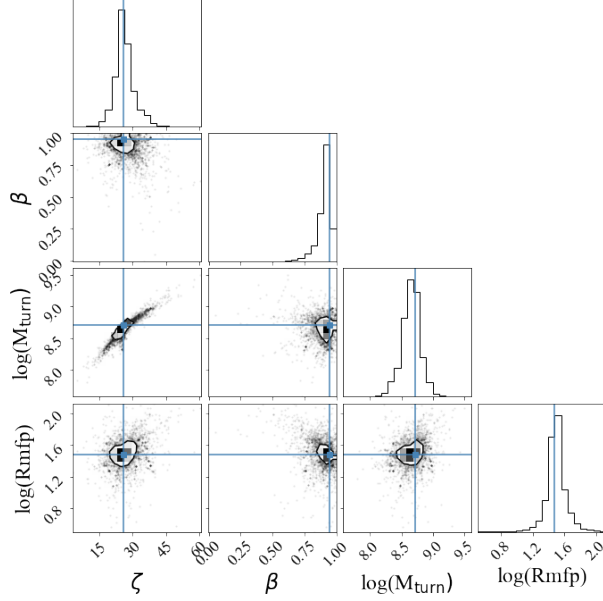


**Figure 3.6:** Posterior distributions for measurement of  $\overline{DM}$  for  $10^5$  FRBs distributed between redshifts  $8 \leq z \leq 10$  according to the source count distribution in Section 3.4.1. Using such a measurement, we can rule out uncorrelated and outside-in reionization scenarios at 68%CR.

translating the distribution along the horizontal axis. By examining the 68% credibility regions (CR) in Figure 3.5, we can see that measurement of  $N = 10^4$  FRBs within these redshift bins can constrain  $\zeta$  to  $\zeta = 25.5^{+11.5}_{-10.5}$  and  $\log(M_{\text{turn}}) = 8.65^{+0.29}_{-0.49}$ . By placing constraints on these parameters (the ionizing efficiency and the halo mass scale of the UV sources), one can place constraints on the timing and duration of reionization. We find that with  $N = 10^4$  FRBs in these redshift ranges, we can constrain the duration,  $\Delta z$ , of reionization (duration between  $0.25 \leq \bar{x}_{\text{HII}} \leq 0.75$ ) to  $\Delta z = 2.1^{+0.50}_{-0.30}$ , and the midpoint  $z_{\text{mid}} = 7.8^{+0.20}_{-0.20}$ , at 68% credibility. Referring to the posterior in Figure 3.6, the constraints on  $\zeta$  and  $M_{\text{turn}}$  are tighter for the extreme case of  $N = 10^5$  FRBs where we can constrain  $\zeta$  to within  $\zeta = 25^{+7}_{-9}$  at 95%CR and  $\log(M_{\text{turn}}) = 8.76^{+0.14}_{-0.46}$  at 95%CR. With constraints on these parameters we can place constraints on the duration of reionization,  $\Delta z = 2.0^{+0.5}_{-0.4}$ , at %95CR and the midpoint of reionization,  $z = 7.8^{+0.4}_{-0.2}$  at 95%CR.

The correlation parameter  $\beta$  does not share degeneracies with these parameters since it does not affect the timing of reionization, rather it affects the mean density,  $\bar{n}_e$ , of free electrons in the ionized region. We find from the posterior that measurement of  $10^4$  FRBs can distinguish between

the sign of  $\beta$ . Since the sign of  $\beta$  corresponds to the type of correlation between  $\delta$  and  $x_{\text{HII}}$ , we find that measurement of  $\overline{\text{DM}}$  using  $10^4$  FRBs can rule out  $\beta < 0$  (outside-in) scenarios and  $\beta = 0$  (uncorrelated scenarios) at 95% CR. In the more extreme case of  $N = 10^5$  FRBs, we can further rule out uncorrelated and outside-in scenarios at 99% CR. Measurement of  $10^4$  FRBs between  $8 < z < 10$  is sufficient to constrain the order of magnitude of  $R_{\text{mfp}}$  at 68%CR. For the case of  $N = 10^5$  FRBs, our models can constrain the order of magnitude of  $R_{\text{mfp}}$  at 95%CR.

### 3.5.2 Smaller Sample Sizes

In this scenario we measure 100 FRBs distributed across redshift bins between  $8 \leq z \leq 10$ , again using the source count distribution outlined in section 3.4.1. We show the posterior of such a measurement in Figure 3.7. Our interpretation of the degeneracy between the parameters is identical to 3.5.1. We see from the posterior of Figure 3.7 that smaller samples of FRBs lead to biased fits due to cosmic variance. However even with such small sample sizes, 68% of the contours lie within  $\beta > 0$  suggesting that we can still rule out both uncorrelated and outside-in reionization scenarios at 68%CR. We see from the posterior that we can rule out models with  $\zeta$  and  $M_{\text{turn}}$  outside the range  $23 \leq \zeta \leq 55$  and  $4 \times 10^9 M_{\odot} \leq M_{\text{turn}} \leq 3 \times 10^9 M_{\odot}$  at 68%CR. Ruling out this region of parameter space is tantamount to setting broad constraints on the timeline of reionization. For example, this region excludes scenarios where the Universe is still neutral at redshift  $z = 10$ , which would severely flatten  $\overline{\text{DM}}(z)$  between  $8 \leq z \leq 10$ . We can rule these models out at 68%CR. Similarly this region excludes models where the Universe is more than 60% ionized by redshift  $z = 8$ , which would reduce the flattening of  $\overline{\text{DM}}$  between  $8 \leq z \leq 10$ . We can rule out these scenarios at 68%CR.

## 3.6 Conclusion

The DM of FRBs depends on the free electrons along the line of sight, and so the DM of high redshift FRBs will naturally contain information about the ionization state of the IGM. This makes detection of high redshift FRBs a potentially useful probe to study cosmic reionization. Here we

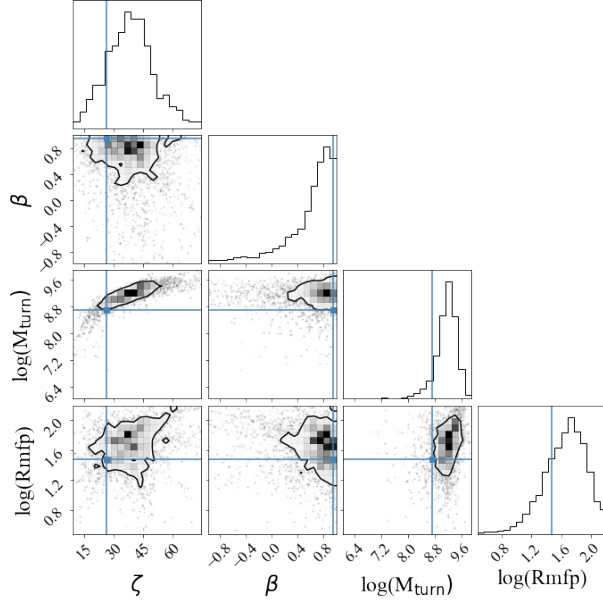


**Figure 3.7:** Posterior distributions for measurement of  $\overline{\text{DM}}$  for 100 FRBs distributed between  $8 \leq z \leq 10$  according to the source count distribution in Section 3.4.1. The 68% credibility regions of our measurements are shown. This measurement can rule out extreme EoR models, for example, scenarios where the Universe is ionized by  $z = 8$ .

study how the astrophysics and morphology of the EoR affects the mean DM of high redshift FRBs. We use a parametrization,  $\beta$ , that tracks the density-ionization correlation in the EoR and common astrophysical parameters to bracket the range of physical EoR scenarios. We find that  $\overline{\text{DM}}$  is sensitive to the astrophysics and morphology of reionization and can influence fluctuations in  $\overline{\text{DM}}$  up to  $1000 \text{pc cm}^{-2}$ . In particular, the ionizing efficiency and mass scale of the ionizing sources cause the greatest fluctuations in  $\overline{\text{DM}}$ , which we physically attribute to being caused by the modified timing of reionization. The EoR morphology impacts  $\overline{\text{DM}}$  by changing the density of free electrons within the ionized regions. We find that inside-out reionization scenarios produce the greatest density of free electrons within the ionized bubbles which increases the mean DM of high redshift FRBs with respect to outside-in reionization scenarios. To gauge the viability of such a probe, we perform numerical forecasts to study the types of constraints that can be placed on the astrophysical and correlation parameters using measurements of highly dispersed FRBs. Using a fiducial inside-out reionization scenario with midpoint of reionization,  $z = 2.0$  and duration

$\Delta z = 7.8$ , we find that samples of 100 FRBs can rule out uncorrelated reionization at 68%CR. Using samples of  $10^4$  FRBs in the same redshift range can rule out uncorrelated and outside-in reionization at 95%CR. We also find that samples of 100 FRBs between  $8 \leq z \leq 10$  can rule out scenarios where the Universe is entirely neutral at  $z = 10$  with 68%CR. Further, this measurement can also rule out EoR scenarios where the IGM is more than 60% ionized at  $z = 8$ . Larger sample sizes ( $\geq 10^4$ ), of high redshift FRBs, distributed in redshift from  $8 \leq z \leq 10$  according to the theoretically motivated source count distributions, can constrain the duration of reionization (duration between mean ionized fractions 0.25 to 0.75) to  $\Delta z = 2.1_{-0.30}^{+0.50}$  and midpoint  $z = 7.8_{-0.20}^{+0.20}$  at 68%CR. Finally, we find that samples of  $\geq 10^5$  high redshift FRBs can constrain the duration of reionization (duration between mean ionized fractions 0.25 to 0.75) to  $\Delta z = 2.0_{-0.4}^{+0.5}$  and midpoint  $z = 7.8_{-0.2}^{+0.4}$  at 95%CR.

For future work, we would like to further this proof of concept by using the full distribution of DMs at each  $z$  in our forecasts, and by making use of observational constraints as well as the intrinsic constraints outlined in this paper. There are, most obviously, observational constraints that play a role in the feasibility of such parameter fitting with real data. While high-DM (DM > 4000) events have not yet been observed, [9] notes that one can design an experiment that has a higher detection rate of highly dispersed events by trading time resolution for higher frequency resolution. [63] note that FAST and SKA will have the capability of making such detections and most recently [19] show that observations from SKA phase 2 will indeed reveal our reionization history. It must be noted, however, that the FRB progenitor will ultimately dictate whether there exists an FRB population during the EoR. In addition, a more sophisticated simulation would allow one to explore correlations between  $M_{\text{turn}}$ ,  $\zeta$ , and the FRB source count distribution since these three parameters ultimately depend on the stellar population. Folding everything into one framework would allow one to study such correlations as well as take clustering of FRBs into account.

Cosmic Dawn did not occur as a single bright event, but rather individual stars, one by one, lit our dark universe. Similarly, we will likely not understand Cosmic Dawn and the Epoch of Reionization from one observation alone, but rather we will need to make use of many tools which, one by one, will illuminate our understanding of this mysterious time in our universe's history. We

propose here that the careful study of highly dispersed FRB observables can serve as such a tool which will, along with many others, help us understand the Epoch of Reionization.

## **Acknowledgements**

We would like to extend our deepest thanks to Wenbin Lu for encouraging us to work on this project and for providing us with key insights and guidance. We would also like to thank Adrian Liu and Jordan Mirocha for their helpful comments. There was no explicit funding for this work, though we acknowledge support from the New Frontiers in Research Fund Exploration grant program, a Natural Sciences and Engineering Research Council of Canada (NSERC) Discovery Grant and a Discovery Launch Supplement, the Fonds de recherche du Québec – Nature et technologies (FRQNT), the Sloan Research Fellowship, the William Dawson Scholarship at McGill, as well as the Canadian Institute for Advanced Research (CIFAR) Azrieli Global Scholars program. This research was enabled in part by support provided by Calcul Quebec ([www.calculquebec.ca](http://www.calculquebec.ca)), WestGrid ([www.westgrid.ca](http://www.westgrid.ca)) and Compute Canada ([www.computecanada.ca](http://www.computecanada.ca)).

## **Data Availability**

The software code underlying this article will be shared on reasonable request to the corresponding authors.

## **Bibliography**

- [1] Kevin Bandura, Graeme E. Addison, Mandana Amiri, J. Richard Bond, Duncan Campbell-Wilson, Liam Connor, Jean-François Cliche, Greg Davis, Meiling Deng, Nolan Denman, Matt Dobbs, Mateus Fandino, Kenneth Gibbs, Adam Gilbert, Mark Halpern, David Hanna, Adam D. Hincks, Gary Hinshaw, Carolin Höfer, Peter Klages, Tom L. Landecker, Kiyoshi Masui, Juan Mena Parra, Laura B. Newburgh, Ue-li Pen, Jeffrey B. Peterson, Andre Recnik, J. Richard Shaw, Kris Sigurdson, Mike Sitwell, Graeme Smecher, Rick Smegal, Keith

- Vanderlinde, and Don Wiebe. Canadian Hydrogen Intensity Mapping Experiment (CHIME) pathfinder. In Larry M. Stepp, Roberto Gilmozzi, and Helen J. Hall, editors, *Ground-based and Airborne Telescopes V*, volume 9145 of *Society of Photo-Optical Instrumentation Engineers (SPIE) Conference Series*, page 914522, July 2014.
- [2] Paz Beniamini, Pawan Kumar, Xiangcheng Ma, and Eliot Quataert. Exploring the epoch of hydrogen reionization using frbs. *Monthly Notices of the Royal Astronomical Society*, Feb 2021.
- [3] Mukul Bhattacharya, Pawan Kumar, and Eric V. Linder. Fast radio burst dispersion measure distribution as a probe of helium reionization, 2020.
- [4] Judd D. Bowman, Iver Cairns, David L. Kaplan, Tara Murphy, Divya Oberoi, Lister Staveley-Smith, Wayne Arcus, David G. Barnes, Gianni Bernardi, Frank H. Briggs, Shea Brown, John D. Bunton, Adam J. Burgasser, Roger J. Cappallo, Shami Chatterjee, Brian E. Corey, Anthea Coster, Avinash Deshpande, Ludi deSouza, David Emrich, Philip Erickson, Robert F. Goeke, B. M. Gaensler, Lincoln J. Greenhill, Lisa Harvey-Smith, Bryna J. Hazelton, David Herne, Jacqueline N. Hewitt, Melanie Johnston-Hollitt, Justin C. Kasper, Barton B. Kincaid, Ronald Koenig, Eric Kratzenberg, Colin J. Lonsdale, Mervyn J. Lynch, Lynn D. Matthews, S. Russell McWhirter, Daniel A. Mitchell, Miguel F. Morales, Edward H. Morgan, Stephen M. Ord, Joseph Pathikulangara, Thiagaraj Prabu, Ronald A. Remillard, Timothy Robishaw, Alan E. E. Rogers, Anish A. Roshi, Joseph E. Salah, Robert J. Sault, N. Udaya Shankar, K. S. Srivani, Jamie B. Stevens, Ravi Subrahmanyan, Steven J. Tingay, Randall B. Wayth, Mark Waterson, Rachel L. Webster, Alan R. Whitney, Andrew J. Williams, Christopher L. Williams, and J. Stuart B. Wyithe. Science with the Murchison Widefield Array. *Publ. Astron. Soc. Australia*, 30:e031, April 2013.
- [5] Judd D. Bowman, Alan E. E. Rogers, and Jacqueline N. Hewitt. Toward Empirical Constraints on the Global Redshifted 21 cm Brightness Temperature During the Epoch of Reionization. *ApJ*, 676(1):1–9, March 2008.

- [6] M Caleb, C Flynn, and B W Stappers. Constraining the era of helium reionization using fast radio bursts. *Monthly Notices of the Royal Astronomical Society*, 485(2):2281–2286, Feb 2019.
- [7] CHIME/FRB Collaboration, B. C. Andersen, K. M. Bandura, M. Bhardwaj, A. Bij, M. M. Boyce, P. J. Boyle, C. Brar, T. Cassanelli, P. Chawla, T. Chen, J. F. Cliche, A. Cook, D. Cubranic, A. P. Curtin, N. T. Denman, M. Dobbs, F. Q. Dong, M. Fandino, E. Fonseca, B. M. Gaensler, U. Giri, D. C. Good, M. Halpern, A. S. Hill, G. F. Hinshaw, C. Höfer, A. Josephy, J. W. Kania, V. M. Kaspi, T. L. Landecker, C. Leung, D. Z. Li, H. H. Lin, K. W. Masui, R. McKinven, J. Mena-Parra, M. Merryfield, B. W. Meyers, D. Michilli, N. Milutinovic, A. Mirhosseini, M. Münchmeyer, A. Naidu, L. B. Newburgh, C. Ng, C. Patel, U. L. Pen, T. Pinsonneault-Marotte, Z. Pleunis, B. M. Quine, M. Rafei-Ravandi, M. Rahman, S. M. Ransom, A. Renard, P. Sanghavi, P. Scholz, J. R. Shaw, K. Shin, S. R. Siegel, S. Singh, R. J. Smegal, K. M. Smith, I. H. Stairs, C. M. Tan, S. P. Tendulkar, I. Tretyakov, K. Vanderlinde, H. Wang, D. Wulf, and A. V. Zwaniga. A bright millisecond-duration radio burst from a Galactic magnetar. *Nature*, 587(7832):54–58, November 2020.
- [8] Tirthankar Roy Choudhury, Martin G. Haehnelt, and John Regan. Inside-out or outside-in: the topology of reionization in the photon-starved regime suggested by  $\text{Ly}\alpha$  forest data. *MNRAS*, 394(2):960–977, April 2009.
- [9] Liam Connor. Interpreting the distributions of FRB observables. *MNRAS*, 487(4):5753–5763, August 2019.
- [10] David R. DeBoer, Aaron R. Parsons, James E. Aguirre, Paul Alexander, Zaki S. Ali, Adam P. Beardsley, Gianni Bernardi, Judd D. Bowman, Richard F. Bradley, Chris L. Carilli, Carina Cheng, Eloy de Lera Acedo, Joshua S. Dillon, Aaron Ewall-Wice, Gcobisa Fadana, Nicolas Fagnoni, Randall Fritz, Steve R. Furlanetto, Brian Glendenning, Bradley Greig, Jasper Grobbelaar, Bryna J. Hazelton, Jacqueline N. Hewitt, Jack Hickish, Daniel C. Jacobs, Austin Julius, MacCalvin Kariseb, Saul A. Kohn, Telalo Lekalake, Adrian Liu, Anita Loots, David MacMahon, Lourence Malan, Cresshim Malgas, Matthys Maree, Zachary Martinot, Nathan

- Mathison, Eunice Matsetela, Andrei Mesinger, Miguel F. Morales, Abraham R. Neben, Nipanjana Patra, Samantha Pieterse, Jonathan C. Pober, Nima Razavi-Ghods, Jon Ringuette, James Robnett, Kathryn Rosie, Raddwine Sell, Craig Smith, Angelo Syce, Max Tegmark, Nithyanandan Thyagarajan, Peter K. G. Williams, and Haoxuan Zheng. Hydrogen Epoch of Reionization Array (HERA). *PASP*, 129(974):045001, April 2017.
- [11] P. E. Dewdney, P. J. Hall, R. T. Schilizzi, and T. J. L. W. Lazio. The square kilometre array. *Proceedings of the IEEE*, 97(8):1482–1496, 2009.
- [12] K. Dolag, B. M. Gaensler, A. M. Beck, and M. C. Beck. Constraints on the distribution and energetics of fast radio bursts using cosmological hydrodynamic simulations. *MNRAS*, 451(4):4277–4289, August 2015.
- [13] Aaron Ewall-Wice, Jacqueline Hewitt, Andrei Mesinger, Joshua S. Dillon, Adrian Liu, and Jonathan Pober. Constraining high-redshift X-ray sources with next generation 21-cm power spectrum measurements. *MNRAS*, 458(3):2710–2724, May 2016.
- [14] Anastasia Fialkov and Abraham Loeb. A fast radio burst occurs every second throughout the observable universe. *The Astrophysical Journal*, 846(2):L27, sep 2017.
- [15] Daniel Foreman-Mackey, David W. Hogg, Dustin Lang, and Jonathan Goodman. emcee: The MCMC Hammer. *PASP*, 125(925):306, March 2013.
- [16] Steven R. Furlanetto and S. Peng Oh. Taxing the rich: recombinations and bubble growth during reionization. *MNRAS*, 363(3):1031–1048, November 2005.
- [17] Steven R. Furlanetto, S. Peng Oh, and Frank H. Briggs. Cosmology at low frequencies: The 21cm transition and the high-redshift universe. *Physics Reports*, 433(4-6):181–301, Oct 2006.
- [18] Steven R. Furlanetto, Matias Zaldarriaga, and Lars Hernquist. The Growth of H II Regions During Reionization. *ApJ*, 613(1):1–15, September 2004.
- [19] Tetsuya Hashimoto, Tomotsugu Goto, Ting-Yi Lu, Alvina Y. L. On, Daryl Joe D. Santos, Seong Jin Kim, Ece Kilerci Eser, Simon C. C. Ho, Tiger Y. Y. Hsiao, and Leo Y. W. Lin.

- Revealing the cosmic reionization history with fast radio bursts in the era of Square Kilometre Array. *MNRAS*, 502(2):2346–2355, April 2021.
- [20] Kunihiro Ioka. The Cosmic Dispersion Measure from Gamma-Ray Burst Afterglows: Probing the Reionization History and the Burst Environment. *ApJ*, 598(2):L79–L82, December 2003.
- [21] S. Johnston, R. Taylor, M. Bailes, N. Bartel, C. Baugh, M. Bietenholz, C. Blake, R. Braun, J. Brown, S. Chatterjee, J. Darling, A. Deller, R. Dodson, P. Edwards, R. Ekers, S. Ellingsen, I. Feain, B. Gaensler, M. Haverkorn, G. Hobbs, A. Hopkins, C. Jackson, C. James, G. Joncas, V. Kaspi, V. Kilborn, B. Koribalski, R. Kothes, T. Landecker, E. Lenc, J. Lovell, J. P. Macquart, R. Manchester, D. Matthews, N. McClure-Griffiths, R. Norris, U. L. Pen, C. Phillips, C. Power, R. Protheroe, E. Sadler, B. Schmidt, I. Stairs, L. Staveley-Smith, J. Stil, S. Tingay, A. Tzioumis, M. Walker, J. Wall, and M. Wolleben. Science with ASKAP. The Australian square-kilometre-array pathfinder. *Experimental Astronomy*, 22(3):151–273, December 2008.
- [22] V. K. Kapahi and S. Ananthakrishnan. Astronomy with the Giant Metrewave Radio Telescope (GMRT). *Bulletin of the Astronomical Society of India*, 23:265, September 1995.
- [23] J. I. Katz. Inferences from the Distributions of Fast Radio Burst Pulse Widths, Dispersion Measures, and Fluences. *ApJ*, 818(1):19, February 2016.
- [24] Laura C. Keating and Ue-Li Pen. Exploring the dispersion measure of the Milky Way halo. *MNRAS*, 496(1):L106–L110, July 2020.
- [25] Nicholas S. Kern, Adrian Liu, Aaron R. Parsons, Andrei Mesinger, and Bradley Greig. Emulating Simulations of Cosmic Dawn for 21 cm Power Spectrum Constraints on Cosmology, Reionization, and X-Ray Heating. *ApJ*, 848(1):23, October 2017.
- [26] Pawan Kumar, Wenbin Lu, and Mukul Bhattacharya. Fast radio burst source properties and curvature radiation model. *MNRAS*, 468(3):2726–2739, July 2017.
- [27] Eric V. Linder. Detecting helium reionization with fast radio bursts. *Physical Review D*, 101(10), May 2020.

- [28] Adrian Liu and Aaron R. Parsons. Constraining cosmology and ionization history with combined 21 cm power spectrum and global signal measurements. *MNRAS*, 457(2):1864–1877, April 2016.
- [29] Adrian Liu and J. Richard Shaw. Data Analysis for Precision 21 cm Cosmology. *PASP*, 132(1012):062001, June 2020.
- [30] Adrian Liu and Max Tegmark. How well can we measure and understand foregrounds with 21-cm experiments? *Monthly Notices of the Royal Astronomical Society*, 419(4):3491–3504, 2012.
- [31] Abraham Loeb and Steven R. Furlanetto. *The First Galaxies in the Universe*. Princeton University Press, 2013.
- [32] D. R. Lorimer, M. Bailes, M. A. McLaughlin, D. J. Narkevic, and F. Crawford. A Bright Millisecond Radio Burst of Extragalactic Origin. *Science*, 318(5851):777, November 2007.
- [33] Wenbin Lu, Pawan Kumar, and Bing Zhang. A unified picture of Galactic and cosmological fast radio bursts. *MNRAS*, 498(1):1397–1405, August 2020.
- [34] Jean-Pierre Macquart. Probing the Universe’s baryons with fast radio bursts. *Nature Astronomy*, 2:836–838, October 2018.
- [35] Piero Madau, Henry C. Ferguson, Mark E. Dickinson, Mauro Giavalisco, Charles C. Steidel, and Andrew Fruchter. High-redshift galaxies in the Hubble Deep Field: colour selection and star formation history to  $z \sim 4$ . *MNRAS*, 283(4):1388–1404, December 1996.
- [36] Piero Madau and Francesco Haardt. Cosmic Reionization after Planck: Could Quasars Do It All? *ApJ*, 813(1):L8, November 2015.
- [37] Piero Madau, Lucia Pozzetti, and Mark Dickinson. The Star Formation History of Field Galaxies. *ApJ*, 498(1):106–116, May 1998.

- [38] Andrei Mesinger, Andrea Ferrara, and David S. Spiegel. Signatures of X-rays in the early Universe. *MNRAS*, 431(1):621–637, May 2013.
- [39] Andrei Mesinger, Steven Furlanetto, and Renyue Cen. 21CMFAST: a fast, seminumerical simulation of the high-redshift 21-cm signal. *MNRAS*, 411(2):955–972, February 2011.
- [40] Andrei Mesinger, Matthew McQuinn, and David N. Spergel. The kinetic Sunyaev-Zel’dovich signal from inhomogeneous reionization: a parameter space study. *MNRAS*, 422(2):1403–1417, May 2012.
- [41] I. F. Mirabel, M. Dijkstra, P. Laurent, A. Loeb, and J. R. Pritchard. Stellar black holes at the dawn of the universe. *A&A*, 528:A149, April 2011.
- [42] Jordi Miralda-Escudé, Martin Haehnelt, and Martin J. Rees. Reionization of the Inhomogeneous Universe. *ApJ*, 530(1):1–16, February 2000.
- [43] Miguel F. Morales and J. Stuart B. Wyithe. Reionization and Cosmology with 21-cm Fluctuations. *ARA&A*, 48:127–171, September 2010.
- [44] Rendong Nan, Di Li, Chengjin Jin, Qiming Wang, Lichun Zhu, Wenbai Zhu, Haiyan Zhang, Youling Yue, and Lei Qian. The Five-Hundred Aperture Spherical Radio Telescope (fast) Project. *International Journal of Modern Physics D*, 20(6):989–1024, January 2011.
- [45] L. B. Newburgh, K. Bandura, M. A. Bucher, T. C. Chang, H. C. Chiang, J. F. Cliche, R. Davé, M. Dobbs, C. Clarkson, K. M. Ganga, T. Gogo, A. Gumba, N. Gupta, M. Hilton, B. Johnstone, A. Karastergiou, M. Kunz, D. Lokhorst, R. Maartens, S. Macpherson, M. Mdlalose, K. Moodley, L. Ngwenya, J. M. Parra, J. Peterson, O. Recnik, B. Saliwanchik, M. G. Santos, J. L. Sievers, O. Smirnov, P. Stronkhorst, R. Taylor, K. Vanderlinde, G. Van Vuuren, A. Weltman, and A. Witzemann. HIRAX: a probe of dark energy and radio transients. In Helen J. Hall, Roberto Gilmozzi, and Heather K. Marshall, editors, *Ground-based and Airborne Telescopes VI*, volume 9906 of *Society of Photo-Optical Instrumentation Engineers (SPIE) Conference Series*, page 99065X, August 2016.

- [46] Yuu Niino. Fast Radio Bursts' Recipes for the Distributions of Dispersion Measures, Flux Densities, and Fluences. *ApJ*, 858(1):4, May 2018.
- [47] Michael Pagano and Adrian Liu. Quantifying density-ionization correlations with the 21-cm power spectrum. *MNRAS*, 498(1):373–384, August 2020.
- [48] Jaehong Park, Andrei Mesinger, Bradley Greig, and Nicolas Gillet. Inferring the astrophysics of reionization and cosmic dawn from galaxy luminosity functions and the 21-cm signal. *MNRAS*, 484(1):933–949, March 2019.
- [49] Aaron Parsons, Jonathan Pober, Matthew McQuinn, Daniel Jacobs, and James Aguirre. A SENSITIVITY AND ARRAY-CONFIGURATION STUDY FOR MEASURING THE POWER SPECTRUM OF 21 cm EMISSION FROM REIONIZATION. *The Astrophysical Journal*, 753(1):81, jun 2012.
- [50] E. Petroff, E. D. Barr, A. Jameson, E. F. Keane, M. Bailes, M. Kramer, V. Morello, D. Tabbara, and W. van Straten. FRBCAT: The Fast Radio Burst Catalogue. *Publ. Astron. Soc. Australia*, 33:e045, September 2016.
- [51] Planck Collaboration, P. A. R. Ade, N. Aghanim, M. Arnaud, M. Ashdown, J. Aumont, C. Baccigalupi, A. J. Banday, R. B. Barreiro, J. G. Bartlett, N. Bartolo, E. Battaner, R. Battye, K. Benabed, A. Benoît, A. Benoit-Lévy, J. P. Bernard, M. Bersanelli, P. Bielewicz, J. J. Bock, A. Bonaldi, L. Bonavera, J. R. Bond, J. Borrill, F. R. Bouchet, F. Boulanger, M. Bucher, C. Burigana, R. C. Butler, E. Calabrese, J. F. Cardoso, A. Catalano, A. Challinor, A. Chamballu, R. R. Chary, H. C. Chiang, J. Chluba, P. R. Christensen, S. Church, D. L. Clements, S. Colombi, L. P. L. Colombo, C. Combet, A. Coulais, B. P. Crill, A. Curto, F. Cuttaia, L. Danese, R. D. Davies, R. J. Davis, P. de Bernardis, A. de Rosa, G. de Zotti, J. Delabrouille, F. X. Désert, E. Di Valentino, C. Dickinson, J. M. Diego, K. Dolag, H. Dole, S. Donzelli, O. Doré, M. Douspis, A. Ducout, J. Dunkley, X. Dupac, G. Efstathiou, F. Elsner, T. A. Enßlin, H. K. Eriksen, M. Farhang, J. Fergusson, F. Finelli, O. Forni, M. Frailis, A. A. Fraisse, E. Franceschi, A. Frejsel, S. Galeotta, S. Galli, K. Ganga, C. Gauthier, M. Gerbino,

T. Ghosh, M. Giard, Y. Giraud-Héraud, E. Giusarma, E. Gjerløw, J. González-Nuevo, K. M. Górski, S. Gratton, A. Gregorio, A. Gruppuso, J. E. Gudmundsson, J. Hamann, F. K. Hansen, D. Hanson, D. L. Harrison, G. Helou, S. Henrot-Versillé, C. Hernández-Monteagudo, D. Herranz, S. R. Hildebrandt, E. Hivon, M. Hobson, W. A. Holmes, A. Hornstrup, W. Hovest, Z. Huang, K. M. Huffenberger, G. Hurier, A. H. Jaffe, T. R. Jaffe, W. C. Jones, M. Juvela, E. Keihänen, R. Keskitalo, T. S. Kisner, R. Kneissl, J. Knoche, L. Knox, M. Kunz, H. Kurki-Suonio, G. Lagache, A. Lähteenmäki, J. M. Lamarre, A. Lasenby, M. Lattanzi, C. R. Lawrence, J. P. Leahy, R. Leonardi, J. Lesgourgues, F. Levrier, A. Lewis, M. Liguori, P. B. Lilje, M. Linden-Vørnle, M. López-Cañiego, P. M. Lubin, J. F. Macías-Pérez, G. Maggio, D. Maino, N. Mandolesi, A. Mangilli, A. Marchini, M. Maris, P. G. Martin, M. Martinelli, E. Martínez-González, S. Masi, S. Matarrese, P. McGehee, P. R. Meinhold, A. Melchiorri, J. B. Melin, L. Mendes, A. Mennella, M. Migliaccio, M. Millea, S. Mitra, M. A. Miville-Deschênes, A. Moneti, L. Montier, G. Morgante, D. Mortlock, A. Moss, D. Munshi, J. A. Murphy, P. Naselsky, F. Nati, P. Natoli, C. B. Netterfield, H. U. Nørgaard-Nielsen, F. Noviello, D. Novikov, I. Novikov, C. A. Oxborrow, F. Paci, L. Pagano, F. Pajot, R. Paladini, D. Paoletti, B. Partridge, F. Pasian, G. Patanchon, T. J. Pearson, O. Perdereau, L. Perotto, F. Perrotta, V. Pettorino, F. Piacentini, M. Piat, E. Pierpaoli, D. Pietrobon, S. Plaszczynski, E. Pointecouteau, G. Polenta, L. Popa, G. W. Pratt, G. Prézeau, S. Prunet, J. L. Puget, J. P. Rachen, W. T. Reach, R. Rebolo, M. Reinecke, M. Remazeilles, C. Renault, A. Renzi, I. Ristorcelli, G. Rocha, C. Rosset, M. Rossetti, G. Roudier, B. Rouillé d'Orfeuil, M. Rowan-Robinson, J. A. Rubiño-Martín, B. Rusholme, N. Said, V. Salvatelli, L. Salvati, M. Sandri, D. Santos, M. Savelainen, G. Savini, D. Scott, M. D. Seiffert, P. Serra, E. P. S. Shellard, L. D. Spencer, M. Spinelli, V. Stolyarov, R. Stompor, R. Sudiwala, R. Sunyaev, D. Sutton, A. S. Suur-Uski, J. F. Sygnet, J. A. Tauber, L. Terenzi, L. Toffolatti, M. Tomasi, M. Tristram, T. Trombetti, M. Tucci, J. Tuovinen, M. Türler, G. Umana, L. Valenziano, J. Valiviita, F. Van Tent, P. Vielva, F. Villa, L. A. Wade, B. D. Wandelt, I. K. Wehus, M. White, S. D. M. White, A. Wilkinson, D. Yvon, A. Zacchei, and A. Zonca. Planck 2015 results. XIII. Cosmological parameters. *A&A*, 594:A13, September 2016.

- [52] E. Platts, A. Weltman, A. Walters, S.P. Tendulkar, J.E.B. Gordin, and S. Kandhai. A living theory catalogue for fast radio bursts. *Physics Reports*, 821:1–27, Aug 2019.
- [53] Z. Pleunis, D. Michilli, C. G. Bassa, J. W. T. Hessels, A. Naidu, B. C. Andersen, P. Chawla, E. Fonseca, A. Gopinath, V. M. Kaspi, V. I. Kondratiev, D. Z. Li, M. Bhardwaj, P. J. Boyle, C. Brar, T. Cassanelli, Y. Gupta, A. Josephy, R. Karuppusamy, A. Keimpema, F. Kirsten, C. Leung, B. Marcote, K. Masui, R. Mckinven, B. W. Meyers, C. Ng, K. Nimmo, Z. Paragi, M. Rahman, P. Scholz, K. Shin, K. M. Smith, I. H. Stairs, and S. P. Tendulkar. LOFAR Detection of 110-188 MHz Emission and Frequency-Dependent Activity from FRB 20180916B. *arXiv e-prints*, page arXiv:2012.08372, December 2020.
- [54] Jonathan C. Pober, Adrian Liu, Joshua S. Dillon, James E. Aguirre, Judd D. Bowman, Richard F. Bradley, Chris L. Carilli, David R. DeBoer, Jacqueline N. Hewitt, Daniel C. Jacobs, Matthew McQuinn, Miguel F. Morales, Aaron R. Parsons, Max Tegmark, and Dan J. Werthimer. What Next-generation 21 cm Power Spectrum Measurements can Teach us About the Epoch of Reionization. *ApJ*, 782(2):66, February 2014.
- [55] Jonathan R Pritchard and Abraham Loeb. 21 cm cosmology in the 21st century. *Reports on Progress in Physics*, 75(8):086901, Jul 2012.
- [56] J. Xavier Prochaska and Marcel Neeleman. The astrophysical consequences of intervening galaxy gas on fast radio bursts. *MNRAS*, 474(1):318–325, February 2018.
- [57] Emanuele Sobacchi and Andrei Mesinger. The clustering of Lyman  $\alpha$  emitters at  $z \approx 7$ : implications for reionization and host halo masses. *MNRAS*, 453(2):1843–1854, October 2015.
- [58] S. P. Tendulkar, C. G. Bassa, J. M. Cordes, G. C. Bower, C. J. Law, S. Chatterjee, E. A. K. Adams, S. Bogdanov, S. Burke-Spolaor, B. J. Butler, P. Demorest, J. W. T. Hessels, V. M. Kaspi, T. J. W. Lazio, N. Maddox, B. Marcote, M. A. McLaughlin, Z. Paragi, S. M. Ransom, P. Scholz, A. Seymour, L. G. Spitler, H. J. van Langevelde, and R. S. Wharton. The Host

- Galaxy and Redshift of the Repeating Fast Radio Burst FRB 121102. *ApJ*, 834(2):L7, January 2017.
- [59] Anthony Walters, Yin-Zhe Ma, Jonathan Sievers, and Amanda Weltman. Probing diffuse gas with fast radio bursts. *Phys. Rev. D*, 100(10):103519, November 2019.
- [60] Anthony Walters, Amanda Weltman, B M Gaensler, Yin-Zhe Ma, and Amadeus Witzemann. Future cosmological constraints from fast radio bursts. *The Astrophysical Journal*, 856(1):65, 2018.
- [61] C. A. Watkinson and J. R. Pritchard. Distinguishing models of reionization using future radio observations of 21-cm 1-point statistics. *MNRAS*, 443(4):3090–3106, October 2014.
- [62] Shintaro Yoshiura and Keitaro Takahashi. The variance of dispersion measure of high-redshift transient objects as a probe of ionized bubble size during reionization. *MNRAS*, 473(2):1570–1575, January 2018.
- [63] Z. J. Zhang, K. Yan, C. M. Li, G. Q. Zhang, and F. Y. Wang. Intergalactic Medium Dispersion Measures of Fast Radio Bursts Estimated from IllustrisTNG Simulation and Their Cosmological Applications. *ApJ*, 906(1):49, January 2021.
- [64] Z. Zheng, E. O. Ofek, S. R. Kulkarni, J. D. Neill, and M. Juric. Probing the intergalactic medium with fast radio bursts. *The Astrophysical Journal*, 797(1):71, Nov 2014.

## Chapter 4

# Lyman Alpha Emitters and the 21cm Power Spectrum as Probes of Density-Ionization Correlation in the Epoch of Reionization

### Addendum for thesis

This chapter directly builds on the work presented in Chapter 2. Prof. James Rhoads visited McGill in Spetember 2019 and he gave a talk regarding how Lyman Alpha Emitters (LAEs) can probe inhomogenous reionization. Following the talk, Adrian and I had a discussion about how the observed clustering of LAEs would be affected by the density-ionization correlation during the EoR. We thought that we could use our  $\beta$  parametrization (see Chapter 2) to study the signature of density-ionization correlation on LAE statistics.

We placed constraints on  $\beta$  using existing LAE surveys at  $z = 6.6$ . Our results ultimately showed that the clustering of LAEs at  $z = 6.6$  alone cannot be used to rule out uncorrelated and outside-in reionization at 68%. This means that we need observations of LAEs at higher redshifts in order to place stronger constraints on  $\beta$ .

To this end, and building on our previous work, we combined measurements of the 21cm power spectrum through HERA (see Chapter 2 for details) with LAE observations to show that by combining these probes we can place the strongest constraints on  $\beta$ .

## Abstract

Due to the large cross section of Ly $\alpha$  photons with hydrogen, Lyman Alpha Emitters (LAEs) are sensitive to the presence of neutral hydrogen in the intergalactic medium (IGM) during the Epoch of Reionization (EoR): the period in the Universe's history where neutral hydrogen in the IGM is ionized. The type of correlation between the ionized regions of the IGM with respect to the underlying intrinsic LAEs has a pronounced effect on the number of observed LAEs and their apparent clustering. As a result, observations of LAEs during the EoR can be used as a probe of the EoR morphology. Here we build on previous works where we parametrize the density-ionisation correlation during the EoR, and study how the observed number density and angular correlation function (ACF) of LAEs depends on this parametrization. Using Subaru measurements of the number density of LAEs and their ACF at  $z = 6.6$ , we place constraints on the EoR morphology. We find that measurements of LAEs at  $z = 6.6$  alone cannot distinguish between different density-ionization models at 68% credibility. However, adding information regarding the number density, and ACF, of LAEs at  $z = 6.6$  to 21cm power spectrum measurements using the hydrogen Epoch of Reionization Array (HERA) at the midpoint of reionization can rule out uncorrelated and outside-in reionization at 99% credibility.

## 4.1 Introduction

The Epoch of Reionization (EoR) is the period in our Universe's history where the neutral hydrogen making up the intergalactic medium (IGM) is systematically ionized. The timing, duration and morphology of the EoR is still poorly understood. In order to place constraints on these quantities, a number of observational probes have been proposed. One such probe uses the hyperfine transition

of hydrogen, where a 21cm wavelength photon is absorbed or emitted as electrons flip their spin relative to their nucleus [16, 37, 38, 51, 62]. The advantage of using this line as a probe of the EoR is that primordial hydrogen is abundant in the early Universe and measuring the redshifting of this photon enables a three dimensional mapping of the neutral hydrogen. The photon is part of the radio spectrum and is measured in contrast to the Cosmic Microwave Background (CMB). The contrasting temperature between the photon and the CMB is referred to as a differential brightness temperature and is given by

$$\begin{aligned} \delta T_b(\mathbf{r}, z) \approx & (27 \text{ mK}) \left( \frac{T_s(\mathbf{r}, z) - T_\gamma(z)}{T_s(\mathbf{r}, z)} \right) [1 - x_{\text{HII}}(\mathbf{r}, z)] [1 + \delta(\mathbf{r}, z)] \\ & \times \left[ \frac{H(z)/(1+z)}{dv_r/dr} \right] \left( \frac{1+z}{10} \frac{0.15}{\Omega_m h^2} \right)^{1/2} \left( \frac{\Omega_b h^2}{0.023} \right), \end{aligned} \quad (4.1)$$

where  $\mathbf{r}$  is the position vector and  $z$  is the redshift. The local ionization fraction and overdensities are given by  $x_{\text{HII}}(\mathbf{r}, z)$  and  $\delta(\mathbf{r}, z)$  while  $H(z)$  is the Hubble parameter and  $dv_r/dr$  is the line of sight velocity gradient,  $\Omega_b$  and  $\Omega_m$  are the normalized baryon and matter densities and  $h$  is the normalized Hubble parameter [16]. The temperature  $T_s(\mathbf{r}, z)$  is the spin temperature of the hydrogen atoms which describes the relative number hydrogen atoms in their excited Hyperfine states versus ground states. The CMB temperature is given by  $T_\gamma$ . The product of  $x_{\text{HII}}(\mathbf{r}, z)$  and  $\delta(\mathbf{r}, z)$  depends on the morphology of reionization. The way these fields couple to one another in configuration space is referred to as the density-ionization correlation. In general, there are two extreme ways in which these two fields can correlate. The first is having overdense regions in  $\delta$  correspond to ionized regions of  $x_{\text{HII}}$ , conversely, underdense regions in  $\delta$  match neutral regions in the ionization field. This is the inside-out reionization morphology. In this model, ionization bubbles grow around overdense regions of  $\delta$  until adjacent bubbles coalesce and the IGM is fully ionized [15]. Other works based on radiative transfer simulations have found that reionization proceeds rapidly starting from overdense regions, with filamentary structures being ionized last. This leads to an inside-outside-middle (IOM) scenario. This morphology occurs because filaments do not have the necessary star forming efficiency to self ionize [12]. The second extreme morphology is outside-in reionization. In this model, overdense regions in  $\delta$  correspond

with neutral regions of hydrogen. Conversely, underdense regions in  $\delta$  correspond to ionized regions in  $x_{\text{HII}}$ . In this scenario, the underdense regions are ionized first and the overdense regions ionized last [4, 49]. We refer to inside-out reionization as having positively correlated statistics between  $\delta$  and  $x_{\text{HII}}$  in contrast to outside-in reionization scenarios which has negatively correlated statistics between the ionization and density fields. The type of correlation between these fields is indicative of a particular reionization morphology. Previous works have studied how these different models affect the brightness temperature  $\delta T_b$  as well as statistical quantities that depend on it [1, 75]. The correlation between these fields can vary in position and as a function of redshift resulting in correlations between  $\delta$  and  $x_{\text{HII}}$  with statistical combinations of inside-out and outside-in [14, 39]. A method to parametrize the correlation between these fields has previously been proposed by [53].

The way these two fields correlate also has consequences for other probes of the EoR. Another such probe is the measurement of Lyman alpha flux from emitting sources during the EoR. Due to the large cross-section of Lyman alpha photons with hydrogen, even traces of neutral hydrogen left in the IGM during reionization can significantly reduce the observed Lyman alpha flux. As a result, the number of observed LAEs is expected to significantly decrease as we observe higher redshifts, making observation of LAEs a useful probe of reionization [7, 9, 23, 25, 40, 43, 45, 46, 63, 72, 76]. Due to the sensitivity of intervening hydrogen along the line of sight, the observed number density as well as the clustering of the LAEs is influenced by the morphology of the ionization field [2, 26, 29]. As a result, we can make deductions about the ionization state of the IGM through measurement of the statistics of LAEs during the EoR. However in order to study how the morphology of the EoR affects the flux, number count and positions of visible LAEs, we must model the intrinsic luminosity of the LAEs as they leave their host halos. Assessing the intrinsic luminosity of LAEs has been difficult because the line profile of  $\text{Ly}\alpha$  flux depends on the highly uncertain dynamics of the interstellar medium (ISM). Since galaxies are not homogeneous (rather they are clumpy) and may have complex inflows and outflows, the  $\text{Ly}\alpha$  line profile emerging from the galaxy is potentially complex, requiring radiative transfer analysis for the outflowing/inflowing material [19, 20, 22, 72, 73]. As a result, the intrinsic luminosity of LAEs are subject to many uncertainties, which has led previous studies to adopt models that capture the physical range of intrinsic scenarios [5, 10].

In this paper we build on our previous work, where we parametrized the density-ionization correlations in the EoR, and study the dependence of LAE statistics on this parametrization. In order to study how the EoR morphology affects the intrinsic statistics of LAEs, we adopt a model for the intrinsic luminosity of LAEs as they leave their host haloes, which was introduced in [67,74]. This model allows for flexibility in the physical range of intrinsic luminosities of LAEs. Using existing measurements of LAE statistics at redshift  $z = 6.6$  from the Subaru Survey, we place constraints on this parametrization and therefore the EoR morphology. We then forecast the type of constraints that can be placed on the EoR morphology by combining the HSC Subaru experiment at  $z = 6.6$  and a measurement of the 21cm power spectrum using the hydrogen Epoch of Reionization Array (HERA). Since such a hypothetical 21cm measurement does not yet exist, we simulate such a measurement assuming the HERA instrument is running at its forecasted sensitivities. In these forecasts, we also include the astrophysical parameters that have been used to model EoR physics, exploring any new degeneracies that arise from the inclusion of arbitrary density-ionization correlations.

This paper is structured as follows. In Section 4.2 we describe the parameters used in our simulation as well as introduce our parametrization of the ionization-density correlation. At the end of Section 4.2 we describe how the 21cm power spectrum depends on this parametrization. In Section 4.3 we describe our model for the intrinsic luminosity of the LAEs as well as their optical depth through the IGM. In Section 4.4 we describe the statistical properties of LAEs and study how they vary as a function of the density-ionization correlation. In Section 4.5 we describe the Subaru Survey of LAEs at  $z = 6.6$  which we use to place constraints on our parametrization. Since measurements of the 21cm power spectrum do not yet exist, we also introduce our fiducial 21cm instrument (HERA) in order to forecast the constraints that can be placed on our parametrization using hypothetical measurements of the 21cm power spectrum and LAEs. Finally in Section 4.6 we present our results and conclude in Section 6.7. Throughout this work we set the  $\Lambda$ CDM parameters to  $\sigma_8 = 0.81$ ,  $\Omega_m = 0.31$ ,  $\Omega_b = 0.048$ ,  $h = 0.68$ , consistent with Planck 2015 results [57]

## 4.2 EoR Simulation

To generate temperature fields, halo fields, density and ionization boxes representative of different EoR models we use the 21cmFAST package [47]. Density fields are obtained through the Zeldovich approximation while the excursion set formalism of [17] is employed to generate the ionization and halo boxes. Using the evolved density fields, halo boxes are generated by computing the collapsed fraction of matter, larger than a threshold halo mass. The halo boxes are generated on high resolutions grids of  $800^3$  voxels corresponding to a comoving side length of 200 Mpc while the density and ionization fields use coarser boxes of  $200^3$  voxels corresponding to the same comoving side length. For further details about how 21cmFAST generates reionization models see [47, 66].

We generate different EoR scenarios by varying a number of adjustable parameters whose goal is to capture variations in the detailed astrophysics of reionization. We maximize the physical range of EoR scenarios by adjusting the parameters  $M_{\text{turn}}$ ,  $R_{\text{mfp}}$  and  $\zeta$ . Physically, the turnover mass  $M_{\text{turn}}$  determines the mass of a halo at which star formation is efficient. Values of  $M_{\text{turn}} \simeq 10^8 M_{\odot}$  correspond to a virial temperature of  $T_{\text{vir}} \simeq 2 \times 10^4 \text{K}$  at  $z = 9$ . Halo masses below  $M_{\text{turn}}$  have exponential suppression in star formation. The smallest halos have suppressed star formation due to supernova feedback. Roughly, this sets the mass scale for the ionizing sources. The unitless astrophysical parameter  $\zeta$  determines the ionizing efficiency of the sources. The ionizing efficiency depends on other astrophysical parameters such as the escape fraction of ionizing photons (the fractions of UV photons which escape their host halos). A large value of  $\zeta$  will imply more ionizing photons per stellar baryon while a smaller ionizing efficiency will entail less ionizing photons are emitted for each ionizing source. Previous studies using radiative hydrodynamical simulations have found that the ionizing efficiency depends on halos mass [18, 32, 35, 77]. In this paper we approximate  $\zeta$  to be constant. The cutoff-radius  $R_{\text{mfp}}$  sets the maximum size of the ionized bubbles. Recently, [6] have developed a more realistic implementation of a cutoff-radius, which better suppresses large scale structure as compared to the standard treatment of  $R_{\text{mfp}}$ . This implementation involves modifying the excursion set conditions of [17] to account for the excess photons required to ionize a region. We leave this for future work. Variation of

these parameters affect the timing and duration of reionization and have been studied in previous studies [11, 31, 36, 54, 58]. We use these parameters to generate a wide variety of EoR models that bracket physical scenarios. However these parameters operate under a predominately inside-out formalism in which the density field  $\delta$  is positively correlated with the ionization field  $x_{\text{HII}}$  and therefore do not capture the different density-ionization correlations indicative of different EoR morphologies. In order to extend the physical scenarios bracketed by the astrophysical parameters to outside-in morphologies, we need to modify the simulation. This procedure was the focus of previous work in [75] and [53]. We briefly reproduce it here.

### 4.2.1 Extending 21cmFAST to outside-in

In order to produce outside-in reionization morphologies we require that the temperature field  $\delta T_b$  be made from density field and ionization fields which are negatively-correlated. To do this, we flip the sign of the density field at its high-redshift initial conditions [61]. Once the resulting overdensity field has evolved and undergone non-linear evolution, overdense regions will be inverted to underdense regions while underdense regions will be inverted to overdense regions. The resulting ionization field will be inverted with respect to the original, non-sign flipped field. If the inverted ionization field is paired with its original, non-sign flipped, density field in Equation (4.1), then the resulting temperature field will contain the negatively correlated density-ionization statistics. The underdense regions in the temperature field are now coupled to ionized bubbles while overdense regions are coupled to neutral regions, i.e. the temperature field will contain the statistics of outside-in reionization.

### 4.2.2 $\beta$ Parametrization

We can produce EoR scenarios where the density and ionization field are correlated by arbitrary amounts. To do this we draw a random phase  $\phi$  from a Gaussian of standard deviation  $\sigma$ , and phase shift each Fourier mode of the Fourier transformed density field  $\tilde{\delta}$ , by  $\phi$ . When returning the overdensity box to configuration space, overdense and underdense regions in  $\delta$  will have shifted

**Table 4.1:** Lexicon for physical models and their respective correlations

$\beta$	Moniker for Field correlations $x_{\text{HII}} \delta$	Physical Model
1	Correlated	Inside-out
$1 > \beta > 0$	Partially correlated	Mostly inside-out
0	Uncorrelated	Random
$0 < \beta < -1$	Partially anti-correlated	Mostly outside-in
-1	Anti-correlated	Outside-in

from their original positions, decorrelating the density field from its original corresponding ionized fraction box. We apply this procedure to the density field at high redshift, i.e. at the initial conditions, before the density field undergoes non-linear evolution.

The decorrelation  $\sigma$ , and sign flip are folded into a single parameter which controls the correlation between the ionization field and density field. This parameter is denoted by  $\beta$  and is defined as

$$\beta \equiv \begin{cases} \text{sgn}(\sigma) \left(1 - \frac{|\sigma|}{\pi}\right) & \sigma \neq 0 \\ \pm 1 & \sigma = 0 \end{cases} \quad (4.2)$$

where  $\text{sgn}(\sigma)$  is the sign of  $\sigma$  which indicates whether we are decorrelating from an outside-in model ( $\text{sgn}(\sigma) = -1$ ) or an inside-out model ( $\text{sgn}(\sigma) = +1$ ). The case  $\sigma = 0$  leads to two values of  $\beta$ , corresponding to the original inside-out and outside-in models. We assign these cases the values  $\beta = +1$  and  $\beta = -1$  respectively. The resulting parameterization can be continuously dialled from +1 to -1 to go from a fully inside-out scenario to a fully outside-in scenario. Positive values of  $\beta$  indicate scenarios where an initially correlated density and ionization field are decorrelated by  $\sigma$  while a negative  $\beta$  indicates a scenario where a negatively correlated density and ionization field are decorrelated by  $\sigma$ . We summarize the terminology of this parameterization in Table 4.1. We can see from Figure 4.1 that the statistics of observed LAEs is sensitive to  $\beta$ . In Section 4.4 we explore this dependence.

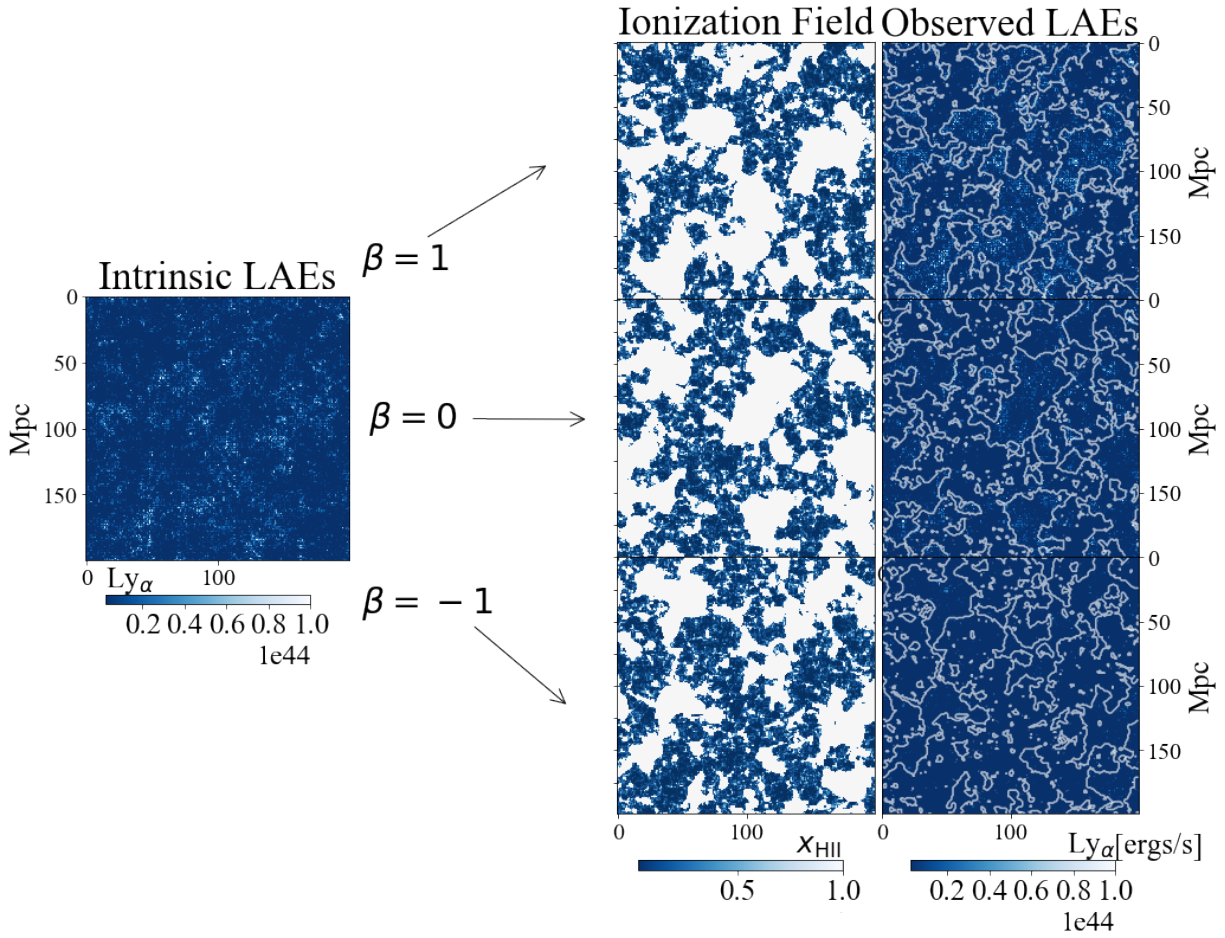


**Figure 4.1:** Example fields demonstrating the effect that different  $\beta$  correlations have on the observed LAEs. The intrinsic LAEs (left) roughly traces the underlying density field. When computing the Ly $\alpha$  optical depth using the ionization field  $x_{\text{HII}}$  (middle), we arrive at the observed LAEs (right). Neutral regions suppress Ly $\alpha$  radiation from the observer. The ionized regions from the ionization field are superimposed as contours on the observed LAEs to emphasize the correlation between the two fields. Inside-out scenarios (with  $\beta > 0$ ) have positively correlated density and ionization fields. Conversely, outside-in scenarios (with  $\beta < 0$ ) have negatively correlated fields. The case  $\beta = 0$  refers to the scenario where the ionization field and density field are entirely uncorrelated. These boxes are at redshift  $z = 7.6$  with fiducial astrophysical parameters  $\zeta_0 = 25$ ,  $M_{\text{turn},0} = 5 \times 10^8 M_{\odot}$ ,  $R_{\text{mfp},0} = 30 \text{Mpc}$ .

### 4.2.3 Variation of $\Delta_{21}^2(z)$ as a Function of $\beta$

Our forecasts presented in Section 4.5 make use of both LAE observations and measurement of the 21cm power spectrum. To gain intuition on how  $\beta$  affects the 21cm power spectrum  $\Delta_{21}^2$ , we briefly summarize previous work (see [53] for more detail). The correlation parameter  $\beta$  affects  $\Delta_{21}^2$ , which is defined through the brightness temperature field as

$$\Delta_{21}^2(k) \equiv \frac{k^3}{2\pi^2} \frac{\langle |\widehat{\delta T_b}(\mathbf{k})|^2 \rangle}{V} \quad (4.3)$$

where  $V$  is the survey volume,  $\widehat{\delta T_b}$  is the Fourier transform of the brightness temperature field (into a space defined by spatial wavevector  $\mathbf{k}$ ), and the angular brackets indicate an average over shells of constant  $k \equiv |\mathbf{k}|$ . The brightness temperature is sensitive to the inside-out versus outside-in morphology through the cross term  $x_{\text{HII}}\delta$  in Equation (4.1). Consider an inside-out ( $\beta = 1$ ) model. Decreasing  $\beta$  decreases the density field's original correlation with  $x_{\text{HII}}$ , and increases the chances that neutral regions overlap with overdense regions in  $\delta$ . As a result, we find increasing power on large scales as we decrease  $\beta$  from +1 to -1. During the first half of reionization, the ionized bubbles are still small and so reionization has yet to make a significant imprint on the brightness temperature field. Altering the density-ionization correlation via  $\beta$  thus has little effect on the power spectrum and all the  $\beta$  models converge at high  $z$ . As one approaches a global ionization fraction of  $\sim 0.5$ , the ionized bubble morphology has its largest influence on the power spectrum, and thus it is there that one sees the greatest sensitivity to  $\beta$ . At the late stages of reionization, the IGM is increasingly ionized and  $\Delta_{21}^2$  loses its sensitivity to  $\beta$ .

## 4.3 LAE Models

In order to infer the morphology of the EoR using Ly $\alpha$  radiation arriving at an observer, we need to model the absorption of the Ly $\alpha$  photons by the neutral hydrogen in the IGM, as well as model the intrinsic properties of the source. Our model entails two steps, assigning an intrinsic luminosity to the LAEs before the photons enter the IGM, and then computing the Lyman alpha optical depth

along the line of sight, taking into account the reionization of the Universe. We first discuss the optical depth of the Lyman alpha photons and then discuss how we model the intrinsic luminosity of the LAEs.

### 4.3.1 Ly $\alpha$ Optical Depth

Following the approach of [28, 41, 69, 76], we model the optical depth  $\tau_\alpha$  for Lyman alpha photons moving through a neutral hydrogen gas cloud of number density  $n_{\text{HI}}(z)$  from emitted redshift  $z_e$  to observed redshift  $z_{\text{obs}}$  by

$$\tau_\alpha = \int_{z_{\text{obs}}}^{z_e} dz \frac{cdt}{dz} x_{\text{HI}}(z) n_{\text{HI}}(z) \sigma_\alpha(\nu, T_k), \quad (4.4)$$

where  $x_{\text{HI}}(z)$  is the fraction of neutral hydrogen and  $\sigma_\alpha(\nu, T_k)$  is cross section for Lyman alpha photons at frequency  $\nu$  within a hydrogen gas cloud at temperature  $T_k$ . The frequency dependence of  $\sigma_\alpha$  accounts for the redshifting of the Ly $\alpha$  photons as they move through the IGM. As the photon moves away from line center, it becomes less likely to be scattered by the intervening hydrogen. Typically the frequency dependence of  $\sigma_\alpha$  is parametrized in terms of the dimensionless frequency  $x = (\nu - \nu_\alpha)/\Delta\nu_\alpha$  where  $\nu$  is the frequency of the Ly $\alpha$  photons as they encounter a clump of neutral hydrogen gas and  $\nu_\alpha = 2.47 \times 10^{15}$  Hz is the emitted frequency of a Ly $\alpha$  photon in the rest frame. The quantity  $\Delta\nu_\alpha$  is the thermal width of the line  $\Delta\nu_\alpha = \sqrt{2k_B T \nu_\alpha^2 / m_p c^2}$ , where  $m_p$  is the mass of the proton and  $k_B$  is the Boltzmann constant. The integration variable in Equation 4.4 occurs over the redshift  $z$  which is related to the frequency  $\nu$  of the Ly $\alpha$  photons using  $1 + z = \nu_\alpha / \nu$ . Typically  $x$  can be thought of as the ratio of frequency distance from line center to the thermal width of the line. The Ly $\alpha$  cross section can be written as the product

$$\sigma_\alpha(\nu, T_k) = \sigma_{\alpha_0} \phi(x) \quad (4.5)$$

where  $\sigma_{\alpha_0}$  is the cross section at line center and  $\phi(x)$  is a function which takes into account how  $\sigma_\alpha$  varies as a function of this dimensionless frequency (as it moves along its line of sight). The

cross section  $\sigma_{\alpha_0}$  at line center is given by

$$\sigma_{\alpha_0} = \frac{1}{\sqrt{\pi}\Delta_{\nu_\alpha}} \frac{f_\alpha \pi e^2}{m_e c} \simeq 5.9 \times 10^{-14} \sqrt{\frac{T_k}{10^4 \text{K}}} \quad (4.6)$$

where  $f_\alpha = 0.416$  is the Ly $\alpha$  oscillator strength,  $e$  is the charge of the electron,  $m_e$  is the mass of the electron and  $c$  is the speed of light. Typically how  $\sigma_\alpha$  varies along the line of sight can be broken into two regimes: (1) frequencies close to line center which we refer to as the core of the line (Gaussian line shape) and (2) frequencies further away from line center which we refer to as the wing (Lorentzian line shape). Both these regimes can be folded into the Voigt function defined by:

$$\phi(x) = \frac{a_\nu}{\pi} \int_{-\infty}^{\infty} dy \frac{e^{-y^2}}{(y-x)^2 + a_\nu^2} \quad (4.7)$$

where  $a_\nu = 4.7 \times 10^{-4} \sqrt{\frac{T_k}{10^4 \text{K}}}$  is the Voigt parameter. To evaluate Equation (4.7), we use the approximation made in [69]. The cross section  $\sigma_\alpha(\nu, T_k)$  is tightly peaked close to line center  $\nu_{\alpha_0}$  and then drops rapidly as a function of  $x$ . The cross-over from core to wing occurs at  $x \simeq 3$ , which occurs on sub-grid scales in our simulation. In order to properly model the absorption of Ly $\alpha$  photons by neutral hydrogen within the core of the line, one must have sufficient resolutions of  $n_{\text{HI}}$  and  $x_{\text{HII}}$  to track the propagation of photons for  $x < 3$  which correspond to physical scales of  $\ll 1\text{Mpc}$ . Since our density and ionization boxes described in Section 4.2 have resolution of 1.5Mpc per pixel we use a weighted average of  $\sigma(x)$  for values of  $x \ll 3$  and then switch to wing absorption through the wing for  $x > 3$  through Equation (4.7). This cross-over point from core to wing has a weak dependence on the temperature  $T_k$  of the gas. The LAEs are assumed to lie within ionized bubbles, and so we set  $T = 10^4\text{K}$  which is consistent with a photoionised gas at the mean density [24]. This yields the cross-over point  $x \simeq 3$ . Beyond the cross-over point, the absorption of Ly $\alpha$  photons in the IGM also depends on the temperature of the neutral hydrogen in the IGM. Depending on the particular reionization model chosen, the temperature  $T_k$  of the gas has a physically motivated range of  $1\text{K} < T_k < 10^3\text{K}$ . There are physically motivated arguments for both extreme temperature scenarios; the  $10^3\text{K}$  scenario is due to x-ray heating of the neutral IGM, for

example. In the neutral IGM, we set the temperatures of the gas to be  $T_k = 1\text{K}$ , which is consistent with an adiabatically cooled gas [41]. This is not expected to be valid for models where x-rays have heated the IGM. This negligibly affects our transmission profile. Our conclusions presented in Section 4.6 do not depend on how one chooses to model the temperature of the gas.

### 4.3.2 LAE Intrinsic Luminosity

We assume that the intrinsic Ly $\alpha$  luminosity of the emitters is proportional the mass of the halo in which it resides. This model is similar to one used in [67, 74]. The intrinsic luminosity is spread out over the line profile of the Ly $\alpha$  photons emerging from the ISM. We test two different emerging profiles: a Gaussian profile at line center, i.e. centered at  $v = 0\text{ km/s}$ , with standard deviation  $\Delta v = 200\text{ km/s}$  where  $v$  is the velocity offset from systemic, and a Dirac delta function at line center  $v = 0\text{ km/s}$ . We ensure that the Ly $\alpha$  flux underneath both line profiles is identical. Due to the large scales of our simulations, we average over the intrinsic line profile of the Ly $\alpha$  photons as they leave the ISM by computing an effective cross section for subgrid scales. This approximation, which is discussed in Section 4.3.1, leads to both line profiles giving similar results. For computational simplicity, we use the delta function line profile in our analysis. In reality, the line profile of the Ly $\alpha$  photons is much more complex, requiring radiative transfer analysis for the outflowing/inflowing material. Our simple model does not intend to capture the small scale radiative transfer physics in the ISM which are required to realistically model the intrinsic luminosities of LAEs. These models have been studied in other works such as [7, 27, 28, 76]. Rather, we use this framework to bracket the physical range of intrinsic clustering by providing flexibility to the high degree of uncertainty regarding the intrinsic properties of the source. We then study how the EoR morphology, imprinted through the opacity in Equation (4.4), affects the luminosity, clustering and number densities of the intrinsic LAEs. To this objective, we have also studied offsetting our line profiles to  $\pm 200\text{ km/s}$  with no affect to our conclusions and results. The intrinsic luminosity of a Ly $\alpha$  emitter residing in a halo of mass  $M_h$ , before the Ly $\alpha$  flux is altered by the IGM, is given by,

$$L_\alpha^{\text{int}} = L_\alpha^{\text{min}} \left( \frac{M_h}{M_\alpha^{\text{min}}} \right)^\gamma \chi \quad (4.8)$$

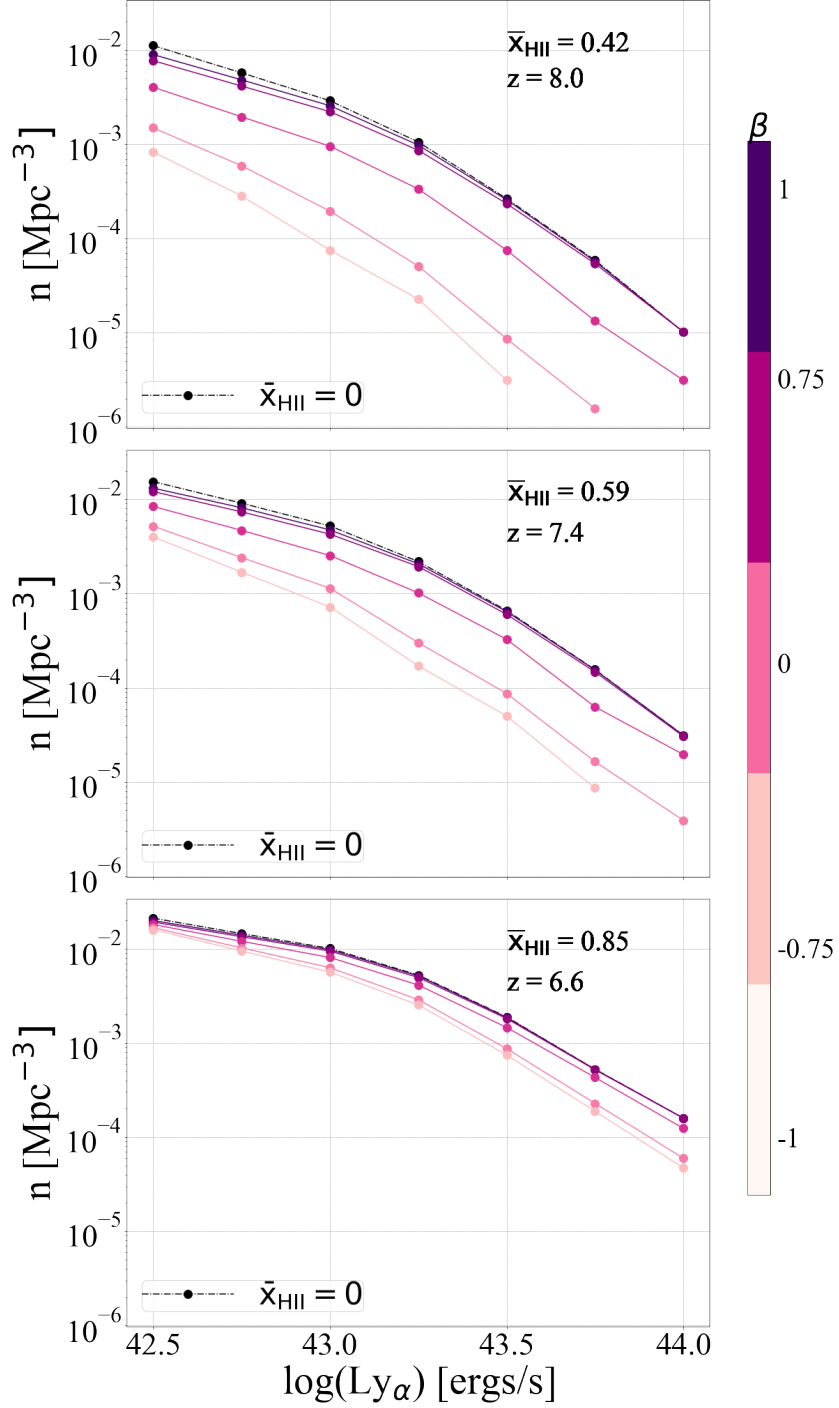


**Figure 4.2:** The Ly $\alpha$  luminosity function of LAEs as a function of  $\beta$ , at three different stages of reionization. In each panel, the dotted curve corresponds to the luminosity function of the intrinsic field (i.e. with  $\bar{x}_{\text{HII}} = 0$ ). Notice that extreme outside-in reionization scenarios ( $\beta \sim -1$ ), lead to concealing the intrinsically brightest LAEs. At high redshift, where there are fewer intrinsically bright LAEs, this leads to a sharp drop-off of the Ly $\alpha$  luminosity function. In each of these curves, the detection threshold  $\text{Ly}\alpha^{\text{min}}$  corresponds to mass  $M_{\alpha}^{\text{min}} \sim 10^{10}M_{\odot}$  with  $f_{\text{duty}} = 1$ .

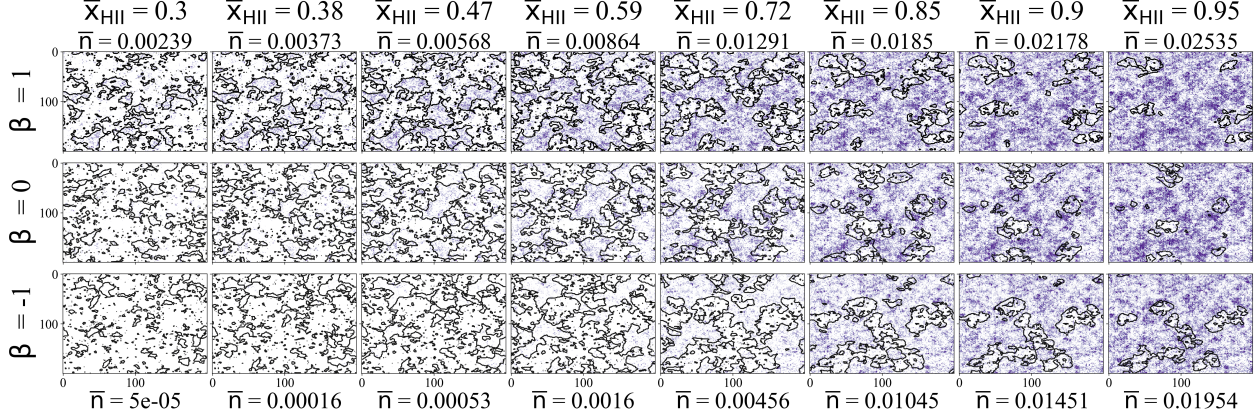


**Figure 4.3:** Evolution in the number of observed LAEs for positively correlated models ( $\beta > 1$ ), uncorrelated models ( $\beta = 0$ ), and negatively correlated models ( $\beta = -1$ ) at different mean ionized fractions. The mean number density of LAEs  $\bar{n}$ , for the extreme  $\beta = 1$  and  $\beta = -1$  models are noted. Notice the rapid change in the number of LAEs for  $\beta = -1$  models. As the ionized regions grow large enough to encompass the high density regions, the number of LAEs increases rapidly. The uncorrelated model has ionized regions which are random with respect to the underlying density field. Positively correlated models have the ionized regions that always correspond to the high density regions, where the intrinsic number density of LAEs is greatest.

where  $\chi = 0$  or  $1$  is a random variable that encodes the uncertainty whether a given halo hosts an LAE. The probability that a halo hosts an LAE, i.e. the probability that  $\chi = 1$ , is equal to the duty cycle  $f_{\text{duty}}$ . We assume  $f_{\text{duty}}$  to be independent of its mass. The luminosity  $L_{\alpha}^{\text{min}}$  is the instrumental threshold for detection of an LAE, which we set to be  $L_{\alpha}^{\text{min}} = 2.5 \times 10^{42}$  ergs/s, corresponding to the detection limit of the HSC Ultra Deep Field at redshift  $z = 6.6$ . The mass  $M_{\alpha}^{\text{min}}$  is the halo mass corresponding to the detection threshold of  $L_{\alpha}^{\text{min}}$ . Haloes with masses less than  $M_{\alpha}^{\text{min}}$  lead to intrinsic LAE luminosities that are below the detection threshold and so unobservable. The factor of  $\gamma$  is the power law index which controls the inclination of the intrinsic Ly $\alpha$  luminosity function. These parameters provide the necessary flexibility in the intrinsic Ly $\alpha$  luminosity function to bracket the physical range of the clustering signal [67]. Take for example the normalization constant  $M_{\alpha}^{\text{min}}$ , which shifts the intrinsic luminosity function of the LAEs left and right. Values of  $M_{\alpha}^{\text{min}} \simeq 10^{11} M_{\odot}$  allow only the largest LAEs to be observable (i.e. above the detection threshold  $L_{\alpha}^{\text{min}}$ ). This leads to a scenario where only the largest haloes contribute

to the survey. In contrast, a lower  $M_\alpha^{\min}$  means that the smaller LAEs will also be observable by our instruments, which allow us to measure LAEs in the underdense regions of the Universe. The normalization mass  $M_\alpha^{\min}$  will therefore affect the statistics of the intrinsic LAEs. The duty cycle  $f_{\text{duty}}$ , adjusts the number of halos in the survey which shifts the intrinsic luminosity function up and down. The parameter  $f_{\text{duty}}$  affects the number densities of intrinsic LAEs but doesn't affect the clustering of the intrinsic LAEs. Finally  $\gamma$  tilts the LAE luminosity function. For example, reducing  $\gamma$  from 1 to  $\gamma = 2/3$  decreases the number of intrinsically bright LAEs and increases the number of faint LAEs. Varying  $\gamma$  within the range  $1/2 \leq \gamma \leq 1$  does not significantly affect the clustering signal of the LAEs or the observed number density of LAEs (see Sections 4.4.2, 4.4.3). For the remainder of the analysis we set  $\gamma = 1$  without loss of generality. A possible shortcoming of this model is that the brightest LAEs are assumed to reside in the overdense regions of  $\delta$ , the location of the largest halos. This might not be the case if one takes into account the UV reddening of dusty galaxies in the vicinity of larger halos. Such a scenario would cause an apparent dimming of bright LAEs hosted in large dusty halos [50]. We leave these broader range of scenarios for future work.

Simulations have also suggested that the escape fraction of ionization photons from their host halos may decrease within increasing halo mass [32, 35, 77]. Since the recombination of hydrogen atoms in the ISM are the primary producer of Ly $\alpha$  photons, scenarios where  $f_{\text{esc}}$  decreases with  $M_h$  yield a halo mass dependent intrinsic luminosity that scales as  $1 - f_{\text{esc}}$ . As a result, a halo mass dependent  $f_{\text{esc}}$  simultaneously affects both Ly $\alpha$  transmission through the IGM, as well as the intrinsic luminosity of the LAEs. For example, if  $f_{\text{esc}}$  decreases with  $M_h$  then the intrinsically brightest LAEs are hosted by the largest halos which may have suppressed ionizing efficiency  $\zeta$  compared to smaller mass halos. Although an intrinsically brighter LAE would make it easier to observe, it would correspond to a region where IGM transmission is made more difficult by decreased  $\zeta$ . Similarly, the intrinsically dimmest LAEs (small  $M_h$ ) may have enhanced Ly $\alpha$  transmission through the IGM due to larger  $\zeta$ . This scenario is in contrast with our model where we assume a constant ionizing efficiency  $\zeta$ . Adoption of a halo mass dependent  $f_{\text{esc}}$  that decreases with  $M_h$  into our models would require modification of Equation 4.8 while simultaneously modifying

the bubble sizes around the LAEs, which affects IGM transmission. However in our models, adjusting the bubble sizes doesn't have a dominant effect on the observability of an LAE. To see this, recall that in Section 4.3.1 we perform a weighted average of the Ly $\alpha$  cross-section for subgrid scales. This makes the ionization state of the first few pixels important in determining the observational properties of the LAE. Therefore perturbing the existing bubble size around an LAE will not significantly affect IGM transmission as compared to the intrinsic properties of the source. However, a halo mass dependent  $\zeta$  can alter the timeline of reionization, which might affect whether a region is ionized at all or not. Our assumption of a constant  $\zeta$  would potentially underestimate the contribution of UV photons by small mass halos and overestimate the contribution of UV photons from large halos. However our fiducial model (introduced in Section 4.5.4) is one where the halos size are in the middle of these two extremes, where the assumption of a constant  $\zeta$  is most appropriate.

We assign an intrinsic Ly $\alpha$  luminosity to each halo in our simulation box according to Equation (4.8). The observed luminosity of the LAE after the Ly $\alpha$  photons pass through the IGM is given by

$$L_\alpha = L_\alpha^{\text{int}} e^{-\tau_\alpha}, \quad (4.9)$$

where  $e^{-\tau_\alpha}$  is computed by integrating Equation (4.4) along the line of sight for a given reionization scenario. LAEs with apparent luminosity  $L_\alpha$  satisfying  $L_\alpha < L_\alpha^{\text{min}}$  are removed from our mock survey since they have Ly $\alpha$  luminosity below the detection threshold. To mimic the LAEs observed by the Subaru Survey, which has redshift thickness  $\Delta z = 0.1$  (corresponding to  $\sim 37\text{Mpc}$  at  $z = 6.6$ ), we slice our observed LAEs corresponding to the same redshift thickness,  $\Delta z = 0.1$  (see Section 4.5.1). In the following Section we study how the morphology of the EoR affects the observability of these LAEs.

## 4.4 Dependence of LAE Statistics on $\beta$

The observed Ly $\alpha$  flux from a LAE is very sensitive to any neutral hydrogen that lies along its line of sight. Consequently, the Ly $\alpha$  flux from LAEs which reside near neutral regions is severely

attenuated. These LAEs are less likely to be observed over the detection threshold  $L_{\alpha}^{\min}$ . Conversely, LAEs coupled to regions of high  $x_{\text{HII}}$  (ionized bubbles) are more likely to be observed. Since the underlying intrinsic LAEs roughly trace the density field  $\delta$ , we can control how the intrinsic LAEs couple to  $x_{\text{HII}}$  by varying  $\beta$ , which controls the coupling between  $\delta$  and  $x_{\text{HII}}$ . In this Section, we study the effect that different EoR morphologies have on our measurements of the LAEs. In Section 4.4.1 and 4.4.2 we study how  $\beta$  affects the LAE luminosity function and mean number density of LAEs, while in Section 4.4.3 we study how the clustering of LAEs depends on the EoR morphology.

#### 4.4.1 Dependence of the Observed LAE Luminosity Function on $\beta$

Let us consider the underlying intrinsic LAEs at redshift  $z$ . Recall that the value of  $\beta$  changes how the ionization field couples to the intrinsic LAEs. Values of  $\beta \simeq 1$  imply an inside-out reionization scenario where the ionization field is correlated with the underlying density field. In this scenario, LAEs found in overdense regions will correspond to regions of high  $x_{\text{HII}}$  which reduces the effect of the attenuation factor in Equation (4.4) and makes these LAEs more likely to be observed. Conversely, LAEs which reside in underdense regions of  $\delta$  will correspond to regions of low  $x_{\text{HII}}$ , where the presence of neutral hydrogen will obscure them. Since the overdense regions are more likely to host the intrinsically brightest LAEs,  $\beta = 1$  will tend to allow the brightest LAEs to be observed. This maximizes the amount of intrinsically bright LAEs which are observable. We can see the effect that an inside-out reionization scenario has on the observability of the LAEs in Figure 4.1.

Figure 4.2 illustrates the effect of decreasing  $\beta$  on the LAE luminosity function. As we decrease  $\beta$  from  $\beta = 1$ , ionized bubbles in  $x_{\text{HII}}$  become increasingly decorrelated from the underlying density field  $\delta$ , and so the placement of the ionized regions are increasingly randomized in relation to the intrinsic LAEs. This means that some overdense regions in  $\delta$  will now couple to regions of low  $x_{\text{HII}}$ , obscuring the LAEs which reside in that region. This leads to a decrease in the bright end of the LAE luminosity function from the purely inside-out ( $\beta = 1$ ) scenario. As we continue to decrease  $\beta$  to  $\beta \simeq -1$ , corresponding to an outside-in reionization scenario, ionized bubbles

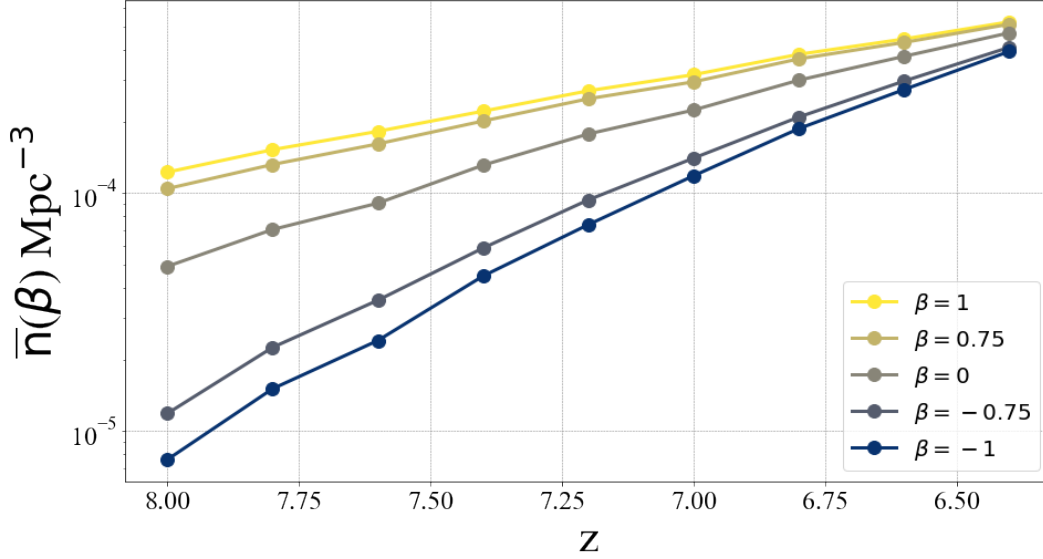


**Figure 4.4:** Evolution of the number density of LAEs for different reionization morphologies. Inside-out driven models ( $\beta > 0$ ) initially have more observable LAEs since the intrinsically densest regions of the IGM are ionized first. As the ionized regions grow to encapsulate the underdense regions in  $\delta$ , the mean number density grows slowly as compared to outside-in driven models ( $\beta < 0$ ), where the underdense regions are first to be ionized. In this scenario, the number density of LAEs increases rapidly as the intrinsically densest regions are ionized. We use the same fiducial model as in Figure 4.1

will be increasingly coupled to underdense regions in  $\delta$ . LAEs which reside in the underdense regions become more likely to be observed by experiment, while the flux from LAEs which reside in overdense regions in  $\delta$  will be coupled to regions of low  $x_{\text{HII}}$ , and therefore severely attenuated. Since the brightest LAEs reside in the overdense regions, we notice a sharp decrease in the bright end of the LAE luminosity function. We can see the sharp dropoff of bright LAEs for outside-in driven models in Figure 4.2. This sharp dropoff of bright LAEs for outside-in driven models becomes even more pronounced at higher redshift where there are fewer intrinsically bright LAEs. As outside-in reionization proceeds, the ionized regions grow and expose the overdense regions where the brightest LAEs reside. By the end of outside-in reionization, only the intrinsically brightest LAEs are still unobservable. Referring again to Figure 4.2, this tilts the Ly $\alpha$  luminosity function compared to extreme inside-out models.

#### 4.4.2 Dependence of the Mean Number Density of LAEs on $\beta$

From the LAE luminosity function we can extract another useful quantity, the mean number density  $\bar{n}$ , of the observed LAEs. This quantity represents the number of observable LAEs per unit volume and can be derived by summing over the luminosity function:

$$\bar{n} = \int_{M_{\alpha}^{\min}}^{\infty} n(M_h) dM_h, \quad (4.10)$$

where  $M_{\alpha}^{\min}$  corresponds to the detection threshold  $L_{\alpha}^{\min}$ . The number density of LAEs has already been constrained to be  $\bar{n} = 4.1_{-0.8}^{+0.9} \times 10^{-4} \text{Mpc}^{-3}$  at  $z = 6.6$  corresponding to a minimum threshold luminosity of  $L_{\alpha}^{\min} = 2.5 \times 10^{42} \text{ergs/s}$  [52]. The EoR morphology will influence which LAEs in the intrinsic field are observable, and so will influence the measured number density of LAEs,  $n_{\text{obs}}$ .

To see how  $\beta$  influences  $n_{\text{obs}}$ , note that the intrinsic LAEs trace the underlying halo field (Equation (4.8)). Therefore overdense regions of  $\delta$  contain many more LAEs than the underdense regions of  $\delta$ . For inside-out reionization scenarios ( $\beta = 1$ ), overdense regions in  $\delta$  correspond to regions of high  $x_{\text{HII}}$  in the ionization field. The intrinsically densest regions of LAEs are most likely to be observed first. As the ionized bubbles grow, the underdense regions in  $\delta$  become observable which contain statistically fewer LAEs. The measured number density of LAEs,  $n_{\text{obs}}$ , increases slowly as reionization progresses. In Figure 4.3 we show the LAE number field. We can see the evolution in the number of LAEs for  $\beta = 1$  in the top row of Figure 4.3. Notice that since the densest regions are ionized first, LAEs are observable at low mean ionized fraction. Consider now the outside-in model of reionization ( $\beta = -1$ ), where the underdense regions are ionized first. Since the underdense regions are less likely to host LAEs, then only the intrinsically sparsest regions of LAEs are observable early in reionization. This may make high redshift LAEs difficult to find for outside-in models [42]. However, as reionization progresses, the ionized regions grow and overdense regions are increasingly coupled to low  $x_{\text{HII}}$  which allows the regions with the intrinsically densest regions of LAEs to be observed. From the bottom row of Figure 4.3 we can see that there are fewer LAEs observable at low mean ionized fraction compared to  $\beta = 1$  models. In Figure 4.4 we can see how this translates to the redshift evolution of  $\bar{n}_{\text{obs}}$  for various  $\beta$  values. Outside-in models

produce scenarios where  $n_{\text{obs}}$  increases rapidly as reionization progresses. As we increase  $\beta$  from its extremum,  $\beta = -1$ , the number density,  $\bar{n}_{\text{obs}}$ , increases monotonically until it is maximized with respect to  $\beta$  for inside-out reionization scenarios ( $\beta = 1$ ). As reionization progresses, the IGM becomes increasingly ionized and the number density of LAEs become insensitive to  $\beta$ . All models converge to the intrinsic number density of LAEs (see Figure 4.4). In Section 4.5, we use existing constraints on  $n_{\text{obs}}$  at  $z = 6.6$  to place constraints on  $\beta$ . In the following Section, we introduce the angular correlation function (ACF) as another statistical tool to study LAEs, which along with  $n_{\text{obs}}$ , has already been constrained at  $z = 6.6$ .

### 4.4.3 Dependence of the ACF on $\beta$

The probability of finding a pair of LAEs at a distance  $R$  from one another is

$$dP_{12} = \bar{n}^2 [1 + \xi(R)] dV_1 dV_2 \quad (4.11)$$

where  $\bar{n}$  is the mean number density of LAEs,  $dV_1$ , and  $dV_2$ , are volume elements of the survey in the vicinity of each LAE, and  $\xi(R)$  is the two point correlation function. The two point angular correlation function is the excess probability as compared to a random Poisson distribution, that two LAEs be located a distance  $R$  from one another. To compute  $\xi(R)$ , we first form the overdensity  $\delta_n$  :

$$\delta_n(\mathbf{x}, z) = \frac{n_{\text{LAE}}(\mathbf{x}, z)}{\bar{n}} - 1, \quad (4.12)$$

where  $\bar{n}$  is the mean number of LAEs at redshift  $z$  and  $n_{\text{LAE}}(\mathbf{x}, z)$  is the number density field which describes the fluctuations in the number of LAEs about the mean (according to position  $\mathbf{x}$  and redshift  $z$ ). We can compute  $\xi(R)$  directly from the Fourier transformed overdensity field  $\tilde{\delta}_n$ ,

$$\xi(R) = \left\langle \int d^3\mathbf{k} e^{i\mathbf{k}\cdot\mathbf{x}} |\tilde{\delta}_n(\mathbf{k})|^2 \right\rangle_{\mathbf{x}\in R}. \quad (4.13)$$

where the angular brackets indicate a spatial average. Physically, we interpret the correlation function as the clustering of the LAEs at separation  $R$ . Larger values of  $\xi$  imply more clustering

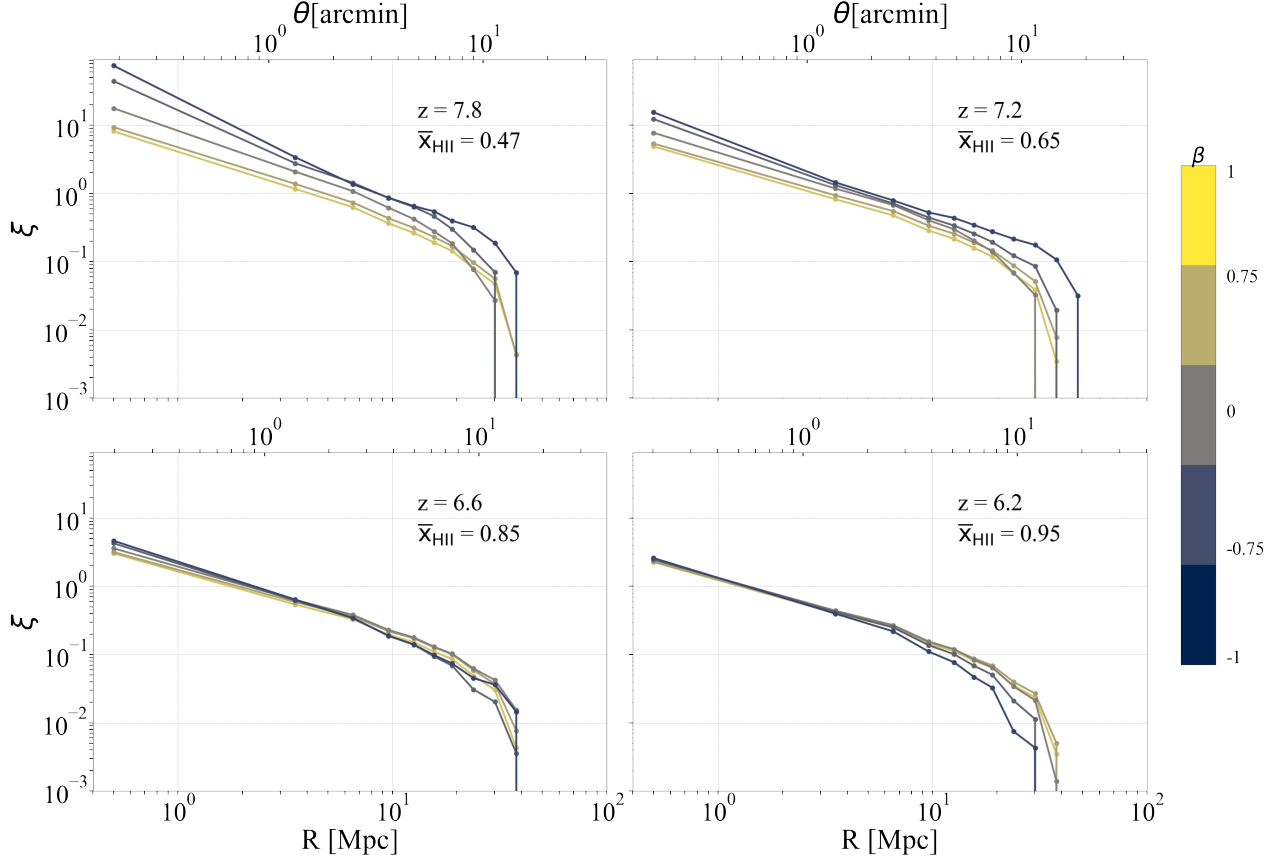


**Figure 4.5:** ACF of various  $\beta$  scenarios at different stages of reionization. Outside-in driven reionization scenarios ( $\beta < 0$ ) produce the largest clustering of LAEs. The contrast between the different  $\beta$  models is greatest at high redshifts where the ionization of the IGM has the largest imprint on LAE observability. As reionization proceeds it becomes more difficult to distinguish between these scenarios. We use fiducial parameters  $\zeta_0 = 25$ ,  $M_{\text{turn},0} = 5 \times 10^8 M_\odot$ ,  $R_{\text{mfp},0} = 30$  Mpc, and  $\beta_0 = 0.936$ ,  $f_{\text{duty}} = 1$  and  $M_\alpha^{\text{min}} = 10^{10} M_\odot$ .

of LAEs. The two point correlation function  $\xi$  of LAEs can be expressed as a function of angular separation  $\theta$  on the sky. This is the angular correlation function (ACF), denoted by  $\xi(\theta)$ . Note that in a LAE survey, one actually measures  $\xi(\theta)$ . However, to build intuition in our theory interpretation, we use  $\xi(R)$  to study the clustering of LAEs. For small angular separations and thin layers in  $\Delta z$ , we can simply convert  $\xi(R)$  to  $\xi(\theta)$  using  $D_c$  which is a conversion factor from  $\theta$  to transverse comoving distance  $R$ , and is given by

$$D_c \equiv \frac{R}{\theta} = \frac{c}{H_0} \int_0^z \frac{dz'}{E(z')} \quad (4.14)$$

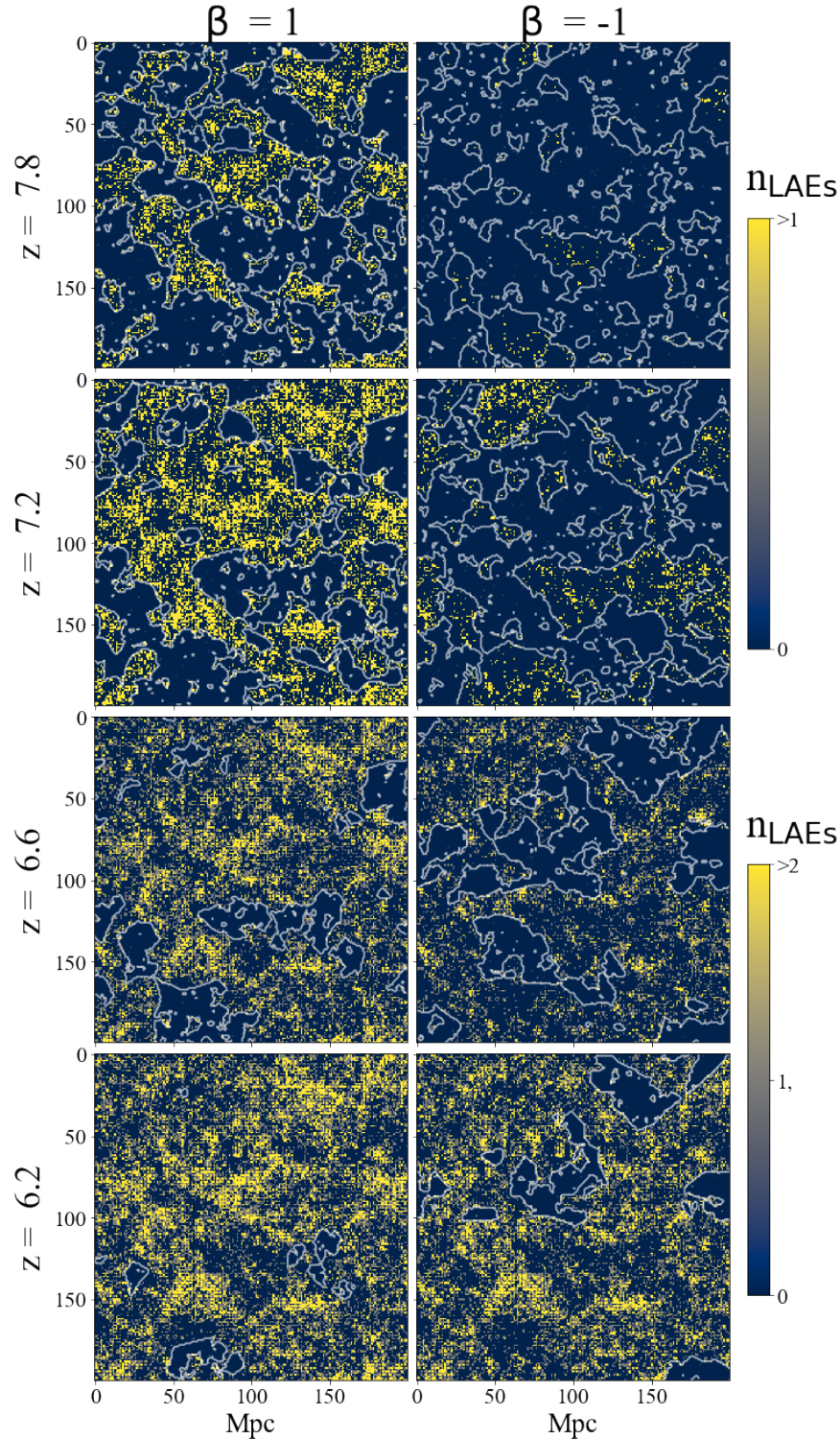


**Figure 4.6:** The number density of observed LAEs for different  $\beta$  models and at different redshifts. For inside-out models at high redshifts (top two rows), LAEs are spread across the entire ionized regions, while outside-in models produce fewer LAEs which are spread across a limited volume. This serves to increase the clustering of LAEs for  $\beta = -1$  models. The scale is binary to accentuate the difference in the spatial distributions of LAEs between the two models. Later in reionization (bottom two rows), the LAEs of both inside-out and outside-in models are spread over similar ionized volumes. However the number density of LAEs within these ionized volumes is larger for

with  $c$  the speed of light,  $H_0$  the Hubble parameter today,  $E(z) \equiv \sqrt{\Omega_m(1+z)^3 + \Omega_\Lambda}$  and  $\Omega_\Lambda$  the normalized dark energy density [65]. For the remainder of this paper we work with  $\xi(R)$ , recognizing that one can easily convert  $\xi(R)$  to  $\xi(\theta)$  using Equation (4.14) under the Limber approximation [65].

The ACFs of the intrinsic LAEs under different density-ionisation correlation scenarios are shown in Figure 4.5. We split our discussion of the  $\beta$  dependent ACF into two different redshift regimes: higher redshifts (Figure 4.5 top two rows), and lower redshifts (Figure 4.5 bottom two rows). Consider first the higher redshift regime, outside-in scenarios ( $\beta = -1$ ), lead to more clustering as compared to inside-out models ( $\beta = 1$ ). To see why this is, consider LAEs in the ionized regions of an outside-in ( $\beta = -1$ ) scenario, where the ionized regions correspond to underdense regions in  $\delta$ . We can see from the top two rows in Figure 4.6, the LAEs are rare and occupy an only fairly limited portion of the ionized volume. Due to the limited volume that they occupy, any LAEs observed in  $\beta = -1$  models tend to be clustered together. This produces a strong clustering signal for  $\beta = -1$  models. Now let us consider LAEs in the ionized regions of inside-out models. There is a significant increase in the number of LAEs compared to outside-in models. Referring again to the top two rows in Figure 4.6, the excess LAEs in  $\beta = 1$  models are spread over the entire volume of the ionized region. This reduces the excess probability  $\xi(R)$  in Equation (4.11) of finding LAEs separated by distances smaller than the bubble size, leading to a decrease in clustering compared to outside-in driven models. As we decrease  $\beta$  from  $\beta = 1$  to  $\beta = -1$ , we find that there is an increase in the clustering signal. This conclusion is also true when the extreme  $\beta$  models are constrained to have a fixed number density of LAEs. We can study this scenario by tuning the duty cycle  $f_{\text{duty}}$  of both models, so that they have the same number density of LAEs. This entails decreasing  $f_{\text{duty}}$  for  $\beta = 1$  models, such that the number of LAEs within the ionized regions are the same as for  $\beta = -1$  models. In this scenario the LAEs for the inside-out scenario are still spread over a larger volume as compared to the LAEs within the ionized regions of outside-in models, leading to the same conclusions as above.

Our above conclusions are essentially due to LAEs being spread over a larger ionized volume for inside-out models, while outside-in models produce localized fluctuations of LAEs within the

ionized regions. Let us now focus on the behavior of  $\xi$  at lower redshifts where this is no longer true. At the end of reionization, more structures have collapsed to form haloes, and so the number of LAEs in the underdense regions of the intrinsic field dramatically increases. Referring to the bottom two rows in Figure 4.6, the ionized regions of outside-in reionization maps now contain LAEs that are spread over the entire ionized volume. Consider LAEs separated by  $R$  within these ionized volumes, where  $R$  is much smaller than the typical ionized bubble. Since there are more LAEs within the ionized volumes of inside-out driven models compared to  $\beta = -1$  models, there are a larger fraction of LAEs separated within  $R$  increasing the clustering compared to outside-in driven models. Equivalently, the ionized volumes of inside-out regions allow us to observe the highest mass halos, which tend to be the most biased traces tracers of the density field, i.e. the most clustered. In Figure 4.7, we can see the non-monotonic behaviour of  $\beta$  in  $\xi$  at separations of  $R = 10\text{Mpc}$ , a length scale entirely contained within the ionized regions at these redshifts. At low redshifts, the outside-in driven models ( $\beta < 0$ ), produce the smallest clustering of LAEs. As reionization continues to proceed, the ionized regions grow, exposing both overdense and underdense regions, which narrows the contrast of  $\xi(R)$  between the extreme models,  $\beta = -1$  and  $\beta = 1$ . Finally as the IGM is entirely ionized, the clustering signatures of the extreme models become indistinguishable and  $\xi(R)$  is no longer sensitive to  $\beta$ . We also find that the dependence of the ACF on  $\beta$  is robust to different values of  $M_\alpha^{\min}$ . The increase in clustering signature when decreasing  $\beta$  from 1 to  $-1$  still holds at different values of  $M_\alpha^{\min}$ . For example, decreasing  $M_\alpha^{\min}$  allows the LAEs hosted by smaller haloes to be detected by surveys. Because low mass halos are abundant in both overdense and underdense regions, *both* the underdense regions and overdense regions receive an increase in the number of observed LAEs, resulting in the same conclusions as above.

In Section 4.6, we shall see that at redshift  $z = 6.6$ , the differences in  $\xi(R)$  between extreme models are not significant enough to distinguish between them using existing data. Since the astrophysical parameters  $M_{\text{turn}}$ ,  $R_{\text{mfp}}$  and  $\zeta$ , affect the size of the ionized regions at each  $z$ , they will also influence the observed clustering of and number density of LAEs. In the next section we use existing measurements of  $\xi(R)$  and  $\bar{n}$  to place constraints on these parameters as well as  $\beta$ .

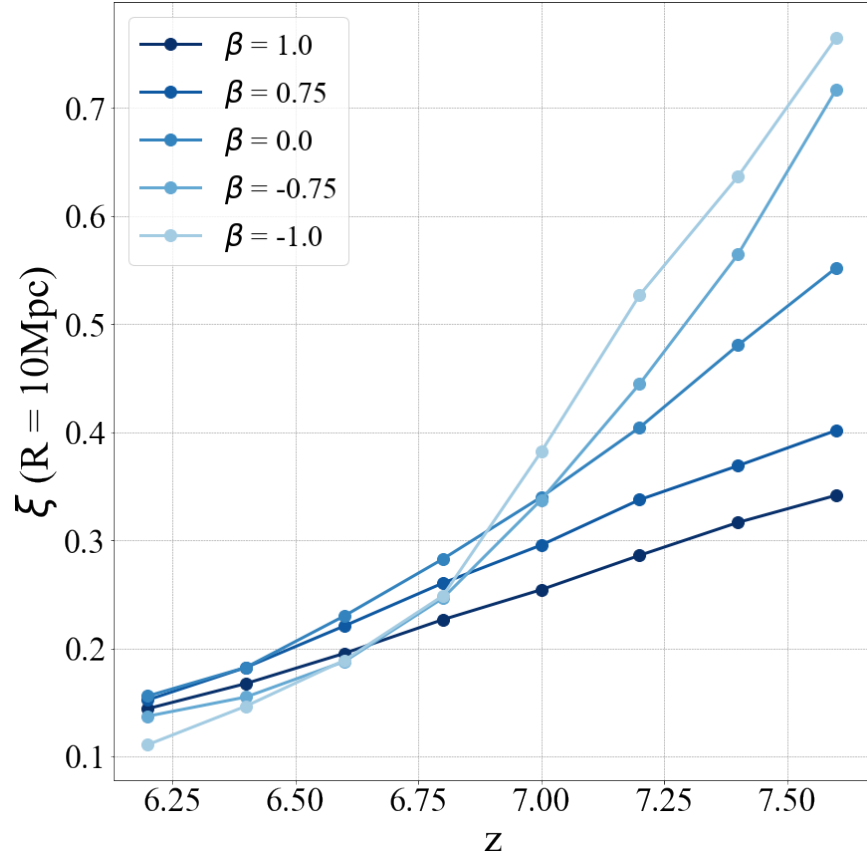


**Figure 4.7:** Angular correlation function as a function of  $z$  for various  $\beta$  models at separations of 10Mpc. Note the non-monotonic behaviour of  $\beta$ . Early in reionization, the LAEs of inside-out models are spread over larger volumes within the ionized regions as compared to outside-in models, where the LAEs tend to be more localized. This produces a stronger clustering signal for outside-in driven models. This behaviour is inverted later in reionization where there are enough intrinsic LAEs to fill the entire volume of ionized regions for outside-in models.

## 4.5 Forecasts and Constraints

In Section 4.2.2 we developed a framework where we can track the density-ionization correlations during the EoR. In Section 4.4, we developed an intuition on how the observed clustering, number density and luminosity function of the LAEs depend on this correlation. In this section, we use measurements of the number density and clustering of LAEs at  $z = 6.6$  made by the Subaru survey to place constraints on the correlation parameter  $\beta$ , as well as the other EoR parameters. Further, we forecast the type of constraints that can be placed on  $\beta$  using a joint measurement of LAE and the 21cm power spectrum using HERA. We discuss the HERA instrument as well as its fiducial instrument parameters. We present the results of these forecasts in Section 4.6.

### 4.5.1 Subaru Survey

To place constraints on our EoR parameters including  $\beta$ , we use measurements of  $\bar{n}$  and  $\xi(\theta)$  at redshift 6.6 from the Subaru/XMM-Newton Deep Survey (SXDS) survey [52]. Here we summarize the analysis done by [52] in computing  $\bar{n}$  and  $\xi(\theta)$ . Measurement of  $\bar{n}$  is made indirectly by first measuring the  $Ly\alpha$  luminosity function using the  $Ly\alpha$  line profiles based on 207  $Ly\alpha$  emitters at  $z = 6.6$  on the 1-deg<sup>2</sup> sky, which have redshift uncertainty  $\Delta z \simeq 0.1$ . Using these measurements, the constraints are placed on the  $Ly\alpha$  luminosity function which is modeled as a Schechter function, defined as

$$\phi(L)dL = \phi^*(L/L_*)^\alpha e^{-L/L_*} d(L/L_*) \quad (4.15)$$

where  $L$  is the luminosity of the LAEs and  $L^*$  is the characteristic LAE luminosity beyond which the power-law form of the function drops off rapidly. Using the 207 LAEs sampled from the Subaru survey and 58 additional LAE measurements made from [30], the best fit Schechter parameters are found to be  $\phi^* = 8.5_{-2.2}^{+3.0} \times 10^{-4} \text{Mpc}^{-3}$  and  $L_{Ly\alpha}^* = 4.4_{-0.6}^{+0.6} \times 10^{42} \text{ergs s}^{-1}$  with fixed  $\alpha = -1.5$ . The number densities and  $Ly\alpha$  luminosity functions are calculated by integrating equation (4.15) down to the observed limit of  $L_\alpha^{\min} = 2.5 \times 10^{42} \text{ ergs/s}$  using the best fit Schechter parameters. The number density is computed to be  $\bar{n} = 4.1_{-0.8}^{+0.9} \times 10^{-4} \text{Mpc}^{-3}$  at  $z = 6.6$ . The constraints on

these quantities include cosmic variance estimates. To mitigate such errors in the future, one can alternatively consider Ly $\alpha$  intensity mapping, which can take advantage of a larger field [64].

The angular correlation function,  $\xi(\theta)$ , of the 207 measured LAEs are computed using the Landy & Szalay (LS) estimator. To evaluate the LS estimator, one first creates a pure random catalogue of sources and computes

$$\xi(\theta) = [DD(\theta) - 2DR(\theta) + RR(\theta)]/RR(\theta), \quad (4.16)$$

where  $DD(\theta)$ ,  $RR(\theta)$  and  $DR(\theta)$  are the number of data-data, random-random and data-random pairs normalized by the number of random-random pairs in each angular bin [34]. Observational offsets included in  $\xi(\theta)$  due to limited survey area are evaluated by first assuming the true underlying ACF follows a power law of the form  $\xi(\theta) = A_\xi \theta^{-\gamma}$ , where the values of  $A_\xi$  are fit for using the results on  $\xi(\theta)$ . The observational offset in  $\xi(\theta)$  can then be computed using the integral constraint (see [52], [21]). The angular dependence of  $\xi(\theta)$  is converted to a dependence on comoving distance  $R$  using the Limber approximation [56]. The resulting constraints on  $\xi(R)$  are quoted in Figure 12 of [52]. We only use the constraints placed on  $\xi(R)$  for comoving scales larger than  $> 1.5\text{Mpc}$ , corresponding to the resolution of our simulation boxes described in Section 4.2, which corresponding to comoving angular scales larger than  $\theta \simeq 35$  arcsec.

## 4.5.2 HERA instrument and Sensitivities

To forecast the constraints that can be placed on  $\beta$  using both the Subaru data and a measurement of the 21cm power spectrum, we use HERA as our fiducial 21cm instrument. When completed, HERA will consist of 350 parabolic dishes, each 14 m in diameter with observing frequencies from 50 MHz to 250 MHz. Based on its forecasted sensitivities,  $> 20\sigma$  detections of the 21 cm power spectrum from the EoR will likely be possible [8, 58]. Although we use HERA as our fiducial instrument, the qualitative conclusions presented in Section 4.6 are also valid for other instruments such as the Murchison Widefield Array [3, 70], the Square Kilometre Array [33], and the Low Frequency Array [71].

We model HERA’s sensitivities on measurements of  $\Delta_{21}^2$  using the publicly available code 21cmSense [58, 60]. The code computes the sensitivities on  $\Delta_{21}^2$  by modeling the instrumental thermal noise using HERA’s interferometric design and survey parameters. Beyond instrumental effects, the code then adds sample variance to the sensitivities. The resulting errors on  $\Delta_{21}^2$  are computed as

$$\varepsilon(k) = D_c^2 Y \frac{k^3 \xi_{\text{eff}} T_{\text{sys}}^2}{2\pi^2 2t_{\text{int}}} + \varepsilon_{\text{sample}} \quad (4.17)$$

where the first term is the thermal noise specific to HERA and the second term adds sample variance. In the first term,  $T_{\text{sys}}$  is the antenna temperature of HERA and  $\Omega_{\text{eff}}$  is the effective solid angle of the primary beam of each dish [55]. Meanwhile  $D_c$  converts angular separations on the sky to comoving distances (see Equation (4.14)) and  $Y$  converts radial comoving distances  $\Delta r_{\parallel}$  to frequency intervals  $\Delta \nu$  defined through

$$Y \equiv \frac{\Delta r_{\parallel}}{\Delta \nu} = \frac{c}{H_0 \nu_{21}} \frac{(1+z)^2}{E(z)}. \quad (4.18)$$

where  $\nu_{21} \approx 1420$  MHz is the rest frequency of the 21 cm line. The sample variance is generated using a fiducial EoR inside-out model. Using different fiducial EoR scenarios does not qualitatively change the results in Section 4.6.

The 21cm signal is expected to be several orders of magnitude dimmer than the “foreground” contaminants. The foregrounds are astrophysical in nature and dominate the low-frequency radio spectrum. Fortunately, the foregrounds are spectrally smooth and are expected to lie in the characteristic “wedge” of cylindrically decomposed Fourier space. The “wedge” is defined as

$$k_{\parallel} \leq \left( \frac{D_c}{\nu Y} \right) k_{\perp}, \quad (4.19)$$

where  $\nu$  is the observing frequency,  $k_{\perp}$  and  $k_{\parallel}$  are the wavenumbers perpendicular and parallel to the line of sight in cylindrical Fourier space. In generating Equation (4.17), we adopt the “moderate” foreground setting in 21cmSense which states that modes satisfying Equation (4.19), and additional modes up to  $0.1 h\text{Mpc}^{-1}$  higher in  $k_{\parallel}$ , are contaminated by the foregrounds and so omitted in our

analysis (i.e. foreground avoidance rather than foreground subtraction). This additional “buffer” accounts for the degree of spectral unsmoothness in the foregrounds which may cause a leakage to higher  $k_{\parallel}$  [59].

### 4.5.3 Markov Chain Monte Carlo Setup for Subaru Constraints

In this Section we discuss our Markov Chain Monte Carlo (MCMC) setup which we use to place constraints on the EoR parameters. In our MCMC we use only the measurements from the Subaru survey discussion in the previous Section. We place the correlation parameter  $\beta$ , the EoR parameters,  $\zeta$ ,  $M_{\text{turn}}$ , and  $R_{\text{mfp}}$ , as well as  $f_{\text{duty}}$  and  $M_{\alpha}^{\text{min}}$  into a single vector  $\theta$ . In order to place constraints on  $\theta$ , we need to infer the probability of obtaining a particular instance of  $\theta$  given the Subaru dataset  $\mathbf{d}_S$ . This probability distribution,  $p(\theta|\mathbf{d}_S)$ , is the posterior in Bayes’ theorem

$$p(\theta|\mathbf{d}_S) \propto p(\mathbf{d}_S|\theta)p(\theta), \quad (4.20)$$

where  $p(\mathbf{d}_S|\theta)$  is the likelihood function and  $p(\theta)$  is our prior. We place uniform priors on all parameters. For the correlation parameter  $\beta$ , and duty parameter  $f_{\text{duty}}$ , we use a uniform prior of  $-1 \leq \beta \leq 1$  and  $0 \leq f_{\text{duty}} \leq 1$  respectively. These ranges encapsulate the entire allowable regions of both their parameter spaces. Values of  $\beta$  between  $-1 \leq \beta \leq 1$  span the entire range of correlations, while by construction,  $f_{\text{duty}}$  can only have values  $0 \leq f_{\text{duty}} \leq 1$ . For  $\zeta$ , we place the range  $10 < \zeta < 100$  which spans the range of values which are consistent with previous studies such as [48]. For  $M_{\text{turn}}$ , we adopt values of  $10^7 M_{\odot} < M_{\text{turn}} < 10^{10} M_{\odot}$ , which are motivated by the atomic cooling threshold and by current constraints on the faint end of UV luminosity functions [54]. For  $R_{\text{mfp}}$  we use  $3 \text{ Mpc} < R_{\text{mfp}} < 80 \text{ Mpc}$  which spans the expected range [68]. Finally, for  $M_{\alpha}^{\text{min}}$ , we adopt a uniform prior with  $10^9 M_{\odot} \leq M_{\alpha}^{\text{min}} \leq 10^{11} M_{\odot}$ . These bounds are motivated by [67] which find values outside this range to be inconsistent with constraints placed on the  $Ly\alpha$  luminosity function by [44] and [52].

We use 21cmFAST to generate a box of intrinsic LAEs at the redshift of interest  $z$ . To do this we generate the underlying halo field and then assign an intrinsic LAE luminosity to each virialized

halo using Equation (4.8). We resolve all haloes above the virialized mass scale  $M = 5 \times 10^8 M_\odot$ . The resulting halos are assigned an intrinsic luminosity according to equation (4.8) using model parameters  $f_{\text{duty}}$  and the normalization  $M_\alpha^{\text{min}}$ . The resulting box of intrinsic LAEs extends 300Mpc along the line of sight (see Section 4.2 for simulation details). To mimic the the intrinsic LAEs observed by the Subaru Survey which has redshift thickness  $\Delta z = 0.1$  (corresponding to  $\sim 37\text{Mpc}$  at  $z = 6.6$ ), we slice our box of intrinsic LAEs into slabs corresponding to a redshift thickness of  $\Delta z = 0.1$ , in accordance with the redshift uncertainty of the Subaru HSC data. To compute the likelihood  $p(\mathbf{d}_S|\boldsymbol{\theta})$ , we use 21cmFAST to generate the density and ionization fields for a given set of model parameters  $\zeta$ ,  $R_{\text{mfp}}$ , and  $M_{\text{turn}}$ . The ionization field is computed from a density field which has been decorrelated with the desired level of  $\beta$ . For each set of model parameters, we pair the new ionization field to the original box of intrinsic LAEs. We perform separate forecasts using different randomly generated density realizations to account for the cosmic variance. Our conclusions are unchanged for each of these different realizations. The number density  $\bar{n}$  and ACF  $\xi$  of the model LAEs are computed and compared to the corresponding Subaru measurements of the number densities  $\bar{n}_S$ , and ACF  $\xi_S$ , through the likelihood given by

$$p_{\text{LAE}}(\mathbf{d}|\boldsymbol{\theta}) \propto \exp \left[ -\frac{1}{2} \sum_R \frac{(\xi_{\text{model}} - \xi_S)^2}{\varepsilon_\xi^2} \right] \exp \left[ -\frac{1}{2} \frac{(\bar{n}_{\text{model}} - \bar{n}_S)^2}{\varepsilon_n^2} \right], \quad (4.21)$$

where  $\varepsilon_n$  are the Subaru errorbars on the mean LAE number density and  $\varepsilon_\xi$  are the errors on the Subaru measurements of the ACF given in [52]. We symmetrize the errorbars on  $\bar{n}$  and  $\xi_\xi$ . In each case we take a conservative approach and symmetrize using the larger error limit. We take measurements of  $\bar{n}$  and  $\xi(R)$  to be statistically independent which is a reasonable assumption since  $\bar{n}$  depends on the mean number of LAEs while  $\xi$  depends only on the overdensity  $\delta_n$ , which is mean zero. We approximate the  $R$  bins in  $\xi(R)$  as being statistically independent.

#### 4.5.4 Markov Chain Monte Carlo Setup for Joint Subaru & 21cm Forecasts

In this Section we build on the setup from the previous Section and explore the constraints that can be placed on  $\beta$  using measurement of the 21cm power spectrum  $\Delta_{21}^2$  in addition to the Subaru

measurements described in Section 4.6.1. If we assume these probes are independent from one another, the posterior for joint measurements between LAE and 21cm probes can be written using Bayes theorem as,

$$p(\boldsymbol{\theta}|\mathbf{d}_S, \Delta_{21}^2) \propto p_{21}(\Delta_{21}^2|\boldsymbol{\theta})p_{\text{LAE}}(\mathbf{d}_S|\boldsymbol{\theta})p(\boldsymbol{\theta}), \quad (4.22)$$

where  $p_{\text{LAE}}(\mathbf{d}|\boldsymbol{\theta})$  is the likelihood function for the Subaru measurements (discussed in the previous Section),  $p_{21}(\mathbf{d}|\boldsymbol{\theta})$  is the likelihood for measurements of the 21cm power spectrum and  $p(\boldsymbol{\theta})$  is the prior on our parameters. Our priors are identical to those in Section 4.5.3.

To evaluate the likelihood  $p_{21}(\mathbf{d}|\boldsymbol{\theta})$ , we generate model predictions for the density, ionization fields and temperature fields from 21cmFAST simulations for a given set of model parameters  $\boldsymbol{\theta}$ . To account for the decorrelation between the ionization and density fields, we regenerate the ionization field for this set of EoR parameters, but with the desired level of decorrelation from the original ionization field as specified by the  $\beta$  parameter. This updated ionization field is then used with the original density field to form a brightness temperature field using Equation (4.1). The power spectrum  $\Delta_{\text{model}}^2$  of  $\delta T_b$  is computed using Equation (4.3). We compare the power spectrum  $\Delta_{\text{model}}^2$  of the model temperature field to the fiducial power spectrum  $\Delta_{21}^2(k, z)$  using the likelihood,

$$p_{21}(\mathbf{d}|\boldsymbol{\theta}) \propto \exp \left[ -\frac{1}{2} \sum_{z,k} \frac{(\Delta_{\text{model}}^2 - \Delta_{21}^2)^2}{\epsilon^2} \right], \quad (4.23)$$

where we have assumed that all the  $k$  and  $z$  bins are statistically independent. We consider redshifts  $7.5 \leq z \leq 8.5$  in steps of  $\Delta z = 0.5$ , corresponding to observational bandwidth  $\Delta \nu \equiv \nu_{21} \Delta z / (1 + z)^2$  of each redshift bin. We choose these redshift ranges because they correspond to one of HERA's relatively clean observation windows. We exclude bins  $k > 0.75 \text{ Mpc}^{-1}$  for computational simplicity as the HERA error bars are large in that regime and inclusion of larger  $k$  bins do not add alter our forecasts significantly. In this forecast, we use a mock HERA observation of the power spectrum generated using a fiducial set of EoR parameter values,  $\zeta_0 = 25$ ,  $M_{\text{turn},0} = 5 \times 10^8 M_\odot$ ,  $R_{\text{mfp},0} = 30 \text{ Mpc}$ , and  $\beta_0 = 0.936$  unless otherwise indicated. To sample our posterior distribution, we use the affine invariant MCMC package `emcee` [13].

## 4.6 Results

In this section we present the results of our MCMCs and discuss their implications. We separate the results into two sections. In Section 4.6.1, we place constraints on the EoR parameters using existing measurements of the number density, and ACF, of LAEs at redshift  $z = 6.6$  from the Subaru experiment, discussed in Section 4.5.1. In Section 4.6.2, we forecast the types on constraints that we can place on the EoR parameters (including  $\beta$ ), using measurements of the 21cm power spectrum and  $\bar{n}$ ,  $\xi$ , of LAEs. For this multiple probe forecast we use Subaru measurements of the number density and ACF of LAEs at redshift  $z = 6.6$  and a HERA measurement of the 21cm power spectrum between redshifts  $z = 7.5$  to  $z = 8.5$ .

### 4.6.1 Subaru Constraints

In Figure 4.8 we show the posterior of our MCMC analysis using the Subaru measurements of  $\bar{n}$ , and  $\xi$ , at  $z = 6.6$ . We find an evident degeneracy between  $M_\alpha^{\min}$  and  $f_{\text{duty}}$ . To see why, consider an intrinsic LAE field with LAE detection threshold  $M_\alpha^{\min}$  corresponding to the minimum luminosity detectable by our experiment,  $L_\alpha^{\min}$ . Physically,  $M_\alpha^{\min}$  is the halo mass that corresponds to the minimum luminosity  $L_\alpha^{\min}$  (the faintest luminosity detectable by our instruments). Larger values of  $M_\alpha^{\min}$  decrease the number of intrinsic LAEs that would be detectable by our instruments. This in turn decreases the measured number density of LAEs. In order to fit to the number density  $\bar{n} = 4.1_{-0.8}^{+0.9} \times 10^{-4}$  by Subaru, this scenario requires increasing  $f_{\text{duty}}$  which leads to the observed degeneracy. Values of  $M_\alpha^{\min}$  larger than  $M_\alpha^{\min} > 10^{11} M_\odot$  require  $f_{\text{duty}} > 1$  in order to be consistent with the already constrained value of  $\bar{n}$ . This is not possible and so models which require values  $M_\alpha^{\min} > 10^{11} M_\odot$ , have already been ruled out [67]. We do not find an explicit degeneracy between  $\beta$  and the other EoR parameters. Ruling out an outside-in driven reionization is tantamount to placing constraints on the sign of  $\beta$ . However we see from the 1D  $\beta$  posterior in Figure 4.8 that the 68% credibility region (CR) of  $\beta$  is not entirely contained within the  $\beta > 0$  region, suggesting that measurements of  $\bar{n}$  and  $\xi$  at  $z = 6.6$  alone is insufficient to rule out uncorrelated, or outside-in scenarios. In Figure 4.8 we see that all  $\beta$  models are broadly consistent with measurements of  $\xi$

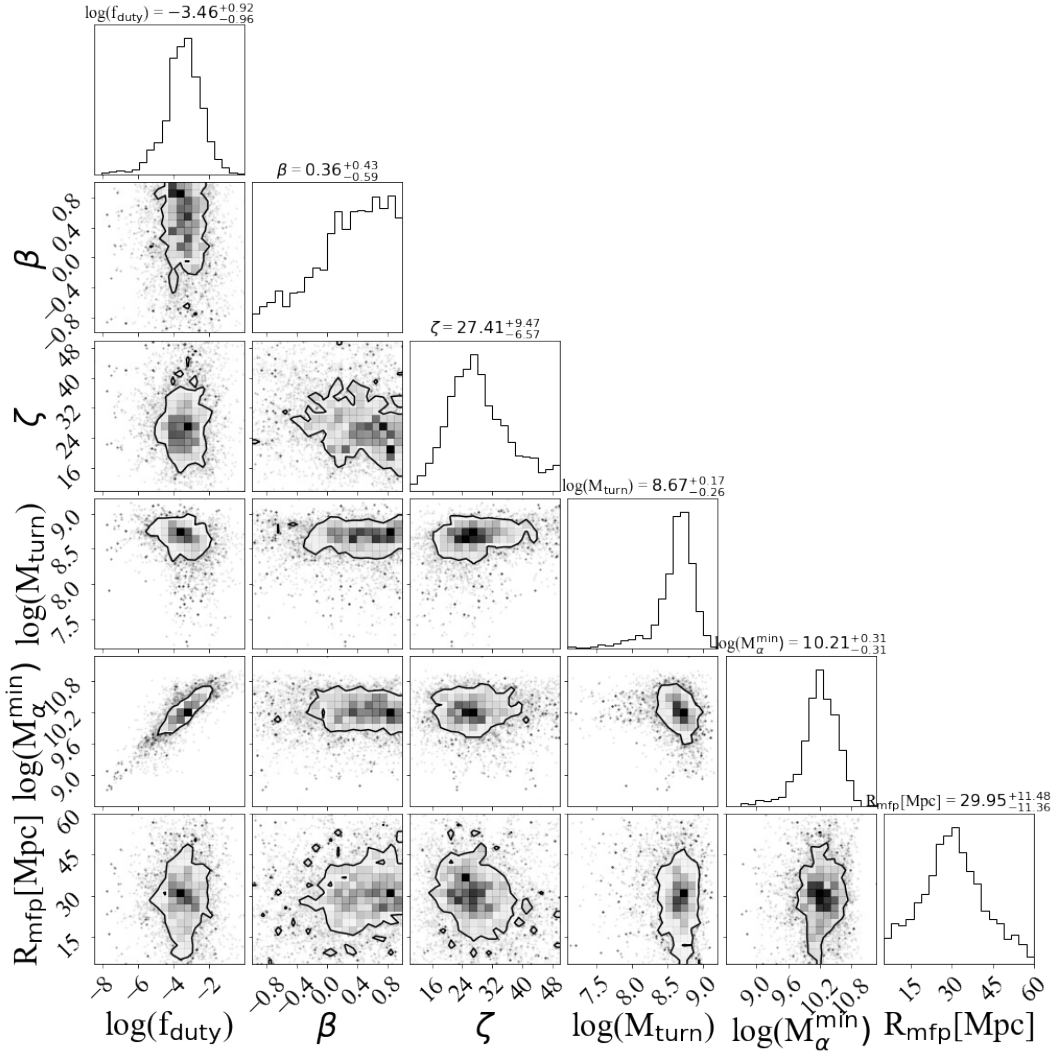


**Figure 4.8:** Posterior distribution for the EoR and LAE parameters using the Subaru data described in Section 4.5.3. Displayed are the 68% CR contours. Since the 68% CR contours include both the  $\beta > 0$ , and  $\beta < 0$  regions of parameter space, measurement of  $\bar{n}$  and  $\xi$  at  $z = 6.6$  cannot constrain the sign of  $\beta$  to within 68% credibility.

from Subaru. We see that our models can't distinguish between the extreme inside-out models. The Universe is significantly ionized at redshift  $z = 6.6$ , and so the number density and ACF of LAEs is not very sensitive to changes in  $\beta$ . As a result, the Subaru data is unable to concretely rule out uncorrelated and outside-in reionization scenarios at 68%CR. At higher redshift, there is increased sensitivity of  $\bar{n}$  and  $\xi$  to  $\beta$ . Measurements of  $\bar{n}$  and  $\xi$  at higher redshifts are required in order to place tighter constraints on the EoR morphology using only LAE data.

From the posterior, we see that 68% of the 1D marginalized posterior of  $M_{\text{turn}}$  lie within the range  $\log M_{\text{turn}} = 8.67^{+0.17}_{-0.26}$ . Therefore we find that using the Subaru data, we can place constraints on the order of magnitude of  $M_{\text{turn}}$  at 68% CR, while  $\zeta$  is constrained within  $\zeta = 27.41^{+9.47}_{-6.57}$  at 68% CR.

Recent studies have shown that the escape fraction of ionizing photons can depend on the halo mass  $M_h$  [32,35,77]. This would make  $\zeta$  halo mass dependent. In such a scenario it is worth noting the limitations of our model (which assumes a constant ionizing efficiency). For example, consider a scenario where the escape fraction of ionizing photons decreases with  $M_h$ . The largest virialized halos have decreased capacity to contribute UV photons to the reionization process. Our approach of a constant  $\zeta$  with halo mass, would potentially underestimate the contribution of UV photons by small mass halos. Conversely, models where the escape fraction increases with halo mass, our assumption of a constant  $\zeta$  would overestimate the contribution of small mass halos. Therefore our approach is most appropriate for models where reionization is driven by moderately sized halos. We find this to be the case in our parameter constraints in Figure 4.8. Further, as discussed in Section 4.3.2, a halo mass dependent escape fraction simultaneously affects the intrinsic luminosity of the LAEs as well as the transmission of Ly $\alpha$  photons through the IGM. Both of these mechanisms affect the observed LAE luminosity function of the LAEs. A halo mass dependent  $f_{\text{esc}}$  can also tilt the observed LAE luminosity function by favoring a particular size of halo mass. In our intrinsic LAE model, this has an effect similar to varying the power law index in Equation 4.8. As discussed in Section 4.3.2, our results in this section are not affected by small variations in the power law index.

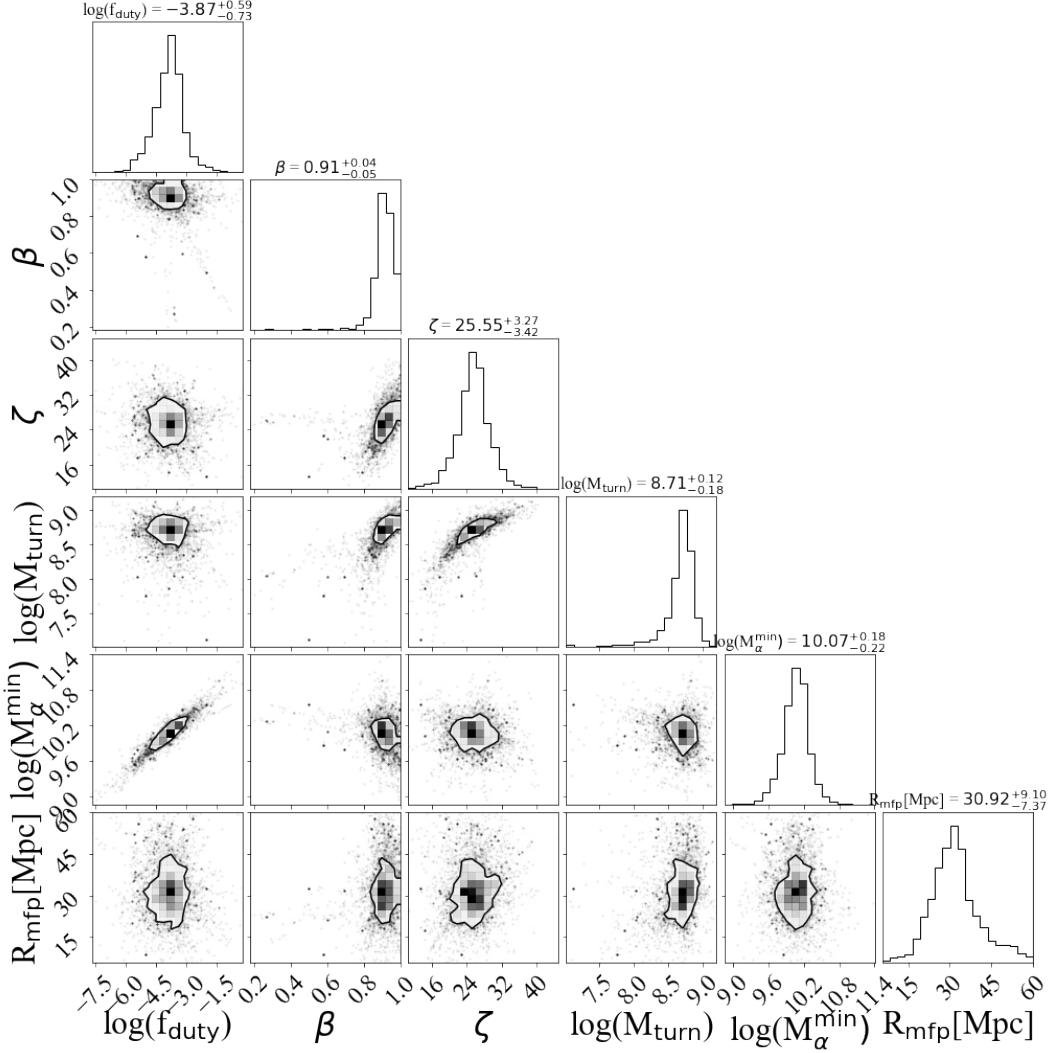


**Figure 4.9:** Posterior distribution for the EoR and LAE parameters using the Subaru data at  $z = 6.6$  and the 21cm power spectrum from  $7.5 \leq z \leq 8.5$ . The 68% CR are entirely contained within  $\beta > 0$  suggesting that if reionization proceeds as inside-out, measurement of  $\bar{n}$  and  $\xi$  of LAE as well as  $\Delta_{21}^2$  can rule out uncorrelated and outside-in reionization with 68% credibility.

#### 4.6.2 Joint Subaru & HERA Forecasts

In this scenario we forecast the type of constraints that can be placed on the EoR morphology using joint measurements of the LAE number density and ACF, along with a HERA measurement of the 21cm power spectrum between redshifts  $z = 7.5$  to  $z = 8.5$ . These redshifts are chosen to maximize the greatest signal to noise ratio for  $\beta$  in  $\Delta_{21}^2$  after taking the instrument sensitivities of  $\Delta_{21}^2$  into account. Since these 21cm observations do not yet exist, we use a fiducial inside-out reionization

model with fiducial parameters  $\zeta_0 = 25$ ,  $M_{\text{turn},0} = 5 \times 10^8 M_\odot$ ,  $R_{\text{mfp},0} = 30 \text{Mpc}$  and  $\beta_0 = 0.936$ . This fiducial reionization scenario is consistent with the constraints placed on these parameters using the Subaru measurements of  $\bar{n}$  and  $\xi$  in Section 4.8.

The results of this forecast are shown in Figure 4.9. Our interpretation of the degeneracies between  $f_{\text{duty}}$  and  $M_\alpha$  are identical to Section 4.6.1. We see that adding information from  $\Delta_{21}^2$  significantly improves our ability to discern between EoR models. From the posterior of this measurement in Figure 4.9, we see that the 99% credibility region of  $\beta$  lie entirely within  $\beta > 0$ . This is the predominantly inside-out region of  $\beta$  parameter space. Therefore measurements of  $\bar{n}$  and  $\xi$  of LAEs at  $z = 6.6$ , and a HERA measurement of  $\Delta_{21}^2$  at  $7.5 \leq z \leq 8.5$  can rule out uncorrelated and outside-in reionization scenarios with 99% credibility. An identical forecast performed in [53] using the same  $k$  bins, redshift range, and fiducial reionization model, but without the LAE data, was previously studied. In this forecast it was found that  $\beta$  models in the range  $0.9 \leq \beta \leq 1$ , i.e. extreme inside-out scenarios, were equally likely. This suggests that measurement of the 21cm power from Section 4.5.4 alone is not able to distinguish between extreme inside-out  $\beta$  models. From the  $\beta$  contours in Figure 4.9, we see that the inclusion of Subaru data allows us to distinguish between these extreme inside-out scenarios.

## 4.7 Conclusion

The correlation between density and ionization fields is crucial to our understanding of reionization. Many probes of the EoR are sensitive to this underlying correlation. LAEs are one such probe because Ly $\alpha$  photons are sensitive to the coupling of the ionized regions with respect to the underlying intrinsic LAEs. In this paper we explore how the statistics of LAEs are affected by the morphology of the EoR. To do this we introduce a parameter  $\beta$ , which parameterizes the correlation between density and ionization fields. Under this parametrization we study how the correlation between density and ionization fields affects the number density and clustering of LAEs. We find that changing  $\beta$  results in altering the number density of LAEs. Outside-in driven reionization scenarios ( $\beta < 0$ ), decrease the mean number density of LAEs compared to inside-out driven

scenarios ( $\beta > 0$ ). We also find that varying  $\beta$  affects the apparent clustering of LAEs. At higher redshifts, outside-in driven reionization scenarios produce an increase in the clustering signal of LAEs compared to that of inside-out. We find these conclusions are robust to different values of  $M_\alpha^{\min}$  and also hold for models where the escape fraction of ionizing photons depends on halo mass.

Using Subaru measurements of the clustering and number density of LAEs at  $z = 6.6$ , we place constraints on  $\beta$ . We find that measurements of these quantities alone cannot rule out uncorrelated scenarios at 68% credibility. The ACF and mean number density of LAEs have reduced sensitivity to  $\beta$  late in reionization where most of the IGM is ionized. Upcoming HERA limits of the 21cm power spectrum will also allow us to place constraints on  $\beta$ . We forecast the type of constraints that we can place on  $\beta$  using both HERA measurements of  $\Delta_{21}^2$  at the midpoint of reionization, and Subaru measurements of the LAE number density and ACF at  $z = 6.6$ . We find that including Subaru measurements of  $\bar{n}$  and  $\xi$  at  $z = 6.6$  can improve the constraints placed on  $\beta$  using only HERA measurements of  $\Delta_{21}^2$ . The LAE information at  $z = 6.6$  can help distinguish between extreme inside-out scenario and further rule out uncorrelated scenarios to levels over 99% credibility. These results show that LAE information at  $z = 6.6$ , i.e. when reionization is expected to be nearing its end, are already enough to help distinguish between models with different density ionization correlations. As we observe LAEs at higher redshifts, combining these probes will have even greater potential, and will help shed light on one of the most crucial properties of reionization.

## Acknowledgements

The authors are delighted to acknowledge helpful discussions with Anne Hutter, Jordan Mirocha and Hannah Fronenberg. We acknowledge support from the New Frontiers in Research Fund Exploration grant program, a Natural Sciences and Engineering Research Council of Canada (NSERC) Discovery Grant and a Discovery Launch Supplement, the Sloan Research Fellowship, the William Dawson Scholarship at McGill, as well as the Canadian Institute for Advanced Research (CIFAR) Azrieli Global Scholars program. This research was enabled in part by support provided by

Calcul Quebec ([www.calculquebec.ca](http://www.calculquebec.ca)), WestGrid ([www.westgrid.ca](http://www.westgrid.ca)) and Compute Canada ([www.computecanada.ca](http://www.computecanada.ca)).

## Data Availability

The software code underlying this article will be shared on reasonable request to the corresponding author.

## Bibliography

- [1] T. Binnie and J. R. Pritchard. Bayesian model selection with future 21cm observations of the epoch of reionization. *MNRAS*, 487(1):1160–1177, July 2019.
- [2] James S. Bolton and Martin G. Haehnelt. The observed ionization rate of the intergalactic medium and the ionizing emissivity at  $z \geq 5$ : evidence for a photon-starved and extended epoch of reionization. *MNRAS*, 382(1):325–341, November 2007.
- [3] Judd D. Bowman, Iver Cairns, David L. Kaplan, Tara Murphy, Divya Oberoi, Lister Staveley-Smith, Wayne Arcus, David G. Barnes, Gianni Bernardi, Frank H. Briggs, Shea Brown, John D. Bunton, Adam J. Burgasser, Roger J. Cappallo, Shami Chatterjee, Brian E. Corey, Anthea Coster, Avinash Deshpande, Ludi deSouza, David Emrich, Philip Erickson, Robert F. Goeke, B. M. Gaensler, Lincoln J. Greenhill, Lisa Harvey-Smith, Bryna J. Hazelton, David Herne, Jacqueline N. Hewitt, Melanie Johnston-Hollitt, Justin C. Kasper, Barton B. Kincaid, Ronald Koenig, Eric Kratzenberg, Colin J. Lonsdale, Mervyn J. Lynch, Lynn D. Matthews, S. Russell McWhirter, Daniel A. Mitchell, Miguel F. Morales, Edward H. Morgan, Stephen M. Ord, Joseph Pathikulangara, Thiagaraj Prabu, Ronald A. Remillard, Timothy Robishaw, Alan E. E. Rogers, Anish A. Roshi, Joseph E. Salah, Robert J. Sault, N. Udaya Shankar, K. S. Srivani, Jamie B. Stevens, Ravi Subrahmanyan, Steven J. Tingay, Randall B. Wayth, Mark Waterson, Rachel L. Webster, Alan R. Whitney, Andrew J. Williams, Christopher L. Williams,

- and J. Stuart B. Wyithe. Science with the Murchison Widefield Array. *Publ. Astron. Soc. Australia*, 30:e031, April 2013.
- [4] Tirthankar Roy Choudhury, Martin G. Haehnelt, and John Regan. Inside-out or outside-in: the topology of reionization in the photon-starved regime suggested by Ly $\alpha$  forest data. *MNRAS*, 394(2):960–977, April 2009.
- [5] Andrew S. Chung, Mark Dijkstra, Benedetta Ciardi, and Max Gronke. Blue wings and bumps via Fermi-like acceleration of Ly  $\alpha$  photons across shocks. *MNRAS*, 455(1):884–891, January 2016.
- [6] Frederick B. Davies and Steven R. Furlanetto. Improved treatments of the ionizing photon mean free path in semi-numerical simulations of reionization. *arXiv e-prints*, page arXiv:2103.09821, March 2021.
- [7] Pratika Dayal and Noam I. Libeskind. Local Group progenitors: Lyman Alpha bright? *MNRAS*, 419(1):L9–L13, January 2012.
- [8] David R. DeBoer, Aaron R. Parsons, James E. Aguirre, Paul Alexander, Zaki S. Ali, Adam P. Beardsley, Gianni Bernardi, Judd D. Bowman, Richard F. Bradley, Chris L. Carilli, Carina Cheng, Eloy de Lera Acedo, Joshua S. Dillon, Aaron Ewall-Wice, Gcobisa Fadana, Nicolas Fagnoni, Randall Fritz, Steve R. Furlanetto, Brian Glendenning, Bradley Greig, Jasper Grobbelaar, Bryna J. Hazelton, Jacqueline N. Hewitt, Jack Hickish, Daniel C. Jacobs, Austin Julius, MacCalvin Kariseb, Saul A. Kohn, Telalo Lekalake, Adrian Liu, Anita Loots, David MacMahon, Lourence Malan, Cresshim Malgas, Matthys Maree, Zachary Martinot, Nathan Mathison, Eunice Matsetela, Andrei Mesinger, Miguel F. Morales, Abraham R. Neben, Nipanjana Patra, Samantha Pieterse, Jonathan C. Pober, Nima Razavi-Ghods, Jon Ringuette, James Robnett, Kathryn Rosie, Raddwine Sell, Craig Smith, Angelo Syce, Max Tegmark, Nithyanandan Thyagarajan, Peter K. G. Williams, and Haoxuan Zheng. Hydrogen Epoch of Reionization Array (HERA). *PASP*, 129(974):045001, April 2017.

- [9] Mark Dijkstra. Ly $\alpha$  Emitting Galaxies as a Probe of Reionisation. *Publ. Astron. Soc. Australia*, 31:e040, October 2014.
- [10] Mark Dijkstra, Andrei Mesinger, and J. Stuart B. Wyithe. The detectability of Ly $\alpha$  emission from galaxies during the epoch of reionization. *MNRAS*, 414(3):2139–2147, July 2011.
- [11] Aaron Ewall-Wice, Jacqueline Hewitt, Andrei Mesinger, Joshua S. Dillon, Adrian Liu, and Jonathan Pober. Constraining high-redshift X-ray sources with next generation 21-cm power spectrum measurements. *MNRAS*, 458(3):2710–2724, May 2016.
- [12] Kristian Finlator, Feryal Özel, Romeel Davé, and Benjamin D. Oppenheimer. The late reionization of filaments. *MNRAS*, 400(2):1049–1061, December 2009.
- [13] Daniel Foreman-Mackey, David W. Hogg, Dustin Lang, and Jonathan Goodman. emcee: The MCMC Hammer. *PASP*, 125(925):306, March 2013.
- [14] Steven R. Furlanetto and S. Peng Oh. Taxing the rich: recombinations and bubble growth during reionization. *MNRAS*, 363(3):1031–1048, November 2005.
- [15] Steven R. Furlanetto and S. Peng Oh. Reionization through the lens of percolation theory. *MNRAS*, 457(2):1813–1827, April 2016.
- [16] Steven R. Furlanetto, S. Peng Oh, and Frank H. Briggs. Cosmology at low frequencies: The 21 cm transition and the high-redshift Universe. *Phys. Rep.*, 433(4-6):181–301, October 2006.
- [17] Steven R. Furlanetto, Matias Zaldarriaga, and Lars Hernquist. The Growth of H II Regions During Reionization. *ApJ*, 613(1):1–15, September 2004.
- [18] Bradley Greig and Andrei Mesinger. 21cmcmc: an mcmc analysis tool enabling astrophysical parameter studies of the cosmic 21 cm signal. *MNRAS*, 449:4246–4263, 2015.
- [19] Max Gronke, Mark Dijkstra, Michael McCourt, and S. Peng Oh. From Mirrors to Windows: Lyman-alpha Radiative Transfer in a Very Clumpy Medium. *ApJ*, 833(2):L26, December 2016.

- [20] Max Gronke, Mark Dijkstra, Michael McCourt, and S. Peng Oh. Resonant line transfer in a fog: using Lyman-alpha to probe tiny structures in atomic gas. *A&A*, 607:A71, November 2017.
- [21] E. J. Groth and P. J. E. Peebles. Statistical analysis of catalogs of extragalactic objects. VII. Two- and three-point correlation functions for the high-resolution Shane-Wirtanen catalog of galaxies. *ApJ*, 217:385–405, October 1977.
- [22] Siddhartha Gurung-López, Álvaro A. Orsi, Silvia Bonoli, Nelson Padilla, Cedric G. Lacey, and Carlton M. Baugh. Ly  $\alpha$  emitters in a cosmological volume II: the impact of the intergalactic medium. *MNRAS*, 491(3):3266–3289, January 2020.
- [23] Zoltán Haiman and Marco Spaans. Models for Dusty Ly $\alpha$  Emitters at High Redshift. *ApJ*, 518(1):138–144, June 1999.
- [24] Lam Hui and Nickolay Y. Gnedin. Equation of state of the photoionized intergalactic medium. *MNRAS*, 292(1):27–42, November 1997.
- [25] Anne Hutter, Pratika Dayal, and Volker Müller. Clustering and lifetime of Lyman Alpha Emitters in the Epoch of Reionization. *MNRAS*, 450(4):4025–4034, July 2015.
- [26] Anne Hutter, Pratika Dayal, Volker Müller, and Cathryn M. Trott. Exploring 21cm-Lyman Alpha Emitter Synergies for SKA. *ApJ*, 836(2):176, February 2017.
- [27] Anne Hutter, Pratika Dayal, Adrian M. Partl, and Volker Müller. The visibility of Lyman  $\alpha$  emitters: constraining reionization, ionizing photon escape fractions and dust. *MNRAS*, 441(4):2861–2877, July 2014.
- [28] Hannes Jensen, Peter Laursen, Garrelt Mellema, Ilian T. Iliev, Jesper Sommer-Larsen, and Paul R. Shapiro. On the use of Ly $\alpha$  emitters as probes of reionization. *MNRAS*, 428(2):1366–1381, January 2013.

- [29] Koki Kakiichi, Mark Dijkstra, Benedetta Ciardi, and Luca Graziani. Ly $\alpha$ -emitting galaxies as a probe of reionization: large-scale bubble morphology and small-scale absorbers. *MNRAS*, 463(4):4019–4040, December 2016.
- [30] Nobunari Kashikawa, Kazuhiro Shimasaku, Matthew A. Malkan, Mamoru Doi, Yuichi Matsuda, Masami Ouchi, Yoshiaki Taniguchi, Chun Ly, Tohru Nagao, Masanori Iye, Kentaro Motohara, Takashi Murayama, Kouji Murozono, Kyoji Nariai, Kouji Ohta, Sadanori Okamura, Toshiyuki Sasaki, Yasuhiro Shioya, and Masayuki Umemura. The End of the Reionization Epoch Probed by Ly $\alpha$  Emitters at  $z = 6.5$  in the Subaru Deep Field. *ApJ*, 648(1):7–22, September 2006.
- [31] Nicholas S. Kern, Adrian Liu, Aaron R. Parsons, Andrei Mesinger, and Bradley Greig. Emulating Simulations of Cosmic Dawn for 21 cm Power Spectrum Constraints on Cosmology, Reionization, and X-Ray Heating. *ApJ*, 848(1):23, October 2017.
- [32] Taysun Kimm and Renyue Cen. Escape Fraction of Ionizing Photons during Reionization: Effects due to Supernova Feedback and Runaway OB Stars. *ApJ*, 788(2):121, June 2014.
- [33] L. Koopmans, J. Pritchard, G. Mellema, J. Aguirre, K. Ahn, R. Barkana, I. van Bemmell, G. Bernardi, A. Bonaldi, and F. Briggs. The Cosmic Dawn and Epoch of Reionisation with SKA. In *Advancing Astrophysics with the Square Kilometre Array (AASKA14)*, page 1, Apr 2015.
- [34] Stephen D. Landy and Alexander S. Szalay. Bias and Variance of Angular Correlation Functions. *ApJ*, 412:64, July 1993.
- [35] Joseph S. W. Lewis, Pierre Ocvirk, Dominique Aubert, Jenny G. Sorce, Paul R. Shapiro, Nicolas Deparis, Taha Dawoodbhoj, Romain Teyssier, Gustavo Yepes, Stefan Gottlöber, Kyungjin Ahn, Ilian T. Iliev, and Jonathan Chardin. Galactic ionizing photon budget during the epoch of reionization in the Cosmic Dawn II simulation. *MNRAS*, 496(4):4342–4357, August 2020.

- [36] Adrian Liu and Aaron R. Parsons. Constraining cosmology and ionization history with combined 21 cm power spectrum and global signal measurements. *MNRAS*, 457(2):1864–1877, April 2016.
- [37] Adrian Liu and J. Richard Shaw. Data Analysis for Precision 21 cm Cosmology. *PASP*, 132(1012):062001, June 2020.
- [38] Abraham Loeb and Steven R. Furlanetto. *The First Galaxies in the Universe*. Princeton University Press, 2013.
- [39] Piero Madau and Francesco Haardt. Cosmic Reionization after Planck: Could Quasars Do It All? *ApJ*, 813(1):L8, November 2015.
- [40] Sangeeta Malhotra and James E. Rhoads. Luminosity Functions of Ly $\alpha$  Emitters at Redshifts  $z=6.5$  and  $z=5.7$ : Evidence against Reionization at  $z \leq 6.5$ . *ApJ*, 617(1):L5–L8, December 2004.
- [41] Charlotte A. Mason and Max Gronke. Measuring the properties of reionised bubbles with resolved Lyman alpha spectra. *arXiv e-prints*, page arXiv:2004.13065, April 2020.
- [42] Charlotte A. Mason, Tommaso Treu, Stephane de Barros, Mark Dijkstra, Adriano Fontana, Andrei Mesinger, Laura Pentericci, Michele Trenti, and Eros Vanzella. Beacons into the Cosmic Dark Ages: Boosted Transmission of Ly $\alpha$  from UV Bright Galaxies at  $z \gtrsim 7$ . *ApJ*, 857(2):L11, April 2018.
- [43] Charlotte A. Mason, Tommaso Treu, Mark Dijkstra, Andrei Mesinger, Michele Trenti, Laura Pentericci, Stephane de Barros, and Eros Vanzella. The Universe Is Reionizing at  $z \sim 7$ : Bayesian Inference of the IGM Neutral Fraction Using Ly $\alpha$  Emission from Galaxies. *ApJ*, 856(1):2, March 2018.
- [44] Jorryt Matthee, David Sobral, Sérgio Santos, Huub Röttgering, Behnam Darvish, and Bahram Mobasher. Identification of the brightest Ly $\alpha$  emitters at  $z = 6.6$ : implications for the evolution of the luminosity function in the reionization era. *MNRAS*, 451(1):400–417, July 2015.

- [45] Matthew McQuinn, Lars Hernquist, Matias Zaldarriaga, and Suvendra Dutta. Studying reionization with Ly $\alpha$  emitters. *MNRAS*, 381(1):75–96, October 2007.
- [46] Andrei Mesinger, Aycin Aykutanalp, Eros Vanzella, Laura Pentericci, Andrea Ferrara, and Mark Dijkstra. Can the intergalactic medium cause a rapid drop in Ly $\alpha$  emission at  $z > 6$ ? *MNRAS*, 446(1):566–577, January 2015.
- [47] Andrei Mesinger, Steven Furlanetto, and Renyue Cen. 21CMFAST: a fast, seminumerical simulation of the high-redshift 21-cm signal. *MNRAS*, 411(2):955–972, February 2011.
- [48] Andrei Mesinger, Matthew McQuinn, and David N. Spergel. The kinetic Sunyaev-Zel’dovich signal from inhomogeneous reionization: a parameter space study. *MNRAS*, 422(2):1403–1417, May 2012.
- [49] Jordi Miralda-Escudé, Martin Haehnelt, and Martin J. Rees. Reionization of the Inhomogeneous Universe. *ApJ*, 530(1):1–16, February 2000.
- [50] Jordan Mirocha, Charlotte Mason, and Daniel P. Stark. Effects of self-consistent rest-ultraviolet colours in semi-empirical galaxy formation models. *MNRAS*, 498(2):2645–2661, October 2020.
- [51] Miguel F. Morales and J. Stuart B. Wyithe. Reionization and Cosmology with 21-cm Fluctuations. *ARA&A*, 48:127–171, September 2010.
- [52] Masami Ouchi, Kazuhiro Shimasaku, Hisanori Furusawa, Tomoki Saito, Makiko Yoshida, Masayuki Akiyama, Yoshiaki Ono, Toru Yamada, Kazuaki Ota, Nobunari Kashikawa, Masanori Iye, Tadayuki Kodama, Sadanori Okamura, Chris Simpson, and Michitoshi Yoshida. Statistics of 207 Ly $\alpha$  Emitters at a Redshift Near 7: Constraints on Reionization and Galaxy Formation Models. *ApJ*, 723(1):869–894, November 2010.
- [53] Michael Pagano and Adrian Liu. Quantifying density-ionization correlations with the 21-cm power spectrum. *MNRAS*, 498(1):373–384, August 2020.

- [54] Jaehong Park, Andrei Mesinger, Bradley Greig, and Nicolas Gillet. Inferring the astrophysics of reionization and cosmic dawn from galaxy luminosity functions and the 21-cm signal. *MNRAS*, 484(1):933–949, March 2019.
- [55] Aaron R. Parsons, Adrian Liu, James E. Aguirre, Zaki S. Ali, Richard F. Bradley, Chris L. Carilli, David R. DeBoer, Matthew R. Dexter, Nicole E. Gugliucci, Daniel C. Jacobs, Pat Klima, David H. E. MacMahon, Jason R. Manley, David F. Moore, Jonathan C. Pober, Irina I. Stefan, and William P. Walbrugh. New Limits on 21 cm Epoch of Reionization from PAPER-32 Consistent with an X-Ray Heated Intergalactic Medium at  $z = 7.7$ . *ApJ*, 788(2):106, June 2014.
- [56] P. J. E. Peebles. *The large-scale structure of the universe*. 1980.
- [57] Planck Collaboration, P. A. R. Ade, N. Aghanim, M. Arnaud, M. Ashdown, J. Aumont, C. Baccigalupi, A. J. Banday, R. B. Barreiro, J. G. Bartlett, N. Bartolo, E. Battaner, R. Battye, K. Benabed, A. Benoît, A. Benoit-Lévy, J. P. Bernard, M. Bersanelli, P. Bielewicz, J. J. Bock, A. Bonaldi, L. Bonavera, J. R. Bond, J. Borrill, F. R. Bouchet, F. Boulanger, M. Bucher, C. Burigana, R. C. Butler, E. Calabrese, J. F. Cardoso, A. Catalano, A. Challinor, A. Chamballu, R. R. Chary, H. C. Chiang, J. Chluba, P. R. Christensen, S. Church, D. L. Clements, S. Colombi, L. P. L. Colombo, C. Combet, A. Coulais, B. P. Crill, A. Curto, F. Cuttaia, L. Danese, R. D. Davies, R. J. Davis, P. de Bernardis, A. de Rosa, G. de Zotti, J. Delabrouille, F. X. Désert, E. Di Valentino, C. Dickinson, J. M. Diego, K. Dolag, H. Dole, S. Donzelli, O. Doré, M. Douspis, A. Ducout, J. Dunkley, X. Dupac, G. Efstathiou, F. Elsner, T. A. Enßlin, H. K. Eriksen, M. Farhang, J. Fergusson, F. Finelli, O. Forni, M. Frailis, A. A. Fraisse, E. Franceschi, A. Frejsel, S. Galeotta, S. Galli, K. Ganga, C. Gauthier, M. Gerbino, T. Ghosh, M. Giard, Y. Giraud-Héraud, E. Giusarma, E. Gjerløw, J. González-Nuevo, K. M. Górski, S. Gratton, A. Gregorio, A. Gruppuso, J. E. Gudmundsson, J. Hamann, F. K. Hansen, D. Hanson, D. L. Harrison, G. Helou, S. Henrot-Versillé, C. Hernández-Monteagudo, D. Herranz, S. R. Hildebrandt, E. Hivon, M. Hobson, W. A. Holmes, A. Hornstrup, W. Hovest, Z. Huang, K. M. Huffenberger, G. Hurier, A. H. Jaffe, T. R. Jaffe, W. C. Jones, M. Ju-

vela, E. Keihänen, R. Keskitalo, T. S. Kisner, R. Kneissl, J. Knoche, L. Knox, M. Kunz, H. Kurki-Suonio, G. Lagache, A. Lähteenmäki, J. M. Lamarre, A. Lasenby, M. Lattanzi, C. R. Lawrence, J. P. Leahy, R. Leonardi, J. Lesgourgues, F. Levrier, A. Lewis, M. Liguori, P. B. Lilje, M. Linden-Vørnle, M. López-Cañiego, P. M. Lubin, J. F. Macías-Pérez, G. Maggio, D. Maino, N. Mandolesi, A. Mangilli, A. Marchini, M. Maris, P. G. Martin, M. Martinelli, E. Martínez-González, S. Masi, S. Matarrese, P. McGehee, P. R. Meinhold, A. Melchiorri, J. B. Melin, L. Mendes, A. Mennella, M. Migliaccio, M. Millea, S. Mitra, M. A. Miville-Deschênes, A. Moneti, L. Montier, G. Morgante, D. Mortlock, A. Moss, D. Munshi, J. A. Murphy, P. Naselsky, F. Nati, P. Natoli, C. B. Netterfield, H. U. Nørgaard-Nielsen, F. Noviello, D. Novikov, I. Novikov, C. A. Oxborrow, F. Paci, L. Pagano, F. Pajot, R. Paladini, D. Paoletti, B. Partridge, F. Pasian, G. Patanchon, T. J. Pearson, O. Perdereau, L. Perotto, F. Perrotta, V. Pettorino, F. Piacentini, M. Piat, E. Pierpaoli, D. Pietrobon, S. Plaszczynski, E. Pointecouteau, G. Polenta, L. Popa, G. W. Pratt, G. Prézeau, S. Prunet, J. L. Puget, J. P. Rachen, W. T. Reach, R. Rebolo, M. Reinecke, M. Remazeilles, C. Renault, A. Renzi, I. Ristorcelli, G. Rocha, C. Rosset, M. Rossetti, G. Roudier, B. Rouillé d'Orfeuill, M. Rowan-Robinson, J. A. Rubiño-Martín, B. Rusholme, N. Said, V. Salvatelli, L. Salvati, M. Sandri, D. Santos, M. Savelainen, G. Savini, D. Scott, M. D. Seiffert, P. Serra, E. P. S. Shellard, L. D. Spencer, M. Spinelli, V. Stolyarov, R. Stompor, R. Sudiwala, R. Sunyaev, D. Sutton, A. S. Suur-Uski, J. F. Sygnet, J. A. Tauber, L. Terenzi, L. Toffolatti, M. Tomasi, M. Tristram, T. Trombetti, M. Tucci, J. Tuovinen, M. Türler, G. Umana, L. Valenziano, J. Valiviita, F. Van Tent, P. Vielva, F. Villa, L. A. Wade, B. D. Wandelt, I. K. Wehus, M. White, S. D. M. White, A. Wilkinson, D. Yvon, A. Zacchei, and A. Zonca. Planck 2015 results. XIII. Cosmological parameters. *A&A*, 594:A13, September 2016.

- [58] Jonathan C. Pober, Adrian Liu, Joshua S. Dillon, James E. Aguirre, Judd D. Bowman, Richard F. Bradley, Chris L. Carilli, David R. DeBoer, Jacqueline N. Hewitt, Daniel C. Jacobs, Matthew McQuinn, Miguel F. Morales, Aaron R. Parsons, Max Tegmark, and Dan J. Werthimer. What Next-generation 21 cm Power Spectrum Measurements can Teach us About the Epoch of Reionization. *ApJ*, 782(2):66, February 2014.

- [59] Jonathan C. Pober, Aaron R. Parsons, James E. Aguirre, Zaki Ali, Richard F. Bradley, Chris L. Carilli, Dave DeBoer, Matthew Dexter, Nicole E. Gugliucci, Daniel C. Jacobs, Patricia J. Klima, Dave MacMahon, Jason Manley, David F. Moore, Irina I. Stefan, and William P. Walbrugh. Opening the 21 cm Epoch of Reionization Window: Measurements of Foreground Isolation with PAPER. *ApJ*, 768(2):L36, May 2013.
- [60] Jonathan C. Pober, Aaron R. Parsons, David R. DeBoer, Patrick McDonald, Matthew McQuinn, James E. Aguirre, Zaki Ali, Richard F. Bradley, Tzu-Ching Chang, and Miguel F. Morales. The Baryon Acoustic Oscillation Broadband and Broad-beam Array: Design Overview and Sensitivity Forecasts. *AJ*, 145(3):65, March 2013.
- [61] Andrew Pontzen, Anže Slosar, Nina Roth, and Hiranya V. Peiris. Inverted initial conditions: Exploring the growth of cosmic structure and voids. *Phys. Rev. D*, 93(10):103519, May 2016.
- [62] Jonathan R. Pritchard and Abraham Loeb. 21 cm cosmology in the 21st century. *Reports on Progress in Physics*, 75(8):086901, August 2012.
- [63] Michael R. Santos. Probing reionization with Lyman  $\alpha$  emission lines. *MNRAS*, 349(3):1137–1152, April 2004.
- [64] Marta B. Silva, Mario G. Santos, Yan Gong, Asantha Cooray, and James Bock. Intensity Mapping of Ly $\alpha$  Emission during the Epoch of Reionization. *ApJ*, 763(2):132, February 2013.
- [65] P. Simon. How accurate is Limber’s equation? *A&A*, 473(3):711–714, October 2007.
- [66] Emanuele Sobacchi and Andrei Mesinger. Inhomogeneous recombinations during cosmic reionization. *MNRAS*, 440(2):1662–1673, May 2014.
- [67] Emanuele Sobacchi and Andrei Mesinger. The clustering of Lyman  $\alpha$  emitters at  $z \approx 7$ : implications for reionization and host halo masses. *MNRAS*, 453(2):1843–1854, October 2015.

- [68] Antoinette Songaila and Lennox L. Cowie. The Evolution of Lyman Limit Absorption Systems to Redshift Six. *ApJ*, 721(2):1448–1466, October 2010.
- [69] Argyro Tasitsiomi. Ly $\alpha$  radiative transfer in cosmological simulations and application to  $z \approx 8$  Ly $\alpha$  emitter. *The Astrophysical Journal*, 645(2):792–813, jul 2006.
- [70] S. J. Tingay, R. Goeke, J. D. Bowman, D. Emrich, S. M. Ord, D. A. Mitchell, M. F. Morales, T. Boller, B. Crosse, R. B. Wayth, C. J. Lonsdale, S. Tremblay, D. Pallot, T. Colegate, A. Wicenec, N. Kudryavtseva, W. Arcus, D. Barnes, G. Bernardi, F. Briggs, S. Burns, J. D. Bunton, R. J. Cappallo, B. E. Corey, A. Deshpande, L. Desouza, B. M. Gaensler, L. J. Greenhill, P. J. Hall, B. J. Hazelton, D. Herne, J. N. Hewitt, M. Johnston-Hollitt, D. L. Kaplan, J. C. Kasper, B. B. Kincaid, R. Koenig, E. Kratzenberg, M. J. Lynch, B. Mckinley, S. R. McWhirter, E. Morgan, D. Oberoi, J. Pathikulangara, T. Prabu, R. A. Remillard, A. E. E. Rogers, A. Roshi, J. E. Salah, R. J. Sault, N. Udaya-Shankar, F. Schlagenhauser, K. S. Srivani, J. Stevens, R. Subrahmanyan, M. Waterson, R. L. Webster, A. R. Whitney, A. Williams, C. L. Williams, and J. S. B. Wyithe. The Murchison Widefield Array: The Square Kilometre Array Precursor at Low Radio Frequencies. *Publ. Astron. Soc. Australia*, 30:e007, January 2013.
- [71] M. P. van Haarlem, M. W. Wise, A. W. Gunst, G. Heald, J. P. McKean, J. W. T. Hessels, A. G. de Bruyn, R. Nijboer, J. Swinbank, R. Fallows, M. Brentjens, A. Nelles, R. Beck, H. Falcke, R. Fender, J. Hörandel, L. V. E. Koopmans, G. Mann, G. Miley, H. Röttgering, B. W. Stappers, R. A. M. J. Wijers, S. Zaroubi, M. van den Akker, A. Alexov, J. Anderson, K. Anderson, A. van Ardenne, M. Arts, A. Asgekar, I. M. Avruch, F. Batejat, L. Bähren, M. E. Bell, M. R. Bell, I. van Bemmelen, P. Bennema, M. J. Bentum, G. Bernardi, P. Best, L. Bîrzan, A. Bonafede, A. J. Boonstra, R. Braun, J. Bregman, F. Breitling, R. H. van de Brink, J. Broderick, P. C. Broekema, W. N. Brouw, M. Brüggen, H. R. Butcher, W. van Cappellen, B. Ciardi, T. Coenen, J. Conway, A. Coolen, A. Corstanje, S. Damstra, O. Davies, A. T. Deller, R. J. Dettmar, G. van Diepen, K. Dijkstra, P. Donker, A. Doorduyn, J. Dromer, M. Drost, A. van Duin, J. Eislöffel, J. van Enst, C. Ferrari, W. Frieswijk, H. Gankema, M. A. Garrett, F. de Gasperin, M. Gerbers, E. de Geus, J. M. Grießmeier, T. Grit, P. Gruppen, J. P. Hamaker, T. Hassall, M. Hoeft,

H. A. Holties, A. Horneffer, A. van der Horst, A. van Houwelingen, A. Huijgen, M. Iacobelli, H. Intema, N. Jackson, V. Jelic, A. de Jong, E. Juette, D. Kant, A. Karastergiou, A. Koers, H. Kollen, V. I. Kondratiev, E. Kooistra, Y. Koopman, A. Koster, M. Kuniyoshi, M. Kramer, G. Kuper, P. Lambropoulos, C. Law, J. van Leeuwen, J. Lemaitre, M. Loose, P. Maat, G. Macario, S. Markoff, J. Masters, R. A. McFadden, D. McKay-Bukowski, H. Meijering, H. Meulman, M. Mevius, E. Middelberg, R. Millenaar, J. C. A. Miller-Jones, R. N. Mohan, J. D. Mol, J. Morawietz, R. Morganti, D. D. Mulcahy, E. Mulder, H. Munk, L. Nieuwenhuis, R. van Nieuwpoort, J. E. Noordam, M. Norden, A. Noutsos, A. R. Offringa, H. Olofsson, A. Omar, E. Orrú, R. Overeem, H. Paas, M. Pandey-Pommier, V. N. Pandey, R. Pizzo, A. Polatidis, D. Rafferty, S. Rawlings, W. Reich, J. P. de Reijer, J. Reitsma, G. A. Renting, P. Riemers, E. Rol, J. W. Romein, J. Roosjen, M. Rüter, A. Scaife, K. van der Schaaf, B. Scheers, P. Schellart, A. Schoenmakers, G. Schoonderbeek, M. Serylak, A. Shulevski, J. Sluman, O. Smirnov, C. Sobey, H. Spreeuw, M. Steinmetz, C. G. M. Sterks, H. J. Stiepel, K. Stuurwold, M. Tagger, Y. Tang, C. Tasse, I. Thomas, S. Thoudam, M. C. Toribio, B. van der Tol, O. Usov, M. van Veelen, A. J. van der Veen, S. ter Veen, J. P. W. Verbiest, R. Vermeulen, N. Vermaas, C. Vocks, C. Vogt, M. de Vos, E. van der Wal, R. van Weeren, H. Weggemans, P. Weltevrede, S. White, S. J. Wijnholds, T. Wilhelmsson, O. Wucknitz, S. Yatawatta, P. Zarka, A. Zensus, and J. van Zwieten. LOFAR: The LOw-Frequency ARray. *A&A*, 556:A2, August 2013.

[72] A. Verhamme, D. Schaerer, and A. Maselli. 3D Ly $\alpha$  radiation transfer. I. Understanding Ly $\alpha$  line profile morphologies. *A&A*, 460(2):397–413, December 2006.

[73] Anne Verhamme, Ivana Orlitová, Daniel Schaerer, and Matthew Hayes. Using Lyman- $\alpha$  to detect galaxies that leak Lyman continuum. *A&A*, 578:A7, June 2015.

[74] Eli Visbal and Matthew McQuinn. The Impact of Neutral Intergalactic Gas on Ly $\alpha$  Intensity Mapping during Reionization. *ApJ*, 863(1):L6, August 2018.

[75] C. A. Watkinson and J. R. Pritchard. Distinguishing models of reionization using future radio observations of 21-cm 1-point statistics. *MNRAS*, 443(4):3090–3106, October 2014.

- [76] Lewis H. Weinberger, Martin G. Haehnelt, and Girish Kulkarni. Modelling the observed luminosity function and clustering evolution of Ly  $\alpha$  emitters: growing evidence for late reionization. *MNRAS*, 485(1):1350–1366, May 2019.
- [77] John H. Wise, Vasiliy G. Demchenko, Martin T. Halicek, Michael L. Norman, Matthew J. Turk, Tom Abel, and Britton D. Smith. The birth of a galaxy - III. Propelling reionization with the faintest galaxies. *MNRAS*, 442(3):2560–2579, August 2014.

## **Chapter 5**

# **Characterization Of Inpaint Residuals In Interferometric Measurements of the Epoch Of Reionization**

### **Addendum for thesis**

This chapter addresses one of the dominant systematics encountered by 21cm instruments: Radio Frequency Interference (RFI). Interference is prevalent in instruments that operate in the radio band, so 21cm measurements are plagued by RFI. This has led some experiments to place instruments in radio quiet zones like the Karoo desert. However, this still does not totally eliminate RFI. RFI is an even larger problem for interferometers measuring the 21cm power spectrum (such as HERA). Inpainting techniques have been developed to mitigate some of the issues caused by RFI and there are existing inpainting methods that are commonly used in astronomy to do this task. Adrian Liu and I sought to build a convolutional neural network (CNN) that is capable of inpainting RFI corrupted data. In this work, I demonstrate the effectiveness of our CNN by comparison with existing techniques.

There has not yet been a detection of the 21cm power spectrum; however, we are making progress. Since inpainting is frequently done as part of the data analysis pipeline of interferometric

instruments looking to measure the 21cm power spectrum, it is important to understand the types of errors caused by inpainting. This work quantifies the errors due to inpainting techniques in the data analysis pipeline. Along with existing inpainting methods that are commonly used in astronomy, we use Monte Carlo realizations to study the errors due to inpainting in the 21cm power spectrum.

## **Abstract**

Radio Frequency Interference (RFI) is one of the systematic challenges preventing 21cm interferometric instruments from detecting the Epoch of Reionization (EoR). To mitigate the effects of RFI on data analysis pipelines, numerous inpaint techniques have been developed to crudely restore RFI corrupted data. In this paper we examine the qualitative and quantitative errors introduced into the visibilities and power spectrum due to inpainting. We perform our analysis on simulated data as well as real data from the Hydrogen Epoch of Reionization Array (HERA) Phase 1 upper limits. We also introduce a convolutional neural network that is capable of inpainting RFI corrupted data. We train our network on simulated data and show that our network is capable at inpainting real data without requiring to be retrained. We find that techniques that incorporate high wavenumbers in delay space in their modeling are best suited for inpainting over narrowband RFI. We also show that with our fiducial parameters Discrete Prolate Spheroidal Sequences (DPSS) and CLEAN provide the best performance for intermittent RFI while Gaussian Process Regression (GPR) and Least Squares Spectral Analysis (LSSA) provide the best performance for larger RFI gaps. However we caution that these qualitative conclusions are sensitive to the chosen hyperparameters of each inpainting technique. We find these results to be consistent in both simulated and real visibilities. We show that all inpainting techniques reliably reproduce foreground dominated modes in the power spectrum. Since the inpainting techniques should not be capable of reproducing noise realizations, we find that the largest errors occur in the noise dominated delay modes. We show that in the future, as the noise level of the data comes down, CLEAN and DPSS are most capable of reproducing the fine frequency structure in the visibilities of HERA data.

## 5.1 Introduction

The Epoch of Reionization (EoR) plays a crucial role in the evolution of the Universe since it is the period in which the intergalactic medium (IGM) transitions from neutral to ionized. The precise details of how the EoR unfold are currently observationally unconstrained. In most models of the EoR, the onset of the first generation galaxies give rise to ionizing photons which gradually disperse across the IGM and ionize the neutral hydrogen marking the beginning of the EoR [8, 25, 32, 37]. One method to directly measure the neutral hydrogen in the IGM during the EoR is to use the 21cm hyperfine transition of hydrogen in which a 21cm wavelength photon is released when the electron flips its spin relative to the proton [7, 9, 28]. Thus the 21cm line directly probes the neutral hydrogen in the IGM during the EoR. The emitted 21cm-wavelength photon is then redshifted into radio wavelengths and is potentially observable in contrast to the CMB, enabling tomographic measurements of neutral hydrogen. Ground based interferometric instruments such as the Hydrogen Epoch of Reionization array (HERA) [4], Square Kilometer Array (SKA) [5], Precision Array for Probing the Epoch of Re-ionization (PAPER) [35], Murchison Widefield Array (MWA) [27], Low Frequency Array (LOFAR) [47] have the ability to measure the spatial fluctuations of the 21cm line.

One of the challenges in measuring radio photons using ground based instruments is the frequent data flagging due to radio frequency interference (RFI). Most RFI sources are due to terrestrial transmitters and satellites which lead to narrowband flagging in the data analysis. Other wideband sources of RFI, such as communication satellites, require flagging more substantive portions of the raw data. The excision of RFI in the data analysis introduces gaps in the data which cause artifacts in the 21cm power spectrum. Data analysis pipelines which try to separate the foregrounds from the cosmological signal in the Fourier domain will be directly affected by the RFI gaps in the data. This impedes measurement of the EoR (for example see [49]). A conservative approach to mitigate the effect of RFI on the power spectrum is to avoid all frequency bands where RFI has corrupted data which ensures that there aren't artifacts in the power spectrum. Doing so severely restricts the available frequency channels to use as part of our analysis thereby preventing us from

accessing all redshifts. Further, this approach is not ideal since it decreases the signal to noise of the measurement.

Data analysis pipelines which are affected by RFI use “inpainting” techniques to partially restore the RFI corrupted data. A number of algorithms have been developed to perform inpainting, most notably the CLEAN algorithm which was originally introduced in [15]. Although bearing the same name, we use a modified version of CLEAN to fit the inpainting needs in the HERA data analysis pipeline [34]. Besides CLEAN, other inpainting techniques have been explored as well such as least square spectral analysis (LSSA), Gaussian process regression (GPR) [11, 19] and discrete prolate spheroidal sequence (DPSS) [6, 42]. These inpainting methods use the uncorrupted data to form a crude model for the corrupted data which is then replaced into the RFI flagged regions, thereby reducing the effect that RFI has on the 21cm power spectrum. However, the crudely restored data are imperfect and thus they too introduce errors in the analysis. In this paper we critically evaluate the performance of existing inpainting techniques CLEAN, LSSA, GPR, and DPSS in reconstructing corrupted visibility data. In this paper we study the HERA implementations of these inpainting techniques however similar variations of these techniques have been implemented in other instruments such as [33] in the LOFAR experiment and [2] in the MWA. Outside of 21cm cosmology, inpainting has been frequently done in CMB studies [12, 43, 46] and gravitational waves analyses [51].

We also introduce a Convolutional Neural Network (CNN) dubbed as “U-Paint” as an alternative to inpainting RFI corrupted data. CNNs have been previously explored as an inpainting technique by [26, 30, 40, 44, 50, 53] but not in the context of radio astronomy experiments. U-Paint marks the introduction of CNNs as an inpainting technique in the data analysis pipelines of radio astronomy. By assessing its effectiveness as compared to existing techniques we show that convolutional neural networks show great promise as an inpainting technique. Using a series of Monte Carlo realizations, we propagate the errors of the inpainted visibilities through to the 21cm power spectrum. We quantify the performance of each inpainting technique and parametrize their errors in the power spectrum. We perform our analysis using the HERA instrument; however, our approach is general enough to apply to any interferometer. This paper is structured as follows. In Section 5.2 we

introduce our fiducial instrument HERA as well as sources of RFI which affect the data analysis pipeline. In Section 5.3 we discuss existing inpainting techniques CLEAN, LSSA, GPR, and DPSS as well as quantifying their performance in inpainting corrupted visibilities. In Section 5.3.5 we introduce U-Paint which we use to inpaint corrupted data. In Section 5.6 we assess its performance relative to existing inpainting methods. In Section 5.7 we propagate the inpainting errors through the analysis and characterize their effect on the power spectrum. In Section 5.8 we apply our analysis on real HERA data. We conclude in Section 6.7.

## 5.2 HERA Observations

In this section we introduce the HERA instrument, an interferometer located in the Karoo desert designed to measure the 21cm power spectrum during Cosmic Dawn and the EoR. Though we use the HERA instrument as the test-bed for analysis, our results and procedures are not strictly limited to HERA and are thus applicable to any interferometer. When completed, HERA will be comprised of 350 14m dishes capable of observing at frequencies 50MHz to 225MHz. In this paper however, we consider the instrumental parameters taken from Phase 1 data used to set the recent HERA upper limits [14] which span frequencies 100MHz to 200MHz in 1024 channels using 39 dishes. In this Section we review the data analysis pipeline established in HERA’s Phase 1 upper limits, which we use in this paper for consistency. In doing so, we establish notation for the remainder of this paper. We begin in Section 5.2.2 where we discuss the Phase 1 data analysis pipeline from [14] while in Section 5.2.1 we discuss RFI scenarios which affect interferometric measurements at low frequencies. In Section 5.2.3 we discuss the simulated datasets that we use as part of our analysis as well as real data from the Phase 1 data release.

### 5.2.1 RFI Flagging

Though we discuss the effect of RFI on our fiducial instrument HERA, the systematics caused by RFI are equally applicable to other instruments. Radio experiments located on the ground ubiquitously experience RFI. The origin of the RFI are either terrestrial in nature or due to satellites. Terrestrial

sources can range from cell-phones, WiFi as well any other radio producing mechanism sourced on the ground. This includes FM radio and broadcast television. The amount of terrestrial RFI can be minimized by operating the instrument in radio quiet zone, such as the Karoo desert in HERA's case. This minimizes terrestrial RFI but does not totally eliminate it [14, 21–23, 55]. For brevity, we find it useful to organize RFI by the number of frequency channels they occupy. We shall denote RFI which occupies relatively few channels ( $\sim 1 - 3$ ) as narrowband RFI. We assign the RFI to be wideband if it occupies a more significant fraction of the frequency band. Note that we are not setting a strict definition of narrowband or wideband RFI, rather we find it convenient to use this notation in our analysis. In Figure 5.1 we show example HERA flags. The most frequent type of RFI are narrowband emitters which can occur irregularly in  $\nu$  and  $t$  creating a scattered assortment of flags in the visibilities. However other wideband types of RFI can occur more predictably in the dataset. For example, ORBCOMM satellite communication at  $\nu = 136 - 138\text{MHz}$ , broadcast television at  $\nu > 174\text{MHz}$ . While a FM radio broadcast occupies a single frequency channel, frequencies  $\nu < 111\text{MHz}$  are reserved for FM broadcast.

HERA searches for RFI in the visibilities by scanning the data for localized irregularities. Adjacent data in  $\nu$  and local sidereal time (LST) are used to differentiate between RFI and thermal noise fluctuations. This procedure is applied after the absolute calibration step of the visibilities so that any issues with the instrument can also be flagged (see Figure 3 in [14] for a detailed description of the HERA data analysis pipeline). For example, in this flagging scheme, intermittent correlator integration failures (a source of wideband flags) can also be flagged. The LST binned visibilities are also manually scanned for narrowband RFI that was undetected by the automated flagging process.

## 5.2.2 Power Spectrum

HERA Phase 1 observed the radio sky at frequencies 100MHz to 200MHz over 1024 channels corresponding to a channel width of  $\Delta\nu \simeq 0.1\text{MHz}$ . These frequencies are measured at time cadence of  $\Delta t = 10.7\text{s}$ . The raw data taken from correlated antennas in the interferometer are termed the visibilities  $V$ , which depend on the observation frequency  $\nu$ , and the time of observation “LST”. The visibilities are complex valued and thus can be expressed either in terms of their real

and imaginary components or amplitude and phase. We denote the amplitude of the visibilities as  $|V|$  and the phase of the visibilities as  $\phi$ . Since the visibilities are the product of correlated antennas, the visibilities are simultaneously measured on all antenna combinations within the HERA antenna array. The visibilities measured by the HERA interferometer using the  $i$ th antenna at position  $\mathbf{x}_i$  and  $j$ th antenna at position  $\mathbf{x}_j$  form a baseline  $\mathbf{b} = \mathbf{x}_i - \mathbf{x}_j$ . It was shown by [34, 36] that for a single baseline  $\mathbf{b}$  at observation frequency  $\nu$ , the visibilities can be written as

$$V(u, \nu) = \int dl dm A(l, m, \nu) T(l, m, \nu, t) e^{-2\pi i \nu \tau_g} \quad (5.1)$$

where  $A(l, m)$  is the primary beam of the instrument and  $T(l, m)$  is the temperature of the sky. The time dependence arises because the sky rotates above the instrument. The terms  $l \equiv \sin(\theta_x)$  and  $m \equiv \sin(\theta_y)$  encode the angular components of the sky and  $\tau_g$  is given by

$$\tau_g \equiv \frac{\mathbf{b} \cdot \hat{\mathbf{s}}}{c} = \frac{1}{c} \left( b_x l + b_y m + b_z \sqrt{1 - l^2 - m^2} \right) \quad (5.2)$$

where  $\tau_g$  is the geometric delay corresponding to the projection of the baseline  $\mathbf{b} = (b_x, b_y, b_z)$  in the direction  $\hat{\mathbf{s}} = (l, m, \sqrt{1 - l^2 - m^2})$  and where  $c$  is the speed of light. Although the baseline  $\mathbf{b}$  in Equation 5.2 can represent any antenna pairing in the HERA array, in this paper we focus our analysis to only the shortest baselines, i.e. adjacent antenna pairs. The Fourier transform of the visibilities in Equation 5.1 along the frequency direction is defined as

$$\tilde{V}(\tau, t) = \int d\nu dl dm A(l, m, \nu) T(l, m, \nu, t) \phi(\nu) e^{2\pi i \nu (\tau - \tau_g)} \quad (5.3)$$

where  $\tau$  is the Fourier dual to frequency in the Fourier transform called the delay. The term  $\phi(\nu)$  denotes a tapering function that defines our spectral window of observation. For consistency with analysis from the Phase 1 upper limits, we use the Blackman-Harris window function as our tapering function  $\phi(\nu)$ . The delay power spectrum can be estimated by the square of  $\tilde{V}(\mathbf{b}, \tau)$ :

$$P(k_\perp, k_\parallel) = \frac{X^2 Y}{\Omega_{pp} B} \left| \tilde{V}(\mathbf{u}, \tau) \right|^2 \quad (5.4)$$

where  $k_{\perp}$  is the wavenumber corresponding to the plane of the sky and  $k_{\parallel}$  parallel to the line of sight. The visibility coordinates  $\mathbf{u}$  are related to the frequency  $\nu$  through  $\mathbf{u} = \nu \mathbf{b}/c$ . The term  $\Omega_{\text{pp}}$  gives the angular area by integrating the square of the primary beam, while  $B$  is an effective bandwidth given by  $\int d\nu |\phi|^2$ . The term  $k_{\perp}$  can be related to the baseline  $\mathbf{b}$  using  $k_{\perp} = \frac{2\pi\nu\mathbf{b}}{cX}$ . The term  $k_{\parallel}$  can be written as  $k_{\parallel} = \frac{2\pi\tau}{Y}$  where  $\tau$  is the Fourier dual to the frequency axis  $\nu$  with dimensions of  $1/\nu$ . The factor  $X$  converts comoving distance  $r_{\perp}$  to angular separation  $\theta$ , while  $Y$  converts radial comoving distances  $r_{\parallel}$  to frequency intervals  $\Delta\nu$ :

$$X \equiv \frac{r_{\perp}}{\theta} = \frac{c}{H_0} \int_0^z \frac{dz'}{E(z')} \quad (5.5)$$

$$Y \equiv \frac{\Delta r_{\parallel}}{\Delta\nu} = \frac{c}{H_0\nu_{21}} \frac{(1+z)^2}{E(z)} \quad (5.6)$$

and where  $H_0$  is the Hubble parameter,  $E(z) \equiv \sqrt{\Omega_m(1+z)^3 + \Omega_{\Lambda}}$  and  $\Omega_{\Lambda}$  the normalized dark energy density and  $\nu_{21} \approx 1420\text{MHz}$ , the rest frequency of the 21cm line. For a drift scan telescope like HERA, one typically first averages  $\tilde{V}(\mathbf{u}, \tau)$  at identical LSTs across different sidereal days. This process is referred to as coherent averaging. Once the power spectrum of the coherently averaged visibilities is computed, one then averages  $P(k_{\perp}, k_{\parallel})$  across different LSTs, a process known as incoherent averaging. In an observationally realistic data analysis pipeline (i.e. that aims to measure cosmological signal), instead of directly computing  $P(k_{\perp}, k_{\parallel})$  using Equation 5.4, one instead forms the cross spectra using different times or baselines in order to avoid a noise bias. In this scenario one forms the product of the visibilities at different times or baselines within the context of Equation 5.4. Since the objective of this paper is to characterize the statistical properties of inpaint models, and not to measure cosmological signal, we do not form the cross-spectra as described above. Thus, the noise bias will be present in our estimates of power spectra. To evaluate the power spectrum in Equation 5.4, we use the publicly available code `hera_pspec`<sup>1</sup>.

The delay power spectrum in Equation 5.4 is dominated by galactic and extra-galactic sources of radio emission referred to as the ‘‘foregrounds’’. The foregrounds are orders of magnitude brighter than the anticipated 21cm signal. The foregrounds are spectrally smooth, and thus can be crudely

<sup>1</sup>[https://github.com/HERA-Team/hera\\_pspec](https://github.com/HERA-Team/hera_pspec)

approximated by a flat spectrum. Under this assumption the temperature of the sky in Equation 5.1 loses its dependence on frequency,  $T(l, m, \nu, t) \simeq T(l, m, t)$ . If the beam and spectral window are also frequency independent, with a infinitely large bandpass then the delay  $\tau$  in Equation 5.4 is geometrically limited by the baseline length  $\mathbf{b}$  and the speed of light to values:

$$\tau_g \leq \frac{|\mathbf{b}|}{c}. \quad (5.7)$$

Under these idealistic assumptions the foregrounds are confined to within  $\tau_g$ ; however, since the foregrounds are only approximately smooth as a function of frequency and both the primary beam and  $\phi$  are also not frequency independent. Thus the foregrounds spread outside the confines of  $\tau_g$  [24]. Though in this paper we separate our analysis for  $\tau$  modes inside and outside of  $\tau_g$ , it should be noted that our analysis is not stringent on the true value of  $\tau_g$ , rather  $\tau_g$  serves as a convenient marker for modes which are mostly dominated by the foregrounds and modes which are relatively foreground free. Also note that in computing the power spectrum (Equation 5.4) we apply the Blackman-Harris tapering function. Since this operation is a convolution, this spreads power from each bin to neighbouring bins. Thus  $\tau_g$  modes which are dominated by the foregrounds are spread into adjacent bins. The objective of this work is to establish the errors in the data analysis pipeline due to inpainting. The errors do not strictly depend on which  $\tau$  modes are part of the wedge. Thus we conservatively include  $\tau$  modes satisfying  $|\tau| < 500\text{ns}$  to capture the spillover of foreground power into neighbouring  $\tau$  bins and for brevity we refer to all of these modes as the “wedge”.

The presence of flagged channels in the dataset complicates the above power spectrum analysis. Equation 5.4 is a Fourier transform of the visibilities along the frequency direction. Performing a Fourier transform of a dataset which contains masked regions will cause artifacts in the resulting Fourier spectrum. This effect is similar to carrying out a Fourier analysis of a top-hat function which creates a “ringing” at high delay modes. We thus expect excess power in the large  $\tau$  domain. **Thus analyses which sample the visibilities in the EoR window at high delay will be especially affected the by the artifacts due to flags in the data.** One conservative approach to circumvent this issue is to avoid frequency channels which have been flagged and select cleaner windows in

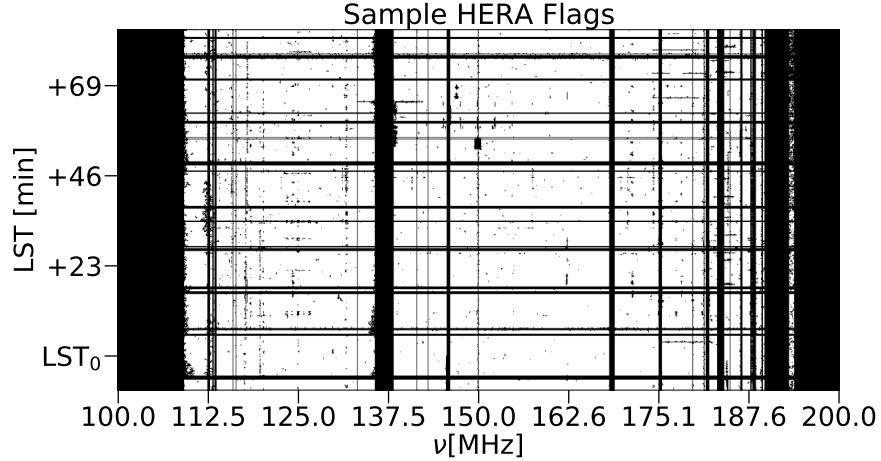


**Figure 5.1:** Sample HERA flags split from 100MHz-200MHz. Frequency channels below 110MHz are reserved for FM radio. The ORBCOMM satellite is responsible for RFI at  $\nu = 136$ MHz. Frequency channels above  $\nu = 174$ MHz are flagged due to broadcast television.

the visibilities which are unaffected by RFI. This strategy reduces the amount of data in the analysis and thus decreases the signal to noise.

### 5.2.3 Datasets

In this Section we introduce the datasets (i.e. visibilities) which we use as part of our analysis. We consider two separate sets of visibilities, real HERA data and simulations of HERA observations. For the simulated visibilities we also consider different noise scenarios.

For the real data we use HERA’s phase 1 visibilities (hereafter denoted as P1V) in [14], we use data from the IDR2 dataset which spans a range of right ascensions from 0 to 12 hours. The instrument parameters match those from Section 5.2.3. Since raw HERA data is propagated through a data analysis pipeline there are a number of places along the pipeline where we might choose to apply our analysis. We choose to use the visibilities after they have been absolutely calibrated. Our primary motivation for this is because the LST binning process results in averaging the visibilities by the number of observation nights resulting in lower noise. This makes it slightly easier for the inpainting algorithms due to the lower noise and also since there is intermittent RFI that isn’t present every day. In future work we can take advantage of the symmetries between visibility data

on different days by implementing network changes such as in [29] which are optimized to take advantage of symmetries in datasets.

For simulated data, we use the simulations from the HERA validation pipeline in [1]. The simulated visibilities in [1] are designed to be a realistic representation of the sky as seen through the HERA instrument and thus the instrumental parameters match those of the true visibilities. We briefly review the simulated data here though the reader is encouraged to see [1] for further details. To create a model of the sky composed of a foreground, and EoR component are put through a mock HERA observation simulator, RIMEz, an internally developed software which correctly simulates HERA’s drift scan capabilities, and is capable of sampling the sky at the cadence of HERA time sampling over HERA’s full frequency resolution and bandwidth. Though RIMEz simulation also take into account instrumental effects such as cross-coupling and reflection systematics, we do not include them in our simulations. The sky model is generated by adding an EoR component to the foregrounds. The EoR component is modeled as a Gaussian random temperature field with power spectrum  $P_{\text{EoR}} = A_0 k^{-2}$  **where this relationship approximates those which are obtained by simulations** and where  $A_0$  is the amplitude of the power spectrum. The EoR component is added to foreground model which is composed of GLEAM sources and diffuse emission. Only GLEAM sources with an associated spectral model are considered. The GLEAM sources are composed of approximately  $2.4 \times 10^5$  sources in the catalog which [16], each with a power law emission spectrum given by

$$I_p(\nu, \hat{s}) = \sum_n^{240 \times 10^3} F_n \left( \frac{\nu}{\nu_0} \right)^\beta \delta(1 - \hat{s} \cdot \hat{s}_n) \quad (5.8)$$

where  $F_n$  is the flux of the  $n$ th point source,  $\beta$  the spectral index which characterizes the power law and  $\hat{s}$  is its position. Note that since the GLEAM catalog has coverage gaps in regions within HERA’s spatial observation window, the observing times of the simulations are chosen as to avoid times where these gaps coincide with HERA’s primary beam. The diffuse emission component of the foregrounds is simulated based on the Global Sky Model in [54] and [3]. Thermal noise is generated and added to the simulations by drawing samples from a Gaussian distribution with zero mean and standard deviation  $\hat{\sigma}_0$  that depends on the time and frequency of observation as well as

the amplitude of the auto-correlation of each baseline through the radiometer equation

$$\hat{\sigma}_0(\nu, t) = \alpha \frac{\kappa(\nu)\Omega(\nu) (T_{\text{auto}}(\nu, t) + T_{\text{rx}})}{\sqrt{\Delta\nu\Delta t}} \quad (5.9)$$

where  $\Delta t$  is the time integration of 10.7s for HERA,  $\Delta\nu$  is HERA’s channel width, i.e.  $\Delta\nu \simeq 0.1\text{MHz}$  and  $T_{\text{rx}}$  is the receiver temperature (assumed to be uniform in  $\nu$  and independent of antenna, see [1] for precise values) in units of K/str. The term  $\kappa(\nu)\Omega(\nu)$  is a conversion factor from K/str to Jy through  $\kappa(\nu) = (2k_B \times 10^{26})/(A(\nu)\Omega(\nu))$  where  $k_B$  is the Boltzmann constant, and  $A(\nu)$  is the effective area and  $\Omega(\nu)$  is the solid angle of the beam. The parameter  $\alpha$  is a dimensionless parameter which we use to simulate scenarios with higher levels of thermal noise. We consider values of  $\alpha = [1, 2, 3, 4, 7]$ . In our fiducial noise level  $\alpha = 1$ . The total simulated visibilities spans roughly 13 hour observations corresponding to over  $\gtrsim 4000$  time integrations of 10.7 seconds each. The simulation data is composed of 39 operational antennas with north and east pointing polarisations. We consider only the shortest baselines (i.e. antennas separated by 14.7m) in this work. We find that our results do not depend on the specific antennas used to form the 14.7m baseline. Thus without loss of generality we perform our analysis using the antenna pair (84, 85), including multiple linear polarisations ( EE and NN ). We have repeated our subsequent analyses for redundant baselines using other antenna pairs and have found no significant differences in our qualitative or quantitative results. Since this is a simulated dataset, there are not any RFI corrupted regions. To imitate a scenario where RFI has corrupted regions of our simulated visibilities, we apply the HERA flags discussed in the previous section to our dataset.

### 5.3 Inpainting Techniques

In this section we describe the inpainting methods that we use as part of our analysis. We begin by introducing CLEAN and LSSA in Sections 5.3.1 and 5.3.2. In these sections we also compute the optimal value of CLEAN and LSSA hyperparameters to optimize their respective performances. In Section 5.3.3 we introduce the covariance-Based Inpainting methods, GPR & DPSS. Finally in Section 5.3.5 we introduce the neural network architecture of U-Paint.

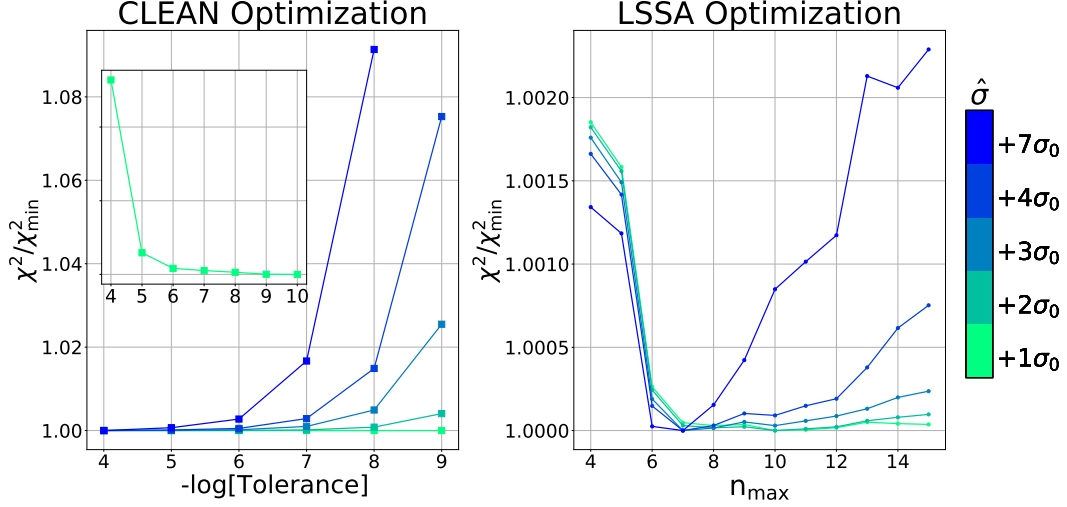


**Figure 5.2:** The results of our parameter optimization procedure for CLEAN and LSSA inpainting methods. In the left image fractional increase in  $\chi^2$  is plotted as a function of tolerance parameter values (see Section 5.3.1). The coloured curves represent different noise levels. As the thermal noise level in the dataset increases the optimal tolerance decreases. The inset provides a closer examination of  $\chi^2/\chi_{\min}^2$  for fiducial noise level  $\alpha = 1$ . Similarly on the right image, the fractional increase in  $\chi^2$  is plotted as a function of  $n_{\max}$ , the number of Fourier components to include in LSSA models. As we increase the thermal noise of the dataset, the optimal number of Fourier components to include in the model decreases.

### 5.3.1 CLEAN

The implementation of the CLEAN inpainting algorithm in HERA is similar in concept to the algorithm originally introduced in [15]. The original algorithm is essentially a deconvolution algorithm for 2D images. The procedure has been slightly modified to fit the needs of inpainting flagged data in the HERA analysis [14, 20, 34]. For example, the original CLEAN algorithm operates in the image plane whereas the HERA implementation operates in the  $\tau$  and  $\nu$  domain. More broadly, the original algorithm operates on 2D images whereas the HERA implementation acts independently at each LST taking only the 1D frequency spectrum as input. Since CLEAN operates at each LST independently, LSTs where the entire frequency band are flagged remain flagged. The algorithm works by computing the Fourier transform of the visibilities  $\tilde{V}(\mathbf{b}, \tau, \nu)$  along the frequency axis in accordance with Equation 5.4. In doing so, the algorithm has an adjustable

parameter called the “zeropad” parameter, which is the number of bins to zeropad on both sides of the frequency axis. The additional padding around the frequency axis increases the delay space resolution which provides the algorithm with a finer set of discretized  $\tau$  modes. The algorithm then iteratively searches and selects the mode  $\tau_i$  that has the largest amplitude  $\tilde{V}_{\max}(\mathbf{b}, \tau_i, \mathbf{t})$ , which is then subtracted from the original quantity, i.e.  $\tilde{V}_1(\mathbf{b}, \tau_i, \mathbf{t}) = \tilde{\mathbf{V}}(\mathbf{b}, \tau, \mathbf{t}) - \tilde{V}_{\max}$ . This process is repeated  $n$  times until the largest remaining delay modes  $\tilde{V}_n(\mathbf{b}, \tau_i, \mathbf{t})$  are consistent with the desired tolerance threshold. The tolerance threshold is an adjustable parameter which sets the level at which the algorithm converges. Decreasing this parameter improves performance but is computationally expensive. Another adjustable parameter which determines minimum delay  $\tau_{dc}$  is used in estimating the noise, i.e. only delays  $\tau > \tau_0$  are used in estimating the noise. This sets a hard cutoff to which modes will be included in the inpainted image. The subtracted delay modes are then used to reconstruct the visibilities in the flagged regions. The CLEAN predictions are referred to the CLEAN model component, whereas the remaining modes are used to construct the CLEAN residual component.

The accuracy of the CLEAN predictions depend on the input values of the zeropad and tolerance parameters. Thus we need to optimize these parameters. Since the optimal values of the zeropad and tolerance depend on the properties of the dataset, this procedure is repeated for each noise scenario in the simulated data discussed in Section 5.2.3. We find that  $\tau_{dc}$  parameter does not dominantly affect the performance and keep the parameter fixed to  $\tau_{dc} = 2000\text{ns}$  unless otherwise noted. To determine the set of optimal parameters of the tolerance and zeropad parameters we compute the sum of the square of the residuals  $\epsilon_r$  of Equation 5.16 between the model visibilities and the true visibilities:

$$\chi^2 = \sum_{\text{LST}_i, \nu_j} [V_{\text{model}}(\text{LST}_i, \nu_j) - V_{\text{true}}(\text{LST}_i, \nu_j)]^2 \quad (5.10)$$

where we have explicitly made mention to that this sum occurs over all LSTs and frequency channels in the visibilities. Note that it is not necessary to select only the flagged pixels in this sum (i.e. by applying the inverse mask of Equation 5.15 and 5.16), since non-flagged pixels do not contribute

to the sum in Equation 5.10. The optimal values of these parameters are such that  $\chi^2$  in Equation 5.10 between inpainted predictions relative to the true visibilities are minimized. In Figure 5.2 we show the  $\chi^2$  for various values of the tolerance parameter at different thermal noise levels of the dataset. As we increase the noise level, the optimal values the tolerance increase. We find that the behaviour of the zeropad parameter is similar for different thermal noise levels, i.e. increasing the thermal noise of the dataset results necessitates decreasing the value of the zeropad parameter. For the remainder of this paper use CLEAN parameters  $\text{tol} = 10^{-10}$ ,  $\text{zp} = 256$  for the fiducial thermal noise scenario in Section 5.2.3 (i.e.  $\alpha = 1$ ). For  $\alpha = 2, 3, 4$  and  $7$  we use  $\text{tol} = 10^{-9}, 10^{-5}, 10^{-5}, 10^{-4}$ . For the zeropad parameter we use  $\text{zp} = 256, 256, 128, 128, 64$  respectively.

### 5.3.2 Least Squares Spectral Analysis (LSSA)

The HERA implementation of LSSA follows a generalized least squares estimator. It finds a best-fit smooth model derived from the Fourier components of the dataset and uses that model to fill in the flagged regions. This approach is similar in approach to what CLEAN does (see Section 5.3.1), except this uses a linear fit rather than the non-linear algorithm of CLEAN. As a result LSSA is computationally less expensive than CLEAN and in principle the error properties are easier to compute. Like the CLEAN algorithm, the code operates at each LST independently, i.e. the best fitting model is derived using the frequency information at each LST. Thus LSSA does not provide a model for LSTs where all frequency channels are flagged. Consider flagged visibilities at  $V(\mathbf{b}, \nu, t)$  at time  $t$ , the model for the flagged regions in the visibilities is constructed by expressing  $V_{\text{model}}(\mathbf{b}, \nu, t)$  as a linear combination of the Fourier basis, i.e

$$V_{\text{model}}(\mathbf{b}, \nu, t) = \sum_{n=-n_{\text{max}}}^{n=n_{\text{max}}} c_n e^{i\nu n t / \text{BW}} \quad (5.11)$$

where  $\text{BW}$  is the bandwidth of the instrument,  $n_{\text{max}}$  are the number of user-specified Fourier modes used to model the dataset and  $c_n$  are the undetermined coefficients for each Fourier mode. To solve for the coefficients the code uses a linear least squares optimizer, which minimizes the  $\chi^2$  residual from Equation 5.10. The solution to Equation 5.10 is the well known least squares solution.

The best fitting  $c_n$  from Equation 5.10 are then used to construct the model for the visibilities  $V_{\text{model}}(\mathbf{b}, \nu, t)$  in Equation 5.11. The inpainted data are then obtained by replacing  $V_{\text{model}}(\mathbf{b}, \nu, t)$  into the RFI flagged regions of  $V_{\text{data}}(\mathbf{b}, \nu, t)$ .

Since the performance of the LSSA algorithm depends on the number of Fourier components  $n_{\text{max}}$  to include in the model, we need to select  $n_{\text{max}}$  such that the performance is optimized. We repeat our procedure for each noise scenario in the simulated data discussed in Section 5.2.3. Fewer  $n_{\text{max}}$  results in a smoother inpainted model while larger values of  $n_{\text{max}}$  result in producing inpaint models with fine frequency features. For datasets with a greater fraction of flags or larger amplitude of thermal noise, increasing  $n_{\text{max}}$  too far can hinder the performance due to numerical instabilities. In the case of high percentage of flags, this occurs because there is not enough data to distinguish between the values of the largest Fourier modes. Similarly increasing the thermal noise will expand the error bars of the dataset making it difficult to break the degeneracies between the largest Fourier modes of the LSSA model. In such scenarios performance will be improved with a limited number of modes. We chose  $n_{\text{max}}$  to strike a balance between goodness of fit and numerical instabilities. To find the optimal value of  $n_{\text{max}}$ , we use the LSSA method to generate models for the RFI flagged regions in the visibilities discussed in Section 5.2.3. We repeat this procedure for multiple values of  $n_{\text{max}}$  ranging from  $n_{\text{max}}$  from 2 to 60. At each instance we compute the sum of the square of the residuals  $\epsilon_r$  of Equation 5.16 between the model visibilities and the true visibilities, i.e. Equation 5.10. As discussed earlier, note that it is not necessary to select only the flagged pixels in this sum, since non-flagged pixels do not contribute to the sum in Equation 5.10. Note that the optimal value of  $n_{\text{max}}$  depends on which flagged channels we include in our computation of Equation 5.10. For example including only the wideband RFI gaps would lead to solutions where fewer modes (smoother functions) are preferred. Conversely applying our optimization to narrowband RFI gaps (for example, the 120MHz - 130MHz in Figure 5.1) would favour a larger number of Fourier modes. Thus by using all flagged channels in our computation of Equation 5.10 we strike a balance between models which are best suited for wideband RFI and narrowband RFI. In Figure 5.2 we show the  $\chi^2$  as a function of  $n_{\text{max}}$  for various thermal noise levels. From this we can see that fewer Fourier components lead to better results. We also see that the number of Fourier components to include

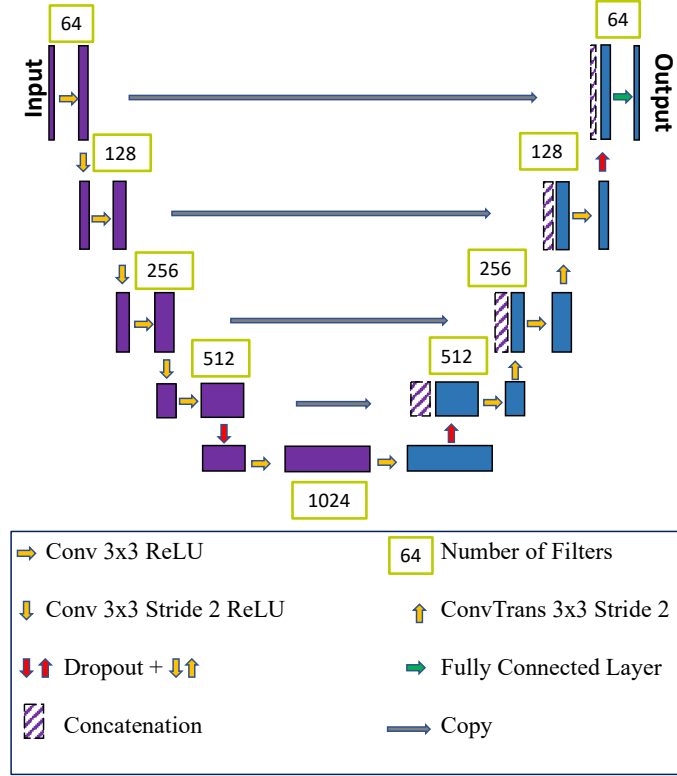


**Figure 5.3:** Block diagram showing the U-PAINT architecture.

in the LSSA model decreases with increasing thermal noise. For the remainder of this paper use  $n_{\max} = 10$  for the fiducial noise scenario, i.e.  $\alpha = 1$  in Equation 5.9. For the  $\alpha = 2, 3, 4, 7$  thermal noise scenarios we use  $n_{\max} = 9, 7, 7, 6$  respectively.

### 5.3.3 Covariance-Based Inpainting (GPR)

A powerful technique for the reconstruction or interpolation of a noisy signal is the Wiener filter [48], which has a long history in cosmology [45,52]. A generalization of the Wiener filter is the Gaussian process regression (GPR) formalism [38,41]. Both are, in essence, techniques that down-weight the observed data by its covariance, and then up-weight by the signal covariance. Recently, GPR has been used in 21 cm cosmology as a tool for signal separation [11,31] and for simultaneous filtering and inpainting [19]. Following [19], the expectation value of the conditioned signal model

in a Gaussian process model can be computed as

$$E[s] = C_s(C_s + C_n + C_{\text{other}})^{-1}d, \quad (5.12)$$

where  $d$  is our data vector,  $E[s]$  is the expectation value of our statistical model for the signal, and  $C_s$ ,  $C_n$ , and  $C_{\text{other}}$  are the covariance matrices for the signal, noise and extraneous components of our data model. This “best-fit” also has a covariance given by

$$\text{Cov}[s] = C_s - C_s(C_s + C_n + C_{\text{other}})^{-1}C_s. \quad (5.13)$$

Ignoring the  $C_{\text{other}}$  term in Equation 5.12, we see that this indeed simplifies to the standard Wiener filter. Note that [19] showed that the GPR foreground subtraction formalism used in 21 cm cosmology is closely related to the widely studied inverse covariance weighting found in the quadratic estimator literature, in the sense that one first weights the data by its inverse covariance, and the up-weights the residual by a normalization factor. More generally, typical applications of GPR involve fitting for the hyperparameters of analytic covariance functions, but at the end of the day, GPR is simply an inverse covariance weighting, as shown above. Further note that any covariance function can be implemented within the GPR framework discussed above [11].

In this work, we adopt a simple squared-exponential covariance function for modeling the 21 cm foregrounds, and a diagonal matrix for modeling the (uncorrelated) thermal noise. The hyperparameters of these covariances (e.g. the squared-exponential length scale and the noise variance) were set manually via inspection of the data: although one could choose to regress for these automatically on the data, given our understanding of the datasets at-hand we found that manual selection yielded similar results.

Another recent example of covariance-based modeling for 21 cm is the DAYENU formalism of [6]. Fundamentally, DAYENU is an inverse-covariance technique that explicitly assumes a Sinc model for the frequency-frequency covariance of the visibilities. Note that DAYENU was designed as a filter to remove foregrounds, however, the construction of the filter to remove this signal is similar to that of Equation 5.12. In fact, although not explicitly shown in [6], one can see that

DAYENU is exactly the same as Equation 5.12 in the case of a signal covariance that is the identity matrix, and a noise covariance that is a sinc function. The set of vectors that diagonalize this sinc covariance are the discrete prolate spheroidal sequences (DPSS), which have a long history in signal processing as the solution to the spectral concentration problem [42].

### 5.3.4 DPSS Least Squares (DPSS-LS)

The LSSA technique discussed in the previous section can be generalized to model functions (instead of just fourier components). In general, we can model the visibility data at a single time as

$$V_{\text{model}}(\text{LST}_i, \nu_j) = \sum_{\alpha} A_{\alpha}(\text{LST}_i) u_{\alpha}(\text{LST}_i, \nu_j) \quad (5.14)$$

where  $u_{\alpha}$  are a set of vectors that ideally span all possible foreground shapes while having minimal overlap with modes outside the wedge. Since foregrounds within the wedge are heavily “band-limited” – are ideally only contained within a compact range of delays, sets of functions whose Fourier transforms maximize power within a band-limited region are ideal for describing these foregrounds. The Discrete Prolate Spheroidal Sequences (DPSS) [42] maximize the ratio of power within some bandlimited region  $B_{\tau}$  to the total power of the sequence and are thus an ideal basis for per-baseline modeling of the wedge. [6] applied these sequences to modeling and filtering foregrounds with the DAYENU technique in which the covariance matrix of foregrounds is approximated as a Sinc matrix which is diagonalized by DPSS modes or DAYENUREST which performs linear least-squares inpainting.

Although the DAYENU (i.e. DPSS) formalism presented in [6] and discussed above is presented as a covariance-based technique similar to the Wiener filter and GPR, there are other ways to use the DPSS vectors for data modeling and inpainting. The DAYENUREST variant presented in [6] does just this, and instead of inpainting via Equation 5.12, it uses the DPSS vectors as a basis-set for performing least-squares fitting in the visibility. In this sense, the DAYENUREST (or DPSS least squares) is more akin to the LSSA formalism discussed above, except with a DPSS basis set instead of discrete Fourier modes. Hereafter, when we refer to “DPSS” in the paper we refer specifically

to the DPSS least squares technique, which is distinctly separate from the pure covariance-based inpainting techniques like GPR. Similar to LSSA we must specify how many modes to include in our DPSS basis-set. To do this, one specifies the parameter  $\tau_{dc}$  which determines the the finest spectral scale that DPSS inpaints over, i.e.  $1/\tau_{dc}$ . Increasing  $\tau_{dc}$  results in capturing finer frequency structures while decreasing  $\tau_{dc}$  results in modeling only the smoothest frequency structures. Thus the maximum RFI gap that is inpainted is proportional to  $1/\tau_{dc}$ . Similar to selecting  $n_{max}$  in Section 5.3.2, our selection of  $\tau_{dc}$  has consequences for the performance of the model in narrowband relative to wideband RFI. For example, increasing  $\tau_{dc}$  results in inpaint models which can account for fine frequency structure, which optimizes the performance for narrowband RFI. Conversely, this means that there is a maximum RFI gap size  $1/\tau_{dc}$  for which we can inpaint over which reduces performance in wideband RFI gaps. In this paper we use  $\tau_{dc} = 1000\text{ns}$ . This makes our DPSS technique optimized at inpainting intermittent (i.e. narrowband) RFI and introducing a maximum gap size of  $1/\tau_{dc} = 0.5\text{MHz}$ . Since this technique is similar to that of LSSA, and because our parameter choices for DPSS and LSSA optimize performance for different RFI properties, our analysis essentially brackets the range of performance for DPSS and LSSA techniques.

### 5.3.5 U-Paint Architecture

Our desired network configuration is one which is capable at making precise predictions of the data in flagged regions using the unflagged features in the visibilities. To do this we use a U-net architecture, introduced by [39] which have been shown to be robust for these type problems [17]. Our U-Net construction closely follows the architecture of [39] and [10]. We show the schematic of our network in Figure 5.3. Starting from the input of Figure 5.3, we input images of size  $512 \times 512$ . As discussed in Section 5.2.3, we use data from antennas (84, 85) and (0, 1) to perform our analysis. Thus all data from these antennas are removed before training. As discussed in Section 5.2.3 the HERA visibilities are measures of 1024 frequency channels over 4000 time integrations (i.e  $\times N_{LSTs}$ ). Thus we divide the total HERA visibilities into input visibilities of size  $512 \times 512$  corresponding to 90min of data and a band width of 50MHz. Thus the frequency band is split into two sections 100MHz-150MHz and 150MHz-200MHz at 90min observation intervals.

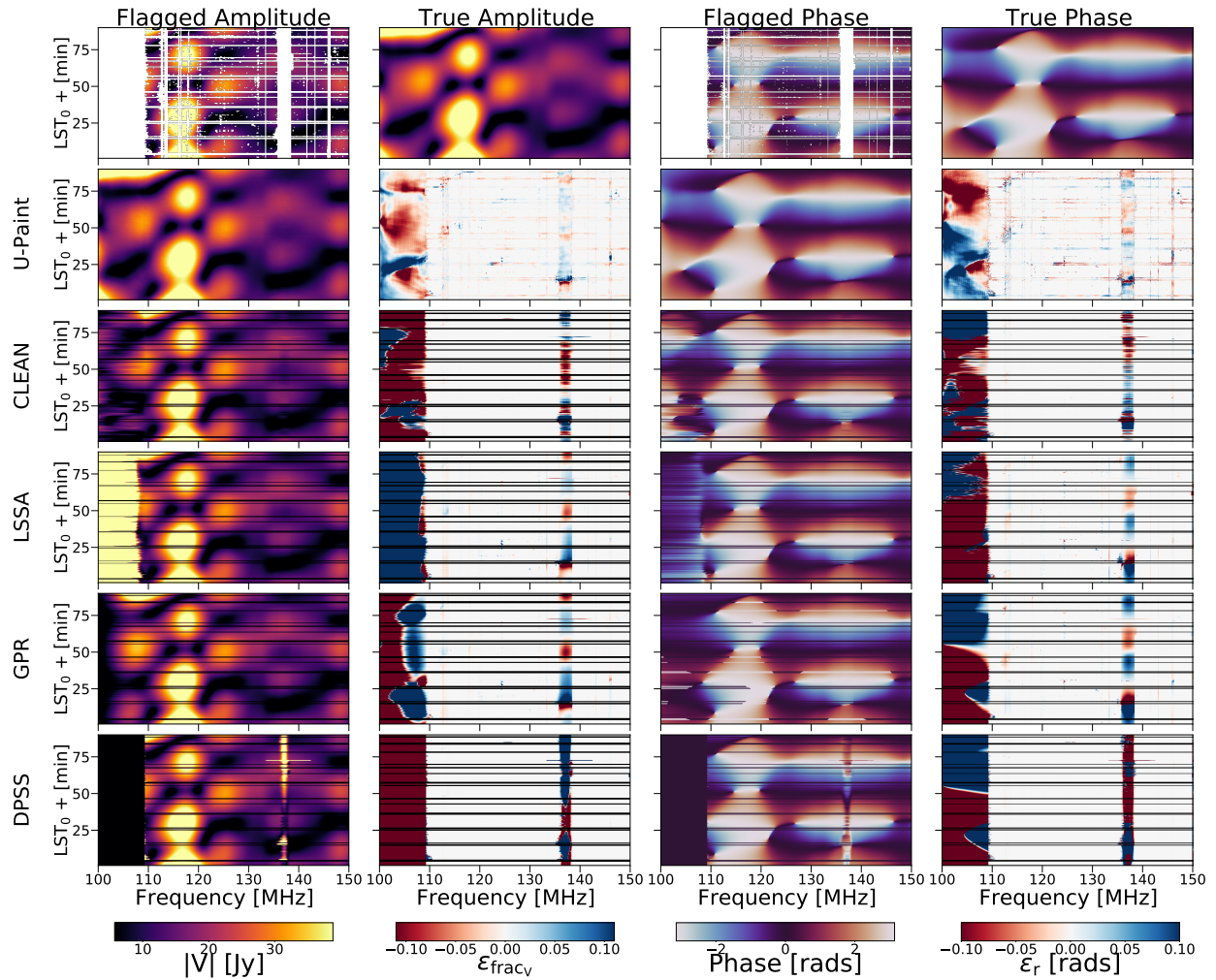


**Figure 5.4:** First row: The amplitude and phase components of the RFI flagged visibilities are shown in the first and third column. In the second and fourth column are the amplitude and phase component of the true visibilities. The visibilities are simulated (see Section 5.2.3). Second through fifth rows: in each row we show the amplitude and phase components of the RFI flagged visibilities but with the inpaint models filled into the RFI gaps. Each subsequent row correspond to U-Paint, CLEAN, LSSA, GPR, and DPSS inpainting methods. In the second and fourth column of each row we show the fractional error of the model amplitude and the residuals of the model phase (see Section 5.5).

Our motivation for selecting visibility sizes of  $512 \times 512$  is to establish a balance between two considerations: we need to divide the visibilities enough times to generate a large enough dataset for training and while simultaneously allowing a large enough image to allow the network to recognize typical features in HERA visibilities. Segmenting the data into too small a size will obscure the larger features in the visibilities. Conversely, making the image size too large will reduce the amount of images in our training set. Note that we find that the performance of the network is similar when using image sizes of  $256 \times 256$ ; however, we find that the performance of the network is decreased below this threshold. Each visibility image is then split into 5 input channels<sup>2</sup> for the initial convolutional layer. Thus the input has shape  $512 \times 512 \times 5$ . Our input channels are as follows: in channels 1 & 2 we input the real and imaginary component of the visibilities, respectively, defined in Equation 5.1 where the flagged regions of the real and imaginary component of the visibilities have been set to 0. In channel 3 we input the flags, which are a binarized  $512 \times 512$  map where a 0 pixel represents an unflagged region in the visibilities and 1 represents a flagged region in the visibilities. In order to ensure continuity at the boundary between flagged regions and the unflagged regions, i.e. between our inpainted predictions and the existing visibilities, we extend the flagged regions by two adjacent pixels along both axes (i.e. in LST and  $\nu$ ). This encourages the network’s model of the visibilities to be consistent with the existing information in the unflagged regions. In channels 4 & 5 we input the real and imaginary component of  $\tilde{V}(\mathbf{b}, \tau, t)$ , i.e. Equation 5.4 is applied to the visibilities  $V(\mathbf{b}, \tau, t)$  within channels 1 & 2 respectively. This is done to encourage the network to take advantage of the delay information. The reason this is effective is because our data is structured in the delay domain: high power at low delays due to the foregrounds and then lower power at high delays due to noise.

Referring again to architecture of the network in Figure 5.3, the objective of left branch of the U-net is to capture context of the images and propagate them downward through each level. We choose convolutional kernels of size  $(2 \times 2)$  which gives us a reasonable balance between the spatial resolutions and context for the features comprising the image. At each level we use a “ReLU” activation function. As the input data is propagated through each level, the network increasingly

---

<sup>2</sup>In this subsection, “channels” refers to the inputs to convolutional layers and not frequency channels. Outside of this subsection, channels refers to frequency channels.

forms an abstraction of the elements in the image. The bottom of the U-net can be interpreted as a classification type step, i.e., at this stage the network has understood the various elements in the image and has formed an abstract classification of these items. The objective of the right side of the U-net is to use the abstract classification of the items in the image to make predictions of the data in flagged regions of the input dataset. To do this the network uses a convolutional layer which upscales the size of each image. Throughout this process the network has lost all context about the superficial placement of these features. To re-introduce the necessary superficial context to each level on the right side of the U-net, skip connections between the levels on the left branch of the U-net and right branch of the U-net are formed. The image on the left hand side of the U-net is combined with the corresponding level on the right hand side through concatenation. The output at the right of Figure 5.3 has shape  $512 \times 512$  and contains the network’s model for the flagged regions. We extract the network predictions for the flagged regions of the visibilities and insert them into the corresponding flagged regions of the original flagged data set. In other words, we discard the network’s predictions for the data in unflagged regions.

To compare the training set to the labels, we define difference between the model visibilities  $V_{\text{model}}(\nu, t)$  and labels  $V_{\text{true}}(\nu, t)$  as  $\Delta = V_{\text{model}}(\nu, t) - V_{\text{true}}(\nu, t)$ . We use a loss function

$$\chi^2 = \sum_n [(1 - M(\nu, t)) \Delta]^\dagger \cdot [(1 - M(\nu, t)) \Delta] \quad (5.15)$$

where the sum is over  $n$ , the number of images in the batch. The  $\dagger$  refers to complex conjugation and a transpose. The term  $1 - M(\nu, t)$  essentially inverts the flags, i.e. the unflagged regions are 0 and the flagged regions are 1. The inverse flags prevent non-flagged regions from contributing to the loss. This is done to encourage the network to focus on learning the features of the flagged regions, which speeds up our training process.

We use  $\sim 350$  images from the the simulated visibilities discussed in Section 5.2.3 as part of our training set, and a test set of 35, with a batch size of 12. The network is trained for 80 epochs and a learning rate of  $lr = 10^{-4}$  using an Adam optimizer.

## 5.4 Inpaint Models

In this section we use the inpainting methods to make predictions for the RFI corrupted simulated visibilities from Section 5.2.3. We also provide a high level qualitative overview of the inpainted models in their amplitude and phase components. In Figure 5.4 we show sample inpaint predictions for the amplitude and phase of the RFI corrupted visibilities. The upper left panel of Figure 5.4 corresponds to the flagged visibilities while the top of the second column corresponds to the true visibilities. The first column in each subsequent row corresponds to visibilities where the inpaint models have been replaced in the RFI flagged regions. The first row corresponds to U-Paint models, the second row corresponds to CLEAN models, the third row corresponds to LSSA models and the final two rows correspond to GPR and DPSS models respectively. The attributes of the predictions shown in this image are characteristic of the models for each inpainting method. By visual inspection we can see that the U-Paint network has learned to assimilate the features in the amplitude and phase into the RFI corrupted regions, and thus it is apparent that the network is capable of reproducing the features of the true visibilities in the RFI corrupted regions. Another distinguishing feature of the network predictions are that the network organically inpaints over LSTs that do not contain any frequency information. In contrast to the other inpaint algorithms which do not naturally provide predictions for these LSTs, U-Paint can take advantage of all the information of the visibilities. This highlights U-Paint's ability to extrapolate data to LSTs in which there are none. Currently LSTs without any frequency information are not used as part of HERA's data analysis pipeline; however, in the future one may be able to take advantage of these LSTs either from the analysis perspective or simply to avoid discontinuities in the data. We can also see that all inpainting methods do a reasonable job at filling in the narrowband RFI portion of the visibilities making it difficult to discern between the true visibilities and the inpaint models. In contrast, regions where wideband RFI has been replaced with inpaint models are still obvious. Referring to the 2MHz RFI gap at 136MHz, we can see that wideband RFI is still easily identifiable in the model visibilities of each inpainting technique. There appear to be remaining artifacts in the wideband RFI regions which make the characteristics of the inpaint models are apparent. Referring to the top

row, can see that U-Paint produces models with a speckled structure in frequency while CLEAN, LSSA and GPR models tend to be smoother in the frequency domain. DPSS models don't entirely fill in the wideband RFI gap at 136MHz. As discussed in Section 5.3, this is due to our choice of delay cut parameter  $\tau_{dc}$ . The maximum RFI gap that is inpainted is proportional to  $1/\tau_{dc}$ . Since we are using  $\tau_{dc} = 1000\text{ns}$ , then we are limited to RFI gaps larger than  $1/\tau_{dc} = 0.5\text{MHz}$ . Unless otherwise stated we do not include DPSS in our error characterisation for wideband RFI. In the third column of Figure 5.4 we show the phase component of the inpaint predictions. The second through fifth rows again correspond to U-Paint, CLEAN, LSSA, GPR, and DPSS models respectively. We can see that the inpaint models capture the structure of the phase component. As was the case with the amplitude component, regions of inpainted narrowband RFI appear to be seamlessly integrated with the rest of the visibilities while inpainted wideband regions appear to have artifacts.

In the following sections we build a quantitative perspective on the performance of each inpainting technique. In the next section we discuss our methodology in quantifying the error characteristics of the inpaint models.

## 5.5 Statistical Analysis Methodology

We quantify the errors in inpainted predictions relative to the true visibilities by computing the residuals, fractional errors and a modified version of the fractional errors. We use the same metrics to quantify the errors in the model power spectra relative to the true power spectra. The residuals between the inpainted visibilities and the true visibilities are computed as

$$\epsilon_r^V = [1 - M(\nu, t)] \cdot (V_{\text{model}} - V_{\text{true}}), \quad (5.16)$$

where  $M(\nu, t)$  are the flags,  $V_{\text{model}}$  are the flagged visibilities where the inpainted models have been placed into the flagged regions and  $V_{\text{true}}$  are the true visibilities (i.e. without any flags). The term  $1 - M(\nu, t)$  essentially inverts the flags i.e. 1 is a flagged region and 0 signifies unflagged. This is done so that only flagged regions enter the analysis. As discussed in Sections 5.3.1, 5.3.2, and 5.3.3, CLEAN, LSSA, GPR, and DPSS operate at each LST independently and thus do not

inpaint on LSTs where the entire frequency band are flagged. These LSTs are not used in our error characterization analysis even for inpainting methods which do inpaint on these LSTs, i.e. U-Paint. Note that the residuals defined by Equations 5.16 constitute individual error realisations. In Section 5.5 we model the distribution of error realisations to compute the actual error. Using  $\epsilon_r^V$  we can define the fractional error  $\epsilon_{\text{frac}}$ :

$$\epsilon_{\text{frac}}^V = \frac{\epsilon_r^V}{V_{\text{true}}}. \quad (5.17)$$

Since the visibilities are complex, they can be split into real and imaginary components, or amplitude and phase. Within the context of error quantification, Equations 5.16 and 5.17 can be applied to the real, imaginary, and amplitude components of the visibilities. However since the phase of the visibilities are periodic, quantifying the errors using the fractional errors defined in Equation 5.17 becomes meaningless. To quantify the errors for the phase component of the visibilities we use a modified version of the residuals of Equation 5.16. The phase values of the inpainted models  $\phi_{\text{model}}$  and ground truth  $\phi_{\text{true}}$  are mapped from their native range  $[-\pi, \pi]$  to  $[0, 2\pi]$ . The residuals  $\Delta\phi = \phi_{\text{model}} - \phi_{\text{true}}$  are then computed. Since the sign of the phase error does not directly indicate the severity of the error, i.e, a phase error of  $+\Delta\phi$  is the same “angular distance” from the true value as phase error  $-\Delta\phi$ , we define the absolute residual phase error  $\epsilon_\phi$  as

$$\epsilon_\phi = \min (|2\pi - (\phi_{\text{model}} - \phi_{\text{true}})|, |\phi_{\text{model}} - \phi_{\text{true}}|) . \quad (5.18)$$

Therefore we can interpret  $\epsilon_\phi$  to be the smallest angle from  $\phi_{\text{true}}$ . In Sections 5.6 and 5.7 we use these metrics as tools to describe the errors in the model visibilities and power spectra.

To perform our analysis we construct a sample set of RFI flagged channels using all flagged channels between  $\nu = 110\text{MHz}$  and  $\nu = 174\text{MHz}$  (see Section 5.2.1 for details). We exclude LSTs in which all frequency channels are flagged from our analysis. As discussed in Section 5.2.3 we consider only the shortest baselines (i.e. antennas separated by 14.7m) in this work. We find that our results do not depend on the specific antennas used to form the 14.7m baseline. Thus without loss of generality we perform our analysis using the antennas (0, 1) and (84, 85) for strictly east-west baselines, including multiple linear polarisations ( EE and NN ). We have repeated our subsequent

**Table 5.1:** Summary of key error metrics for the amplitude component of simulated visibilities.

Error RFI	$\overline{\sigma}_{\epsilon_{\text{frac}}}$ Narrowband	$\overline{\sigma}_{\epsilon_{\text{frac}}}$ All	$\overline{\mu}_{\epsilon_{\text{frac}}}$ Narrowband	$\overline{\mu}_{\epsilon_{\text{frac}}}$ All
U-Paint	5.5%	5.97%	-0.025%	0.05%
CLEAN	3%	9.7%	0.07%	0.265%
LSSA	1.69%	2.82%	0.05%	-0.16%
GPR	3.09%	3.5%	-0.08%	-0.044%
DPSS	1.52%	-	0.013%	

analyses for redundant baselines using other antenna pairs and have found no significant differences in our qualitative or quantitative results. With the restrictions above, this leads to a sample set of  $10^4$  flagged channels. Using this sample set, we construct the empirical error distribution. We model the empirical error distribution with seven main classes of model probability density functions, which along with their sub-classes, encompass a flexible range of probability profiles. They include the gamma, log normal, skew Cauchy (see [13]), t, skew normal, generalized normal, skew Laplace distributions. These distribution functions comprise a family of distributions in which we find more familiar probability profiles as special cases. We then compare the empirical distribution to  $p_{\text{best}}$  using the Kolmogorov-Smirnov (KS) test introduced in [18]. In the following Sections we apply these metrics to the inpainted predictions of U-Paint, CLEAN, LSSA, GPR, and DPSS.

## 5.6 Inpaint Error Quantification in the Visibilities of Simulated Data

In Section 5.4 we discussed the qualitative features of the inpaint models. We now examine the quantitative aspects of their errors using the metrics from Section 5.5. Since the visibilities are complex valued, they can be expressed in terms of amplitude and phase components. In Section 5.6.1 we apply our analysis to both components of the visibilities. In Section 5.6.2 we discuss the impact that increased thermal noise have on the inpaint models.

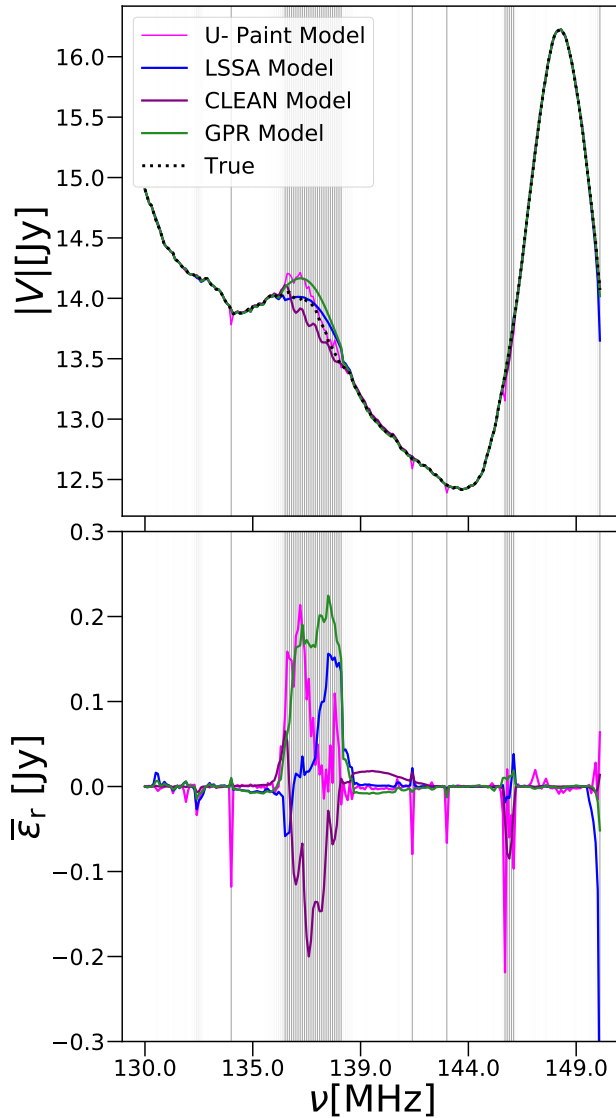


**Figure 5.5:** Top: LST averaged inpaint model visibilities. The true visibilities are shown with the dotted black curve. The vertical shaded regions correspond to the RFI flagged channels. The amount of shade is proportional to the frequency in which those channels are flagged. Thus the Wideband ORBCOMM feature is darkest since it is always flagged. Note that the inpaint models are only filled into RFI gaps, and so the inpaint models only deviate from the true visibilities in shaded regions. The orange curve corresponds to U-Paint, the yellow curve to LSSA, purple curve to CLEAN and blue curve to GPR. DPSS models are not shown since we feature the wideband feature in this image (see Section 5.3). Bottom: The residuals between inpaint models and the true visibilities.

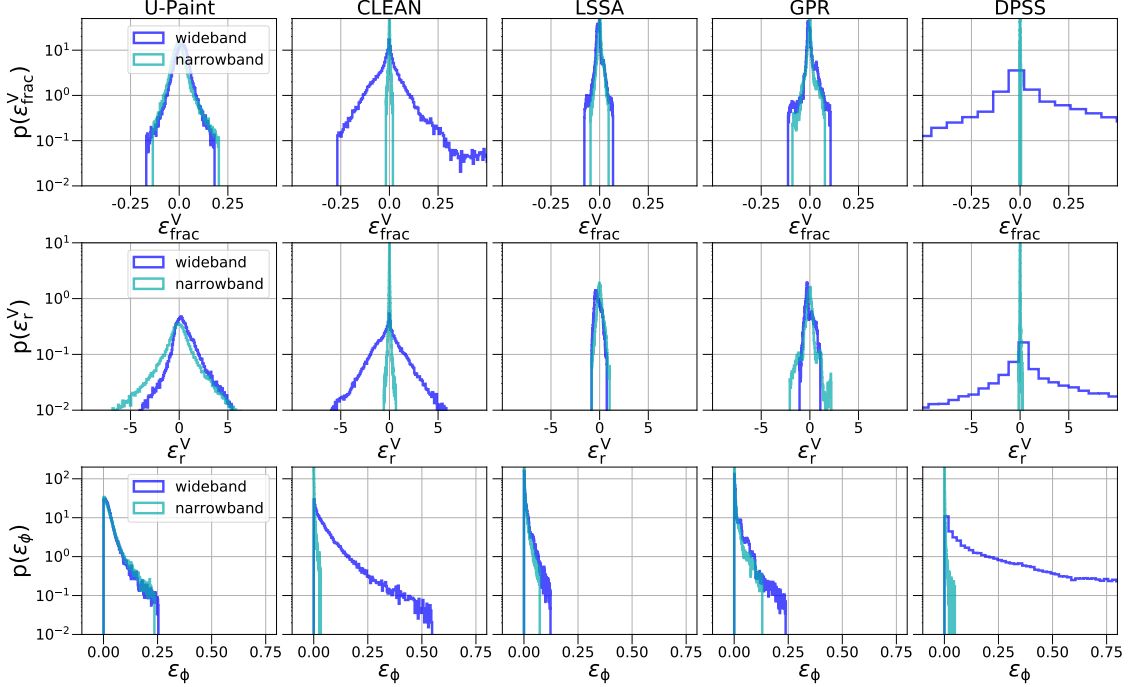


**Figure 5.6:** Top row: probability distribution of the fractional errors  $p(\epsilon_{\text{frac}}^V)$  in the amplitude of the inpainted model visibilities. Second row: residuals in the inpainted model amplitudes  $p(\epsilon_r^V)$ . Third row: residuals of the phase component of the inpaint models  $p(\epsilon_{\text{phi}})$ . The blue curves corresponds to when only wideband RFI is used to construct the samples while the teal curve corresponds to samples constructed using only narrowband RFI. All inpaint methods are applied to the simulated visibilities discussed in Section 5.2.3.

### 5.6.1 Error Characterisation

In the second column of Figure 5.4 we show example fractional errors of the amplitude of the inpaint models. With this metric the errors are normalized by the amplitude of the true visibilities allowing us to ascertain the performance independent of the brightness of the visibilities. Referring to the second row of the second column in Figure 5.4, we find that the mean fractional error in the amplitude of U-Paint models is  $\mu_{\epsilon_{\text{frac}}} = 0.058\%$  and standard deviation  $\sigma_{\epsilon_{\text{frac}}} = 5.5\%$ <sup>3</sup>. Thus the fluctuation in performance is 5.5%. We also find that  $\sigma_{\epsilon_{\text{frac}}}$  is consistent throughout the various types of RFI, i.e in wideband and narrowband RFI. We also find that U-Paint has similar performance in LSTs which are entirely flagged. In rows three through six of Figure 5.4

<sup>3</sup>Note that in this assessment we are not including the model predictions at  $\nu < 110\text{MHz}$ .

we show the fractional error in the amplitude of the inpainted models for CLEAN, LSSA, GPR, and DPSS algorithms. Immediately clear from the fractional errors of the visibility amplitudes are that CLEAN, LSSA, GPR, and DPSS models are more accurate in the narrowband RFI regions as compared to the wideband RFI. The standard deviation of the fractional errors of the inpainted models in narrowband RFI are  $\sigma_{\epsilon_{\text{frac}}}$  are smallest for DPSS at 1.52% and LSSA at 1.69% followed by CLEAN and GPR at 3.0% and 3.09% respectively. When we include flagged channels above 110MHz, the error fluctuations  $\sigma_{\epsilon_{\text{frac}}}$  increase. This is due to the inclusion of wideband RFI gaps where the fractional errors are larger. When including all flagged channels above 110MHz we find that LSSA produces the smallest fluctuations at 2.8% followed by GPR at 3.5%, U-Paint at 5.95%, CLEAN at 9.7% and DPSS at 10.3%. Recall that for DPSS our choice of parameters leads to model limitations on large RFI gaps and thus we do not include DPSS in our error characterisation for wideband RFI. In Table 5.1 we provide a summary of these quantitative results.

Another distinctive characteristic of the amplitude in U-Paint models are that they contain fine frequency structure. In the top panel of Figure 5.5 we show the amplitude of the visibilities as a function of  $\nu$  averaged over 512 time integrations. The dotted black line corresponds to the true visibilities, while the solid colored curves corresponds to the inpaint models. The amount of grey shading represents the average flag occupancy of each frequency bin. In the wideband RFI gap we can closely examine the features of each inpaint model. In the lower panel of Figure 5.5 we can see the spectral structure in the residuals between the inpaint model and true visibilities. **Note the rapid fluctuating components in the U-Paint predictions as compared to the smoother true visibilities.**

In Figure 5.6 we show the probability distributions of the fractional errors  $p(\epsilon_{\text{frac}})$  in the inpainted models. Since the performance and errors depend on the nature of the RFI, we separate our analysis into frequency channels which are dominated by narrowband RFI and frequency channels which are dominated by wideband RFI. For the narrowband RFI we construct a sample set using all flagged pixels from frequency channels 110MHz to 136MHz, where these bounds exclude the wideband features found below 110MHz and above 136MHz. This leads to a sample size of  $\sim 52000$  pixels. For the wideband regions, we isolate the 20 frequency channels corresponding

to the the ORBCOMM RFI feature at 136MHz. This leads to a similar sample size of 54000 pixels. In the top row Figure 5.6 we show the probability density functions of the fractional error  $p(\epsilon_{\text{frac}}^V)$  (Equation 5.17) for the amplitude of the inpainted models in narrowband and wideband RFI regions. The blue curves correspond to the probability distribution constructed using only the wideband RFI samples, while the teal curve corresponds to the probability distribution constructed using only the narrowband RFI samples. For the sake of visualization, we display up to the 99.9 percentile of errors along the horizontal axis. By qualitatively comparing the maximum range of the teal curve to the blue curve in all five panels of the first row in Figure 5.6 we can see that the U-Paint, LSSA, and GPR performances are more consistent across wideband and narrowband RFI regions as compared to CLEAN and DPSS which perform significantly better with narrowband RFI. Note that DPSS does not inpaint over a 2MHz gap given our parameter choices in Section 5.3. We can also see that the maximum range of fractional errors for narrowband RFI is smallest for DPSS inpainting methods and largest for U-Paint. Conversely, for wideband RFI, LSSA and GPR produce the smallest range of fractional errors. Another feature of the distribution of fractional errors  $\epsilon_{\text{frac}}^V$  for wideband RFI using CLEAN is the positive skew, i.e. a disproportionate amount of probability mass is contained in  $p(\epsilon_{\text{frac}}^V) > 0$ . With this exception of this distribution, we find that generalized normal distributions is an optimal probability distribution profile to model the empirical distributions  $p(\epsilon_{\text{frac}}^V)$  for each RFI scenario in Figure 5.6.

To establish the range of absolute temperature errors introduced into the analysis, we now examine the distribution of residuals  $p(\epsilon_r^V)$  in  $|V|$ . The distribution of residuals are shown in the second row of Figure 5.6. Many of the qualitative features in  $p(\epsilon_r^V)$  are similar to the distributions of fractional errors from above. For example, the distribution of residuals in U-Paint, GPR, and LSSA inpainting methods are less sensitive to the type of RFI, i.e. narrowband and wideband. By comparing the maximum range of residuals for narrowband RFI for each inpainting technique we again come to the same conclusion as above: DPSS produces the smallest residuals, followed by CLEAN. Similarly, when for wideband RFI, LSSA and GPR produce the smallest residuals.

We now discuss the distribution of errors in the phase components of the visibilities. Referring to the fourth column of Figure 5.4 we show the residuals between the model phase and true phase.

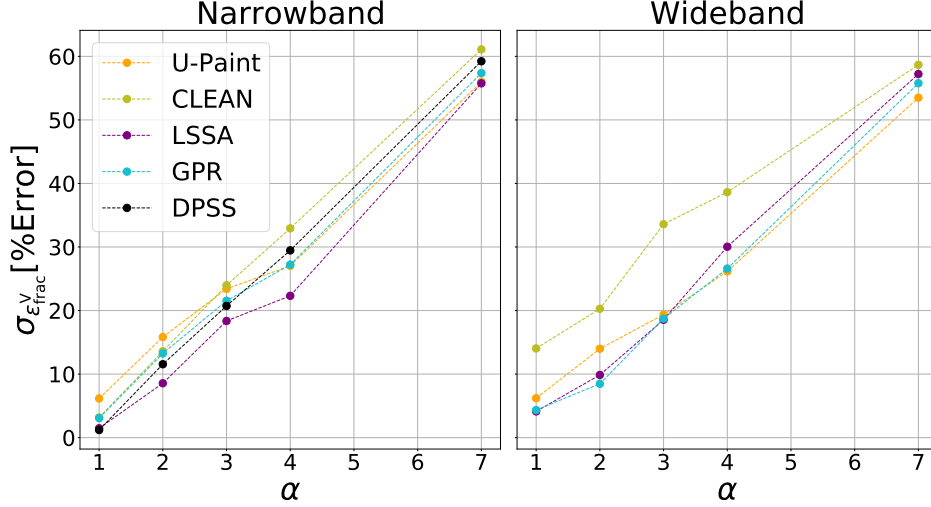


**Figure 5.7:** The standard deviation of the fractional error in the visibilities  $\epsilon_{\text{frac}}^V$  as a function of the thermal noise level in the visibilities. The parameter  $\alpha$  is used as a proxy for the thermal noise level (see Equation 5.9).

We see that with the exception of the wideband models for DPSS inpaint methods, all of the residuals fall between  $|\epsilon_r^\phi| < 0.1\text{rads}$ . The largest residuals are sourced from wideband RFI regions. In the bottom row of Figure 5.6 we show the corresponding distributions of the residual phase errors  $\epsilon_\phi$  as defined in Equation 5.18. Recall that the errors  $\epsilon_\phi$  are bounded between  $\epsilon_\pi = 0$  and  $\epsilon_\phi = \pi$ . We find that the errors in the phase component  $\epsilon_\phi$  of the inpainted models are all characterized by the same type of probability distribution profile, the lognormal probability function. Similar to our descriptions of  $p(\epsilon_r^V)$  and  $p(\epsilon_{\text{frac}}^V)$ , we find that CLEAN and DPSS models provide the most accurate description of the phase in narrowband RFI regions and LSSA providing the best description of the phase in wideband RFI. Relative to DPSS and CLEAN inpainting methods, we again find U-Paint, GPR and LSSA have consistent performance in the phase component for the narrowband and wideband RFI.

## 5.6.2 Thermal Noise

Since the inpainting techniques can not predict exact noise realisations in the dataset, we expect an increase in the amplitude of the fractional errors. In Figure 5.7 we show the evolution of the standard deviation of the fractional error (in percentage of the true visibilities) in the wideband and

narrowband regions of the visibilities as a function of thermal noise level in the visibilities. We use the dimensionless parameter  $\alpha$  as a proxy for the thermal noise level in the dataset (see Equation 5.9). Notice the linear evolution of  $\sigma_{\epsilon_{\text{frac}}^{\text{V}}}$  with  $\alpha$ . This shows that the standard deviation of the fractional error is linearly proportional to the standard deviation of the noise level in the dataset. Thus as one averages down  $\alpha$  through LST binning (or equivalently, other types of averaging), the performance of the inpainting techniques improves linearly. Therefore performing the inpainting before the LST binning in a data analysis pipeline will result in the same performance. In contrast, a non-linear evolution of  $\sigma_{\epsilon_{\text{frac}}^{\text{V}}}$  with  $\alpha$  would describe a scenario where the  $\sigma_{\epsilon_{\text{frac}}^{\text{V}}}$  depends on the standard deviation of the noise beyond just simple sample variance of the noise, i.e. there may be advantages to applying the inpainting technique at a specific noise level before or after LST binning (depending on whether the relationship between  $\sigma_{\epsilon_{\text{frac}}^{\text{V}}}$  and  $\alpha$  is more or less steeper than linear). Thus Figure 5.7 reinforces our assertion that each inpainting technique captures only the underlying sky signal of the dataset.

Building on the intuition of the error properties in the visibilities, we now examine errors in the power spectrum derived from the inpainted visibilities and form connections between the errors of both components.

## 5.7 Power Spectrum Error Characterization

In this section we characterize the type of errors in  $P(\tau)$  due to the inpainting as well as establish the relationship between the errors in the model visibilities and their corresponding delay power spectra. We propagate two versions of the visibilities through the power spectrum. The true visibilities (which do not have any corrupted regions), and the corrupt visibilities (where inpainted models have been replaced in the RFI corrupt regions). Thus we have the power spectrum derived from the model visibilities  $P_{\text{model}}$ , and the true power spectrum  $P_{\text{true}}$  derived from the true visibilities. We can define the residuals analogously to Equations 5.17, i.e  $\epsilon_{\text{r}}^{\text{P}} = P_{\text{model}} - P_{\text{true}}$ . Similarly for the fractional errors  $\epsilon_{\text{frac}}^{\text{P}} = (P_{\text{model}} - P_{\text{true}})/P_{\text{true}}$ . We separate our analysis in terms of delay modes ( $\tau$ ) inside and outside the wedge. This section is structured as follows. In Section 5.7.1 we discuss the

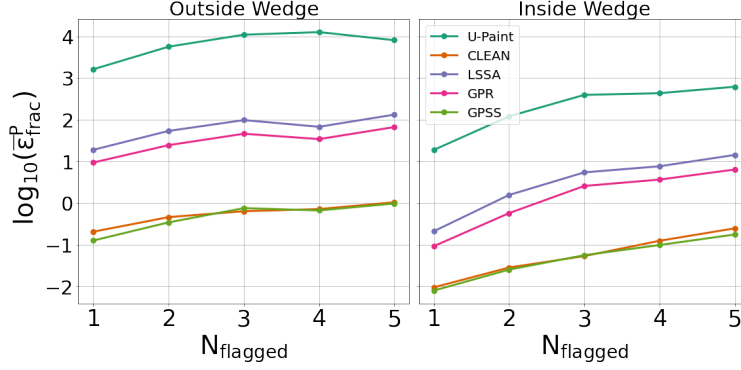


**Figure 5.8:** The fractional errors in the wedge modes (left) and non-wedge modes (right) of inpaint model power spectra  $\epsilon_{\text{frac}}^P$  as a function of the number of flagged channels within the spectral window. The P1V spectral window is used to estimate the power spectra.

properties of the power spectra derived from the model visibilities. In Section 5.7.2 we establish a relationship between the errors in the model visibilities from Section 5.6 and the model power spectra from Section 5.7.1.

### 5.7.1 P1V Spectral Window

We compute the power spectra using the spectral window from 119MHz to 129MHz which is one of the spectral windows used to set upper limits on the power spectrum in HERA Phase 1 Upper Limits. This window contains both flagged and non-flagged regions of the visibilities. Recall that in our example HERA flags in Figure 5.1, this frequency range spans over 100 channels and corresponds to a region of the visibilities with only narrowband RFI. In this spectral range, the number of flagged channels at each LST range from 0-31 frequency channels which corresponds to up to 31% of the spectral window used to compute the power spectra. Recall that the power spectrum is computed independently at each LST and thus there are LSTs where one third of the band is flagged and LSTs without any flags at all. We restrict our analysis to LSTs with at least one flagged channel. This reduces the number of sample power spectra with which we can form our analysis. We find that the key indicator of performance are the number of flagged pixels within the band. Denote the number of flagged channels at each LST by  $N_{\text{flagged}}$ . When  $N_{\text{flagged}} = 0$  we have no errors in  $P(\tau)$ . As we increase  $N_{\text{flagged}}$  a larger fraction of the spectral window are

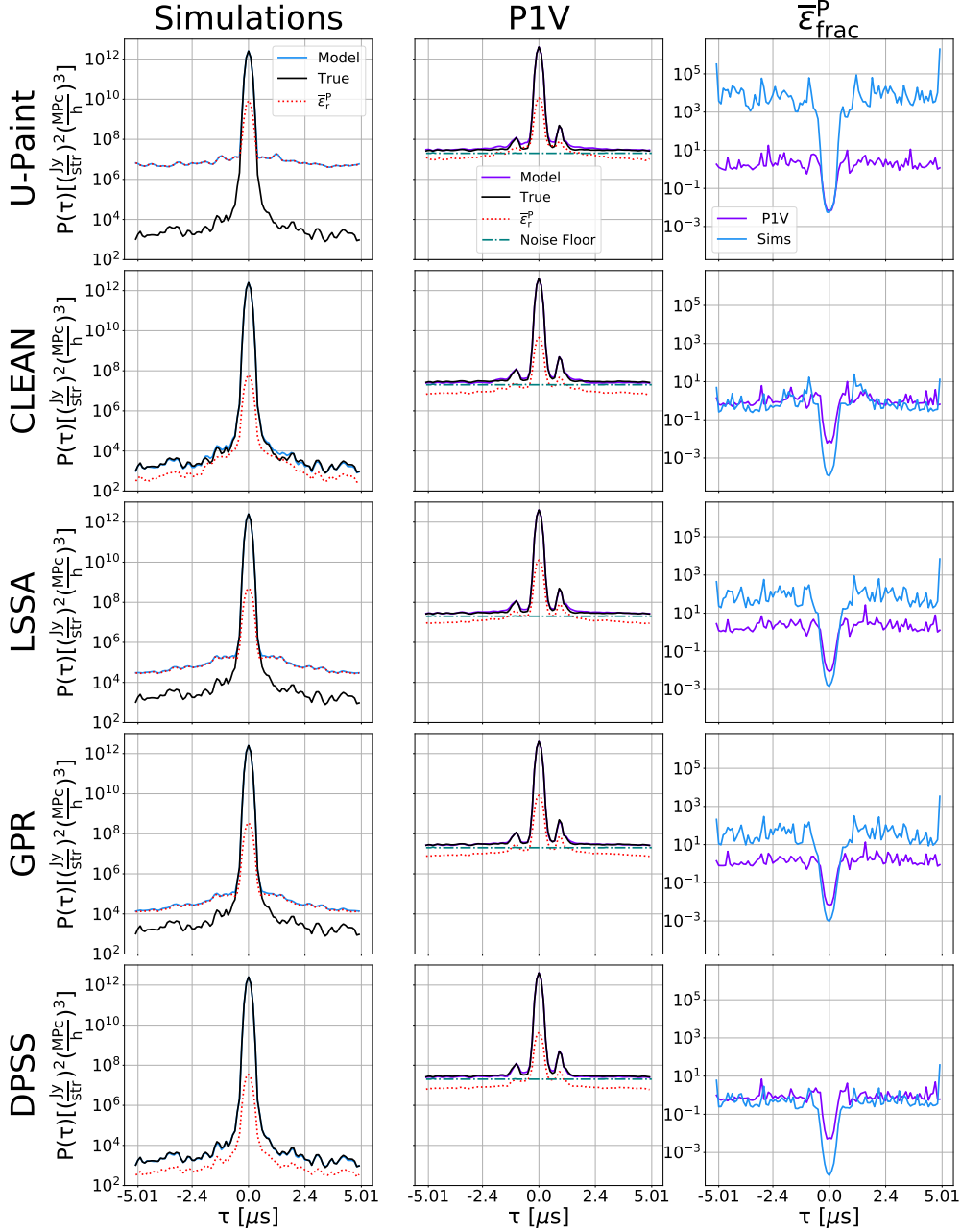


**Figure 5.9:** Each inpainting technique is applied to the simulated data discussed in Section 5.2.3. The P1V spectral window is used to estimate the inpaint model power spectra. Left column: blue curves correspond to inpaint model power spectra. The black curves correspond to the true power spectra and the red dotted curves correspond to the residuals. Each row corresponds to a different inpaint technique used to inpaint RFI flagged simulated visibilities. Second column (see Section 5.8.3): Same as first column but with real P1V data. Purple curves correspond to inpaint model power spectra and black curves the true power spectra. Red curves are the residuals. The third column corresponds to the fractional errors  $\epsilon_{\text{frac}}^{\text{P}}$  in inpaint model power spectra from simulated data (blue) and the P1V data (purple). The dotted teal line corresponds to the power spectrum of the thermal noise floor of P1V data [14].

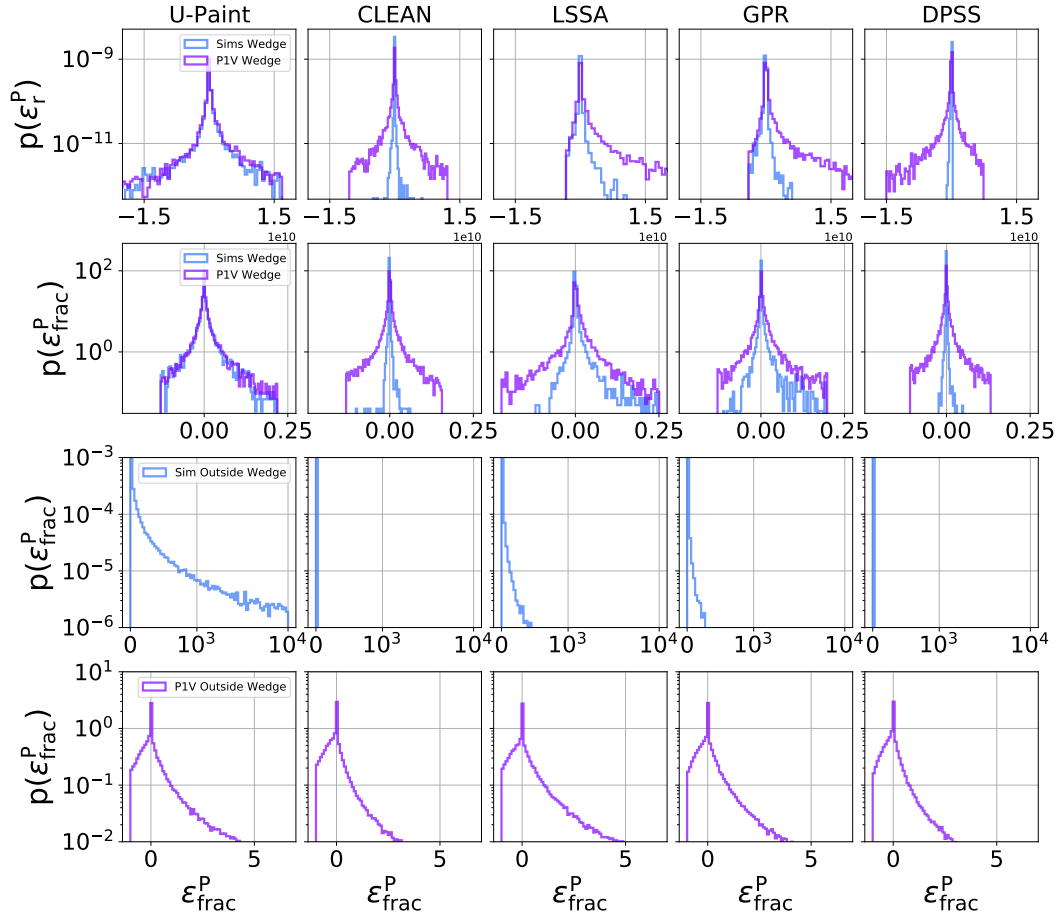


**Figure 5.10:** Blue curves correspond to simulated data and purple curves correspond to PIV data. Distribution of residuals (first row) and fractional errors (second through fourth rows) in the inpaint model power spectra. Residuals are shown for wedge modes while the fractional errors are separated according to  $\tau$  modes lying inside the wedge (second row) and outside the wedge (third and fourth rows). Third row corresponds to simulated data while the fourth row corresponds to PIV data.

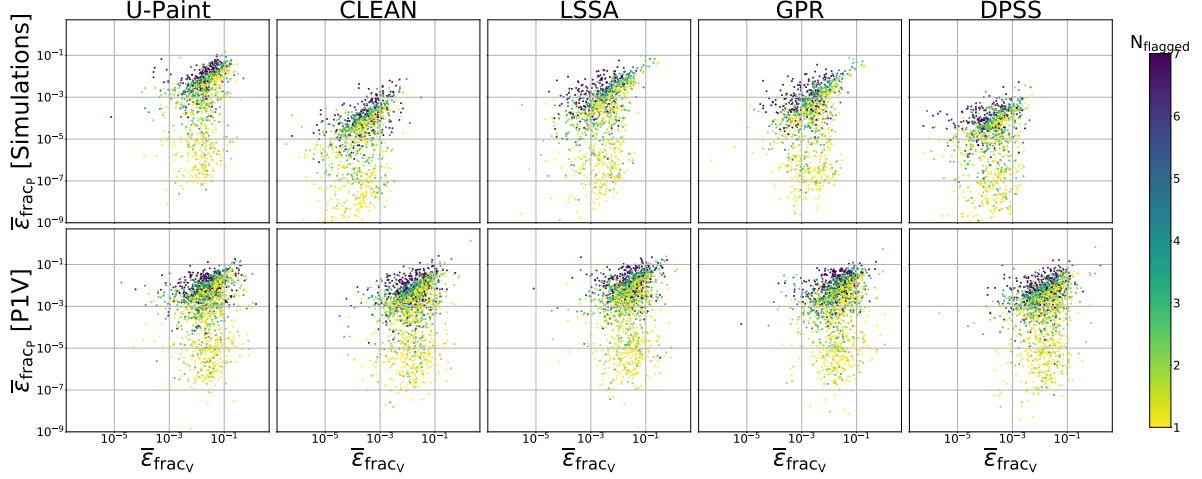


**Figure 5.11:** Relationship between the mean fractional errors in the inpaint model visibilities  $\bar{\epsilon}_{\text{frac}}^V$  and the mean fractional errors in their corresponding power spectra  $\bar{\epsilon}_{\text{frac}}^P$ . We compute the mean fractional error of the inpaint models in RFI flagged frequency channels within the P1V spectral window. This process is repeated at each LST. Their corresponding power spectra are estimated using the same P1V spectral window. The mean of the fractional errors in the model power spectra are computed using  $\tau$  modes inside the wedge. Each LST is plotted as a scatter point. The LSTs are colour coded according to the number of flagged frequency channels at that LST. In the top row this procedure is applied to simulated data while in the bottom row this procedure is applied to P1V data.

flagged. For fixed  $N_{\text{flagged}}$ , the arrangement of the RFI also affects the performance. For example, scenarios with four consecutively flagged channels does not yield similar errors as when the four flagged channels are dispersed. Denote  $N_{\text{max}_c}$  as the number of consecutively flagged channels. When  $N_{\text{max}_c}$  increases we eventually have a wideband feature which have greater fractional errors relative to narrowband RFI. Thus power spectrum estimates derived from wideband RFI features in the visibilities have drastically increased errors relative power spectrum estimates derived from regions of the visibilities with intermittent (i.e narrowband) RFI.

Thus both  $N_{\text{flagged}}$  and their arrangement within the spectral window will affect the errors in the model power spectra. For this analysis we examine the effect of  $N_{\text{flagged}}$  on the model power spectra, i.e. we treat  $N_{\text{flagged}}$  as the dominant effect and  $N_{\text{max}_c}$  as a secondary effect which we leave to future work. In Figure 5.8 we show the mean fractional errors of the model power spectrum  $\bar{\epsilon}_{\text{frac}}^P$  as a

function of  $N_{\text{flagged}}$  separated by modes outside and inside the wedge. Note that the smallest mean fractional error  $\bar{\epsilon}_r^P$  occurs when only one pixel is flagged. In our flags, 25% of all LSTs have only one flagged channel. The mean fractional errors in both wedge and non-wedge modes of the model power spectra increase rapidly as a function of the number of flagged regions for  $N_{\text{flagged}} < 5$ . By  $N_{\text{flagged}} = 5$  the fractional errors for modes outside and inside the wedge are an order of magnitude greater than when only one channel is flagged. On average, 90% of the LSTs in HERA flags have 5 flagged channels or less. Thus most LSTs fall within this error range.

We now look at the model power spectra after averaging over LST. This implicitly averages over  $N_{\text{flagged}}$ . We ignore LSTs that have don't have any flagged channels. In the first column of Figure 5.9 we LST average the model power spectrum (blue curve) and compare it to the LST averaged true power spectrum (black curve). The dotted red curve corresponds on the mean residuals  $\bar{\epsilon}_r^P$  between the model power spectra and the true power spectra. Referring to the fractional errors in the blue curves of the third column, we can see that CLEAN and DPSS produce power spectra models with the smallest fractional errors in the wedge, followed by GPR, LSSA and U-Paint. By examining the larger errors in  $P_{\text{model}}$  for the largest delay modes, it is clear that none of inpainting methods inpaint noise. We can see that the inpainting techniques only capture the sky signal. This leads to larger errors in the largest  $\tau$  modes which are noise dominated. CLEAN and DPSS models have fractional errors on the order  $\sim 10^0$ , while GPR and LSSA are on the order 10 and U-Paint on the order  $10^4$ . This is the due to the fine frequency structure imprinted into the visibilities by U-Paint (see Section 5.6). Note that analysis of the errors the largest  $\tau$  modes of  $P_{\text{model}}$  are only possible since we are using simulated data, which is systematic free, and less noisy than real data. In the future we will continue to make progress on reducing systematics in our data, thus increasing the importance of understanding the behaviour of inpaint models in the largest  $\tau$  modes. In that scenario, spectral structure imprinted into model power spectra by inpaint methods such as U-Paint must be accounted for.

In the top row of Figure 5.10 we show the distribution of residuals errors  $p(\epsilon_r^P)$  for modes inside the wedge (blue solid curves). The residuals are smallest for DPSS and CLEAN inpainting techniques. In the second row of Figure 5.10 we show the distribution of fractional errors  $p(\epsilon_{\text{frac}}^P)$

for wedge modes (solid blue curves) where we again see that DPSS and CLEAN have the smallest range of fractional errors. We find that the profile of  $p(\epsilon_{\text{frac}}^{\text{P}})$  for modes inside the wedge are best described by a generalized normal distribution. For modes outside the wedge (third row in Figure 5.10), LSSA, U-Paint and GPR are characterized by a log normal distribution. Recall that for the  $\tau$  modes outside the wedge,  $P_{\text{model}} \gg P_{\text{true}}$  for U-Paint, LSSA and GPR. Thus their fractional error distributions are composed of samples with  $\epsilon_{\text{frac}}^{\text{P}} \gg 0$ . This gives the distribution long positive tails. <sup>4</sup> Since CLEAN and DPSS have much smaller errors outside the wedge, their distributions  $p(\epsilon_{\text{frac}}^{\text{P}})$  are confined to  $p(\epsilon_{\text{frac}}^{\text{P}}) < 10$ .

### 5.7.2 Relationship Between Visibility and Power Spectrum Errors

In Sections 5.6.1 and 5.7.1 we discussed the error characteristics of the model visibilities and model power spectra. Since the model power spectra are derived from the model visibilities, we expect a relationship to exist between their errors. Since the errors in  $P_{\text{model}}(\tau)$  are different for modes inside and outside the wedge, we expect the relationship between model visibilities and model power spectra to also depend on  $\tau$ . In this Section we explore these relationships.

Consider the 100 frequency channels spanning the frequencies 119MHz-129MHz corresponding to our spectral window. A direct relationship between the errors in each pixel of the model visibilities and the corresponding model power spectra is impractical since the power spectrum is derived from all frequency channels within this spectral window. We therefore find it convenient to establish a relationship between the mean power spectrum errors and the mean amplitude errors of the visibilities. Since the inpaint models do not inpaint noise, and since the large  $\tau$  modes are noise dominated, we establish a relationship between the mean fractional errors of the visibilities  $\bar{\epsilon}_{\text{frac}}^{\text{V}}$ , and the mean fractional errors in the wedge modes of their corresponding power spectra  $\bar{\epsilon}_{\text{frac}}^{\text{P}}$ . The mean fractional error in the visibilities are given by

$$\bar{\epsilon}_{\text{r}}^{\text{V}}(\text{LST}) = \frac{1}{N_{\text{flagged}}} \sum_{i=119}^{i=129} \left[ \frac{V_{\text{model}}(\text{LST}, \nu_i) - V_{\text{true}}(\text{LST}, \nu_i)}{V_{\text{true}}(\text{LST}, \nu_i)} \right]. \quad (5.19)$$

---

<sup>4</sup>Lognormal distributions are only defined for positive values and have long tails making this profile ideal to describe the non-wedge modes of these inpainting techniques

The averaging in Equation 5.19 occurs along the frequency domain which leaves us with  $N_{\text{LST}}$  samples. This translates to  $\sim 5000$  samples in our simulation data. The mean fractional error for the model power spectrum are similarly computed:

$$\bar{\epsilon}_r^{\text{P}}(\text{LST}) = \frac{1}{7} \sum_{i=-\tau_g}^{i=\tau_g} \left[ \frac{P_{\text{model}}(\text{LST}, \tau_i) - P_{\text{true}}(\text{LST}, \tau_i)}{P_{\text{true}}(\text{LST}, \tau_i)} \right] \quad (5.20)$$

where the index  $i$  tracks the  $\tau$  bins in the wedge modes of the power spectrum and 7 corresponds to the number of  $\tau$  modes inside the wedge. The averaging in Equation 5.20 occurs along the  $\tau$  domain which leaves us with  $N_{\text{LST}}$  samples. For intuition we can explore an analytical relationship between  $\bar{\epsilon}_{\text{frac}}^{\text{V}}$  and  $\bar{\epsilon}_{\text{frac}}^{\text{P}}$ . If we approximate the wedge modes of Equation 5.20 as being uniform and equal to the error in  $P(\tau = 0)$  then we can approximate Equation 5.20 as

$$\bar{\epsilon}_{\text{frac}}^{\text{P}} = \left( \frac{\bar{P}_{\text{model}} - \bar{P}_{\text{true}}}{\bar{P}_{\text{true}}} \right)_{\tau=0} = \frac{\bar{V}_{\text{model}}^2 - \bar{V}_{\text{true}}^2}{\bar{V}_{\text{true}}^2}. \quad (5.21)$$

where the last step is due to  $P(\tau = 0)$  corresponding to the square mean of the visibilities. Therefore we can rewrite the right side of Equation 5.21 as

$$\bar{\epsilon}_{\text{frac}}^{\text{P}} = \bar{\epsilon}_{\text{frac}}^{\text{V}} \left( \frac{\bar{V}_{\text{model}} + \bar{V}_{\text{true}}}{\bar{V}_{\text{true}}} \right). \quad (5.22)$$

In scenarios where the mean of the model visibilities  $\bar{V}_{\text{model}}$  is consistently related to the mean of the true visibilities  $\bar{V}_{\text{true}}$  by a constant  $\delta$ , we can write  $\bar{V}_{\text{model}} = \delta \bar{V}_{\text{true}}$ . This is not a bad assumption for LSTs where the amplitude of the visibilities are relatively constant. For example in Figure 5.4 we can see that the fractional error remains reasonably uniform in LSTs in the vicinity of 119MHz to 129MHz. In this situation Equation 5.23 can be recast as

$$\bar{\epsilon}_{\text{frac}}^{\text{P}} = (1 + \delta) \bar{\epsilon}_{\text{frac}}^{\text{V}}, \quad (5.23)$$

which suggests the mean fractional error in the power spectrum  $\bar{\epsilon}_{\text{frac}}^{\text{P}}$  scale linearly with the mean fractional error in the amplitude of the visibilities. Note that we expect this approximation to no

longer be valid as the largest  $\tau$  modes are included into the mean fractional errors of Equation 5.20. In the top row of Figure 5.11 we show the relationship between  $\bar{\epsilon}_{\text{frac}}^{\text{P}}$  and  $\bar{\epsilon}_{\text{frac}}^{\text{V}}$  where each scatter point corresponds to an individual LST. From the previous section, we also expect that the relationship between  $\bar{\epsilon}_{\text{frac}}^{\text{V}}$  and  $\bar{\epsilon}_{\text{frac}}^{\text{P}}$  will depend on the number of flagged channels at each LST. We colour code the scatter points according to the number of flagged channels at that LST. Note that LSTs with  $N_{\text{flagged}} = 1$  (the brightest green, and smallest points in Figure 5.11) are located at the smallest values of  $\bar{\epsilon}_{\text{frac}}^{\text{P}}$  indicating that these LSTs produce the smallest mean errors in  $P(\tau)$ . It is also clear that LSTs with  $N_{\text{flagged}} = 1$  don't appear to strongly cluster together, or follow the same cohesive relationship as when  $N_{\text{flagged}} > 1$ . This is likely due to sample variance, since the mean fractional errors in the visibility and power spectrum are computed using a single channel making  $\bar{\epsilon}_{\text{frac}}^{\text{P}}$  and  $\bar{\epsilon}_{\text{frac}}^{\text{V}}$  prone to scatter. Conversely, LSTs with  $N_{\text{flagged}} \gg 1$  appear to follow a clearer linear trend. We can also see that LSTs with  $N_{\text{flagged}} > 20$  tend to produce the largest values of  $\bar{\epsilon}_{\text{frac}}^{\text{P}}$ .

## 5.8 Application to Phase 1 HERA Data

In Sections 5.6 & 5.7 we discussed the performance of each inpainting technique as well as the types of errors they introduce as part of computation of the power spectrum. However the analysis was performed on simulated data. While our simulated data from Section 5.2.3 does take into account the instrument, it doesn't fully capture all the instrumental effects such as systematics that come along with a real observation. In this section we characterize the errors introduced in an actual HERA analysis pipeline. To do this we apply U-Paint, CLEAN, LSSA, GPR, and DPSS to the P1V HERA data discussed in Section 5.2.3 and repeat our analysis from Sections 5.6 and 5.7. To keep our analysis as similar as possible to the true HERA analysis pipeline, we use the 119MHz-129MHz spectral window to compute the power spectra. In order to quantify the errors in  $V_{\text{model}}$  and  $P_{\text{model}}$  using the same methods in the previous sections, the true (i.e. known) visibilities and power spectrum are required. One hurdle in realizing this goal is that since the true solution to the RFI flagged regions of real P1V data do not exist, therefore we need to modify our analysis procedure. In Section 5.8.1 we discuss our modifications to the procedure outlined in

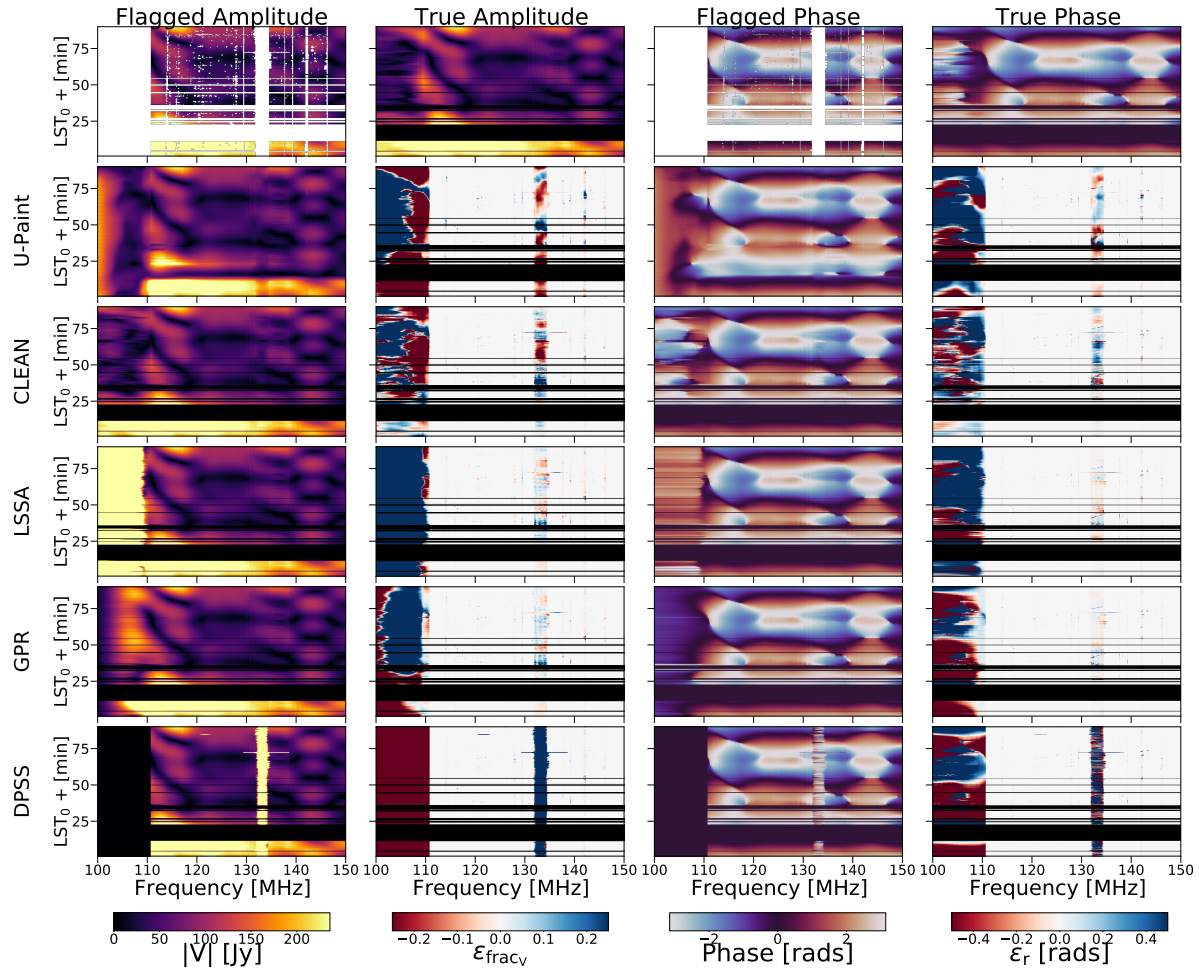


**Figure 5.12:** Same as Figure 5.4 but with the P1V visibilities from Section 5.2.3. The true visibilities in the first row (second and fourth column) have been initially inpainted with the CLEAN algorithm to generate placeholder data for the RFI flagged regions. The inpaint techniques are then applied to a set of flags which are shifted 40 channels to the left. This is done in order to avoid inpainting over the already CLEANed data. See Section 5.8 for more details regarding our procedure. Note that as compared to Figure 5.4 the fractional errors in the model visibilities increase.

Section 5.6. In Sections 5.8.2 and 5.8.3 we discuss our results showing that our intuition and error characterization carries over from the previous sections and thus we can infer the error properties in the true analysis from simulation.

### 5.8.1 Flagged Regions & Analysis Configuration

Denote the flagged regions of the P1V visibilities as  $M_{P1V}$ . To apply the error metrics discussed in Section 5.6.1, the “true” visibilities in  $M_{P1V}$  are required to be known. This is not the case for  $M_{P1V}$  regions of P1V data. This causes several difficulties and prevents us from directly repeating our analysis procedure from Sections 5.6 and 5.7. Furthermore, the presence of RFI flags can introduce artifacts into the power spectrum due to the Fourier transforming the sharp discontinuities between flagged and unflagged regions. To avoid introducing these artifacts into the inpaint models of U-Paint, CLEAN, LSSR, GPR and DPSS we inpaint over the flagged regions of the P1V data using the CLEAN algorithm. We use the CLEAN parameter values that were used in [14]. After this step the flagged regions have been replaced with CLEAN inpaint models. Repeating our error analysis on the  $M_{P1V}$  flagged regions of P1V data now means that we would be using the CLEAN models as the true visibilities (which we wish to avoid). We therefore create a new set of flags by taking  $M_{P1V}$  and shifting them over in frequency space by 40 channels. We refer to the shifted flags which are applied to the visibilities as  $M_{\text{shift}}$ . Applying our analysis on using  $M_{\text{shift}}$  rather than  $M_{P1V}$  allows us to use regions of the visibilities where the true values are known as well as to keep the structure of the real P1V flags. This procedure is not perfect in that there is an overlap of some of the narrowband RFI in the  $M_{\text{shift}}$  and  $M_{P1V}$ . However  $< 5\%$  of the narrowband RFI in  $M_{\text{shift}}$  overlaps with narrowband RFI in  $M_{P1V}$ . This estimate does not include the wideband features below 110MHz and above 174MHz. In such overlapping channels, the true solution is therefore CLEAN inpaint model. Since the overlap percentage is small, we don’t expect this overlap to significantly influence our results. Note that by applying this shifting procedure, certain characteristic broadband RFI features of  $M_{\text{shift}}$  no longer align with their corresponding frequency bins. For example the ORBCOMM feature is characteristically found at 136MHz. Conversely, narrowband RFI is intermittent, and thus  $M_{\text{shift}}$  flags provides us with a statistically representative set of narrowband RFI samples.

To generate the inpainted models for the flagged regions, i.e  $M_{\text{shift}}$  using U-Paint, we consider two network configurations. Each scenario produces comparable results. In the first case we use the weights of the network which has been trained on the simulated data described in Section 5.2.3 (at the fiducial noise level). This is the network which was used in the analysis throughout Sections

**Table 5.2:** Summary of key error metrics for the amplitude component of P1V visibilities.

Error RFI	$\overline{\sigma}_{\epsilon_{\text{frac}}}$ Narrowband	$\overline{\sigma}_{\epsilon_{\text{frac}}}$ All	$\overline{\mu}_{\epsilon_{\text{frac}}}$ Narrowband	$\overline{\mu}_{\epsilon_{\text{frac}}}$ All
U-Paint	24.5%	98.7%	2.1%	4.9%
CLEAN	19.1%	58.2%	0.81%	5.4%
LSSA	44%	81.2%	1.9%	3.6%
GPR	19.2%	41.3%	0.65%	2.1%
DPSS	15%	-	0.5%	-

5.6 and 5.7. For completeness, and to examine the range performance that can be obtained by our network, we try a second scenario. In the second scenario we retrain the network on P1V data after having performed the CLEAN procedure described above. Thus in this scenario an initial CLEAN is still performed and  $M_{\text{shift}}$  are used as our flagged regions. We find that both scenarios produce comparable results on the P1V data. We thus use the network from scenario 1 (i.e. the network which was used in the analysis throughout Sections 5.6 and 5.7 ) to generate inpaint models. To generate inpaint models for CLEAN, LSSA, GPR, and DPSS we use the same parameters described in Section 5.3 for the simulated data at the fiducial noise level.

## 5.8.2 Results

In Figure 5.12 we show an example image of RFI flagged P1V data which has been inpainted. The first panel in the first row corresponds to the P1V visibilities with  $M_{\text{shift}}$  applied. The first panel in the second row corresponds to the P1V visibilities after an initial CLEAN inpaint, from here onward we refer to this as the “true” visibilities. Note that the LSTs where all frequency channels are flagged have unknown true visibilities and haven’t been inpainted over since CLEAN avoids these LSTs. Therefore the “true” visibilities in the upper left panel of Figure 5.12 still appear to have flagged regions. The visibilities where RFI flags have been reapplied are on the upper right. Each subsequent row corresponds to the indicated inpainted model (left) and their fractional errors (right). Note that U-Paint still inpaints over LSTs with no data, however since a fractional error cannot be computed (true visibilities are unknown), we do not display a fractional

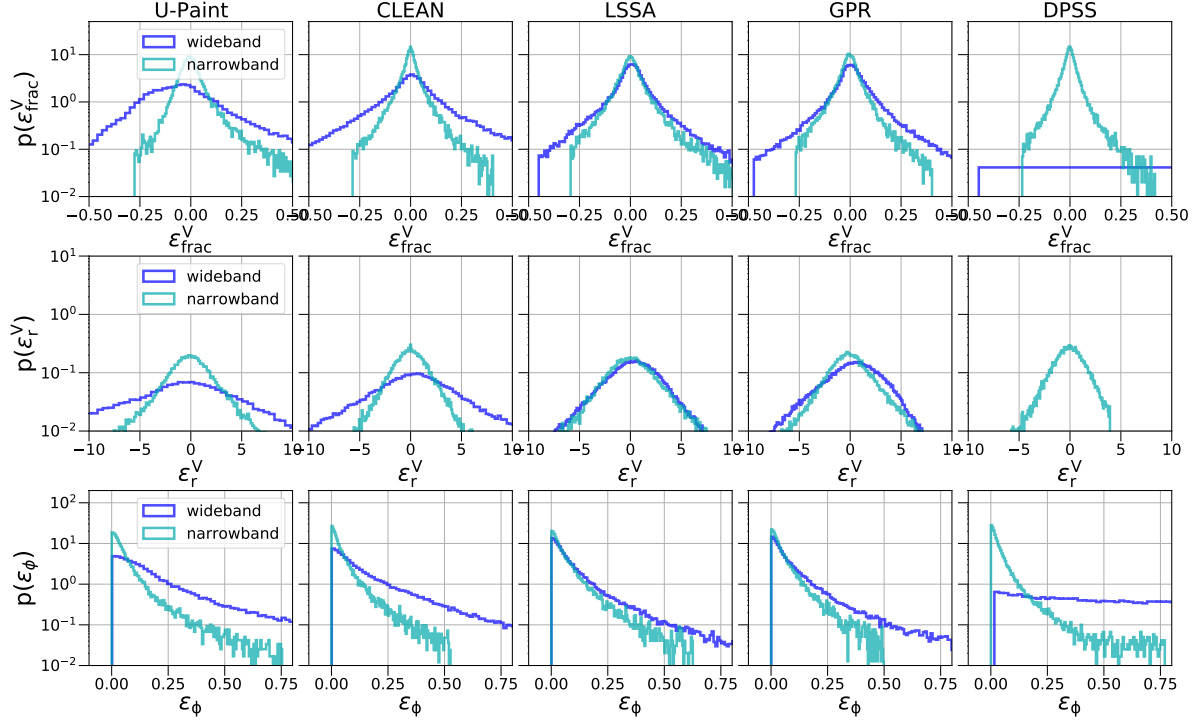


**Figure 5.13:** First row: distribution of fractional errors in the amplitude of P1V visibilities. Second row: distribution of residuals in P1V visibilities. Third row: distributions of phase errors  $\epsilon_\phi$  in the phase of P1V visibilities. In each case the blue curves correspond to distributions constructed using wideband RFI samples only. Teal curves correspond to distributions constructed using narrowband RFI samples only

error. In the two last columns of Figure 5.12 we show the corresponding phase component of the visibilities. Referring to the fractional errors of the amplitude components and residuals in the phase component of Figure 5.12 we can see that the inpainting methods again perform better in the narrowband regions as compared to the wideband regions. Notice that the residuals in the phase component are much larger than their simulated counterparts in Figure 5.4. Similarly comparing the fractional errors in second column of Figure 5.12 to the fractional errors of the inpainted model of the simulated data in 5.4, we see that there are larger fluctuations in fractional error in the P1V inpainted models relative to the simulated data. This is the case for each inpaint method. The standard deviations and the mean of the fractional errors are summarized in Table 5.2.

In Figure 5.13 we show the probability density function of the fractional errors  $p(\epsilon_{\text{frac}}^V)$  (top row), residuals  $p(\epsilon_r^V)$  (middle row) and the distribution of errors  $p(\epsilon_\phi)$  for the phase component of the visibilities (bottom row) as a function of the type of flags, i.e. narrowband and wideband. Focusing on the top row, we can see that the profile of the probability distributions functions  $p(\epsilon_{\text{frac}}^V)$  share many qualitative characteristics with their corresponding distributions from Section 5.6.1. For example, we can again see that DPSS still produces the most accurate results for narrowband RFI followed by CLEAN, GPR, LSSA and U-Paint. However by comparing the extent of the distributions for narrowband RFI, we can see the performances are less discrepant. By examining the range of errors we can see that GPR and LSSA produce the smallest range of fractional errors for narrowband RFI.

In the second row of Figure 5.13 we show the distribution of residuals  $p(\epsilon_r^V)$  for each inpainting technique. Through comparison with the middle row in Figure 5.6 we can see that the residuals using the P1V data are larger than those using the simulated data. As was the case with the distribution of fractional errors  $p(\epsilon_{\text{frac}}^V)$  from above, we can see that the maximum range of residuals in narrowband RFI are similar among the inpainting techniques. For each inpainting technique, we find that the profile of  $p(\epsilon_r^V)$  and  $p(\epsilon_{\text{frac}}^V)$  are best characterized by a generalized normal distribution.

In the bottom row of Figure 5.13 we show the distribution of errors  $\epsilon_\phi$  in the phase component of the P1V inpaint models. We can see that relative to the distributions  $p(\epsilon_\phi)$  in Figure 5.6 which were generated with simulated data there is an apparent performance decrease when applying the inpainting techniques to P1V data. For narrowband RFI, we find that the tails extend into the range  $\epsilon_\phi \sim 0.75\text{rads}$  while the tails of  $p(\epsilon_\phi)$  in wideband RFI regions extend into the range  $\epsilon > \pi/3$  which reflects a more significant deviation in phase relative to the true values. Unlike the distributions in Figure 5.6 which were generated with simulated data, U-Paint does show consistent performance in the phase component. Similar to Section 5.6.1, we find that all distributions functions are best described by a log normal distribution.

### 5.8.3 Power Spectrum

In this section we compute the power spectrum of the inpaint models. To do so we use the P1V spectral window. In the middle column of Figure 5.9 we show the mean model power spectra (purple curve), the mean true power spectra (black curve) and their corresponding residuals (red dotted curve). We show their corresponding mean fractional errors in purple in the third column. As discussed in Section 5.8.1 the P1V visibilities are noisier than the simulated visibilities and contain instrument systematics not present in simulations. This manifests in the true power spectrum as increased amplitude for large  $\tau$  modes, as well as the systematic feature at  $\tau \pm 1.2\mu\text{s}$ . Referring to the model power spectra in the middle column of Figure 5.9, we can see that the inpainting techniques reproduce this systematic feature. Referring to the first row of the second column in Figure 5.9 it appears that  $P_{\text{model}}$  for U-Paint have a similar amplitude as  $P_{\text{true}}$  for large  $\tau$  modes. However referencing  $P_{\text{model}}$  for U-Paint with simulated data (upper left panel) shows that U-Paint models automatically produce this amplitude for large  $\tau$ .

By referring to the mean fractional errors on the right column of Figure 5.9 we can see that the mean fractional errors of each inpainting technique lie within the range  $10^{-3} < \bar{\epsilon}_{\text{frac}}^{\text{P}} < 10$ , where the largest fractional errors occur outside the wedge. The smallest fractional errors are again found for modes inside the wedge. In the wedge modes, the fractional errors are within a fraction of a percent of their true value. Quantitatively, we find that the inpainting techniques are within 1.24%, 0.32%, 1.24%, 1.0%, 0.25% for U-Paint, CLEAN, LSSA, GPR and DPSS respectively.

To generate the probability density function of the errors in the model power spectra, we construct two samples sets. One set using  $\tau$  modes outside the wedge and another set comprised of  $\tau$  modes inside the wedge. In each case we use model power spectra from LSTs with at least one flagged pixel. In the purple curves of Figure 5.10 we show the errors in the model power spectra. In the top row of Figure 5.10 (purple curve) we show the probability density functions of the residuals. We find that U-Paint produces the largest range of errors  $\epsilon_{\tau}^{\text{P}}$ , followed by DPSS, LSSA, GPR and CLEAN. In the second row in Figure 5.10 (purple curve) we show the probability density functions of the fractional errors  $\epsilon_{\text{frac}}^{\text{P}}$  constructed using only wedge modes. Comparing the mean of the fractional error distributions in the wedge modes of model power derived from P1V

data to the mean fractional errors of model power spectra derived from simulated visibilities (blue curve), we find that there is an increase in  $\bar{\epsilon}_{\text{frac}}^{\text{P}}$  using all inpainting techniques. The largest increase in mean fractional errors occurs in DPSS and CLEAN inpainting techniques. With the smallest increase in fractional errors using U-Paint. Conversely, if we construct  $p(\epsilon_{\text{frac}}^{\text{P}})$  using only modes outside the wedge (bottom row in Figure 5.10) we find that the range of fractional errors decreases as compared to its equivalent distribution derived from simulated data (third row). This is due to there being lesser amounts of noise in the simulated data as compared to the PIV data, thereby exposing the spectral errors in the inpaint models.

Using the fractional errors  $\epsilon_{\text{frac}}^{\text{P}}$  we can establish a relationship between the mean fractional errors in the inpainted simulated visibilities and their corresponding power spectra. We proceed similarly as in Section 5.7.1. In the bottom row of Figure 5.11 we show the relationship between the mean fractional errors in the visibilities  $\epsilon_{\text{frac}}^{\text{V}}$  and the mean fractional errors in the power spectrum  $\epsilon_{\text{frac}}^{\text{P}}$ . Comparing this to the top row of Figure 5.11 we demonstrate that the relationship between the mean fractional errors in the inpainted PIV data and their corresponding power spectra follow the same relationship as with the simulated data. This is important since it suggests that intuition and error characterisation drawn from the simulated visibilities in Section 5.7.2 translates to PIV data. This result is perhaps not so surprising given that the fractional errors of the visibilities and power spectrum are described by the same probability profile for the PIV data visibilities and power spectra. Recall above the mean of the fractional error distributions for the power spectra of PIV data are larger (except for U-Paint) than the corresponding mean fractional errors using simulated data. Similarly in Section 5.8.2 we found that there was an increase in  $\epsilon_{\text{frac}}^{\text{V}}$  in the PIV data as compared to the simulated data. These increases essentially shift the center of the scatter plots in the bottom row of Figure 5.11 as compared to the top row (simulated data). In the future we would like to be able to predict the errors in PIV based on the error characterization in the simulated data. However, although the relationship between these quantities remains the same between simulated and PIV, the centering of the distributions still need to be accounted for.

## 5.9 Conclusion

As 21cm instruments continue to push towards a detection of the 21cm power spectrum, quantification of the errors introduced into the data analysis due to inpainting RFI corrupted data can no longer be ignored. In this paper we assessed the performance of existing inpainting techniques at restoring RFI flagged data. Our results are indicative of general trends, but not an exhaustive comparison. We also introduced our convolutional neural network U-Paint which we show to be capable of inpainting RFI corrupted data. Along with existing methods, we quantified the errors introduced in the data analysis pipeline due to RFI. We perform our error quantification analysis on simulated data as well as real data used in HERA's Phase 1 limits. We find that inpainting techniques which incorporate high wavenumbers in delay space in their modeling are best suited for inpainting over narrowband RFI. Our parameter choices for DPSS make DPSS best suited for inpainting over narrowband RFI while our parameter choices for LSSA make LSSA more flexible to wide RFI gaps and narrow RFI gaps. We find that with our fiducial parameters, DPSS and CLEAN provide the best performance for narrowband RFI while GPR provides the best performance for wideband RFI. We also find that the error distributions in the phase component of the visibilities are log normally distributed. We find that these results hold in real data as well as simulated data. Further, we find that the standard deviation of the errors increases monotonically with increasing thermal noise of the simulated dataset.

To characterize the errors that inpainting cause in the 21cm delay power spectrum, we propagate the inpainted visibilities to the 21cm power spectrum. We find that all inpainting techniques can reproduce the wedge modes of the delay power spectrum to within 10% of the true values. Since the inpainting techniques are not capable of inpainting noise, the errors are greatest for the largest delay modes. Currently, systematics and noise prevent instruments from accurately measuring the amplitude of the power spectrum at the largest delay modes. However we show that in the future, as these effects are reduced, CLEAN and DPSS can most accurately reproduce the true power spectra at high delay. **Quantitatively the errors reach the same order of magnitude as the noise.** Conversely we find that U-Paint imparts artificial fine frequency structure into the

visibilities which manifests as an increase in power at the highest delay modes. We also established a relationship between the mean fractional error in the model visibilities and the mean fractional errors in the model power spectrum. We find that this relationship is linear if we restrict the errors in the model power spectrum to only wedge modes. We also show that this is the case for both real and simulated data. Moving forward we have a better understanding of how the inpainting portion of the data analysis pipeline affect the 21cm power spectrum. This is another important step we must undertake on our continued path to make a detection of the 21cm power spectrum.

## Acknowledgements

The authors are delighted to acknowledge helpful discussions with Lisa McBride, Saurabh Singh, Aaron Parsons, Bryna Hazelton, Paul LaPlante, Jonathan Pober, and Andrea Pallottini. N.K. gratefully acknowledges support from the MIT Pappalardo fellowship.

## Data Availability

The software code underlying this article will be shared on reasonable request to the corresponding author.

## Bibliography

- [1] James E. Aguirre, Steven G. Murray, Robert Pascua, Zachary E. Martinot, Jacob Burba, Joshua S. Dillon, Daniel C. Jacobs, Nicholas S. Kern, Piyarat Kittiwisit, Matthew Kolopanis, Adam Lanman, Adrian Liu, Lily Whitler, Zara Abdurashidova, Paul Alexander, Zaki S. Ali, Yanga Balfour, Adam P. Beardsley, Gianni Bernardi, Tashalee S. Billings, Judd D. Bowman, Richard F. Bradley, Philip Bull, Steve Carey, Chris L. Carilli, Carina Cheng, David R. DeBoer, Matt Dexter, Eloy de Lera Acedo, John Ely, Aaron Ewall-Wice, Nicolas Fagnoni, Randall Fritz, Steven R. Furlanetto, Kingsley Gale-Sides, Brian Glendenning, Deepthi Gorthi, Bradley Greig, Jasper Grobbelaar, Ziyaad Halday, Bryna J. Hazelton, Jacqueline N. Hewitt,

- Jack Hickish, Austin Julius, Joshua Kerrigan, Saul A. Kohn, Paul La Plante, Telalo Lekalake, David Lewis, David MacMahon, Lourence Malan, Cresshim Malgas, Matthys Maree, Eunice Matsetela, Andrei Mesinger, Mathakane Molewa, Miguel F. Morales, Tshgofalang Mosiane, Abraham R. Neben, Bojan Nikolic, Aaron R. Parsons, Nipanjana Patra, Samantha Pieterse, Jonathan C. Pober, Nima Razavi-Ghods, Jon Ringuette, James Robnett, Kathryn Rosie, Mario G. Santos, Peter Sims, Saurabh Singh, Craig Smith, Angelo Syce, Nithyanandan Thyagarajan, Peter K. G. Williams, Haoxuan Zheng, and HERA Collaboration. Validation of the HERA Phase I Epoch of Reionization 21 cm Power Spectrum Software Pipeline. *ApJ*, 924(2):85, January 2022.
- [2] N. Barry, A. P. Beardsley, R. Byrne, B. Hazelton, M. F. Morales, J. C. Pober, and I. Sullivan. The FHD/ppsilon Epoch of Reionisation power spectrum pipeline. *Publ. Astron. Soc. Australia*, 36:e026, July 2019.
- [3] Angélica de Oliveira-Costa, Max Tegmark, B. M. Gaensler, Justin Jonas, T. L. Landecker, and Patricia Reich. A model of diffuse Galactic radio emission from 10 MHz to 100 GHz. *MNRAS*, 388(1):247–260, July 2008.
- [4] David R. DeBoer, Aaron R. Parsons, James E. Aguirre, Paul Alexander, Zaki S. Ali, Adam P. Beardsley, Gianni Bernardi, Judd D. Bowman, Richard F. Bradley, Chris L. Carilli, Carina Cheng, Eloy de Lera Acedo, Joshua S. Dillon, Aaron Ewall-Wice, Gcobisa Fadana, Nicolas Fagnoni, Randall Fritz, Steve R. Furlanetto, Brian Glendenning, Bradley Greig, Jasper Grobbelaar, Bryna J. Hazelton, Jacqueline N. Hewitt, Jack Hickish, Daniel C. Jacobs, Austin Julius, MacCalvin Kariseb, Saul A. Kohn, Telalo Lekalake, Adrian Liu, Anita Loots, David MacMahon, Lourence Malan, Cresshim Malgas, Matthys Maree, Zachary Martinot, Nathan Mathison, Eunice Matsetela, Andrei Mesinger, Miguel F. Morales, Abraham R. Neben, Nipanjana Patra, Samantha Pieterse, Jonathan C. Pober, Nima Razavi-Ghods, Jon Ringuette, James Robnett, Kathryn Rosie, Raddwine Sell, Craig Smith, Angelo Syce, Max Tegmark, Nithyanandan Thyagarajan, Peter K. G. Williams, and Haoxuan Zheng. Hydrogen Epoch of Reionization Array (HERA). *PASP*, 129(974):045001, April 2017.

- [5] P. E. Dewdney, P. J. Hall, R. T. Schilizzi, and T. J. L. W. Lazio. The Square Kilometre Array. *IEEE Proceedings*, 97(8):1482–1496, August 2009.
- [6] Aaron Ewall-Wice, Nicholas Kern, Joshua S. Dillon, Adrian Liu, Aaron Parsons, Saurabh Singh, Adam Lanman, Paul La Plante, Nicolas Fagnoni, Eloy de Lera Acedo, David R. DeBoer, Chuneeta Nunhokee, Philip Bull, Tzu-Ching Chang, T. Joseph W. Lazio, James Aguirre, and Sean Weinberg. DAYENU: a simple filter of smooth foregrounds for intensity mapping power spectra. *MNRAS*, 500(4):5195–5213, January 2021.
- [7] Steven R. Furlanetto, Zoltán Haiman, and S. Peng Oh. Fossil Ionized Bubbles around Dead Quasars during Reionization. *ApJ*, 686(1):25–40, October 2008.
- [8] Steven R. Furlanetto, S. Peng Oh, and Frank H. Briggs. Cosmology at low frequencies: The 21 cm transition and the high-redshift Universe. *Phys. Rep.*, 433(4-6):181–301, October 2006.
- [9] Steven R. Furlanetto, Matias Zaldarriaga, and Lars Hernquist. Statistical Probes of Reionization with 21 Centimeter Tomography. *ApJ*, 613(1):16–22, September 2004.
- [10] Samuel Gagnon-Hartman, Yue Cui, Adrian Liu, and Siamak Ravanbakhsh. Recovering the wedge modes lost to 21-cm foregrounds. *MNRAS*, 504(4):4716–4729, July 2021.
- [11] Abhik Ghosh, Florent Mertens, Gianni Bernardi, Mário G. Santos, Nicholas S. Kern, Christopher L. Carilli, Trienko L. Grobler, Léon V. E. Koopmans, Daniel C. Jacobs, Adrian Liu, Aaron R. Parsons, Miguel F. Morales, James E. Aguirre, Joshua S. Dillon, Bryna J. Hazelton, Oleg M. Smirnov, Bharat K. Gehlot, Siyanda Matika, Paul Alexander, Zaki S. Ali, Adam P. Beardsley, Roshan K. Benefo, Tashalee S. Billings, Judd D. Bowman, Richard F. Bradley, Carina Cheng, Paul M. Chichura, David R. DeBoer, Eloy de Lera Acedo, Aaron Ewall-Wice, Gcobisa Fadana, Nicolas Fagnoni, Austin F. Fortino, Randall Fritz, Steve R. Furlanetto, Samavarti Gallardo, Brian Glendenning, Deepthi Gorthi, Bradley Greig, Jasper Grobelaar, Jack Hickish, Alec Josaitis, Austin Julius, Amy S. Igarashi, MacCalvin Kariseb, Saul A. Kohn, Matthew Kolopanis, Telalo Lekalake, Anita Loots, David MacMahon, Lourence Malan, Cresshim Malgas, Matthys Maree, Zachary E. Martinot, Nathan Mathison, Eunice Matsetela,

- Andrei Mesinger, Abraham R. Neben, Bojan Nikolic, Chuneeta D. Nunhokee, Nipanjana Patra, Samantha Pieterse, Nima Razavi-Ghods, Jon Ringuette, James Robnett, Kathryn Rosie, Raddwine Sell, Craig Smith, Angelo Syce, Max Tegmark, Nithyanandan Thyagarajan, Peter K. G. Williams, and Haoxuan Zheng. Foreground modelling via Gaussian process regression: an application to HERA data. *MNRAS*, 495(3):2813–2826, January 2020.
- [12] H. F. Gruetjen, J. R. Fergusson, M. Liguori, and E. P. S. Shellard. Using inpainting to construct accurate cut-sky CMB estimators. *Phys. Rev. D*, 95(4):043532, February 2017.
- [13] A. K. Gupta, F. C. Chang, and W. J. Huang. Some skew-symmetric models. 10(2):133–140, 2002.
- [14] HERA Collaboration, Zara Abdurashidova, James E. Aguirre, Paul Alexander, Zaki S. Ali, Yanga Balfour, Adam P. Beardsley, Gianni Bernardi, Tashalee S. Billings, Judd D. Bowman, Richard F. Bradley, Philip Bull, Jacob Burba, Steve Carey, Chris L. Carilli, Carina Cheng, David R. DeBoer, Matt Dexter, Eloy de Lera Acedo, Taylor Dibblee-Barkman, Joshua S. Dillon, John Ely, Aaron Ewall-Wice, Nicolas Fagnoni, Randall Fritz, Steven R. Furlanetto, Kingsley Gale-Sides, Brian Glendenning, Deepthi Gorthi, Bradley Greig, Jasper Grobbelaar, Ziyaad Halday, Bryna J. Hazelton, Jacqueline N. Hewitt, Jack Hickish, Daniel C. Jacobs, Austin Julius, Nicholas S. Kern, Joshua Kerrigan, Piyanat Kittiwisit, Saul A. Kohn, Matthew Kolopanis, Adam Lanman, Paul La Plante, Telalo Lekalake, David Lewis, Adrian Liu, David MacMahon, Lourence Malan, Cresshim Malgas, Matthys Maree, Zachary E. Martinot, Eunice Matsetela, Andrei Mesinger, Mathakane Molewa, Miguel F. Morales, Tshegofalang Mosiane, Steven G. Murray, Abraham R. Neben, Bojan Nikolic, Chuneeta D. Nunhokee, Aaron R. Parsons, Nipanjana Patra, Robert Pascua, Samantha Pieterse, Jonathan C. Pober, Nima Razavi-Ghods, Jon Ringuette, James Robnett, Kathryn Rosie, Peter Sims, Saurabh Singh, Craig Smith, Angelo Syce, Nithyanandan Thyagarajan, Peter K. G. Williams, Haoxuan Zheng, and HERA Collaboration. First Results from HERA Phase I: Upper Limits on the Epoch of Reionization 21 cm Power Spectrum. *ApJ*, 925(2):221, February 2022.

- [15] J. A. Högbom. Aperture Synthesis with a Non-Regular Distribution of Interferometer Baselines. *A&AS*, 15:417, June 1974.
- [16] N. Hurley-Walker, J. R. Callingham, P. J. Hancock, T. M. O. Franzen, L. Hindson, A. D. Kapińska, J. Morgan, A. R. Offringa, R. B. Wayth, C. Wu, Q. Zheng, T. Murphy, M. E. Bell, K. S. Dwarkanath, B. For, B. M. Gaensler, M. Johnston-Hollitt, E. Lenc, P. Procopio, L. Staveley-Smith, R. Ekers, J. D. Bowman, F. Briggs, R. J. Cappallo, A. A. Deshpande, L. Greenhill, B. J. Hazelton, D. L. Kaplan, C. J. Lonsdale, S. R. McWhirter, D. A. Mitchell, M. F. Morales, E. Morgan, D. Oberoi, S. M. Ord, T. Prabu, N. Udaya Shankar, K. S. Srivani, R. Subrahmanyan, S. J. Tingay, R. L. Webster, A. Williams, and C. L. Williams. GaLactic and Extragalactic All-sky Murchison Widefield Array (GLEAM) survey - I. A low-frequency extragalactic catalogue. *MNRAS*, 464(1):1146–1167, January 2017.
- [17] Fabian Isensee, Jens Petersen, Andre Klein, David Zimmerer, Paul F. Jaeger, Simon Kohl, Jakob Wasserthal, Gregor Koehler, Tobias Norajitra, Sebastian Wirkert, and Klaus H. Maier-Hein. nnU-Net: Self-adapting Framework for U-Net-Based Medical Image Segmentation. *arXiv e-prints*, page arXiv:1809.10486, September 2018.
- [18] Marvin Karson. Handbook of methods of applied statistics. volume i: Techniques of computation descriptive methods, and statistical inference. volume ii: Planning of surveys and experiments. i. m. chakravarti, r. g. laha, and j. roy, new york, john wiley; 1967. *Journal of the American Statistical Association*, 63(323):1047–1049, 1968.
- [19] Nicholas S. Kern and Adrian Liu. Gaussian process foreground subtraction and power spectrum estimation for 21 cm cosmology. *MNRAS*, 501(1):1463–1480, February 2021.
- [20] Nicholas S. Kern, Aaron R. Parsons, Joshua S. Dillon, Adam E. Lanman, Adrian Liu, Philip Bull, Aaron Ewall-Wice, Zara Abdurashidova, James E. Aguirre, Paul Alexander, Zaki S. Ali, Yanga Balfour, Adam P. Beardsley, Gianni Bernardi, Judd D. Bowman, Richard F. Bradley, Jacob Burba, Chris L. Carilli, Carina Cheng, David R. DeBoer, Matt Dexter, Eloy de Lera Acedo, Nicolas Fagnoni, Randall Fritz, Steve R. Furlanetto, Brian Glendenning, Deepthi Gor-

thi, Bradley Greig, Jasper Grobbelaar, Ziyaad Halday, Bryna J. Hazelton, Jacqueline N. Hewitt, Jack Hickish, Daniel C. Jacobs, Austin Julius, Joshua Kerrigan, Piyanat Kittiwisit, Saul A. Kohn, Matthew Kolopanis, Paul La Plante, Telalo Lekalake, David MacMahon, Lourence Malan, Cresshim Malgas, Matthys Maree, Zachary E. Martinot, Eunice Matsetela, Andrei Mesinger, Mathakane Molewa, Miguel F. Morales, Tshegofalang Mosiane, Steven G. Murray, Abraham R. Neben, Aaron R. Parsons, Nipanjana Patra, Samantha Pieterse, Jonathan C. Pober, Nima Razavi-Ghods, Jon Ringuette, James Robnett, Kathryn Rosie, Peter Sims, Craig Smith, Angelo Syce, Nithyanandan Thyagarajan, Peter K. G. Williams, and Haoxuan Zheng. Mitigating Internal Instrument Coupling for 21 cm Cosmology. II. A Method Demonstration with the Hydrogen Epoch of Reionization Array. *ApJ*, 888(2):70, January 2020.

[21] Joshua Kerrigan, Paul La Plante, Saul Kohn, Jonathan C. Pober, James Aguirre, Zara Abdurashidova, Paul Alexander, Zaki S. Ali, Yanga Balfour, Adam P. Beardsley, Gianni Bernardi, Judd D. Bowman, Richard F. Bradley, Jacob Burba, Chris L. Carilli, Carina Cheng, David R. DeBoer, Matt Dexter, Eloy de Lera Acedo, Joshua S. Dillon, Julia Estrada, Aaron Ewall-Wice, Nicolas Fagnoni, Randall Fritz, Steve R. Furlanetto, Brian Glendenning, Bradley Greig, Jasper Grobbelaar, Deepthi Gorthi, Ziyaad Halday, Bryna J. Hazelton, Jack Hickish, Daniel C. Jacobs, Austin Julius, Nicholas S. Kern, Piyanat Kittiwisit, Matthew Kolopanis, Adam Lanman, Telalo Lekalake, Adrian Liu, David MacMahon, Lourence Malan, Cresshim Malgas, Matthys Maree, Zachary E. Martinot, Eunice Matsetela, Andrei Mesinger, Mathakane Molewa, Miguel F. Morales, Tshegofalang Mosiane, Abraham R. Neben, Aaron R. Parsons, Nipanjana Patra, Samantha Pieterse, Nima Razavi-Ghods, Jon Ringuette, James Robnett, Kathryn Rosie, Peter Sims, Craig Smith, Angelo Syce, Nithyanandan Thyagarajan, Peter K. G. Williams, and Haoxuan Zheng. Optimizing sparse RFI prediction using deep learning. *MNRAS*, 488(2):2605–2615, September 2019.

[22] S. A. Kohn, J. E. Aguirre, C. D. Nunhokee, G. Bernardi, J. C. Pober, Z. S. Ali, R. F. Bradley, C. L. Carilli, D. R. DeBoer, N. E. Gugliucci, D. C. Jacobs, P. Klima, D. H. E. MacMahon, J. R. Manley, D. F. Moore, A. R. Parsons, I. I. Stefan, and W. P. Walbrugh. CONSTRAINING PO-

LARIZED FOREGROUNDS FOR EoR EXPERIMENTS. i. 2d POWER SPECTRA FROM THE PAPER-32 IMAGING ARRAY. *The Astrophysical Journal*, 823(2):88, may 2016.

- [23] P. La Plante, P. K. G. Williams, M. Kolopanis, J. S. Dillon, A. P. Beardsley, N. S. Kern, M. Wilensky, Z. S. Ali, Z. Abdurashidova, J. E. Aguirre, P. Alexander, Y. Balfour, G. Bernardi, T. S. Billings, J. D. Bowman, R. F. Bradley, P. Bull, J. Burba, S. Carey, C. L. Carilli, C. Cheng, D. R. DeBoer, M. Dexter, E. de Lera Acedo, J. Ely, A. Ewall-Wice, N. Fagnoni, R. Fritz, S. R. Furlanetto, K. Gale-Sides, B. Glendenning, D. Gorthi, B. Greig, J. Grobbelaar, Z. Halday, B. J. Hazelton, J. N. Hewitt, J. Hickish, D. C. Jacobs, A. Julius, J. Kerrigan, P. Kittiwisit, S. A. Kohn, A. Lanman, T. Lecalake, D. Lewis, A. Liu, D. MacMahon, L. Malan, C. Malgas, M. Maree, Z. E. Martinot, E. Matsetela, A. Mesinger, M. Molewa, M. F. Morales, T. Mosiane, S. Murray, A. R. Neben, B. Nikolic, A. R. Parsons, R. Pascua, N. Patra, S. Pieterse, J. C. Pober, N. Razavi-Ghods, J. Ringuelette, J. Robnett, K. Rosie, M. G. Santos, P. Sims, C. Smith, A. Syce, N. Thyagarajan, and H. Zheng. A Real Time Processing system for big data in astronomy: Applications to HERA. *Astronomy and Computing*, 36:100489, July 2021.
- [24] Adam E. Lanman, Jonathan C. Pober, Nicholas S. Kern, Eloy de Lera Acedo, David R. DeBoer, and Nicolas Fagnoni. Quantifying EoR delay spectrum contamination from diffuse radio emission. *MNRAS*, 494(3):3712–3727, May 2020.
- [25] Adrian Liu and J. Richard Shaw. Data Analysis for Precision 21 cm Cosmology. *PASP*, 132(1012):062001, June 2020.
- [26] Guilin Liu, Fitsum A. Reda, Kevin J. Shih, Ting-Chun Wang, Andrew Tao, and Bryan Catanzaro. Image Inpainting for Irregular Holes Using Partial Convolutions. *arXiv e-prints*, page arXiv:1804.07723, April 2018.
- [27] C. J. Lonsdale, R. J. Cappallo, M. F. Morales, F. H. Briggs, L. Benkevitch, J. D. Bowman, J. D. Bunton, S. Burns, B. E. Corey, L. Desouza, S. S. Doeleman, M. Derome, A. Deshpande, M. R. Gopala, L. J. Greenhill, D. E. Herne, J. N. Hewitt, P. A. Kamini, J. C. Kasper, B. B. Kincaid, J. Kocz, E. Kowald, E. Kratzenberg, D. Kumar, M. J. Lynch, S. Madhavi, M. Matejek, D. A.

- Mitchell, E. Morgan, D. Oberoi, S. Ord, J. Pathikulangara, T. Prabu, A. Rogers, A. Roshi, J. E. Salah, R. J. Sault, N. U. Shankar, K. S. Srivani, J. Stevens, S. Tingay, A. Vaccarella, M. Waterson, R. B. Wayth, R. L. Webster, A. R. Whitney, A. Williams, and C. Williams. The Murchison Widefield Array: Design Overview. *IEEE Proceedings*, 97(8):1497–1506, August 2009.
- [28] Piero Madau, Avery Meiksin, and Martin J. Rees. 21 Centimeter Tomography of the Intergalactic Medium at High Redshift. *ApJ*, 475(2):429–444, February 1997.
- [29] Haggai Maron, Or Litany, Gal Chechik, and Ethan Fetaya. On Learning Sets of Symmetric Elements. *arXiv e-prints*, page arXiv:2002.08599, February 2020.
- [30] Violeta Menéndez González, Andrew Gilbert, Graeme Phillipson, Stephen Jolly, and Simon Hadfield. SaiNet: Stereo aware inpainting behind objects with generative networks. *arXiv e-prints*, page arXiv:2205.07014, May 2022.
- [31] F. G. Mertens, A. Ghosh, and L. V. E. Koopmans. Statistical 21-cm signal separation via Gaussian Process Regression analysis. *MNRAS*, 478(3):3640–3652, August 2018.
- [32] Miguel F. Morales and J. Stuart B. Wyithe. Reionization and Cosmology with 21-cm Fluctuations. *ARA&A*, 48:127–171, September 2010.
- [33] A. R. Offringa, F. Mertens, and L. V. E. Koopmans. The impact of interference excision on 21-cm epoch of reionization power spectrum analyses. *MNRAS*, 484(2):2866–2875, April 2019.
- [34] Aaron R. Parsons and Donald C. Backer. Calibration of Low-Frequency, Wide-Field Radio Interferometers Using Delay/Delay-Rate Filtering. *AJ*, 138(1):219–226, July 2009.
- [35] Aaron R. Parsons, Donald C. Backer, Griffin S. Foster, Melvyn C. H. Wright, Richard F. Bradley, Nicole E. Gugliucci, Chaitali R. Parashare, Erin E. Benoit, James E. Aguirre, Daniel C. Jacobs, Chris L. Carilli, David Herne, Mervyn J. Lynch, Jason R. Manley, and

- Daniel J. Werthimer. The Precision Array for Probing the Epoch of Re-ionization: Eight Station Results. *AJ*, 139(4):1468–1480, April 2010.
- [36] Aaron R. Parsons, Jonathan C. Pober, James E. Aguirre, Christopher L. Carilli, Daniel C. Jacobs, and David F. Moore. A Per-baseline, Delay-spectrum Technique for Accessing the 21 cm Cosmic Reionization Signature. *ApJ*, 756(2):165, September 2012.
- [37] Jonathan R. Pritchard and Abraham Loeb. 21 cm cosmology in the 21st century. *Reports on Progress in Physics*, 75(8):086901, August 2012.
- [38] Carl Edward. Rasmussen and Christopher K I Williams. *Gaussian processes for machine learning*. MIT Press, 2006.
- [39] Olaf Ronneberger, Philipp Fischer, and Thomas Brox. U-Net: Convolutional Networks for Biomedical Image Segmentation. *arXiv e-prints*, page arXiv:1505.04597, May 2015.
- [40] Hiya Roy, Subhjit Chaudhury, Toshihiko Yamasaki, Danielle DeLatte, Makiko Ohtake, and Tatsuaki Hashimoto. Lunar surface image restoration using U-net based deep neural networks. *arXiv e-prints*, page arXiv:1904.06683, April 2019.
- [41] George B. Rybicki and William H. Press. Interpolation, Realization, and Reconstruction of Noisy, Irregularly Sampled Data. *ApJ*, 398:169, October 1992.
- [42] D. Slepian. Prolate spheroidal wave functions, Fourier analysis, and uncertainty. V - The discrete case. *AT T Technical Journal*, 57:1371–1430, June 1978.
- [43] J. L. Starck, M. J. Fadili, and A. Rassat. Low- $\ell$  CMB analysis and inpainting. *A&A*, 550:A15, February 2013.
- [44] Roman Suvorov, Elizaveta Logacheva, Anton Mashikhin, Anastasia Remizova, Arsenii Ashukha, Aleksei Silvestrov, Naejin Kong, Harshith Goka, Kiwoong Park, and Victor Lempitsky. Resolution-robust Large Mask Inpainting with Fourier Convolutions. *arXiv e-prints*, page arXiv:2109.07161, September 2021.

- [45] Max Tegmark, Angélica de Oliveira-Costa, and Andrew J. Hamilton. High resolution foreground cleaned CMB map from WMAP. *Phys. Rev. D*, 68(12):123523, December 2003.
- [46] Cathryn M. Trott, C. H. Jordan, S. Midgley, N. Barry, B. Greig, B. Pindor, J. H. Cook, G. Slep, S. J. Tingay, D. Ung, P. Hancock, A. Williams, J. Bowman, R. Byrne, A. Chokshi, B. J. Hazelton, K. Hasegawa, D. Jacobs, R. C. Joseph, W. Li, J. L. B. Line, C. Lynch, B. McKinley, D. A. Mitchell, M. F. Morales, M. Ouchi, J. C. Pober, M. Rahimi, K. Takahashi, R. B. Wayth, R. L. Webster, M. Wilensky, J. S. B. Wyithe, S. Yoshiura, Z. Zhang, and Q. Zheng. Deep multiredshift limits on Epoch of Reionization 21 cm power spectra from four seasons of Murchison Widefield Array observations. *MNRAS*, 493(4):4711–4727, April 2020.
- [47] M. P. van Haarlem, M. W. Wise, A. W. Gunst, G. Heald, J. P. McKean, J. W. T. Hessels, A. G. de Bruyn, R. Nijboer, J. Swinbank, R. Fallows, M. Brentjens, A. Nelles, R. Beck, H. Falcke, R. Fender, J. Hörandel, L. V. E. Koopmans, G. Mann, G. Miley, H. Röttgering, B. W. Stappers, R. A. M. J. Wijers, S. Zaroubi, M. van den Akker, A. Alexov, J. Anderson, K. Anderson, A. van Ardenne, M. Arts, A. Asgekar, I. M. Avruch, F. Batejat, L. Bähren, M. E. Bell, M. R. Bell, I. van Bemmelen, P. Bennema, M. J. Bentum, G. Bernardi, P. Best, L. Bîrzan, A. Bonafede, A. J. Boonstra, R. Braun, J. Bregman, F. Breitling, R. H. van de Brink, J. Broderick, P. C. Broekema, W. N. Brouw, M. Brüggen, H. R. Butcher, W. van Cappellen, B. Ciardi, T. Coenen, J. Conway, A. Coolen, A. Corstanje, S. Damstra, O. Davies, A. T. Deller, R. J. Dettmar, G. van Diepen, K. Dijkstra, P. Donker, A. Doorduyn, J. Dromer, M. Drost, A. van Duin, J. Eislöffel, J. van Enst, C. Ferrari, W. Frieswijk, H. Gankema, M. A. Garrett, F. de Gasperin, M. Gerbers, E. de Geus, J. M. Grießmeier, T. Grit, P. Gruppen, J. P. Hamaker, T. Hassall, M. Hoeft, H. A. Holties, A. Horneffer, A. van der Horst, A. van Houwelingen, A. Huijgen, M. Iacobelli, H. Intema, N. Jackson, V. Jelic, A. de Jong, E. Jütte, D. Kant, A. Karastergiou, A. Koers, H. Kollen, V. I. Kondratiev, E. Kooistra, Y. Koopman, A. Koster, M. Kuniyoshi, M. Kramer, G. Kuper, P. Lambropoulos, C. Law, J. van Leeuwen, J. Lemaître, M. Loose, P. Maat, G. Macario, S. Markoff, J. Masters, R. A. McFadden, D. McKay-Bukowski, H. Meijering,

H. Meulman, M. Mevius, E. Middelberg, R. Millenaar, J. C. A. Miller-Jones, R. N. Mohan, J. D. Mol, J. Morawietz, R. Morganti, D. D. Mulcahy, E. Mulder, H. Munk, L. Nieuwenhuis, R. van Nieuwpoort, J. E. Noordam, M. Norden, A. Noutsos, A. R. Offringa, H. Olofsson, A. Omar, E. Orrú, R. Overeem, H. Paas, M. Pandey-Pommier, V. N. Pandey, R. Pizzo, A. Polatidis, D. Rafferty, S. Rawlings, W. Reich, J. P. de Reijer, J. Reitsma, G. A. Renting, P. Riemers, E. Rol, J. W. Romein, J. Roosjen, M. Ruiter, A. Scaife, K. van der Schaaf, B. Scheers, P. Schellart, A. Schoenmakers, G. Schoonderbeek, M. Serylak, A. Shulevski, J. Sluman, O. Smirnov, C. Sobey, H. Spreeuw, M. Steinmetz, C. G. M. Sterks, H. J. Stiepel, K. Stuurwold, M. Tagger, Y. Tang, C. Tasse, I. Thomas, S. Thoudam, M. C. Toribio, B. van der Tol, O. Usov, M. van Veelen, A. J. van der Veen, S. ter Veen, J. P. W. Verbiest, R. Vermeulen, N. Vermaas, C. Vocks, C. Vogt, M. de Vos, E. van der Wal, R. van Weeren, H. Weggemans, P. Weltevrede, S. White, S. J. Wijnholds, T. Wilhelmsson, O. Wucknitz, S. Yatawatta, P. Zarka, A. Zensus, and J. van Zwieten. LOFAR: The LOw-Frequency ARray. *A&A*, 556:A2, August 2013.

- [48] Norbert Wiener. *Extrapolation, Interpolation, and Smoothing of Stationary Time Series*. The MIT Press, 1964.
- [49] Michael J. Wilensky, Bryna J. Hazelton, and Miguel F. Morales. Exploring the consequences of chromatic data excision in 21-cm epoch of reionization power spectrum observations. *ApJ*, 510(4):5023–5034, March 2022.
- [50] Zhaoyi Yan, Xiaoming Li, Mu Li, Wangmeng Zuo, and Shiguang Shan. Shift-Net: Image inpainting via Deep Feature Rearrangement. *arXiv e-prints*, page arXiv:1801.09392, January 2018.
- [51] Barak Zackay, Tejaswi Venumadhav, Javier Roulet, Liang Dai, and Matias Zaldarriaga. Detecting gravitational waves in data with non-stationary and non-Gaussian noise. *Phys. Rev. D*, 104(6):063034, September 2021.

- [52] S. Zaroubi, Y. Hoffman, K. B. Fisher, and O. Lahav. Wiener Reconstruction of the Large-Scale Structure. *ApJ*, 449:446, August 1995.
- [53] Yanhong Zeng, Jianlong Fu, Hongyang Chao, and Baining Guo. Learning Pyramid-Context Encoder Network for High-Quality Image Inpainting. *arXiv e-prints*, page arXiv:1904.07475, April 2019.
- [54] H. Zheng, M. Tegmark, J. S. Dillon, D. A. Kim, A. Liu, A. R. Neben, J. Jonas, P. Reich, and W. Reich. An improved model of diffuse galactic radio emission from 10 MHz to 5 THz. *MNRAS*, 464(3):3486–3497, January 2017.
- [55] Paul La Plante. Zhile Chen. Using deep learning to identify rfi in hera data,. *HERA Memorandum*, (108), 12 2021.

## **Chapter 6**

# **A General Bayesian Framework to Account for Foreground Map Errors in Global 21-cm Experiments**

### **Addendum for thesis**

This chapter addresses another type of systematic that is present in 21cm instruments: the foregrounds. Since the foregrounds are significantly brighter than the 21cm signal, mitigation of the foregrounds is not an optional exercise, so experiments must develop ways to deal with them. Broadly, they are either avoided or modeled and subtracted. REACH, a global 21cm signal experiment, models and subtracts the foregrounds. The models are built on sky maps which do not have detailed spatial error maps. Although spatial modeling of the foreground is not in itself crucial in general for a global 21cm signal experiment, it is however crucial to the REACH analysis because of the approach we have taken to detection the global 21cm signal. This means that the foregrounds models are at risk of causing other systematics. Peter Sims, Adrian Liu and I studied the types of systematics than are produced in the REACH data-analysis pipeline due to imperfect foreground models. We constructed a framework that is able to account for the spatial errors in the

REACH foreground model. This type of framework is a tool that can be used to mitigate foreground systematics. Going forward this will be an important piece of the REACH data-analysis pipeline.

## **Abstract**

Measurement of the global 21-cm signal during the Epoch of Reionization (EoR) is made difficult by bright foreground emission which is orders of magnitude larger than the expected signal. Fitting for a physics-motivated parametric forward model of the data within a Bayesian framework provides a robust means to separate the signal from the foregrounds, given sufficient information about the instrument and sky. It has previously been demonstrated that, within such a modelling framework, a foreground model of sufficient fidelity can be generated by dividing the sky into  $N$  regions and scaling a base map assuming a distinct uniform spectral index in each region. Here, we show that, if unaccounted-for, amplitude errors in low-frequency radio maps used for our base map model will prevent recovery of the 21 cm signal within this framework, and that the level of bias in the recovered 21-cm signal is proportional to the amplitude and the correlation length of the base-map errors in the region. We introduce an updated foreground model that is capable of accounting for these measurement errors by fitting for a monopole offset and a set of spatially-dependent scale factors describing the ratio of the true and model sky temperatures, with the size of the set determined by Bayesian evidence-based model comparison. We show that our model is flexible enough to account for multiple foreground error scenarios allowing the 21-cm signal to be detected without bias from simulated observations with a smooth conical log spiral antenna.

## **6.1 Introduction**

One of the remaining unmeasured periods in the history of our Universe is Cosmic Dawn (CD), the period in which the first stars are formed. These first generation stars give rise to the Epoch of Reionization (EoR), the stage in which the neutral hydrogen in the intergalactic medium (IGM) is ionized by the first galaxies. CD and EoR take place after formation of the Cosmic Microwave

Background (CMB), but precede observations of the modern universe. The EoR and CD therefore represent the missing link between the early universe and the structure we see today. Despite its importance, a direct measurement of the EoR has been difficult due to a lack of direct probes. Thus far we have only indirect detection of its existence based on Ly $\alpha$  absorption and CMB optical depth measurements [45].

One of the most promising methods to make direct detection of CD and the EoR is to use the 21-cm hyperfine transition of Hydrogen in which a 21-cm wavelength photon is emitted when the electron flips its spin relative to the Hydrogen nucleus. Thus the 21-cm line directly probes the neutral hydrogen in the IGM during CD and the EoR. The emitted 21-cm wavelength photon is then redshifted according to cosmic expansion, which also allows for tomographic measurements of the neutral hydrogen along the line of sight. The 21-cm radiation falls in the radio portion of the electromagnetic spectrum and is measured in contrast to the CMB. The temperature difference between 21-cm photons and the CMB is referred to as the differential brightness temperature  $\delta T_b$  [23, 35].

There have been two main approaches employed by experiments to measure  $\delta T_b$  during the EoR. One approach uses interferometers. Interferometric approaches are sensitive to the spatial fluctuations of  $\delta T_b$ . This has been the approach of collaborations such as Hydrogen Epoch of Reionization Array (HERA, [16]), The Low-Frequency Array (LOFAR, [64]), The Murchison Widefield Array (MWA, [38]), Precision Array to Probe the Epoch of Reionization (PAPER, [43]), and the Square Kilometre Array (SKA, [17]). An alternative approach to measuring  $\delta T_b$  are 21-cm global signal measurements where the evolution of the spatially averaged  $\delta_b$  as a function of frequency. This has been the approach of experiments such as Broadband Instrument for Global Hydrogen Reionisation Signal (BIGHORNS, [60]), Experiment to Detect the Global EoR Signature (EDGES, [10]), Large aperture Experiment to detect the Dark Ages (LEDA, [46]), Probing Radio Intensity at high-Z from Marion (PRIZM, [44]), The Giant Metrewave Radio Telescope Epoch of Reionization (GMRT, [42]), Radio Experiment for the Analysis of Cosmic Hydrogen (REACH, [14]), and Shaped Antennas to measure the background Radio Spectrum

(SARAS, [59]). In this case, global signal experiments measure the mean of the differential brightness temperature, i.e,  $T_b \equiv \overline{\delta T_b}$  given by:

$$T_b(z) \approx 23 [1 - \bar{x}_{\text{HII}}] \left( \frac{T_s(z) - T_\gamma(z)}{T_s(z)} \right) \left( \frac{\Omega_b h^2}{0.023} \right) \times \left[ \left( \frac{0.15}{\Omega_m h^2} \right) \left( \frac{1+z}{10} \right) \right]^{1/2} \text{ mK} \quad (6.1)$$

where  $\bar{x}_{\text{HII}}$  is the mean ionized fraction of hydrogen,  $H(z)$  is the Hubble parameter (with  $h$  as its dimensionless counterpart),  $T_\gamma(z)$  is the CMB temperature,  $\Omega_m$  is the normalized matter density,  $\Omega_b$  is the normalized baryon density, and where  $z$  is the redshift related to the frequency  $\nu$  of the redshifted 21-cm photons by  $1+z = \nu/\nu_0$  where  $\nu_0$  is the rest frequency of a 21-cm photon. The mean differential brightness temperature (hereafter referred to as the global signal) depends on the spin temperature  $T_s(z)$  of the neutral hydrogen gas, which measures the relative number of HI atoms that are in the excited versus ground hyperfine states.

The global 21-cm signal and is an important probe of CD and the EoR. After the time of recombination,  $T_s$  and  $T_k$  are coupled due to collisional excitations. The remaining free electrons from recombination scatter off CMB photons keeping  $T_\gamma$  coupled with  $T_s$  leading to no 21-cm signal. After redshifts of  $z \sim 150$   $T_s$  and  $T_k$  decouple from  $T_\gamma$ . As the Universe expands the temperature of the neutral hydrogen gas  $T_k$  cools adiabatically. Thus due to collisional coupling and cooling gas temperature, the spin temperature  $T_s$  drops along with the gas temperature  $T_k$ . As the Universe expands collisions become more infrequent and eventually  $T_k$  decouples with  $T_s$  which once again falls into thermal equilibrium with  $T_\gamma$ . Once CD is underway, the first generation stars begin emitting Ly $\alpha$  photons which again couple  $T_s$  to  $T_k$  through the Wouthuysen-Field effect [21, 65]. The spin temperature is again driven to the gas temperature  $T_k$  which creates an absorption signature relative to  $T_\gamma$ . The redshift, duration and amplitude of the absorption trough due to the Ly $\alpha$  coupling directly depends on the details of reionization. Detection of this absorption trough was first reported by EDGES [11]. However, the unexpectedly large amplitude and flattened profile was considerably larger than was predicted by cosmological models [49]. This has spurred theoretical interest in explaining the profile with excess radio background models, millicharged dark matter models and non- $\Lambda$ CDM cosmology [3, 18, 19, 30]. Other works have shown that this profile may be the result of a systematic which was unaccounted for [8, 12, 31, 53, 57, 58]. Finally as

the first generation stars begin emitting x-rays, the gas temperature is heated, causing  $T_s$  to create an emission spectrum relative to  $T_\gamma$  [7, 13, 20, 22, 29, 33, 34, 39, 40, 47]. Clearly, much of the physics of CD and EoR is encoded in precision measurements of the global signal.

One of the difficulties in detecting the global 21-cm signal are the radio foregrounds (hereafter referred to as just foregrounds) which are orders of magnitude brighter than the expected 21-cm signal within the expected redshift range of CD and the EoR. The effect of the foregrounds on global signal experiments has been well characterized in previous works [5, 6, 37, 51]. The foregrounds are mostly due to synchrotron radiation which cause them to be smooth as a function of frequency which have allowed other studies to take advantage of their spectral smoothness to extract the 21-cm signal [36]. Most techniques employ a model and subtract strategy where the global signal is extracted by removing the the foregrounds [24]. In general there are a diverse set of foreground mitigation techniques that have been well developed. [9, 28, 48, 61–63].

Other experiments such as the Radio Experiment for the Analysis of Cosmic Hydrogen (REACH) have embraced a forward modelling approach to mitigate the foregrounds in order to detect the global 21-cm signal. A forward model approach requires modeling the instrument, the atmospheric environment, as well as the individual components of the radio sky, i.e, the galactic and extragalactic radio foregrounds and the cosmic 21-cm signal [1, 2, 52]. These radio components and all relevant errors are propagated though the analysis. Forward modelling the foregrounds requires modeling the spatial distribution of the foregrounds as well as their spectral distribution. This was previously explored in [2]. To model the spatial distribution of the foregrounds, [2] used radio sky models such as [15, 32, 50, 66]. These radio sky maps were measured without detailed error maps, rather only with quoted uncertainties on the offset and scale errors in the map (for example at 150MHz it has been shown by [11, 59] that the uniform scale errors are at the  $\sim 5\%$ - $11\%$  level). Thus, forward modelled foregrounds relying on these maps will contain spatial temperature perturbations (or spatial “amplitude” perturbations) in the forward model relative to the dataset that observer with the instrument. In this paper we extend the foreground model in [2] to account for the spatial errors in the foregrounds.

In this paper we build on the work of [2] and show that perturbations in the amplitude of these radio maps can cause systematics in the analysis of global 21-cm signal experiments which if unaccounted for will bias or make recovery of the true signal impossible. As of yet there is no accepted error model for these radio sky maps. In this work we bracket the range of systematic scenarios by studying a bracketing range of error scenarios and morphologies. We also study the effect that temperature offsets in radio sky maps have on our analysis. We then introduce a framework by which we can account for the amplitude and offset errors within the analysis. We show that our framework can recover the 21-cm signal without bias. We perform the analysis of this framework using the REACH experiment as our fiducial instrument; however, this framework is applicable to any global 21-cm experiment.

This paper is structured as follows. In Section 6.2 we introduce our fiducial global 21-cm experiment REACH and discuss our forward model of the foregrounds as well as our procedure to create simulated datasets. In Section 6.3 we discuss the range of possible error scenarios in radio sky maps and the systematics that they cause in global 21-cm analysis. We also introduce our most realistic foreground map error scenario and use it as our fiducial foreground error realization in our dataset. In Section 6.4 we introduce the amplitude scale factor framework that we use to account for foreground amplitude systematics. In Section 6.5.2 we apply this framework to simulated datasets containing our fiducial foreground errors but assuming perfect knowledge of the spectral structure of the foregrounds. In Section 6.6 we again apply this framework to our simulated datasets containing our fiducial foreground errors but now also assume imperfect a priori knowledge of their spectral structure and jointly fit for this, in the manner described in [2]. We then conclude in Section 6.7.

## 6.2 Fiducial Instrument and Analysis Pipeline

The Radio Experiment for the Analysis of Cosmic Hydrogen (REACH) [14] is a global 21-cm signal experiment located in the South African Karoo Desert. REACH will have observation windows corresponding to frequencies 50MHz to 200MHz corresponding to redshifts  $z \simeq 30 - 6$ . This is the expected redshift range for CD and EoR signals. REACH forward models the 21-cm signal,

antenna beam and the galactic foregrounds as a function of  $\nu$ . The observation data taken over a set of LSTs is time averaged and the forward modelled sky is then fit to the time averaged data plus an additional signal model component. In this section we describe our simulated datasets, foreground model and Bayesian analysis of the simulated datasets.

### 6.2.1 Bayesian Evidence

Given a model  $M$  of the sky which is parameterized by a set of cosmological parameters  $\theta$ , we can infer the probability distribution of  $\theta$  given the measured dataset  $\mathbf{d}$  for our particular model i.e.  $p(\theta|\mathbf{d}, M)$ . This is the posterior distribution in Bayes theorem:

$$p(\theta|\mathbf{d}, M) = \frac{p(\mathbf{d}|\theta, M)p(\theta, M)}{p(\mathbf{d}|M)} \quad (6.2)$$

where  $p(\mathbf{d}|\theta, M)$  is the likelihood,  $p(\theta|M)$  is the prior on the parameter set  $\theta$  and  $p(\mathbf{d}|M)$  is the Bayesian Evidence. Throughout this paper we denote the Bayesian evidence as  $Z$ . The Bayesian Evidence is the normalization factor which ensures that the posterior of Bayes' theorem is a properly normalized probability distribution function. To numerically estimate the posterior probability distributions  $p(\theta|\mathbf{d}, M)$  of the parameters, one draws samples from the prior distribution  $p(\theta)$ . Bayes' theorem can also be used for model selection, where one can determine the relative probabilities of models for the data via calculation of the Bayesian evidence,

$$p(\mathbf{d}|M) = \int d\theta p(\mathbf{d}|\theta, M)p(\theta, M) \quad (6.3)$$

Computing the Bayesian Evidence using Equation 6.3 for each model is computationally expensive since every element of the n-dimensional prior volume must be sampled. This makes traditional Markov Chain Monte Carlo (MCMC) methods non-ideal to compute the Bayesian Evidence since MCMC algorithms only calculate the ratio of likelihood factors from point to point thereby avoiding computation of  $p(d|M)$ .

In order to compute the Bayesian evidence for each model we used the nested sampler POLYCHORD [26, 27] which greatly decreases the computational cost required to compute the Bayesian

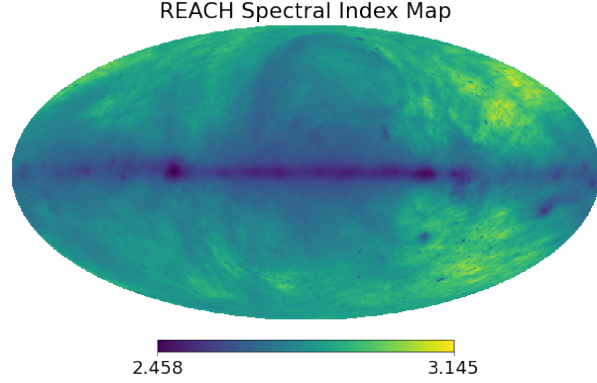


**Figure 6.1:** The spatial variation of the spectral index  $\beta$  as a function of position  $(\theta, \phi)$  on the sky. Bright yellow regions correspond to larger spectral indices while darker regions correspond to small spectral indices. The morphology of  $\beta(\theta, \phi)$  roughly follows the galactic morphology.

Evidence. POLYCHORD operates by placing  $n_{\text{live}}$  points within the prior volume and then slice sampling the prior generating new live points at each iteration. The sampling occurs from regions of low likelihood to high likelihood. The Bayesian evidence is implicitly computed as the sampler gradually makes its way to the region of high likelihood. This sampling technique is also more effective at sampling multi-modal posteriors. The relevant POLYCHORD parameters for our analysis are  $n_{\text{prior}}$ , the number of samples drawn from the prior,  $n_{\text{fail}}$  the number of consecutive failed sample draws at which the algorithm should terminate, the precision criterion which, and  $n_{\text{repeats}}$  which toggles the number of repeats of the slice sampling procedure. Throughout our analysis we use  $n_{\text{live}} = 25n_{\text{dim}}$ ,  $n_{\text{prior}} = 25n_{\text{dim}}$ ,  $n_{\text{fail}} = 25n_{\text{dim}}$  and  $n_{\text{repeats}} = 5n_{\text{dim}}$  where  $n_{\text{dim}}$  are the number of parameters in the inference.

## 6.2.2 Data Simulations

In this section we describe our simulated dataset. The temperature of the sky within our observation band is modeled as the sum of the radio foregrounds, CMB and the cosmological signal  $T_{\text{sky}}(\theta, \phi, \nu) = T_{21}(\nu) + T_{\text{FG}}(\theta, \phi, \nu) + T_{\text{CMB}}$ . The temperature of the radio foregrounds are dominated by synchrotron and free-free radiation emission which are individually well described by

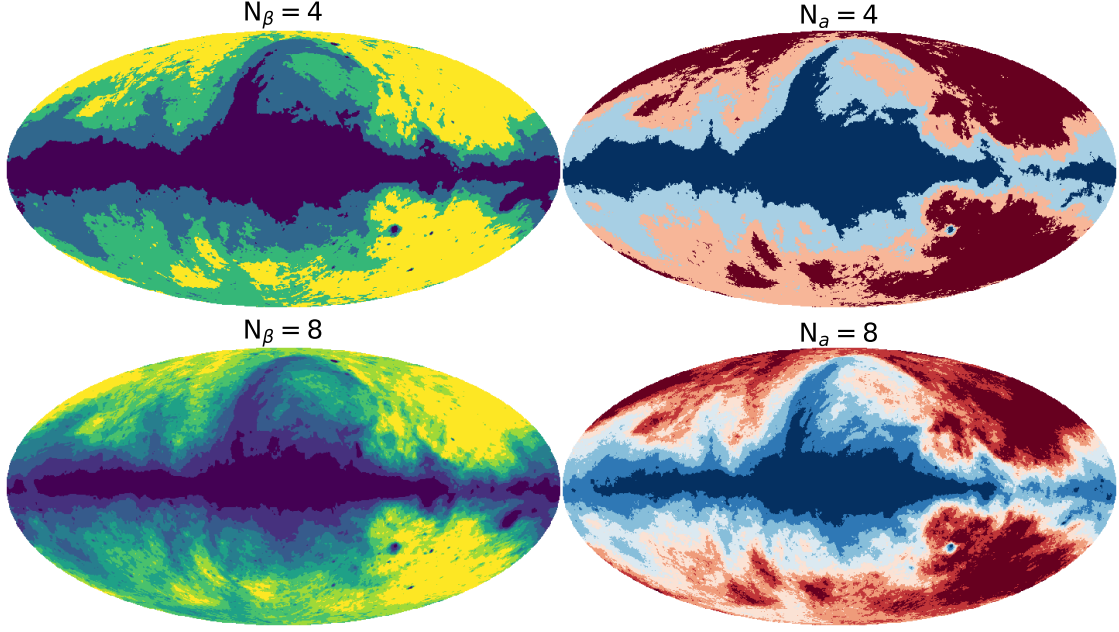


**Figure 6.2:** In each panel we show the division of the regions on the sky. The left column corresponds to splitting the spectral map shown in Figure 6.1 into 4 regions (top) and 8 regions (bottom). On the right column we split the Haslam map from [50] into 4 regions (top) and 8 regions (bottom).

spatially-dependent spectral power laws. Following [2], we form a model for these foregrounds as,

$$T_{\text{FG}}(\theta, \phi, \nu) = (T_{\text{base}}(\theta, \phi, \nu_0) - T_\gamma)(\nu/\nu_0)^{-\beta(\theta, \phi)} \quad (6.4)$$

where  $\beta(\theta, \phi)$  is the spatially varying spectral index and  $\nu_0$  is the reference frequency of the foreground model which we set to 408MHz. A map of spectral index variation across the sky was previously derived in [2]. This was derived by calculating the spectral index required to map each pixel of the Global Sky Model (GSM, [15]) to the corresponding pixel of the Haslman map at 408MHz, i.e.

$$\beta(\theta, \phi) = \frac{\ln \left( \frac{T_{230}(\theta, \phi) - T_\gamma}{T_{408}(\theta, \phi) - T_\gamma} \right)}{\ln(230/408)} \quad (6.5)$$

The resulting spectral index map is shown in Figure 6.1.  $T_{\text{base}}$  is the temperature of the sky measured at a reference frequency  $\nu_0$ . This map, which we refer to as the foreground “basemap” is then extrapolated in frequency according to  $\beta(\theta, \phi)$ . Since REACH is a drift scan experiment, the

resulting temperature of the sky is then rotated for time and observation location of the instrument. The resulting dataset as seen through the beam is then

$$T_{\text{sky}} = \frac{1}{4\pi} \int_0^{4\pi} D(\theta, \phi, \nu) \int_{\text{LST}_0}^{\text{LST}} T_{\text{FG}}(\theta, \phi, \nu, t) dt d\Omega \quad (6.6)$$

where  $D(\theta, \phi, \nu)$  is the antenna's directivity pattern at frequency  $\nu$  and  $\text{LST}_0$ ,  $\text{LST}$  refer to the beginning and end of the observation times. We model the 21-cm signal as a simple Gaussian of amplitude  $A_{21}$ , width  $\sigma_{21}$  centered at frequency  $\nu_{21}$ :

$$T_{21} = A_{21} e^{-\frac{(\nu - \nu_{21})^2}{2\sigma_{21}^2}} \quad (6.7)$$

This model of the 21-cm signal is not meant to be overly realistic, but rather provide enough flexibility to characterize the range of realistic scenarios in our signal recovery analysis. The cosmological signal  $T_{21}$  and the CMB  $T_\gamma$  are taken to be spatially uniform. The temperature of the sky is then computed as

$$T_{\text{data}}(\nu) = T_{\text{sky}}(\nu) + T_{21}(\nu) + T_\gamma + \sigma_{\text{noise}} \quad (6.8)$$

where  $\sigma_{\text{noise}}$  is random uncorrelated Gaussian noise with standard deviation 0.025K.

### 6.2.3 Spectral Model

In the previous section we introduced our fiducial map for the spatially varying spectral index which was used to create the dataset. Since the true spatial variation of the spectral index is not known, the spectral indices must be fit for within our foreground model. This spectral model was the main focus of [2]. We briefly describe it here. Since fitting for the spectral index at each pixel on the sky is computational infeasible, in order to model the spatial variation of the spectral index in a computational feasible manner, the spectral map is split into  $N_\beta$  regions of uniform  $\beta$ . The regions are selected such that the spectral indices are similar within the region. This framework becomes a closer approximation to the true spectral sky as the number of regions  $N_\beta$  is increased. Our foreground model can then be written as

$$T_{\text{FG}}(\theta, \phi, \nu) = \left[ \sum_i^{N_\beta} M_{\beta,i}(\theta, \phi) (T_{\text{base}}(\theta, \phi, \nu_0) - T_\gamma) (\nu/\nu_0)^{-\beta_i} \right] \quad (6.9)$$

where  $i$  are the indices corresponding to  $i$ th spectral region. The values  $M_i(\theta, \phi)$  are masks that take on the value of 0 or 1 thereby determining whether a pixel is part of the  $i$ th spectral region which contains a spectral index  $\beta_i$ . On the left column of Figure 6.2 we show example regions where the spectral map from Figure 6.1 has been split into 4 regions (top) and 8 regions (bottom). The foregrounds are then rotated onto the coordinates of the beam at the specified LSTs (corresponding to the observational times). The sky as measured by the instrument are then computed as

$$T_{\text{sky}}^i(\nu) = \frac{1}{4\pi} \int_0^{4\pi} D(\theta, \phi, \nu) \int_{\text{LST}_0}^{\text{LST}} T_{\text{FG}}^i(\theta, \phi, \nu, N_\beta, t) dt d\Omega. \quad (6.10)$$

where  $T_{\text{sky}}^i$  is the contribution from the  $i$ th region of the sky to the measured spectrum. The mean temperature of the sky is then computed as

$$T_{\text{model}}(\nu) = \sum_i^{N_\beta} T_{\text{sky}}^i(\nu) + T_{21}(A_{21}, \nu, \sigma_{21}) + T_\gamma \quad (6.11)$$

where  $T_{21}(A_{21}, \nu, \sigma_{21})$  refers to the model 21-cm described by Equation 6.7 with amplitude, central frequency and width ( $A_{21}, \nu_{21}, \sigma_{21}$ ). We compare the sky model  $T_{\text{sky}}$  to the simulated dataset  $T_{\text{data}}$  through the Gaussian likelihood

$$\ln L = -\frac{1}{2} \sum_j \ln \left( 2\pi\sigma_n^2 \right) - \frac{1}{2} \left( \frac{T_{\text{data}}(\nu_j) - (T_{\text{model}}(\nu_j) + T_{21}(\nu_j))}{\sigma_n^2} \right)^2 \quad (6.12)$$

where the index  $j$  refers to the frequency bin. We assume statistical independence between each frequency bin. Throughout this paper we place a uniform prior on the spectral indices  $\beta$  between [2.45, 3.15] which encompasses the entire range of spectral indices in the spectral index map in Figure 6.1. Further we place uniform priors on the 21-cm signal parameters ( $A_{21}, \nu_{21}, \sigma_{21}$ ) : [0, 0.25], [50MHz, 150MHz], [10MHz, 20MHz]. In principle, we could jointly estimate the sky model and noise in the data as demonstrated in [2]; however, for computational simplicity, here we

fix the noise estimate at  $\sigma = 0.025\text{K}$  and add a corresponding zero-mean Gaussian noise realisation to the signal when simulating the data. Unless otherwise stated, we use a 1hour observation time starting at 18 : 00 : 00 on 2021 – 01 – 01 with a conical log spiral as our fiducial instrument.

## 6.3 Foreground Errors

Observations of the radio sky at 408MHz [50], at 150MHz [32], 45MHz [25] or the GSM composite model at 230MHz [15] do not have detailed error maps. Therefore any foreground model constructed using these maps will contain uncharacterized errors relative to the true sky  $T_{\text{base}}^{\text{true}}(\theta, \phi)$ . Consequently, our foreground models, which use these errorbar-less radio maps as the basemap  $T_{\text{base}}(\theta, \phi)$  are vulnerable to systematic errors in the form of temperature perturbations  $T_{\text{error}}(\theta, \phi)$  relative to the sky seen by the antenna. Since these maps are not accompanied by detailed error maps, the exact form and morphology of the temperature errors are also unknown. It is possible that the errorbars follow a variety of different morphologies. As a result, in this work we consider multiple error scenarios, bracketing the possible systematic errors caused by amplitude perturbations in the foreground maps, and study the systematics created in the analysis due to each of these cases. In Section 6.3.1 we describe our method to assess whether the foreground error realisations produces significant systematics in our analysis. In Section 6.3.2 we build intuition on different foreground error scenarios, while in Section 6.3.3 we introduce our method for generating more realistic foreground amplitude errors.

### 6.3.1 Methodology For Assessing Foreground Errors in the Analysis

To assess whether a particular foreground error scenario produces significant systematics in our analysis, we create a simulated dataset using the procedure described in Section 6.2.2 but with our noise realization added to the basemap in Equation 6.4, i.e.  $T_{\text{base}}^{\text{true}}(\theta, \phi) = T_{\text{base}}(\theta, \phi) + T_{\text{error}}(\theta, \phi)$  where  $T_{\text{error}}(\theta, \phi)$  is the temperature map of the noise realization. To isolate the effect that the temperature perturbation errors have on the data analysis pipeline, we do not add 21-cm signal in the dataset. Note that for brevity we will refer to the spatial temperature perturbations in the

basemap as amplitude errors). This condition essentially makes our assessment of the foreground errors a null test, i.e. there is no 21-cm signal inside the dataset, and so any recovered 21-cm signal is thus due to a systematic caused by the foreground amplitude errors. Thus the null test is passed if the amplitude of the recovered 21-cm signal is consistent with zero at  $1\sigma$ . Our dataset can be therefore be written as

$$T_{\text{FG}}(\theta, \phi, \nu) = (T_{\text{base}}^{\text{true}}(\theta, \phi) - T_{\gamma})(\nu/\nu_0)^{-\beta}. \quad (6.13)$$

The remainder of the simulated dataset procedure remains the same as discussed in Section 6.2.2. The dataset created using the noisy foreground map is then fit using a version of the foregrounds that do not contain the noise realization, i.e. using the “noiseless”  $T_{\text{base}}$  to construct the foreground model. In our foreground model we fix the number of spectral regions to  $N_{\beta} = 10$  which has been shown in [2] to lead to unbiased recovery of the 21-cm signal. Thus  $N_{\beta}$  provides sufficient flexibility to account for the spatial variation of the spectral index in the sky. By fixing  $N_{\beta} = 10$ , we avoid adding additional spectral components in the foreground model to fit for amplitude perturbations in the foreground basemap <sup>1</sup>. This assumption allows us to better isolate the effect of the amplitude errors in the analysis. <sup>2</sup>. In the following section we consider a range of scenarios for  $T_{\text{error}}(\theta, \phi)$  and using this methodology study their affect on the analysis.

### 6.3.2 Error Scenarios

Since we do not precisely know the nature or morphological structure of the errors present in the foreground map, we consider a range of error scenarios and amplitudes with the aim of bracketing the possibilities for the systematics. Roughly, the errors we have considered fall into two categories :

1. Noise Scenario 1: Homoscedastic errors
2. Noise Scenario 2: Heteroscedastic errors

---

<sup>1</sup>Note that in Section 6.6 we show that spectral components cannot compensate for systematics that are caused by amplitude perturbations in the basemap.

<sup>2</sup>Note that we only fix  $N_{\beta} = 10$  in this section. In Section 6.6 we consider models where this is not the case

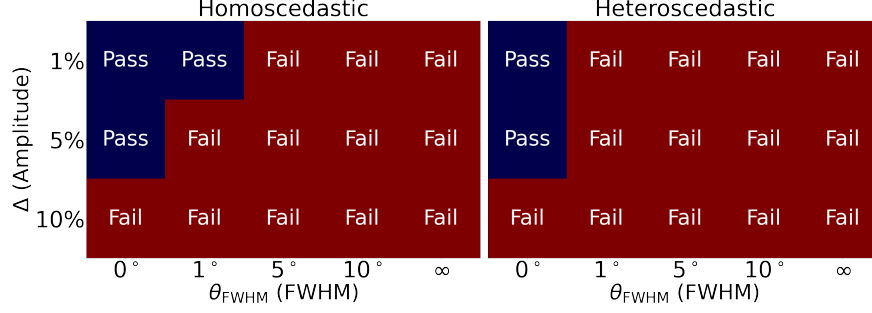


**Figure 6.3:** Summary of the null test results described in Section 6.3.1 for the error scenarios described in Section 6.3.2. The horizontal axis corresponds to the FWHM of the error correlation length while the vertical axis corresponds to the amplitude of the fluctuations. A red panel indicates that the error scenario does leads to a systematic in the analysis large enough such that the null test fails. A blue panel indicates that the error scenario does not lead to a systematic large enough such that the null test fails. The left panel are error scenarios where the standard deviation of the errors are uniform across the sky while the right panel are error scenario that have standard deviation which is spatially dependent.

Scenario 1 corresponds to error realisations where the standard deviation of the errors is uniform over the sky. In Scenario 2 we consider the case where the standard deviation of the errors are proportional to the temperature in each pixel of the basemap. In each scenario, we assess the systematics produced by the presence of these errors in the analysis through the methodology and observation settings discussed in Section 6.3.1. To produce the errors in Scenario 1, we add random Gaussian noise with mean  $\mu = 0$  and of standard deviation  $\sigma_{\text{noise}} = \Delta \cdot \overline{\delta T}_{\text{sky}}$  where  $\overline{\delta T}_{\text{sky}}$  is the mean temperature of the map and the  $\Delta$  is a dimensionless parameter which we vary  $[0.01, 0.05, 0.1]$  corresponding to random Gaussian error fluctuations from 1% to 10% of the mean temperature in the map. To imprint correlation structures into our error realisation we smooth over the map by convolving the error realisation with a Gaussian symmetric beam. By modifying the FWHM of the Gaussian beam we can produce error realisations which are correlated on a physical length scale measured in radians on the sky  $\theta_{\text{FWHM}}$ . We consider noise correlation scales corresponding to the full width half max (FWHM) of  $\theta_{\text{FWHM}} = [0, 1^\circ, 5^\circ, 10^\circ, \infty]$ . The extreme correlation scenarios  $\theta_{\text{FWHM}} \rightarrow \infty$  and  $\theta_{\text{FWHM}} \rightarrow 0$  corresponds to a uniform offset in the map and uncorrelated random Gaussian noise respectively.

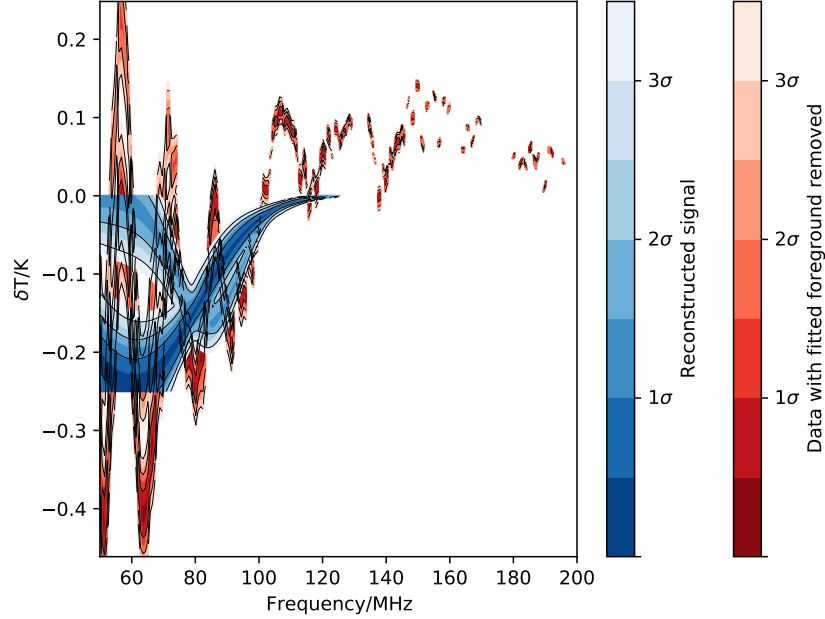


**Figure 6.4:** Signal recovery plot for the heteroscedastic error realisation with  $\Delta = 5\%$  and  $\theta_{\text{FWHM}} = 1^\circ$ . The systematic produced by the errors in the basemap prevent the model from passing the null test described in Section 6.3.1

In the left panel of Figure 6.3 we summarize the results for error Scenario 1. In each noise scenario we indicate whether the error scenario has passed or failed the null test according to our criteria above. We find that uncorrelated Gaussian errors with fluctuations up to 5% the mean temperature of the map do not produce significant enough systematics for our analysis to fail the null test described in Section 6.3.1. As we progressively increase the smoothing scale of the errors from  $\theta = 0$  to  $\theta = 10^\circ$ , we find that the amplitude of systematics introduced into the data increases. In the limit that the errors are smoothed with  $\theta_{\text{FWHM}} \rightarrow \infty$  (i.e. a uniform offset) then even errors at 1% produce a sufficiently large systematic for the null test to fail for the 25mK noise level in the data considered here.

In Scenario 2 we consider the heteroscedastic version of Scenario 1 in which the random Gaussian noise have spatially dependent fluctuations, i.e.  $\sigma_{\text{noise}}$  acquires a spatial dependence. We again produce a range of error scenarios with temperature fluctuations  $\sigma_{\text{noise}} = \Delta \cdot \delta T_{\text{sky}}(\theta, \phi)$  where  $T_{\text{sky}}(\theta, \phi)$  is the temperature of the Haslam at location  $\theta, \phi$  on the sky and  $\Delta$  is a unitless parameter which obtains the same values as Scenario 1. For each value of  $\sigma_{\text{noise}}$  we progressively smooth the

map by convolving the errors with a Gaussian beam with FWHM  $\theta_{\text{FWHM}} = [0, 1^\circ, 5^\circ, 10^\circ, \infty]$ . On the right panel of Figure 6.3 we summarize the results of these tests. Qualitatively, we find that increasing the amplitude of the error fluctuations  $\Delta$  or the correlation length  $\theta_{\text{FWHM}}$  of the errors produce larger systematics in the analysis. Quantitatively, we find that the systematic created by the heteroskedastic noise realization with amplitude  $\Delta > 5\%$  and correlation length  $\theta_{\text{FWHM}} \geq 1^\circ$  is large enough prevent recovery of the 21-cm signal. In Figure 6.4 we show an example systematic created by the scenario  $\Delta = 5\%$ ,  $\theta_{\text{FWHM}} = 1^\circ$ . For fixed  $\Delta$ , increasing  $\theta_{\text{FWHM}}$  increases the likelihood that the null test fails. When  $\theta_{\text{FWHM}} \geq 1^\circ$ , all error scenarios lead to systematics such that the null test outlined in Section 6.3.1 are not passed. The largest systematics are caused by scenarios with  $\theta_{\text{FWHM}} = \infty$  and  $\Delta = 10\%$ . We further test this error scenario with longer observation settings (6hr integration time) as well as observation times where the galactic plane is predominantly below the horizon. The systematics caused by this type of error scenario are present in all observation configurations but are lower for longer integration times and when the galaxy is below the horizon.

We consider the errors generated in scenario 2 to be most realistic, i.e. we make the assumption that the fluctuations of the errors depend on the local temperature. We also assume that the errors have structure with some unknown correlation length  $\theta_{\text{FWHM}}$ . In the following section we build on the intuition developed in this section and introduce our fiducial error scenarios used in our analysis.

### 6.3.3 Fiducial Error Models

In the absence of an error structure for the radio foreground basemap, we need to construct our estimate for a realistic error scenario. Our construction of the errormap is motivated by the expectation that the errors likely have spatial structure, i.e. they are not entirely uncorrelated, and that the magnitude of the errors is proportional to the absolute temperature of the basemap. Thus our expectation is that the error fluctuations are largest in the galactic plane, where the temperature is the largest. We also expect the map to have an offset of 3 K [50]. We do not expect our error

### Absolute Errors [408MHz]

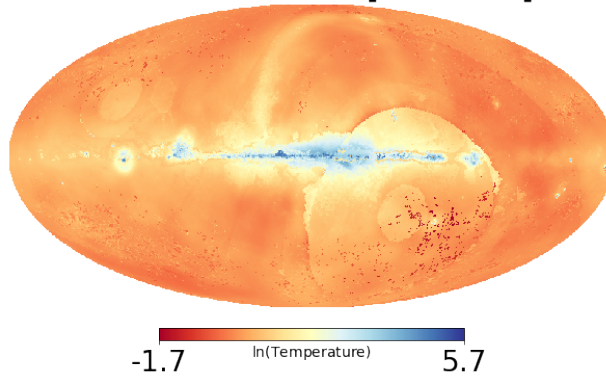


**Figure 6.5:** Absolute errors in the temperature of the sky at 408MHz. Note that the errors roughly trace the galactic morphology. Also apparent are that many low frequency survey data are missing the southern pole which influences the eGSM model in this region.

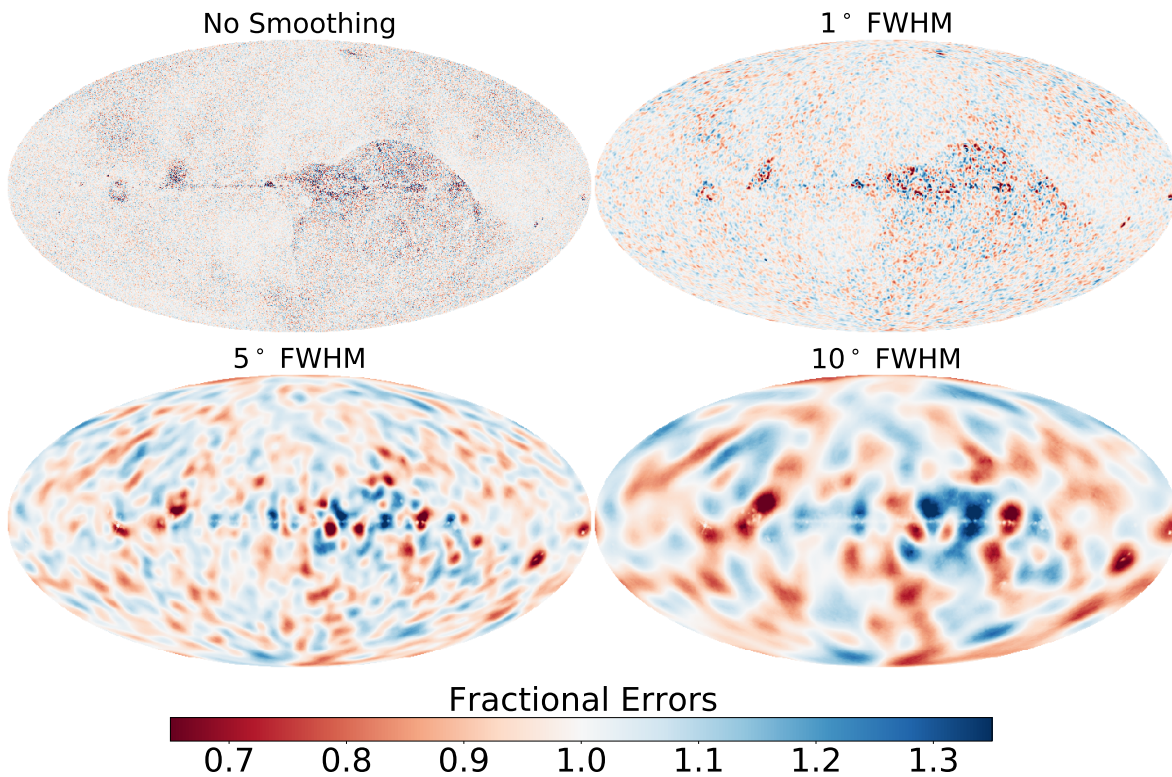


**Figure 6.6:** In this figure we show our fiducial error scenarios at 408MHz. In the top left we show the a heteroskedatic error realization generated by drawing values from a Gaussian distribution of zero mean and standard deviation proportional to the absolute errors at 408MHz. Moving clockwise from the top left panel, the resulting error realisation is smoothed by a Gaussian beam of FWHM equal to 1° (top right), 5° (bottom left), and 10° (bottom right).

realization to exactly match reality, however we use it as our fiducial error realisation to study the effect that such noise scenarios have on our data analysis pipeline.

We now discuss our procedure to generate our error realization. This is a two step process, the first step is to construct the spatial error fluctuations while the second step is to adjust the mean of the map to 3 K. To construct the spatial error fluctuations via a Gaussian generated heteroskedastic errormap with amplitude proportional to the temperature at each location in the sky, we use the extended Global Sky Model (eGSM). Specifically we use the eGSM absolute errors of the 408MHz Haslam map derived from Kim et al. (in prep) which we show in Figure 6.5. The eGSM is a data-driven model similar in spirit to previous global sky models published by [15] and [66], in that it takes empirical data from multiple surveys and interpolates over gaps in frequency and sky coverage using dimensional reduction methods such as principal component analyses. Importantly, the eGSM includes the Monte Carlo propagation of measurement errors in the input surveys through the interpolation process. Admittedly, the final error bars are only rough estimates given that many of the input surveys do not come with published uncertainties, thus making it necessary to simply *assume*  $\sim 10\%$  errors in some input maps. Nonetheless, Figure 6.5 likely captures some of the spatial patterns in the errors of typical sky models and is therefore sufficient for substantiating at least the qualitative lessons of this paper.

To go from the map of error bars in Figure 6.5 to an error *realization*, we first draw a noise realization from the absolute error map at 408MHz. To do this, at each pixel in the basemap we draw a random value from a Gaussian distribution with mean  $\mu = 0$  and standard deviation  $\sigma_{\text{pixel}}$  proportional to the value of the absolute error in that pixel. This produces a heteroscedastic noise realisation of zero mean and with error fluctuations proportional to the absolute errors at 408MHz. The fractional error fluctuations in our noise realization are largest in the galactic plane and smaller away from the galactic center. In the upper left of Figure 6.6 we show the resulting errormap. Note the statistical anisotropies in the southern pole (lower right portion of the basemap). Many low frequency survey data are missing the southern pole which influences the eGSM model in this region. In practice, with particularly poor empirical constraints in those parts of the sky, it would be sensible for experiments to avoid those regions. We select our observation time such that these

regions are below the horizon at the time of observation. We chose to set our observation starting at 6pm on 2021-01-01. Unless otherwise stated, we use this observation time for the remainder of our analysis.

To implement correlations into our noise realization we smooth the map by convolving our noise realization with a Gaussian beam of FWHM of  $\theta_{\text{FWHM}}$ . Since we do not know the true correlation structure of the errors, we consider multiple smoothing scales chosen to encompass a range of physical scenarios. We use  $\theta_{\text{FWHM}} = [1^\circ, 5^\circ, 10^\circ]$ . These correlation scales are chosen to roughly correspond to the resolutions in the 150MHz and 408MHz empirical foregrounds maps from [32, 50] which are approximately  $1^\circ$  and  $5^\circ$  FWHM respectively. We make the assumption that the correlation lengths of the error features roughly match the resolutions of these maps. Convolving our error realisation with a Gaussian beam reduces the total spatial power in the map. We wish to preserve the total power in the map. To quantify how the total power in the map is affected we first express the original (pre-smoothed) error map in spherical harmonics

$$Y_{lm} = \sqrt{\frac{2l+1}{4\pi} \frac{(l-m)!}{(l+m)!}} P_l^m(\cos(\theta)) e^{im\phi} \quad (6.14)$$

where the indicies  $l = 0, \dots, \infty$  are referred to the multipole which represent the angular scale on the sky, and  $-l \leq m \leq +l$ . The  $P_l^m$  are the associated Legendre Polynomials. We can expand the map using

$$\Theta(\hat{n}) = \sum_{l=0}^{\infty} \sum_{m=-l}^{m=+l} a_{lm} Y_{lm}(\hat{n}) \quad (6.15)$$

where

$$a_{lm} = \int \int \Theta(\hat{n}) Y_{lm}^*(\hat{n}) d\Omega. \quad (6.16)$$

We can define the power spectrum  $C_\ell$  of the temperature fluctuations in the map which is the variance of the harmonic coefficients:

$$\langle a_{lm} a_{l'm'}^* \rangle = \delta_{ll'} \delta_{mm'} C_l \quad (6.17)$$

where the angular brackets represent an ensemble average taken over many independent realizations in the map. If we perform the average over different  $m$  modes we can write the angular power spectrum  $C_l$  as

$$C_l = \frac{1}{2l+1} \sum_{m=-l}^{m=l} \langle |a_{lm}|^2 \rangle. \quad (6.18)$$

The total power  $\sum_l^{l_{\max}} C_l$  (where the  $C_l$  are given by Equation 6.18) of the smoothed error map will have decreased power relative to the original (before the convolution). This decrease in total power will result in dampening the error fluctuations, thereby reducing the amplitude of the errors relative to our original noise realization. To correct for the decrease in total angular power of the map and conserve the power of the error fluctuations, we scale the coefficients by  $\sqrt{\sum_l C_{l_0} / \sum_l C_{l_{\text{smooth}}}}$  where  $\sum_l C_{l_0}$  is the total power of the error realisation before the smoothing process and  $\sum_l C_{l_{\text{smooth}}}$  is the total power of the map after smoothing. We then compute the inverse transform of Equation 6.16 to return to configuration space. We then re-adjust the mean by adding a uniform offset of 3 K chosen to match the zero level offset in [50]. We do not expect this error realization to exactly match reality, however we use it as our fiducial error realisation to study its effect on our data analysis pipeline. Note that our framework is applicable to any error scenario. Thus the effectiveness of our framework to precisely recover the 21-cm signal as shown in Section 6.6 are not motivated by our specific choice for the noise realization.

## 6.4 Modeling Amplitude Perturbations in Our Foreground Model

Our foreground model described in Section 6.6 relies on radio sky maps to construct our basemap. Since these radio sky maps are derived from measurements with no detailed error maps, the true amplitude of the radio sky will deviate from that of our foreground basemap by an amount that, given current uncertainties on low frequency sky maps, will (almost) certainly preclude unbiased recovery of the 21 cm signal within a forward modelling analysis of the type described in Section 6.2.2. To account for these temperature fluctuations relative to our model, as well as any global temperature offsets in our map, we introduce a new foreground model, with amplitude

correction factors (amplitude scale factors). Along with a linear offset term, we show that our model can account for these observational uncertainties. In this section we introduce our amplitude scale factor model and discuss our optimization procedure, as well as possible limitations of our framework.

### 6.4.1 Amplitude Scale Factors

In this section we introduce our amplitude scale factor model. Our approach is analogous to the framework discussed in Section 6.2.2, but now applied to fitting for the true base-map in place of the spectral structure on the sky. To implement amplitude correction factors scale factors into our foreground model, we split the foreground basemap into  $N_a$  subregions, with each region having an associated multiplicative scale factor  $a_i$  that adjusts the temperature in the foreground basemap for that subregion. Our updated foreground model, including these amplitude scale factors, is given by,  $T_{\text{FG}}(\theta, \phi, \nu) = \sum_i^{N_a} \sum_j^{N_\beta} [a_i M_{a,i}(\theta, \phi) M_{\beta,j}(\theta, \phi) (T_{\text{base}}(\theta, \phi, \nu_0) - T_\gamma) + \gamma_{\text{offset}}] (\nu/\nu_0)^{-\beta_j}$  where  $M_{a,i}(\theta, \phi)$  are masks applied to the foreground basemap which take on the value of 1 or 0 depending on whether a pixel is part of the  $i$ th scale factor region or not. All pixels in the map comprising a scale factor region are then multiplied by  $a_i$ . Thus any amplitude perturbations in the data relative to the foreground basemap can be adjusted for by scaling the model in that region by  $a_i$ . Similarly  $N_\beta$  are the number of spectral regions and  $M_{\beta,j}(\theta, \phi)$  are the associated masks for the spectral regions (as discussed in Section 6.2.2), where  $\beta_j$  are the associated spectral values for that spectral subregion. The term  $\gamma_{\text{offset}}$  is a constant term added to the foreground model to adjust for any temperature offsets in the basemap relative to the data <sup>3</sup>. Note that an error scenario consisting only of a uniform offset corresponds to the errors in the rightmost columns in the left and right panels of Figure 6.3.

The value of the amplitude scale factor  $a_i$ , in each subregion is adjusted along with the offset  $\gamma$ ,  $N_\beta$  parameters and 21-cm signal parameters using the Bayesian inference framework described in Section 6.2.1 using the likelihood in Equation 6.12, with  $T_{\text{model}}$  now referring to our modified

---

<sup>3</sup>In principle, an temperature offset in the model basemap relative to the data can also be fit for using only the amplitude scale factors. However it is computationally simpler and conceptually more intuitive to separate these effects with the inclusion of a linear offset term  $\gamma_{\text{offset}}$

foreground model (i.e. Equation 6.4.1). To determine the optimal number of regions  $N_a$  required to fit the data, we perform the inference analysis described in Section 6.2.1 for a range of models with different  $N_a$ . For each model we compute the Bayesian Evidence described in Section 6.2.1. The suitable number of regions to split the prior map into is then determined post analysis by selecting the value of  $N_a$  and  $N_\beta$  that maximizes the Bayesian Evidence. The Bayesian Evidence is penalized when additional complexity is added without substantially improving the fit. Determining  $N_a$  and  $N_\beta$  using his method also allows us to avoid using more amplitude scale factors than are required to fit the data and thus prevents an overfitting scenario. For other applications of this methodology in the field of 21-cm cosmology the reader is encouraged to see e.g. [41, 54–56].

## 6.4.2 Prior Maps & Limitations

In the previous section we introduced a foreground model which has the flexibility to account for multiplicative errors in the true temperature of the foregrounds relative to our model. In this section we discuss the importance of an appropriate error prior map to define the number of regions. To define the regions on the sky we require a map which describes the spatial arrangement and amplitude of the errors. This map essentially acts a prior on the amplitude scale factors and thus we refer to the map used to define the regions as the “error prior map”. To construct the regions we bin the pixels of the error prior map into  $N_a$  segments, where  $N_a$  are the number of amplitude scale factors. The boundaries of the  $i$ th bin is determined by computing the temperature corresponding to the  $100i/N_a$  percentile in error, where the width of each bin is  $100/N_a$ . Therefore the  $i$ th bin corresponds to pixels in the map lying between the  $100(i-1)/N_a$  and  $100i/N_a$  percentile. The pixels in each bin are then mapped to their corresponding locations on the sky. Note that this procedure can be applied using any map and thus in principle any map can be used to define the  $N_a$  sub-regions. However since the scale factors are temperature multiplicative factors, grouping regions of the sky with similar temperature perturbations increases the effectiveness of the amplitude scale factors within this framework. In Section 6.5.2 we show that having  $N_a$  sub-regions to coincide with the true fractional errors in the foreground map optimizes this approach by both reducing the number of regions and improving the fits. Thus using our best estimate of the foreground errors as our

error prior is an important step in our procedure. We then proceed in our analysis by presenting two scenarios which act as limiting cases. In a conservative approach we use the 408MHz Haslam basemap to define the regions. In the right column of Figure 6.2 we show example regions using the Haslam basemap. The upper right panel corresponds to  $N_a = 4$  while the lower right column corresponds to  $N_a = 8$ . Using this map as our prior map is conservative since the morphology of the absolute error map roughly follows the galactic structure and so represents a scenario where we haven't included any additional information in our framework regarding the errors. In our second scenario, we consider the limiting case of having perfect knowledge of the spatial structure (but not necessarily amplitude) of the errors in the sky model. For this, we use the true fractional error map to define the region defined as

$$f(\theta, \phi) = \frac{T_{\text{base}}(\theta, \phi) + \varepsilon(\theta, \phi)}{T_{\text{base}}(\theta, \phi)} \quad (6.19)$$

where  $T_{\text{base}}$  refers to the unperturbed basemap and  $\varepsilon$  refers to error realisation contained in the basemap. Information on the per-pixel covariances in the eGSM map may be available in the future and thus would inform our models regarding the correlation structure of the errors. For now, we use this perfect prior map to illustrate the best-case scenario for the performance of this approach. Unless otherwise mentioned we define the  $N_a$  scale factor regions using Haslam basemap from [50].

In the previous section we discussed how the Bayesian Evidence can be used to determine the optimal number of regions. One limitation in using this framework to define the regions is that adjacent  $N_a$  models are not subsets of another another, i.e. a model with  $N_a$  regions is not a subset of a foreground model with  $N_a + 1$  regions. As a result increasing the complexity of the foregrounds models by increasing  $N_a$  do not build on top of another one; instead, each model is an entirely new reconfiguration of regions<sup>4</sup>. This impacts how the Bayesian Evidence of each model depends on  $N_a$ . In general one would expect that as a more parameters are added to the model, the fit of the model to data should improve, thereby increasing the Bayesian up until the additional complexity is no longer required to describe the data, at which point the Bayesian Evidence decreases with

---

<sup>4</sup>Due the percentile splitting, the  $n^{2m}$ th, (where  $m = 0, 1, 2..$ ) regions are all subsets of one another.

$N_a$ . Since, for most values of  $N_a$  the amplitude scale factor regions are not nested, we no longer expect a strict monotonic increase of the Bayesian Evidence as a function of  $N_a$ . This effect will be more pronounced when the error prior map used to define the regions do not coincide with the true temperature perturbations errors in the data. In this scenarios the placement of the regions with respect to the true fractional errors are suboptimal and so there will be certain models with the scale factor regions that are, by chance, better aligned with the true errors. In contrast, in the perfect error structure information scenario the region placement is already aligned with the errors in the map and so the variation in  $\ln(Z)$  from model to model is smaller. Moving forward we denote the scenario as having an ideal prior map.

### 6.4.3 Map Reconstruction

Outside of the context of a global 21-cm signal experiment, one may use this approach to recover a model map of the radio sky without the error perturbations, i.e. performing foreground map reconstruction. To do this one uses the mean posterior model map as the best-fitting model of the sky as seen by the instrument. However using this framework for map construction should be used with discretion. As discussed in Section 6.4, the mean temperature on the sky is the key metric of our model which is being compared to the dataset within our Bayesian inference framework. As a result our inference framework finds the optimally fitting values of  $a_i$  in each sub-region of our foreground model such that the mean temperature of the sky in our model fits the mean temperature of the simulated dataset. Therefore one finds that the optimal value of  $a_i$  in the  $i$ th sub-region is spatially averaged value of all the amplitude perturbations within the  $i$ th sub-region. However because each sub region will contain a distribution of temperature perturbations, and only the mean of  $a_i$  is chosen, the boundaries between adjacent sub-regions will be disjointed. Our framework thus only adjusts the mean in each region, which does not prioritize the smoothing between boundaries of regions. Additional operations would be required to smooth out the map. However increasing the number of scale factor regions  $N_a$  will create a smoother interface at the boundaries improving, the model reconstruction.

The performance of map reconstruction is also dependent on the error prior map used to define the scale factor sub-regions. Using the true fractional error map will decrease the disjointedness at the boundary between regions and increase the performance of the map reconstruction. This is because any region defined using the true fractional errors contained in the data will have a smaller range of amplitude perturbations contained in that region and therefore create a more seamless transition across the boundary. Note that disjointed boundaries between regions do not impact the performance of our framework or cause any systematics in our analysis because the temperature of each sub-region in the sky are summed according to Equation 6.4.1 without any data analysis procedure operating on the boundaries.

## 6.5 Isolated Amplitude Errors

In this section we use our foreground model to fit a dataset which was constructed using a basemap containing the error realizations derived in Section 6.3.3. A 21-cm signal is included in the dataset using Equation 6.7 with amplitude, standard deviation and centering frequency  $A_{21} = 0.155\text{K}$ ,  $\sigma_{21} = 15\text{MHz}$ , and  $\nu_{21} = 85\text{MHz}$  respectively. We make the simplifying assumption that there is no spatial dependence to the spectral index. We fix  $\beta = 2.7$  in the simulated dataset as well as in the foreground model used to fit the dataset. We therefore isolate the effect that amplitude perturbations have on the analysis without the effect of spectral errors. We consider the case of spatially varying spectral index in the following sections. In Section 6.5.1 we apply our amplitude scale factor framework to a single error scenario from Section 6.3.3 to highlight the general trends between the number of amplitude scale factor regions and the Bayesian Evidence. We compute optimal number of regions to describe the simulated dataset and show the recovered 21-cm signal for that model. In Section 6.5.1 we then show how the optimal number of amplitude scale factors changes with the error properties in Section 6.3.3. In Section 6.5.3 we discuss the effect that using the true fractional error map discussed in Section 6.4.2 as a prior map to define the  $N_a$  regions has on the analysis.

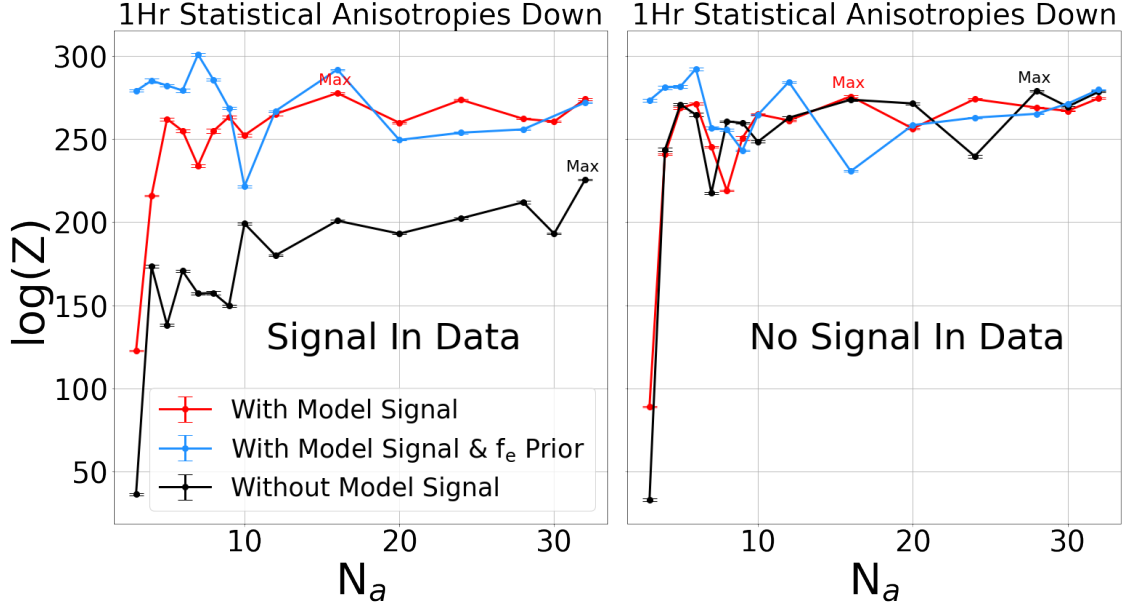


**Figure 6.7:** The Bayesian evidence,  $\ln(Z)$ , as a function of the number of amplitude scale factor regions  $N_a$ . The black curve indicates a scenario where no 21-cm signal is included into the sky model while the red curves indicates sky models when a 21-cm signal is included. Left panel: 21-cm signal is included into the dataset. We see that a 21-cm signal model component is preferred since the maximum value of  $\ln(Z)$  originated from the red curve. Right panel: no 21-cm signal is included in the dataset, in which case a sky model without a 21-cm signal component is preferred since the maximum value of  $\ln(Z)$  occurs in the black curve. The blue curves corresponds to a model where the fractional error map (see Equation 5.17) is used to define the regions. Note that the observation times in this simulation correspond to a one hour duration occurring at a time where the statistical anisotropies in Figure 6.6 in are mostly below the horizon.

### 6.5.1 Spectrally Uniform

In the previous section we introduced our amplitude scale factor framework. In this section we select one error scenario from Section 6.3.3 to highlight our model and illustrate the general trends of the number of scale factors  $N_a$  and the Bayesian evidence. In the following section we apply our framework to all error scenarios introduced in Section 6.3.3. In Figure 6.7 we show the Bayesian evidence as a function of  $N_a$  for  $\Delta = 6\%$  and  $\theta_{\text{FWHM}} = 1^\circ$ . On the left panel 21-cm signal is included in the dataset while on the right panel no 21-cm signal is included in the dataset. For each case, the dataset is fit with a foreground model that has  $N_a$  amplitude scale factors, one offset

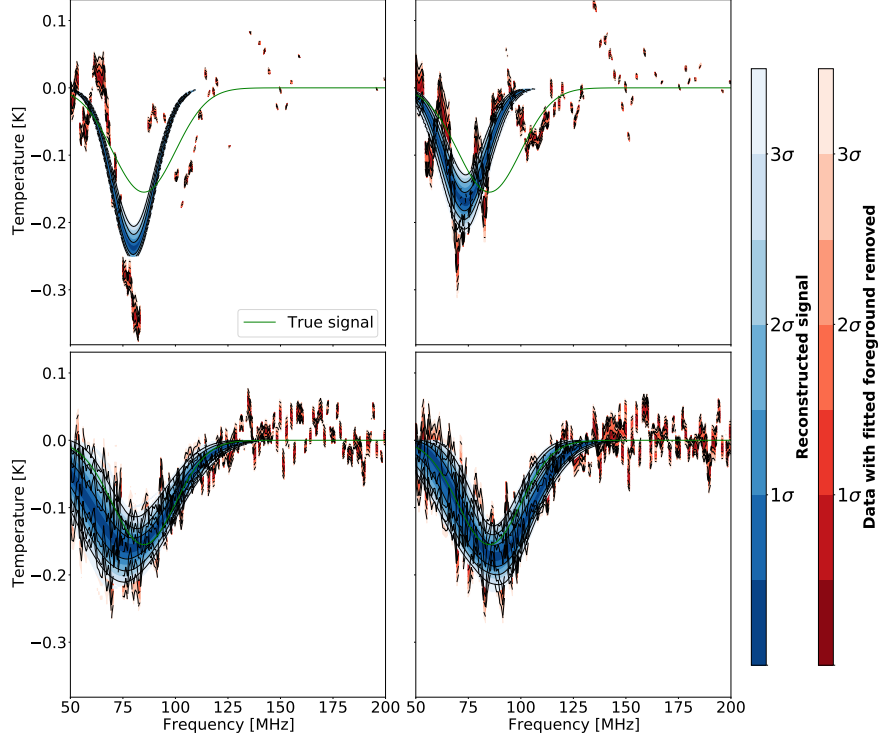


**Figure 6.8:** Each plot shows the results of fitting our foreground model to the simulated data discussed in Section 6.5.1. The upper left panel corresponds to  $N_a = 1$ . Moving clockwise, we have models  $N_a = 3, 16, 32$ . The blue curves corresponds to the fitted 21-cm signal while the red curves correspond to the residuals of the dataset after the fitted foregrounds are removed.

parameter  $\gamma$  and either a signal model (red curves) or no signal model (black curve). Starting from  $N_a = 1$  in the left panel, we can see that as more degrees of freedom are added to the model,  $\ln(Z)$  increases rapidly until where we see that  $N_a = 16$  maximizes the Bayesian Evidence. The residuals for  $N_a = 1$  and  $N_a = 16$  are shown in the first column of Figure 6.8. From this figure, we can see that the systematic created by the amplitude perturbations are substantially reduced as we increase the number of scale factors. Since one scale factor is equivalent to adjusting the mean of the foreground map, this result implies that the presence of the spatial fluctuations of the foreground errors about the mean of the error map also contribute to the bias in the signal recovery within the analysis. Our amplitude scale factor framework can accommodate these fluctuations with more precision by adding more regions to the foreground model. Thus the size of the regions shrink and can begin to accommodate smaller features in the error map. In Figure 6.8 we show the residuals

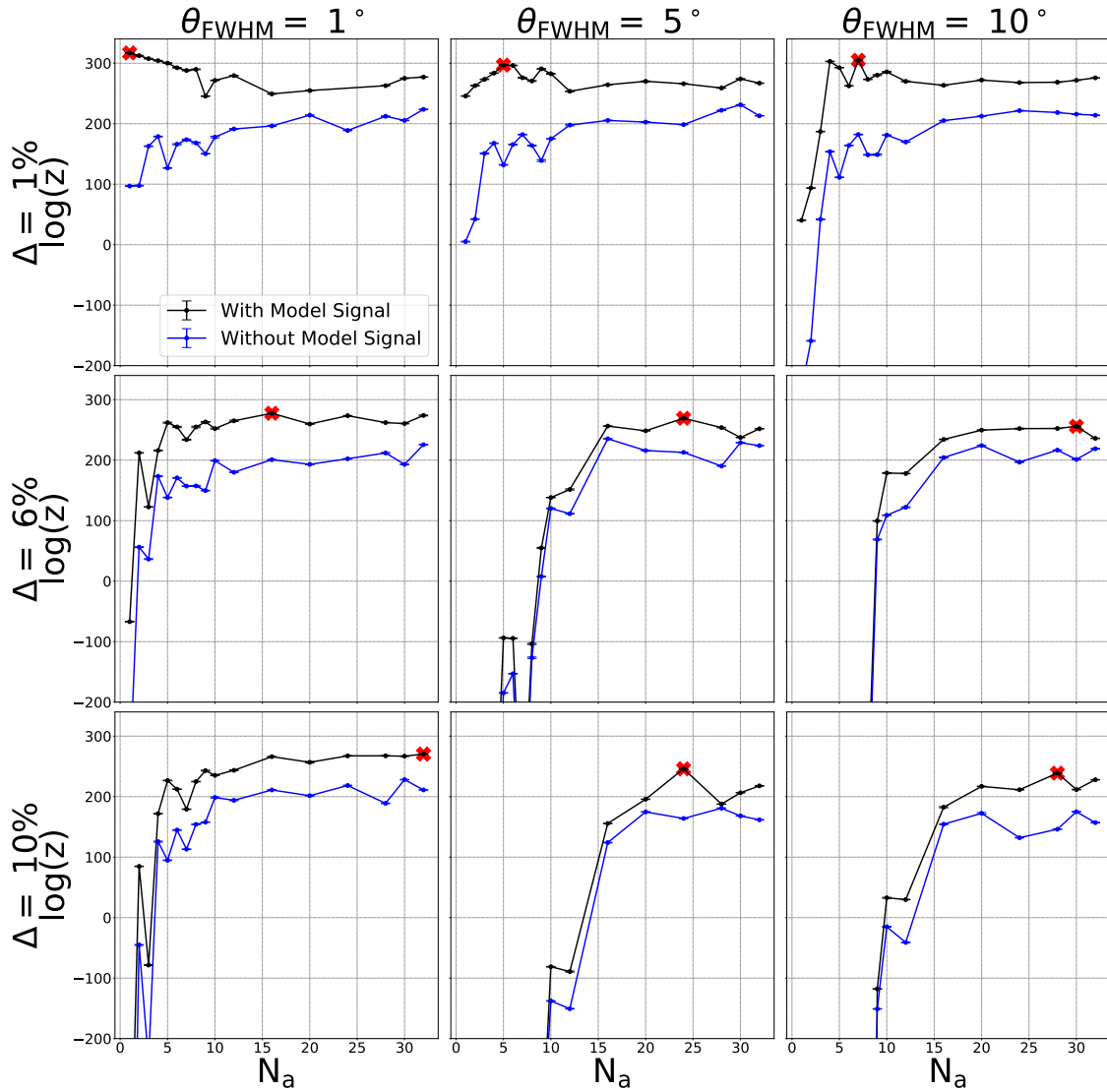


**Figure 6.9:** The Bayesian evidence,  $\ln(Z)$ , as a function of the number of amplitude scale factor regions  $N_a$  for each error scenario described in Section 6.3.3. The black curve indicates a scenario where a 21-cm signal is included into the sky model while the red curves indicates sky models where no 21-cm signal is included. Note that 21-cm signal is included into the dataset leading to black curves having larger  $\ln(Z)$  than the blue curves. Also clear are the the number of amplitude scale factor regions required to maximize  $\ln(Z)$  increases with error fluctuation amplitude  $\Delta$  and correlation length  $\theta_{\text{FWHM}}$ .

for the  $N_a = 3$  model (first row, second column) and see that the bias in the signal recovery has shrunk relative to the  $N_a = 1$  model (first row, first column). In the lower left of Figure 6.8 we show the residuals for the model which maximizes the Bayesian evidence ( $N_a = 16$ ). In this case the amplitude, central frequency and standard deviation of the reconstructed signal are consistent with the true values at  $1\sigma$ . Referring back to Figure 6.9 we see that as we continue increase the regions beyond  $N_a = 16$  the Bayesian Evidence slowly decreases. In the lower right panel of Figure 6.8 we show the residuals for the  $N_a = 32$ . The amplitude and standard deviation of the systematics have decreased further; however, the additional flexibility added to the system beyond  $N_a = 16$  is not required to fit the data, and as a result there is a statistical cost to adding more parameters. This is due to Equation 6.3, whereby we can see that adding additional parameters increases the prior volume which penalizes the Bayesian evidence.

## 6.5.2 Effect of the Amplitude of Fluctuations $\Delta$ and Correlation Length $\theta_{\text{FWHM}}$ of the Errors on the Analysis

In Section 6.3.3 we introduced our fiducial foreground error model, which was parametrized in terms of the amplitude of the fluctuations  $\Delta$ , and the FWHM of correlated features  $\theta_{\text{FWHM}}$ . In this Section we apply our amplitude scale factor foreground model described in section 6.4.1 to a dataset constructed using a foreground map which contains these fiducial error scenarios. In Figure 6.9 we show the Bayesian Evidence for each scenario. We see that the number of amplitude scale factor regions required to maximize the Bayesian Evidence depends on the level of the fluctuations  $\Delta$  and  $\theta_{\text{FWHM}}$  of the error realisation in the datasets. From Figure 6.9 it is evident that for fixed  $\theta_{\text{FWHM}}$ , increasing  $\Delta$  of the errors in the dataset increases the optimal number of amplitude scale factors required to fit the data. This is an expected result. Consider a foreground model with  $N_a$  scale factors regions. Any systematics remaining in the analysis are due to small fractional differences in temperature of the foreground dataset relative to the foreground model. Thus uniformly increasing the mean fractional differences of the entire foreground map used to construct the dataset relative to the basemap will scale any systematics remaining in the analysis. Thus scaling the temperature

fluctuations will require more precision in the foreground model to reduce the systematic. This trend is independent of how the scale factor regions are defined. This behaviour is independent of the prior map used to define the regions.

It is also clear from Figure 6.9 that increasing the FWHM of the error structures results in requiring more scale factors to maximize the Bayesian evidence. To understand this, consider a region of the sky containing many small correlation structures such as in Figure 6.6. This leads to a scenario where many independent error realisations can be contained within a region and thus tend to average out, i.e. the noise is driven to Gaussian random noise. However as the FWHM of the correlation structures increases, a single error feature may overlap into multiple regions, thus requiring more regions to isolate and localize independent error realisation features.

Note that we do not consider multiple values of global temperature offsets in the foreground errors since the linear offset term  $\gamma$  in Equation 6.4.1 allows our model to be robust these scenarios. Thus our model allows the analysis of an error scenario with offset 3K to be equivalent to one with 0K offset.

### 6.5.3 Limiting Cases

In the previous sections, we used the 408MHz Haslam basemap to define the scale factor regions. The regions thus followed the Galactic morphology, which do not have a similar structure to true fractional errors in the basemap. In this section we illustrate the effect that using a suitable prior map to define the  $N_a$  regions has on the performance on our framework. We compute the fractional error map as defined by Equation 6.19 to define the  $N_a$  regions. These two scenarios effectively bracket extreme scenarios, i.e. a scenario where we know precisely the morphology of the amplitude perturbations and a scenario where we simply assume the errors follow the Galactic morphology. In the future information on the per-pixel covariances in the eGSM map may be available. For now, we use this perfect prior map to illustrate the best-case scenario for the performance of this approach.

In Figure 6.7 (blue curve), we show the the evolution of the Bayesian evidence as a function of  $N_a$  using regions derived from the absolute error maps and the ideal prior map for the error

scenario  $\Delta = 6\%$  and  $\theta_{\text{FWHM}} = 1^\circ$ . The behavior of the Bayesian evidence as a function of  $N_a$  using the ideal prior, or absolute errors to define the regions produce similar qualitative trends with two quantitative differences:

1. The Bayesian Evidence for the maximum evidence model is larger when using the fractional error map to define the regions
2. fewer regions are required for models using the fractional errors

These quantitative differences are due to the morphological differences between the absolute error map and the actual amplitude perturbations in the dataset. Since the fractional errors are better aligned with the true multiplicative errors in the map, the number of regions required to optimize the Bayesian Evidence is reduced from  $N_a = 16$  using the absolute error map to define the regions to  $N_a = 7$  using the fractional errors to define the regions. The maximum Bayesian Evidence is also larger using the fractional errors to define the regions. The blue curve on the right panel of Figure 6.7 shows the Bayesian evidence for a sky model without a model component and using the fractional errors to define the regions. Here we can see that this also results in reducing the number of scale factor regions required to maximize the Bayesian evidence from  $N_a = 28$  (black curve) to  $N_a = 6$  (blue curve).

We also find that the residuals are smaller and more “noise-like” when using the fractional error map to define the regions (as compared to using the Haslam map). When using the Haslam map as the prior, this is due to the amplitude scale factor regions not lining up properly with the true fractional errors in the map. As the result, each region defined using the Haslam basemap encompasses a larger distribution of fractional errors. As a result each region cannot capture the finer error features in the foreground error map. This also results in more regions being required to describe the error structure present. Therefore we continue to see a more substantive increase in the residuals between the reconstructed 21-cm signal and the true signal as we go to large  $N_a$  compared to what we saw for large  $N_a$  models in the fractional error prior (where the benefit to the fits were smaller).

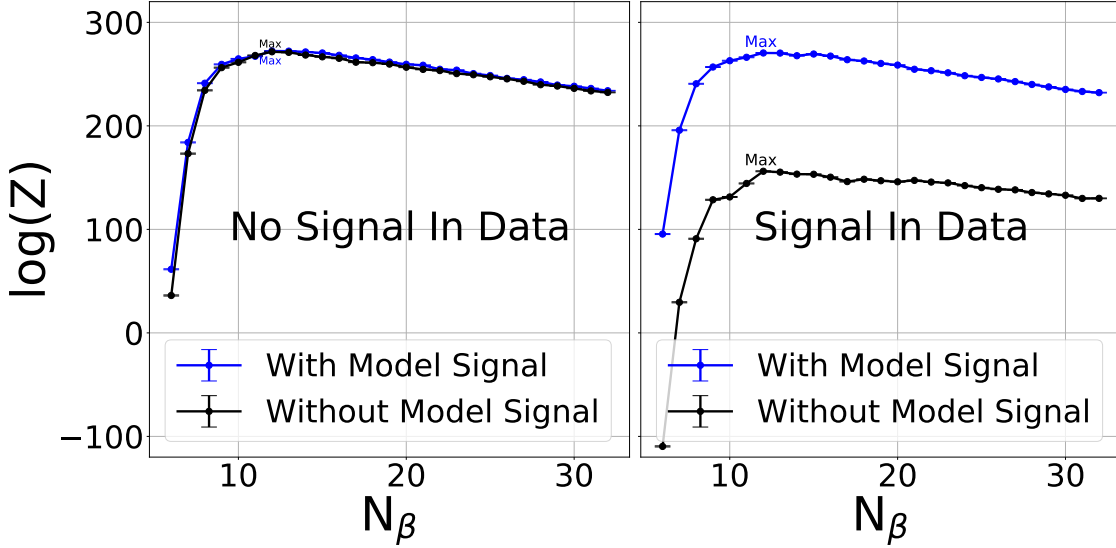


**Figure 6.10:** The Bayesian evidence as a function of the number of spectral parameters  $N_\beta$ . The black curve indicates a scenario where a 21-cm signal is included into the sky model while the red curves indicates sky models where no 21-cm signal is included. Left panel: no 21-cm signal is included into the dataset. We see that a 21-cm signal model component is preferred since the maximum value of  $\ln(Z)$  originated from the red curve. Right panel: a 21-cm signal is included in the dataset, in which case a sky model without a 21-cm signal component is preferred since the maximum value of  $\ln(Z)$  occurs in the black curve.

## 6.6 Spatially Varying Spectral Index

In this section we discuss our more realistic observation scenario, where the foregrounds in the simulated dataset have a spatially varying spectral index and foreground basemap errors. To simulate a realistic data analysis where we do not have access to the true fractional error, we use the 408MHz Haslam basemap to fit our simulated data. Thus we add the formalism introduced in [2] which was described in Section to our analysis. That is, we split the spectral map in Figure 6.1 into  $N_\beta$  sub regions each with uniform  $\beta$  in accordance with Equation 6.4.1. Since the spectral regions do not need to coincide the  $N_a$  amplitude scale factor regions, there are  $N_\beta \times N_a + 1$  parameters required to be optimized in the foreground model. We again use Polychord to compute the Bayesian Evidence for each model. In the interest of reducing computational cost, we use only one error



scenario from Section 6.5.2. In Section 6.6.1 we select our error realisation and in Section 6.6.2 we show our results.

### 6.6.1 Error Selection

In this section we select the most realistic error scenario from Section 6.3.3. To do so, note that we expect that the correlation length of the errors in the basemap will be inversely proportional to its resolution. Since in this work we use the Haslam map to construct our foreground model, we select the correlation length of our fiducial error scenario to match the  $1^\circ$  FWHM resolution of the Haslam map. We therefore use the  $\Delta = 6\%$ ,  $\theta_{\max} = 5^\circ$  scenario from Section 6.5.2.

Furthermore, since the resolution of the basemap is related to its base frequency, maps at lower frequency, will have lower spatial resolution. For example the 150MHz empirically derived map introduced in [32] has a  $5^\circ$  FWHM resolution compared to  $1^\circ$  for Haslam at 408MHz. Under this assumption, we would expect more correlated errors in the Landecker map. For a fixed level of power of errors in the map, we would expect this increased correlation to introduce more significant foreground systematics and, correspondingly, larger biases in the recovered 21-cm signal, in the absence of error modelling. In the context of the sky map error fitting formalism we present in this paper, we would expect a more complex error model to be required to explain the data when using the Landecker map as our base-map in an analysis of instrumental data.<sup>5</sup> Recall from Section 6.3.2 that increasing the FWHM of the errors results in requiring more amplitude scale factor regions to maximize the Bayesian Evidence. Provided there is a negligible change to the morphology of foregrounds as a function of frequency, one can strategically use higher frequency basemaps in the foreground model to reduce the systematic impact of foreground amplitude errors in the analysis. However, increasing the base frequency of the foreground basemap might also increase the number of spectral regions  $N_\beta$  required to model the spatial variation of the spectral index. To see why this is recall that the REACH observational frequencies range from 50MHz to 200MHz. Using a basemap at higher frequencies, i.e. Haslman at 408MHz requires more spectral precision in the

---

<sup>5</sup>This assumes that the error structure follows the Gaussian generated errors discussed in Section 6.3.2

foreground model since the spectral model is extrapolated over a larger frequency range. Thus more spectral regions  $N_\beta$  are required relative to using a basemap set at lower frequencies.

### 6.6.2 Correlations Between $N_a$ and $N_\beta$

The datasets we consider in this section contains spectral complexity as well as errors in the amplitude component of the basemap. Thus to select the model which maximizes the Bayesian evidence, we must optimize  $N_a$  and  $N_\beta$  in a two dimensional grid of models. From Section 6.5.1 we know that without spectral errors,  $N_a = 16$  maximizes the Bayesian evidence. To gain intuition regarding how many spectral parameters might be required to sufficiently describe the spectral component of the dataset without the presence of amplitude scale factors in the basemap, we can perform the same analysis shown in Figure 10 of [2]. Note that the analysis procedures in our work has two modifications as compared to the analysis done in [2]. The primary difference is that we use the percentile splitting methodology discussed in Section 6.4.1 to define the spectral regions. Secondly we construct our foreground model using the Haslam basemap (at 408MHz) rather than GSM (at 230MHz). For completeness we perform the analysis for datasets which contain, and do not contain, a 21-cm signal. In Figure 6.10 we show the the Bayesian evidence as as a function of the number of spectral parameters  $N_\beta$  when the sky signal (i.e. the simulated dataset) does not contain a 21-cm signal (left) or contains a 21-cm signal (right). The blue curves correspond to a sky model that contains a 21-cm signal component while a black curve does not. Note that in the left panel, the highest evidence models occur in the black curve while on the right panel the blue curves corresponds to models with higher Bayesian evidence. In the left panel (without 21-cm signal in the dataset) we see that the model  $N_\beta = 10$  maximizes the Bayesian evidence while on the right panel (with 21-cm signal in the dataset) we see that model  $N_\beta = 12$  maximizes the Bayesian evidence.

The simulation we consider in this section has spectral errors in addition to basemap errors. To get a sense as to where the Bayesian Evidence maximizing model might reside on a two dimensional grid of  $N_\beta$  and  $N_a$  models, recall that in Figure 6.7 we found that  $N_a = 16$  regions was such that the maximized the Bayesian evidence without the presence of spectral complexity in the dataset.

Similarly in Figure 6.10 we see that the model  $N_\beta = 12$  maximizes the Bayesian evidence when the dataset does not contain amplitude errors. Thus we would expect that  $N_a \leq 16$  and  $N_\beta \leq 12$  might maximize the Bayesian evidence. The “ $\leq$ ” is used instead of “ $=$ ” since we allow for the possibility that  $N_a$  and  $N_\beta$  might have some correlation.

In Figure 6.11 we show the Bayesian evidence as a function of the number of amplitude scale factor regions,  $N_a$ , and spectral regions  $N_\beta$  used to construct the foreground model. The brightest regions of the grid correspond to models with the largest Bayesian Evidence. In each square we denote the difference in  $\ln(Z)$  between that particular model and the model which maximizes the Bayesian evidence. Qualitatively we see that the Bayesian evidence is highest along a diagonal strip of models affirming that there is a degree of correlation between models with  $N_a$  and  $N_{\text{beta}}$ . Model  $N_a = 8, N_\beta = 7$  maximizes the Bayesian evidence, and is indicated with a 0 on its grid-point square. If multiple models have comparable Bayesian evidences, then a model averaging technique, where a weighted average is formed using their evidences should be employed. In terms of Figure 6.11, the model with the next highest evidence is model  $N_a = 7, N_\beta = 12$  which is  $\ln(Z) = 9$  below the highest evidence. This corresponds to a  $9\sigma$  difference from  $N_a = 8, N_\beta = 7$  making any model averaging technique simply reduce to outright selecting  $N_a = 8, N_\beta = 7$ . In Figure 6.11, models with  $\ln(Z) < 0$  are labeled with 0. Models with this level of Bayesian evidence have systematics multiple orders of magnitude larger than the signal, making recovery of the 21-cm impossible. Note that models with  $N_a = 0$  correspond to foreground models without any amplitude scale factors. Referring to the models with  $N_a = 0$ , i.e. first column in Figure 6.11, it is evident that increasing the number of spectral regions, even to  $N_\beta = 18$  cannot compensate for the systematics caused by the foreground amplitude errors. Thus amplitude errors in the foreground basemap cannot account for using a foreground model with spectral and linear offset parameters. Similarly by examining the bottom row in Figure 6.12 (i.e,  $N_\beta = 1$ ) we can see that increasing  $N_a$  to 32 regions does not account for the spectral errors in the dataset. Qualitatively, we find that above a threshold value of  $N_a$  and  $N_\beta$  that there is a trade-off between the number of spectral regions and number of amplitude scale factor regions.

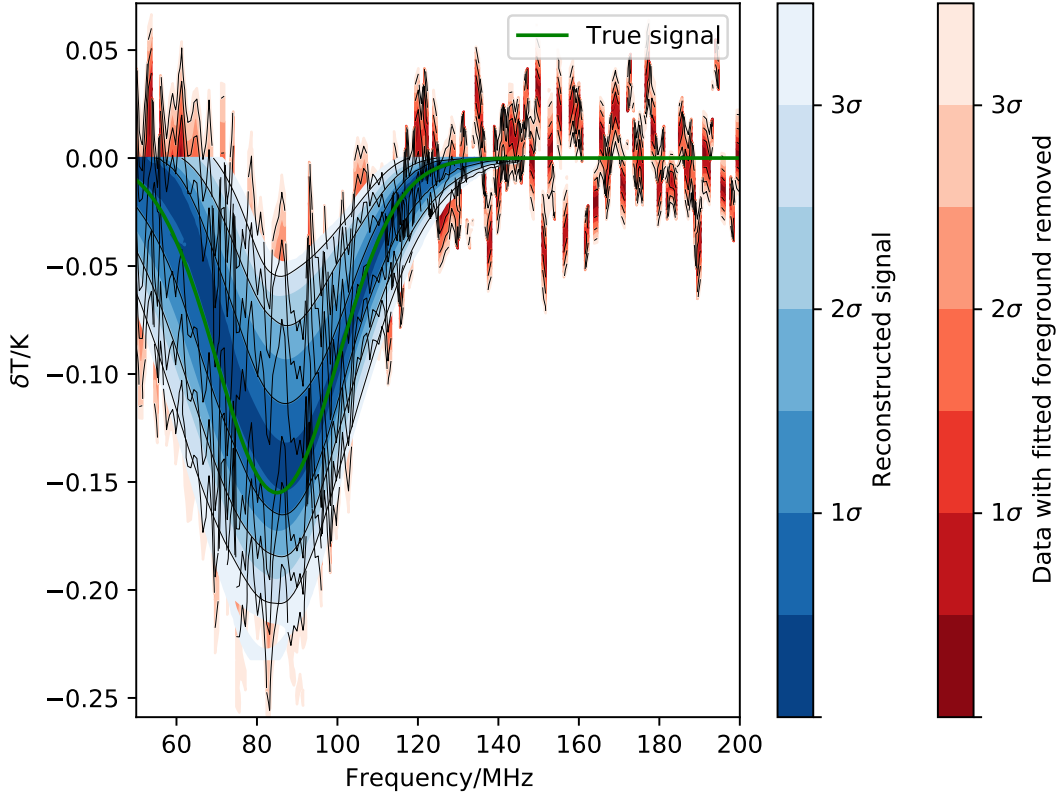


**Figure 6.12:** Signal recovery plot for the Bayesian evidence maximizing model ( $N_a = 7$ ,  $N_\beta = 8$ ) of Figure 6.11. The blue curve indicates the temperature of the fitted 21-cm model while the red curve represents the dataset with the fitted foreground removed. The green curve indicates the simulated 21-cm signal that was inside the dataset.

In Figure 6.12 we show the recovered 21-cm signal for  $N_a = 8$ ,  $N_\beta = 7$  which maximizes the Bayesian evidence. Recall from Section 6.6 that our fiducial signal model has amplitude  $A_{21} = 0.155K$ , standard deviation  $\sigma_{21} = 15\text{MHz}$  and centering frequency  $\nu_{21} = 85$ . Note that the mean amplitude, standard deviation and centering frequency of the recovered 21-cm signal is  $0.136K$ ,  $16.1\text{MHz}$ , and  $85.6\text{MHz}$ . Thus we find that all of the signal parameters are within  $1\sigma$  of the true values.

## 6.7 Conclusion

Detection of the global 21-cm signal is key to our understanding of CD and the EoR. Unfortunately, foreground contaminants are orders of magnitude brighter than all theoretical models of the cosmological signal. While there do exist scientifically interesting constraints that can be made even in the face of imperfect foreground removal (especially when combined with other probes; [4]), realizing the full potential of global 21-cm signal measurements requires a robust foreground mitigation program. Global 21-cm signal experiments which forward model the instrument, the systematics and radio contaminants have the potential to provide us the strongest constraints on the global 21-cm signal. However forward models of the foregrounds rely on observations of the radio sky which lack detailed uncertainty characterisation. Thus approaches that forward model the foregrounds are potentially limited by our empirical knowledge of the temperature of the radio sky. In this paper we have introduced a framework which is able to account for temperature deviations in the radio sky relative to our model foreground map in global 21-cm experiments. We have constructed a foreground model where the sky is segmented into different regions, each with an associated multiplicative scale factor which can adjust the amplitude of the foregrounds for that sub-region of the sky. By fitting for these amplitude scale factors within our Bayesian framework, we can account for temperature perturbations in the true radio sky relative to our foreground model. We select the number of sub-regions in our model by computing the Bayesian Evidence for a large range of  $N_a$  and select the model which maximizes the Bayesian evidence. Though we use the REACH experiment as our fiducial 21-cm experiment, our method is applicable to any global 21-cm experiment.

Since there are no definitive models that describe the amplitude and morphology of the errors in radio sky maps, we parametrically produce a range of simulated foreground errors by drawing a Gaussian noise realisation from the 408MHz absolute error map and then parametrically smoothing the map with a Gaussian beam with various FWHM. We perform our analysis with and without spectral complexity in the sky. We find in either scenario that our framework is effective at reducing the systematics in the analysis due to the presence of the foreground map errors allowing us to

recover the 21-cm signal without bias. We find that our approach is limited by our knowledge of the nature of the errors in the radio sky. Thus our work shows that more work on modelling the foreground errors is needed in order to maximize the effectiveness of our approach. Going forward we might have access to full error covariance in which case we can improve on this approach. With information regarding the correlation structure of the foreground errors we can more effectively construct the regions to match the error structure in the dataset. Since the scale factors are essentially multiplicative factors in the map, defining the regions using a map which informs the model about the location of the amplitude perturbations is an ideal scenario. Without any existing work on foreground error maps, we use the morphology of the Galaxy to define our regions. This conservative approach demonstrates how well our model can do without detailed knowledge of the true error structure. We show that even when using a conservative error map to define these regions, our method is able to construct a sufficiently high fidelity model for the foregrounds for unbiased recovery of the global 21-cm signal. Thus, we have shown that the base-map error fitting framework presented here, in combination with the spectral structure fitting methodology presented in [2], represents a powerful tool for detecting the 21cm global signal.

## **Acknowledgements**

The authors wish to recognize the contributions of Avery Kim and are delighted to acknowledge helpful discussions with Jordan Mirocha, Hannah Fronenberg, Jonathan Sievers. We acknowledge support from the New Frontiers in Research Fund Exploration grant program, a Natural Sciences and Engineering Research Council of Canada (NSERC) Discovery Grant and a Discovery Launch Supplement, the Sloan Research Fellowship, the William Dawson Scholarship at McGill, as well as the Canadian Institute for Advanced Research (CIFAR) Azrieli Global Scholars program. This research was enabled in part by support provided by Calcul Quebec ([www.calculquebec.ca](http://www.calculquebec.ca)), WestGrid ([www.westgrid.ca](http://www.westgrid.ca)) and Compute Canada ([www.computecanada.ca](http://www.computecanada.ca))

## Data Availability

The software code underlying this article will be shared on reasonable request to the corresponding author.

## Bibliography

- [1] Dominic Anstey, John Cumner, Eloy de Lera Acedo, and Will Handley. Informing antenna design for sky-averaged 21-cm experiments using a simulated Bayesian data analysis pipeline. *MNRAS*, 509(4):4679–4693, February 2022.
- [2] Dominic Anstey, Eloy de Lera Acedo, and Will Handley. A general Bayesian framework for foreground modelling and chromaticity correction for global 21 cm experiments. *MNRAS*, 506(2):2041–2058, September 2021.
- [3] Rennan Barkana. Possible interaction between baryons and dark-matter particles revealed by the first stars. *Nature*, 555(7694):71–74, March 2018.
- [4] Joëlle-Marie Bégin, Adrian Liu, and Adélie Gorce. Joint constraints on reionization: A framework for combining the global 21 cm signal and the kinetic Sunyaev-Zel’dovich effect. *Phys. Rev. D*, 105(8):083503, April 2022.
- [5] G. Bernardi, A. G. de Bruyn, M. A. Brentjens, B. Ciardi, G. Harker, V. Jelić, L. V. E. Koopmans, P. Labropoulos, A. Offringa, V. N. Pandey, J. Schaye, R. M. Thomas, S. Yatawatta, and S. Zaroubi. Foregrounds for observations of the cosmological 21 cm line. I. First Westerbork measurements of Galactic emission at 150 MHz in a low latitude field. *A&A*, 500(3):965–979, June 2009.
- [6] G. Bernardi, A. G. de Bruyn, G. Harker, M. A. Brentjens, B. Ciardi, V. Jelić, L. V. E. Koopmans, P. Labropoulos, A. Offringa, V. N. Pandey, J. Schaye, R. M. Thomas, S. Yatawatta, and S. Zaroubi. Foregrounds for observations of the cosmological 21 cm line. II. Westerbork

- observations of the fields around 3C 196 and the North Celestial Pole. *A&A*, 522:A67, November 2010.
- [7] G. Bernardi, J. T. L. Zwart, D. Price, L. J. Greenhill, A. Mesinger, J. Dowell, T. Eftekhari, S. W. Ellingson, J. Kocz, and F. Schinzel. Bayesian constraints on the global 21-cm signal from the Cosmic Dawn. *MNRAS*, 461(3):2847–2855, September 2016.
- [8] H. T. J. Bevens, W. J. Handley, A. Fialkov, E. de Lera Acedo, L. J. Greenhill, and D. C. Price. MAXSMOOTH: rapid maximally smooth function fitting with applications in Global 21-cm cosmology. *MNRAS*, 502(3):4405–4425, April 2021.
- [9] Judd D. Bowman, Miguel F. Morales, and Jacqueline N. Hewitt. Foreground Contamination in Interferometric Measurements of the Redshifted 21 cm Power Spectrum. *ApJ*, 695(1):183–199, April 2009.
- [10] Judd D. Bowman, Alan E. E. Rogers, and Jacqueline N. Hewitt. Toward Empirical Constraints on the Global Redshifted 21 cm Brightness Temperature During the Epoch of Reionization. *ApJ*, 676(1):1–9, March 2008.
- [11] Judd D. Bowman, Alan E. E. Rogers, Raul A. Monsalve, Thomas J. Mozdzen, and Nivedita Mahesh. An absorption profile centred at 78 megahertz in the sky-averaged spectrum. *Nature*, 555(7694):67–70, March 2018.
- [12] Richard F. Bradley, Keith Tauscher, David Rapetti, and Jack O. Burns. A Ground Plane Artifact that Induces an Absorption Profile in Averaged Spectra from Global 21 cm Measurements, with Possible Application to EDGES. *ApJ*, 874(2):153, April 2019.
- [13] Aviad Cohen, Anastasia Fialkov, Rennan Barkana, and Matan Lotem. Charting the parameter space of the global 21-cm signal. *MNRAS*, 472(2):1915–1931, December 2017.
- [14] Eloy de Lera Acedo. Reach: Radio experiment for the analysis of cosmic hydrogen. *2019 International Conference on Electromagnetics in Advanced Applications (ICEAA)*, pages 0626–0629, 2019.

- [15] Angélica de Oliveira-Costa, Max Tegmark, B. M. Gaensler, Justin Jonas, T. L. Landecker, and Patricia Reich. A model of diffuse Galactic radio emission from 10 MHz to 100 GHz. *MNRAS*, 388(1):247–260, July 2008.
- [16] David R. DeBoer, Aaron R. Parsons, James E. Aguirre, Paul Alexander, Zaki S. Ali, Adam P. Beardsley, Gianni Bernardi, Judd D. Bowman, Richard F. Bradley, Chris L. Carilli, Carina Cheng, Eloy de Lera Acedo, Joshua S. Dillon, Aaron Ewall-Wice, Gcobisa Fadana, Nicolas Fagnoni, Randall Fritz, Steve R. Furlanetto, Brian Glendenning, Bradley Greig, Jasper Grobbelaar, Bryna J. Hazelton, Jacqueline N. Hewitt, Jack Hickish, Daniel C. Jacobs, Austin Julius, MacCalvin Kariseb, Saul A. Kohn, Telalo Lekalake, Adrian Liu, Anita Loots, David MacMahon, Lourence Malan, Cresshim Malgas, Matthys Maree, Zachary Martinot, Nathan Mathison, Eunice Matsetela, Andrei Mesinger, Miguel F. Morales, Abraham R. Neben, Nipanjana Patra, Samantha Pieterse, Jonathan C. Pober, Nima Razavi-Ghods, Jon Ringuette, James Robnett, Kathryn Rosie, Raddwine Sell, Craig Smith, Angelo Syce, Max Tegmark, Nithyanandan Thyagarajan, Peter K. G. Williams, and Haoxuan Zheng. Hydrogen Epoch of Reionization Array (HERA). *PASP*, 129(974):045001, April 2017.
- [17] P. E. Dewdney, P. J. Hall, R. T. Schilizzi, and T. J. L. W. Lazio. The Square Kilometre Array. *IEEE Proceedings*, 97(8):1482–1496, August 2009.
- [18] A. Ewall-Wice, T. C. Chang, J. Lazio, O. Doré, M. Seiffert, and R. A. Monsalve. Modeling the Radio Background from the First Black Holes at Cosmic Dawn: Implications for the 21 cm Absorption Amplitude. *ApJ*, 868(1):63, November 2018.
- [19] Anastasia Fialkov and Rennan Barkana. Signature of excess radio background in the 21-cm global signal and power spectrum. *MNRAS*, 486(2):1763–1773, June 2019.
- [20] Anastasia Fialkov, Rennan Barkana, and Matt Jarvis. Extracting the global signal from 21-cm fluctuations: the multitracer approach. *MNRAS*, 491(3):3108–3119, January 2020.
- [21] George B. Field. Excitation of the Hydrogen 21-CM Line. *Proceedings of the IRE*, 46:240–250, January 1958.

- [22] Steven R. Furlanetto. The global 21-centimeter background from high redshifts. *MNRAS*, 371(2):867–878, September 2006.
- [23] Steven R. Furlanetto, S. Peng Oh, and Frank H. Briggs. Cosmology at low frequencies: The 21 cm transition and the high-redshift Universe. *Phys. Rep*, 433(4-6):181–301, October 2006.
- [24] Liron Gleser, Adi Nusser, and Andrew J. Benson. Decontamination of cosmological 21-cm maps. *MNRAS*, 391(1):383–398, November 2008.
- [25] A. E. Guzmán, J. May, H. Alvarez, and K. Maeda. All-sky Galactic radiation at 45 MHz and spectral index between 45 and 408 MHz. *A&A*, 525:A138, January 2011.
- [26] W. J. Handley, M. P. Hobson, and A. N. Lasenby. POLYCHORD: nested sampling for cosmology. *MNRAS*, 450:L61–L65, June 2015.
- [27] W. J. Handley, M. P. Hobson, and A. N. Lasenby. POLYCHORD: next-generation nested sampling. *MNRAS*, 453(4):4384–4398, November 2015.
- [28] Geraint Harker, Saleem Zaroubi, Gianni Bernardi, Michiel A. Brentjens, A. G. de Bruyn, Benedetta Ciardi, Vibor Jelić, Leon V. E. Koopmans, Panagiotis Labropoulos, Garreth Mellema, André Offringa, V. N. Pandey, Joop Schaye, Rajat M. Thomas, and Sarod Yatawatta. Non-parametric foreground subtraction for 21-cm epoch of reionization experiments. *MNRAS*, 397(2):1138–1152, August 2009.
- [29] Geraint J. A. Harker, Jonathan R. Pritchard, Jack O. Burns, and Judd D. Bowman. An MCMC approach to extracting the global 21-cm signal during the cosmic dawn from sky-averaged radio observations. *MNRAS*, 419(2):1070–1084, January 2012.
- [30] J. Colin Hill and Eric J. Baxter. Can early dark energy explain EDGES? *J. Cosmology Astropart. Phys.*, 2018(8):037, August 2018.
- [31] Richard Hills, Girish Kulkarni, P. Daniel Meerburg, and Ewald Puchwein. Concerns about modelling of the EDGES data. *Nature*, 564(7736):E32–E34, December 2018.

- [32] T. L. Landecker and R. Wielebinski. The Galactic Metre Wave Radiation: A two-frequency survey between declinations  $+25^\circ$  and  $-25^\circ$  and the preparation of a map of the whole sky. *Australian Journal of Physics Astrophysical Supplement*, 16:1, January 1970.
- [33] Adrian Liu and Aaron R. Parsons. Constraining cosmology and ionization history with combined 21 cm power spectrum and global signal measurements. *MNRAS*, 457(2):1864–1877, April 2016.
- [34] Adrian Liu, Jonathan R. Pritchard, Max Tegmark, and Abraham Loeb. Global 21 cm signal experiments: A designer’s guide. *Phys. Rev. D*, 87(4):043002, February 2013.
- [35] Adrian Liu and J. Richard Shaw. Data Analysis for Precision 21 cm Cosmology. *PASP*, 132(1012):062001, June 2020.
- [36] Adrian Liu, Max Tegmark, Judd Bowman, Jacqueline Hewitt, and Matias Zaldarriaga. An improved method for 21-cm foreground removal. *MNRAS*, 398(1):401–406, September 2009.
- [37] Adrian Liu, Max Tegmark, and Matias Zaldarriaga. Will point sources spoil 21-cm tomography? *MNRAS*, 394(3):1575–1587, April 2009.
- [38] C. J. Lonsdale, R. J. Cappallo, M. F. Morales, F. H. Briggs, L. Benkevitch, J. D. Bowman, J. D. Bunton, S. Burns, B. E. Corey, L. Desouza, S. S. Doeleman, M. Derome, A. Deshpande, M. R. Gopala, L. J. Greenhill, D. E. Herne, J. N. Hewitt, P. A. Kamini, J. C. Kasper, B. B. Kincaid, J. Kocz, E. Kowald, E. Kratzenberg, D. Kumar, M. J. Lynch, S. Madhavi, M. Matejek, D. A. Mitchell, E. Morgan, D. Oberoi, S. Ord, J. Pathikulangara, T. Prabu, A. Rogers, A. Roshi, J. E. Salah, R. J. Sault, N. U. Shankar, K. S. Srivani, J. Stevens, S. Tingay, A. Vaccarella, M. Waterson, R. B. Wayth, R. L. Webster, A. R. Whitney, A. Williams, and C. Williams. The Murchison Widefield Array: Design Overview. *IEEE Proceedings*, 97(8):1497–1506, August 2009.
- [39] Jordan Mirocha. Astrophysics from the 21-cm background. *arXiv e-prints*, page arXiv:1909.12595, September 2019.

- [40] Jordan Mirocha, Henri Lamarre, and Adrian Liu. Systematic uncertainties in models of the cosmic dawn. *MNRAS*, 504(2):1555–1564, June 2021.
- [41] Steven G. Murray, Judd D. Bowman, Peter H. Sims, Nivedita Mahesh, Alan E. E. Rogers, Raul A. Monsalve, Titu Samson, and Akshatha Konakondula Vydula. A bayesian calibration framework for EDGES. *MNRAS*, September 2022.
- [42] Gregory Paciga, Joshua G. Albert, Kevin Bandura, Tzu-Ching Chang, Yashwant Gupta, Christopher Hirata, Julia Odegova, Ue-Li Pen, Jeffrey B. Peterson, Jayanta Roy, J. Richard Shaw, Kris Sigurdson, and Tabitha Voytek. A simulation-calibrated limit on the H I power spectrum from the GMRT Epoch of Reionization experiment. *MNRAS*, 433(1):639–647, July 2013.
- [43] Aaron R. Parsons, Donald C. Backer, Griffin S. Foster, Melvyn C. H. Wright, Richard F. Bradley, Nicole E. Gugliucci, Chaitali R. Parashare, Erin E. Benoit, James E. Aguirre, Daniel C. Jacobs, Chris L. Carilli, David Herne, Mervyn J. Lynch, Jason R. Manley, and Daniel J. Werthimer. The Precision Array for Probing the Epoch of Re-ionization: Eight Station Results. *AJ*, 139(4):1468–1480, April 2010.
- [44] L. Philip, Z. Abdurashidova, H. C. Chiang, N. Ghazi, A. Gumba, H. M. Heilgendorff, J. M. Jáuregui-García, K. Malepe, C. D. Nunhokee, J. Peterson, J. L. Sievers, V. Simes, and R. Spann. Probing Radio Intensity at High-Z from Marion: 2017 Instrument. *Journal of Astronomical Instrumentation*, 8(2):1950004, January 2019.
- [45] Planck Collaboration, P. A. R. Ade, N. Aghanim, M. Arnaud, M. Ashdown, J. Aumont, C. Baccigalupi, A. J. Banday, R. B. Barreiro, J. G. Bartlett, N. Bartolo, E. Battaner, R. Battye, K. Benabed, A. Benoît, A. Benoit-Lévy, J. P. Bernard, M. Bersanelli, P. Bielewicz, J. J. Bock, A. Bonaldi, L. Bonavera, J. R. Bond, J. Borrill, F. R. Bouchet, F. Boulanger, M. Bucher, C. Burigana, R. C. Butler, E. Calabrese, J. F. Cardoso, A. Catalano, A. Challinor, A. Chamballu, R. R. Chary, H. C. Chiang, J. Chluba, P. R. Christensen, S. Church, D. L. Clements, S. Colombi, L. P. L. Colombo, C. Combet, A. Coulais, B. P. Crill, A. Curto,

F. Cuttaia, L. Danese, R. D. Davies, R. J. Davis, P. de Bernardis, A. de Rosa, G. de Zotti, J. Delabrouille, F. X. Désert, E. Di Valentino, C. Dickinson, J. M. Diego, K. Dolag, H. Dole, S. Donzelli, O. Doré, M. Douspis, A. Ducout, J. Dunkley, X. Dupac, G. Efstathiou, F. Elsner, T. A. Enßlin, H. K. Eriksen, M. Farhang, J. Fergusson, F. Finelli, O. Forni, M. Frailis, A. A. Fraisse, E. Franceschi, A. Frejsel, S. Galeotta, S. Galli, K. Ganga, C. Gauthier, M. Gerbino, T. Ghosh, M. Giard, Y. Giraud-Héraud, E. Giusarma, E. Gjerløw, J. González-Nuevo, K. M. Górski, S. Gratton, A. Gregorio, A. Gruppuso, J. E. Gudmundsson, J. Hamann, F. K. Hansen, D. Hanson, D. L. Harrison, G. Helou, S. Henrot-Versillé, C. Hernández-Monteagudo, D. Herranz, S. R. Hildebrandt, E. Hivon, M. Hobson, W. A. Holmes, A. Hornstrup, W. Hovest, Z. Huang, K. M. Huffenberger, G. Hurier, A. H. Jaffe, T. R. Jaffe, W. C. Jones, M. Juvela, E. Keihänen, R. Keskitalo, T. S. Kisner, R. Kneissl, J. Knoche, L. Knox, M. Kunz, H. Kurki-Suonio, G. Lagache, A. Lähteenmäki, J. M. Lamarre, A. Lasenby, M. Lattanzi, C. R. Lawrence, J. P. Leahy, R. Leonardi, J. Lesgourgues, F. Levrier, A. Lewis, M. Liguori, P. B. Lilje, M. Linden-Vørnle, M. López-Caniego, P. M. Lubin, J. F. Macías-Pérez, G. Maggio, D. Maino, N. Mandolesi, A. Mangilli, A. Marchini, M. Maris, P. G. Martin, M. Martinelli, E. Martínez-González, S. Masi, S. Matarrese, P. McGehee, P. R. Meinhold, A. Melchiorri, J. B. Melin, L. Mendes, A. Mennella, M. Migliaccio, M. Millea, S. Mitra, M. A. Miville-Deschênes, A. Moneti, L. Montier, G. Morgante, D. Mortlock, A. Moss, D. Munshi, J. A. Murphy, P. Naselsky, F. Nati, P. Natoli, C. B. Netterfield, H. U. Nørgaard-Nielsen, F. Noviello, D. Novikov, I. Novikov, C. A. Oxborrow, F. Paci, L. Pagano, F. Pajot, R. Paladini, D. Paoletti, B. Partridge, F. Pasian, G. Patanchon, T. J. Pearson, O. Perdereau, L. Perotto, F. Perrotta, V. Pettorino, F. Piacentini, M. Piat, E. Pierpaoli, D. Pietrobon, S. Plaszczynski, E. Pointecouteau, G. Polenta, L. Popa, G. W. Pratt, G. Prézeau, S. Prunet, J. L. Puget, J. P. Rachen, W. T. Reach, R. Rebolo, M. Reinecke, M. Remazeilles, C. Renault, A. Renzi, I. Ristorcelli, G. Rocha, C. Rosset, M. Rossetti, G. Roudier, B. Rouillé d'Orfeuill, M. Rowan-Robinson, J. A. Rubiño-Martín, B. Rusholme, N. Said, V. Salvatelli, L. Salvati, M. Sandri, D. Santos, M. Savelainen, G. Savini, D. Scott, M. D. Seiffert, P. Serra, E. P. S. Shellard, L. D. Spencer, M. Spinelli, V. Stolyarov, R. Stompor, R. Sudiwala, R. Sunyaev, D. Sutton, A. S. Suur-Uski,

- J. F. Sygnet, J. A. Tauber, L. Terenzi, L. Toffolatti, M. Tomasi, M. Tristram, T. Trombetti, M. Tucci, J. Tuovinen, M. Türler, G. Umana, L. Valenziano, J. Valiviita, F. Van Tent, P. Vielva, F. Villa, L. A. Wade, B. D. Wandelt, I. K. Wehus, M. White, S. D. M. White, A. Wilkinson, D. Yvon, A. Zacchei, and A. Zonca. Planck 2015 results. XIII. Cosmological parameters. *A&A*, 594:A13, September 2016.
- [46] D. C. Price, L. J. Greenhill, A. Fialkov, G. Bernardi, H. Garsden, B. R. Barsdell, J. Kocz, M. M. Anderson, S. A. Bourke, J. Craig, M. R. Dexter, J. Dowell, M. W. Eastwood, T. Eftekhari, S. W. Ellingson, G. Hallinan, J. M. Hartman, R. Kimberk, T. Joseph W. Lazio, S. Leiker, D. MacMahon, R. Monroe, F. Schinzel, G. B. Taylor, E. Tong, D. Werthimer, and D. P. Woody. Design and characterization of the Large-aperture Experiment to Detect the Dark Age (LEDA) radiometer systems. *MNRAS*, 478(3):4193–4213, August 2018.
- [47] Jonathan R. Pritchard and Abraham Loeb. 21 cm cosmology in the 21st century. *Reports on Progress in Physics*, 75(8):086901, August 2012.
- [48] David Rapetti, Keith Tauscher, Jordan Mirocha, and Jack O. Burns. Global 21 cm Signal Extraction from Foreground and Instrumental Effects. II. Efficient and Self-consistent Technique for Constraining Nonlinear Signal Models. *ApJ*, 897(2):174, July 2020.
- [49] Itamar Reis, Anastasia Fialkov, and Rennan Barkana. The subtlety of Ly  $\alpha$  photons: changing the expected range of the 21-cm signal. *MNRAS*, 506(4):5479–5493, October 2021.
- [50] M. Remazeilles, C. Dickinson, A. J. Banday, M. A. Bigot-Sazy, and T. Ghosh. An improved source-subtracted and destriped 408-MHz all-sky map. *MNRAS*, 451(4):4311–4327, August 2015.
- [51] P. A. Shaver, R. A. Windhorst, P. Madau, and A. G. de Bruyn. Can the reionization epoch be detected as a global signature in the cosmic background? *A&A*, 345:380–390, May 1999.
- [52] Emma Shen, Dominic Anstey, Eloy de Lera Acedo, Anastasia Fialkov, and Will Handley. Quantifying ionospheric effects on global 21-cm observations. *MNRAS*, 503(1):344–353, May 2021.

- [53] Peter H. Sims and Jonathan C. Pober. Testing for calibration systematics in the EDGES low-band data using Bayesian model selection. *MNRAS*, 492(1):22–38, February 2020.
- [54] Peter H. Sims and Jonathan C. Pober. Testing for calibration systematics in the EDGES low-band data using Bayesian model selection. *MNRAS*, 492(1):22–38, February 2020.
- [55] Peter H. Sims, Jonathan C. Pober, and Jonathan L. Sievers. A Bayesian approach to high fidelity interferometric calibration I: mathematical formalism. *arXiv e-prints*, page arXiv:2206.13554, June 2022.
- [56] Peter H. Sims, Jonathan C. Pober, and Jonathan L. Sievers. A Bayesian approach to high fidelity interferometric calibration II: demonstration with simulated data. *MNRAS*, July 2022.
- [57] Saurabh Singh, Nambissan T. Jishnu, Ravi Subrahmanyan, N. Udaya Shankar, B. S. Girish, A. Raghunathan, R. Somashekar, K. S. Srivani, and Mayuri Sathyanarayana Rao. On the detection of a cosmic dawn signal in the radio background. *Nature Astronomy*, 6:607–617, February 2022.
- [58] Saurabh Singh and Ravi Subrahmanyan. The Redshifted 21 cm Signal in the EDGES Low-band Spectrum. *ApJ*, 880(1):26, July 2019.
- [59] Saurabh Singh, Ravi Subrahmanyan, N. Udaya Shankar, Mayuri Sathyanarayana Rao, Anastasia Fialkov, Aviad Cohen, Rennan Barkana, B. S. Girish, A. Raghunathan, R. Somashekar, and K. S. Srivani. First Results on the Epoch of Reionization from First Light with SARAS 2. *ApJ*, 845(2):L12, August 2017.
- [60] Marcin Sokolowski, Steven E. Tremblay, Randall B. Wayth, Steven J. Tingay, Nathan Clarke, Paul Roberts, Mark Waterson, Ronald D. Ekers, Peter Hall, Morgan Lewis, Mehran Mossammaparast, Shantanu Padhi, Franz Schlagenhauser, Adrian Sutinjo, and Jonathan Tinker. BIGHORNS - Broadband Instrument for Global HydrOgen ReioNisation Signal. *Publ. Astron. Soc. Australia*, 32:e004, February 2015.

- [61] Keith Tauscher, David Rapetti, and Jack O. Burns. Global 21 cm Signal Extraction from Foreground and Instrumental Effects. III. Utilizing Drift-scan Time Dependence and Full Stokes Measurements. *ApJ*, 897(2):175, July 2020.
- [62] Keith Tauscher, David Rapetti, Jack O. Burns, and Eric Switzer. Global 21 cm Signal Extraction from Foreground and Instrumental Effects. I. Pattern Recognition Framework for Separation Using Training Sets. *ApJ*, 853(2):187, February 2018.
- [63] Keith Tauscher, David Rapetti, Bang D. Nhan, Alec Handy, Neil Bassett, Joshua Hibbard, David Bordenave, Richard F. Bradley, and Jack O. Burns. Global 21 cm Signal Extraction from Foreground and Instrumental Effects. IV. Accounting for Realistic Instrument Uncertainties and Their Overlap with Foreground and Signal Models. *ApJ*, 915(1):66, July 2021.
- [64] M. P. van Haarlem, M. W. Wise, A. W. Gunst, G. Heald, J. P. McKean, J. W. T. Hessels, A. G. de Bruyn, R. Nijboer, J. Swinbank, R. Fallows, M. Brentjens, A. Nelles, R. Beck, H. Falcke, R. Fender, J. Hörandel, L. V. E. Koopmans, G. Mann, G. Miley, H. Röttgering, B. W. Stappers, R. A. M. J. Wijers, S. Zaroubi, M. van den Akker, A. Alexov, J. Anderson, K. Anderson, A. van Ardenne, M. Arts, A. Asgekar, I. M. Avruch, F. Batejat, L. Bähren, M. E. Bell, M. R. Bell, I. van Bemmelen, P. Bennema, M. J. Bentum, G. Bernardi, P. Best, L. Bîrzan, A. Bonafede, A. J. Boonstra, R. Braun, J. Bregman, F. Breitling, R. H. van de Brink, J. Broderick, P. C. Broekema, W. N. Brouw, M. Brüggen, H. R. Butcher, W. van Cappellen, B. Ciardi, T. Coenen, J. Conway, A. Coolen, A. Corstanje, S. Damstra, O. Davies, A. T. Deller, R. J. Dettmar, G. van Diepen, K. Dijkstra, P. Donker, A. Doorduyn, J. Dromer, M. Drost, A. van Duin, J. Eislöffel, J. van Enst, C. Ferrari, W. Frieswijk, H. Gankema, M. A. Garrett, F. de Gasperin, M. Gerbers, E. de Geus, J. M. Grießmeier, T. Grit, P. Gruppen, J. P. Hamaker, T. Hassall, M. Hoeft, H. A. Holties, A. Horneffer, A. van der Horst, A. van Houwelingen, A. Huijgen, M. Iacobelli, H. Intema, N. Jackson, V. Jelic, A. de Jong, E. Jette, D. Kant, A. Karastergiou, A. Koers, H. Kollen, V. I. Kondratiev, E. Kooistra, Y. Koopman, A. Koster, M. Kuniyoshi, M. Kramer, G. Kuper, P. Lambropoulos, C. Law, J. van Leeuwen, J. Lemaitre, M. Loose, P. Maat, G. Macario, S. Markoff, J. Masters, R. A. McFadden, D. McKay-Bukowski, H. Meijering,

H. Meulman, M. Mevius, E. Middelberg, R. Millenaar, J. C. A. Miller-Jones, R. N. Mohan, J. D. Mol, J. Morawietz, R. Morganti, D. D. Mulcahy, E. Mulder, H. Munk, L. Nieuwenhuis, R. van Nieuwpoort, J. E. Noordam, M. Norden, A. Noutsos, A. R. Offringa, H. Olofsson, A. Omar, E. Orrú, R. Overeem, H. Paas, M. Pandey-Pommier, V. N. Pandey, R. Pizzo, A. Polatidis, D. Rafferty, S. Rawlings, W. Reich, J. P. de Reijer, J. Reitsma, G. A. Renting, P. Riemers, E. Rol, J. W. Romein, J. Roosjen, M. Rüter, A. Scaife, K. van der Schaaf, B. Scheers, P. Schellart, A. Schoenmakers, G. Schoonderbeek, M. Serylak, A. Shulevski, J. Sluman, O. Smirnov, C. Sobey, H. Spreeuw, M. Steinmetz, C. G. M. Sterks, H. J. Stiepel, K. Stuurwold, M. Tagger, Y. Tang, C. Tasse, I. Thomas, S. Thoudam, M. C. Toribio, B. van der Tol, O. Usov, M. van Veelen, A. J. van der Veen, S. ter Veen, J. P. W. Verbiest, R. Vermeulen, N. Vermaas, C. Vocks, C. Vogt, M. de Vos, E. van der Wal, R. van Weeren, H. Weggemans, P. Weltevrede, S. White, S. J. Wijnholds, T. Wilhelmsson, O. Wucknitz, S. Yatawatta, P. Zarka, A. Zensus, and J. van Zwieten. LOFAR: The LOw-Frequency ARray. *A&A*, 556:A2, August 2013.

[65] S. A. Wouthuysen. On the excitation mechanism of the 21-cm (radio-frequency) interstellar hydrogen emission line. *AJ*, 57:31–32, January 1952.

[66] H. Zheng, M. Tegmark, J. S. Dillon, D. A. Kim, A. Liu, A. R. Neben, J. Jonas, P. Reich, and W. Reich. An improved model of diffuse galactic radio emission from 10 MHz to 5 THz. *MNRAS*, 464(3):3486–3497, January 2017.

# Chapter 7

## Conclusion

In this thesis we explored solutions to some of the systematic challenges facing 21cm instruments. We also developed new theoretical tools that can be used to place constraints on the EoR.

In Chapter 2 we developed a procedure capable of producing a continuous range of density-ionization correlation scenarios. This is significant since density-ionization scenarios needed to be considered discretely prior to this work. Furthermore, we developed a parametrization ( $\beta$ ) capable of tracking these correlations and studied its dependence in the 21cm power spectrum. We then performed a forecast on the types of constraints that one can place on  $\beta$  using HERA measurements of the power spectrum. We showed that as upper limits on the 21cm power spectrum continue to decrease, and with errorbars at the level of 20mK, we can rule out uncorrelated reionization at 99% credibility.

In Chapters 3 and 4 we explored using indirect probes of the EoR. In Chapter 3 we explored using the DMs of high redshift FRBs as a probe of the EoR. Our work shows that the mean DM of high redshifts FRBs are sensitive to the details of reionization. We show that there is a flattening of the DM-z relation at high redshift corresponding to an increasingly neutral IGM. The timing and duration of the EoR will shift the properties of this flattening. Ultimately, we show that with measurement of  $10^4$  high redshift FRBs we can rule out uncorrelated reionization scenarios at 95% credibility.

In Chapter 4 we study how density-ionization correlation affects the observed statistics from LAE observations. In particular, we study how the clustering, number density and luminosity functions of the LAEs are affected by changing the density-ionization correlations. We use the  $\beta$  parametrization introduced in Chapter 2 to perform this study. We find that the clustering, number density and LAE luminosity function are sensitive to  $\beta$ . Using existing LAE observations at  $z = 6.6$  (Subaru survey), we place constraints on  $\beta$ . We find that the LAEs at  $z = 6.6$  alone cannot rule out uncorrelated or outside-in reionization scenarios. This is due to the weakening EoR signature at  $z = 6.6$ . However, by combining LAEs observations and power spectrum measurements from HERA one can rule out uncorrelated reionization scenarios at 99% credibility.

In Chapters 5 and 6 we turn to some of the systematics present in 21cm experiments. In Chapter 5 we study the errors introduced into the data analysis pipelines of 21cm instruments due to inpainting RFI corrupted data. We introduce a convolutional neural network (“U-Paint”) capable of inpainting RFI corrupted data in 21cm interferometric instruments. We perform our analysis on the visibilities as well as the power spectrum. We find that the inpainting techniques perform better when used on narrowband RFI as compared to wideband RFI. We also find that the inpainting techniques reliably capture the foreground dominated modes in the power spectrum.

In Chapter 6 we examine the systematics introduced into 21cm global signal experiments due to errors in radio sky maps. We show that the presence of errors in the foreground map can lead to biased recovery of the 21cm signal. Furthermore, we show this bias is proportional to amplitude and correlation length of the foreground map errors. We introduce a framework capable of accounting for these errors and show that, with our framework, one can recover unbiased estimates of the global 21cm signal.

The body of work presented in this thesis encompasses some of the theoretical tools that we are building to measure the EoR and the instrumental limitations that stand in the way. In Chapters 5 and 6 we show that we are making progress towards this goal. Our measurements are at the level of precision where the detailed error characterization of inpainting errors matters. In Chapter 6 we demonstrate that there are solutions to foreground mitigation. **We are making progress.** While there is still work to be done, this thesis shows that we are approaching a successful detection of

the EoR; this ultimate achievement will reveal one of the most interesting periods in our Universe's history.